A novel, generic approach to simulate bank retreat in alluvial river channels

Yannick Rousseau

A Thesis
In the Department
of
Geography, Planning and Environment

Presented in Partial Fulfillment of the Requirements
For the Degree of
Doctor of Philosophy (Geography, Urban and Environmental Studies) at
Concordia University
Montreal, Quebec, Canada

April 2018

CONCORDIA UNIVERSITY

SCHOOL OF GRADUATE STUDIES

This is to certify that the thesis prepared

By: Yannick Rousseau

Entitled: A Novel, Generic Approach To Simulate Bank Retreat In Alluvial River Channels

and submitted in partial fulfillment of the requirements for the degree of

Doctor Of Philosophy (Geography, Urban and Environmental Studies)

complies with the regulations of the University and meets the accepted standards with respect to originality and quality.

Signed by the final examining committee:

_____ Chair
Dr. Yves Gélinas

_____ External Examiner
Dr. Colin Rennie

_____ External to Program
Dr. S. Samuel Li

_____ Examiner
Dr. Jeannine-Marie St-Jacques

_____ Examiner
Dr. Leonard Sklar

_____ Thesis Co-Supervisor
Dr. Pascale Biron

_____ Thesis Co-Supervisor
Dr. Marco Van De Wiel

Approved by _____
Dr. Norma Rantisi, Graduate Program Director

Tuesday, June 5, 2018

_____
Dr. André Roy, Dean
Faculty of Arts and Science

Abstract

A novel, generic approach to simulate bank retreat in alluvial river channels

Yannick Rousseau, Ph.D.
Concordia University, 2018

Despite the importance of bank erosion in rivers, most computational fluid dynamics (CFD) models have limited capacity to examine bank retreat and channel-floodplain interactions, as they lack bank stability algorithms and ignore vegetation effects. This research seeks to develop a numerical model to improve our understanding of key properties of bank material and vegetation cover with respect to lateral erosion in river meanders at intermediate spatial (5–10 meander bends) and temporal (2–3 years) scales. Following a comparison of six different morphodynamic models for three sinuous laboratory configurations, the CFD model TELEMAC-2D was chosen to receive a newly developed bank retreat module that respects geotechnical principles and integrates spatial analysis concepts. It was tested against morphological datasets from two contrasted river reaches, the semi-alluvial Medway Creek (Ontario) and alluvial St. François River (Quebec). Statistical analysis, combined with the use of machine learning algorithms, demonstrate that the coupled model is able to fit observed bank retreat location and extent. Some local disagreement with observations along Medway Creek seems associated with the heterogeneity of soil material and stratigraphy, and in vegetation cover present at the field site. The coupled model was also used to identify key geotechnical parameters and optimal parameter values for the studied reaches. An epistemological reflection on the purpose of modelling in fluvial geomorphology leads to the conclusion that the primary model strength lies in its ability to provide explanations on bank retreat mechanisms. Further research should seek to test more thoroughly morphodynamic modelling in complex geomorphological environments.

Acknowledgements

The research summarized in this thesis would not have been possible without the contribution and support from friends, family, professors, and sponsors. In particular, I would like to thank:

My parents, Jean-Paul Rousseau and Lisette Girard, and sister, Marie-France, for supporting me, cheering up, and continually believing in my capacities;

Post-Dr Roberta Bgeginski for your presence, for teaching me organization skills and for suggesting tips against procrastination;

Dr. Eric Desjardins, for our weekly philosophical runs, and for introducing me to ultra trail running, which allowed me to maintain a balanced life during my studies;

Dr. Micha Pazner for being a wonderful human being, a good listener, a good cook and paddler.

Dr. Mohammad Reza Jelokhani Niaraki for our mid-afternoon conversations around a cup of tea;

Dr. Nathaniel Bergman for being an example of resilience, patience and strength, and for generously providing guidance and assistance during data collection and interpretation;

Renee Lazor for your emotional intelligence, and for inspiring me in becoming a better person. I greatly appreciated spending time with you in nature, and undertaking sushi expeditions;

Dr. Pauline Leduc, for our long walks fueled by schnitzel and Delirium Tremens, for your incredible stories, and for your optimism about life;

Mélanie Langlois for providing insights into career development, job search, and spatial analysis, in addition of supporting me emotionally during difficult times;

My supervisors, Dr. Pascale Biron and Dr. Marco Van de Wiel, for being very patient, especially during the model development stage, which took much longer than anticipated;

Dr. Pascale Biron for accompanying me throughout the first eleven years of my academic life, and for advising me soundly. You are a role model with respect to efficiency, professionalism and diplomacy. You are also a great human, always finding the right words to motivate;

Dr. Van de Wiel for his inspiring ability to present complex concepts effectively and for his availability for brainstorming. I greatly appreciated the fact that you included me in multiple projects to help me develop research, presentation and teaching skills;

Concordia University for its excellence in teaching, and Concordia students for being hard workers, socially responsible, environmentally conscious, and present in the community;

Professors from the department of Geography, Planning and Environment, including Dr. Catherine Moore, Dr. Judith Patterson, Dr. Damon Matthews and Dr. David Frost, that have aroused my scientific curiosity and altered my career path;

Dr. Claudine Boyer and Michèle Tremblay for sharing data for one of the field sites used in my research;

Hugues Lachance for inviting me to work at JFSA with his team of geomorphologists, biologists and hydraulic engineers, and providing me with plenty of challenging projects;

The Fonds de recherche du Québec - Nature et Technologies (FQRNT), the Ontario Graduate Scholarship (OGS) program, the Natural Sciences and Engineering Research Council (NSERC) Discovery program, and Concordia University for funding this research;

Anonymous reviews that have contributed to enhance the quality of chapters that have been submitted to scientific journals.

Contribution of Authors

The authors that contributed to the chapters of this thesis, which were submitted to scientific journals, are identified at the beginning of each chapter. Their affiliation is:

- Pascale Biron: Department of Geography, Planning and Environment, Concordia University, 1455 de Maisonneuve Blvd W., Montreal, Quebec, Canada, H3G 1M8
- Marco Van de Wiel: Center for Agroecology, Water and Resilience (CAWR), Coventry University, Coventry, United Kingdom, CV1 5FB
- Eric Desjardins: Department of Philosophy, Rotman Institute of Philosophy, University of Western Ontario, London, Ontario, Canada, N6A 5B8

All manuscripts, except the one submitted to the journal Earth Science Reviews, are directly linked to the primary purpose of this thesis, which is related to the development of an alternative type of morphodynamic modelling that can be used to simulate lateral adjustments in river channels and to the evaluation of this approach against data from the natural environment. In these chapters, the primary author devised numerical experiments, performed field work, developed the model, analysed datasets, and wrote scientific reports. Pascale Biron and Marco Van de Wiel provided a substantial amount of support with respect to planning, analysis and reporting.

The research behind the manuscript submitted to the journal Earth Science Reviews was initially not directly related to the topic addressed in this thesis. However, the model developed for this thesis ended up being a good example of the different modelling modes employed in fluvial geomorphology to carry research, and thus, was included in this thesis. In this manuscript, I wrote the section related to the model, and actively participated to the discussion and redaction.

Table of Contents

List of Figures

List of Tables

List of Equations

List of Special Symbols

Hydraulics

τ_0, τ_c	Shear stress (bed, critical) (kPa)
θ_c	Dimensionless Shields' criterion for incipient motion
S_0, S	Energy slope or longitudinal bed slope
R, B, H, L	Hydraulic radius, channel width, channel depth and channel length (m)
s	Planform sinuosity
λ	Longitudinal position of a cross-section in a meandering channel
ρ_s, γ_s	Mass density (kg/m^3) and weight density (N/m^3) of water
V, Q	Flow velocity (m/s) and discharge (m^3/s)
Fr	Froude number
$K_{Strickler}$, n	Bed roughness coefficient (Strickler or Manning scale)

Hydrology

k_{ASC}, k_{DESC}	Water table adjustment rates with respect to free surface elevation for rising and falling limbs of the hydrography
t_p	Peak time (hours)
Q_t, Q_p	Flow discharge at time t and t_p (m^3/s)
m	Shape parameter in time-contracted γ-distributed hydrograph

Sediment properties

c, ϕ	Soil cohesion (kPa) and friction angle (°)
ρ_s, γ_s	Mass density (kg/m^3) and weight density (N/m^3)
d_{50}	Mean grain size (mm)

Riparian vegetation

c_a	Apparent cohesion due to roots (kPa)
d_a	Root crown radius (m)
$a_{tree,,}$ h_{tree}	Tree age (years) and height (m)
$d_{base,}$ m_{trunk}	Trunk diameter at base (m) and mass (kg)

Physics

t	Time (seconds or hours)
g	Gravitational acceleration due to gravity (m/s^2)

Stability evaluation and genetic algorithm

$trLen$	Transect length (m)
η	Randomly generated crossover ratio [0,1]
$\vec{S}$	Solution, or potential slip surface
F_s	Factor of safety
m	m-term in Bishop (1955)'s equation
b, L	Slice width (m) and length of slice base (m)
α, β	Bank angle (°) and slice base angle (°)
δ	Angle between the result of hydrostatic confining force and normal to failure plane
U	Pore water pressure (kPa)
F_{cp}	Confining pressure exerted by the flow (kPa)
h, h_{wt}, h_{fs}	Bank height, height of water table above bank toe, water depth (m)
z_{WT}, z_{FS}	Elevation of water table and free surface (m)
z_b	Elevation at slice base (m)
W_w, W_s	Weight of water or soil (kg)
τ	Shear stress (kPa)
σ	Soil strength (kPa)

Statistics

J	Youden (1950)'s index of fit between observed and simulated retreat
TP, TN, FP, FN	Components of a confusion matrix, i.e., the number of true positives, true negatives, false positives and false negatives
μ, σ	Standard deviation and mean
P	Probability
erf	Error function

Epistemology

S	State of a system
P	Set of processes
E	External factor
S_0	Initial state of a system (at time zero)
S_t	State of a system at a time t

List of Abbreviations

Monitoring and modelling

CA	Cellular automata modelling
CFD	Computational fluid dynamics modelling
DEM	Digital elevation model
DGPS	Differential GPS
GPS	Global Positioning System
GSD	Grain size distribution
HIPS	Analytical formulation of bank retreat based on the work of Hasegawa (1977) and Ikeda et al. (1981)
LiDAR	Light Detection And Ranging
RMA	Reduced major axis regression statistical analysis
TIN	Triangular Irregular Network
USCS	Unified Soil Classification System
SSIIM	Simulation of Sediment movement In water Intakes with Multiblock option
CCHE	Model by the National Center for Computational Hydroscience and Engineering
iRIC	International River Interface Cooperative
FVM, FEM	Finite volume and finite element discretization schemes
k-ε	A turbulence closure model

Thesis research

HYD	Hydraulic module, e.g., TELEMAC-2D
SED	Sediment transport module, e.g., SISYPHE
GTC	Geotechnical module
RVG	Riparian vegetation module
MC	Medway Creek (field site #1)
SF	St. François River (field site #2)
M_{low}, M_{med}, M_{high}	Meandering channels with a sinuosity of 1.07, 1.51 and 3.70
B_2, C_2, N_2, T_2, T_3, S_3	BASEMENT, CCHE-2D, NAYS, TELEMAC-2D, 3D and SSIIM modelling codes
FL	Flume experiment in a meandering channel

1

Introduction

The term "meandering" refers to the winding character of artificial and natural elements, including rivers and submarine channels (Güneralp et al. 2012), which have long intrigued river scientists (Seminara 2006). Meandering rivers are frequent in low lands near human settlements, where conflicts often arise around the importance attributed to water consumption, economic activities, public security, land use (e.g., use of narrow riparian buffers), and ecological functions (Posner and Duan 2012). Degrading rivers and rising ecological awareness place high demand on the use of vegetation in river restoration (Nielsen 1996) to reduce bed erosion, increase channel stability, improve water quality and create habitat for fish and invertebrates (Simon et al. 2004; Sun et al. 2010). However, despite massive investments (e.g., >1$ billion yearly between 1990–2005 in the United States (Bernhardt et al. 2005)), restoration projects often fail to achieve intended goals (Thompson 2006), which highlights that gaps in our understanding of river processes still exist. Despite these gaps, numerical models are employed in practical applications. For example, the hydro-informatics system open TELEMAC-MASCARET was developed by Électricité de France 25 years ago and used since then to examine coastal and river processes. One specific investigation prevented a catastrophe, saved lives and avoided €12 million in losses, which is significant considering the required yearly investment of €0.5 to €1 million to maintain and improve the modelling suite (Hervouet 2007).

The interaction between meandering river channel dynamics and riparian vegetation has been examined intensively since the late 1990s to gain insight on ecological processes and to tackle river management issues (Perucca et al. 2007). Research has focussed on the role of secondary flow currents (Chen and Tang 2012), riparian vegetation (e.g., Abernethy and Rutherfurd 2000; Millar 2000; Micheli et al. 2004; Pollen 2007), bank erosion and habitat (e.g., Florsheim et al. 2008) as well as disturbance regimes (e.g., Darby et al. 2000; van Dijk et al. 2012) in shaping the morphology and substrate of river channels. A variety of numerical modelling approaches were devised to examine meandering process and lateral erosion at different spatiotemporal scales.

1.1. Meandering processes

Meandering rivers exhibit a regular or irregular sinusoidal planform (Allen 1985b), commonly develop on fine-textured, cohesive alluvial floodplains (Micheli et al. 2004; Anderson and Anderson 2010; Tal and Paola 2010), and continually shift in horizontal and vertical locations (De Barry 2004). Erosion along the concave bank and deposition along the convex bank of a meandering river are responsible for lateral and longitudinal meander migrations (Seminara 2006). River bank stability thus plays an important role in the development of a meandering planform (e.g., Millar 2000). Soil cohesion is necessary for the development of high amplitude meanders (Thorne 1990, Millar 2000, Kleinhans 2010), although the root system of riparian plants modify bank properties by reinforcing soil (Abernethy and Rutherfurd 2001; Pollen 2007) and altering hydrological pathways and storage, both spatially and temporally (Simon and Collison 2002; Pollen-Bankhead and Simon 2010). Meandering rivers are associated with low valley longitudinal gradients and low-to-moderate sediment supply and have fairly stable morphologies (Church 1992). The key morphological aspects of these channels are point bars along convex banks, which are generally gently angled, non-vegetated and graded upwards, a pool along the steep, opposite bank, and riffles located between adjacent pools (Allen 1985b; Anderson and Anderson 2010). Although meandering rivers exist on barren landscapes (i.e., on the surface of planet Mars (Weihaupt 1974); on bedrock, limestone, and glaciers (Zeller 1967)), this research focusses on the study of meandering rivers in unconsolidated soils.

The formation of a meandering planform geometry from an initially straight channel is achieved through a three-stage process (Bridge 2003). Initially, a dynamic upstream perturbation (e.g., due to mass wasting, sediment or flow input) (van Dijk et al. 2012) forces the flow to adopt a sinuous trajectory. As a result of spatially-varied flow velocities, point bars and cutoff banks develop, which contribute to further accentuating the meandering planform. Until fully developed, channel bars can grow and migrate at rates that are inversely related to wavelength (Crosato et al. 2012). Transverse bed slopes are created in the earlier stages of development, after which the rate of change slows down (Chen and Tang 2012). Meander growth is, however, limited in lateral extent by the stabilizing effects of neck and chute cutoffs which reduce channel sinuosity (van Dijk et al. 2012). A chute cutoff is a breach formed across the meander of a low-sinuosity river during a large flood whereas a neck cutoff occurs as a highly-sinuous reach migrates onto itself (Anderson and Anderson 2010). Through these processes, meander belts can migrate laterally and/or longitudinally.

1.2. Controls on meander development and migration

1.2.1. Sediment transport

Flowing water has the potential to displace and carry individual or clustered grains in a river channel as solute, suspended or bed load, the latter two being most relevant to morphological evolution studies (Allen 1985a; Bridge 2003). Suspended sediments are lifted from the bed by eddies and transported over long distances (De Barry 2004), whereas bed load occurs by rolling and saltation (Richards 2004). Widening and deepening of the channel are possible, which increase bank height and steepness, making the river banks more susceptible to mass wasting (Osman and Thorne 1988). Note that the flow may also stabilize river banks due to hydrostatic pressure (Duncan and Wright 2005) or by depositing sediments on the bed. In the eventuality of a river bank failure, the completion of this cycle of erosion by mass wasting depends on the state of basal endpoint control. In the case of impeded removal, i.e., sediment supply rate from the bank being more important than removal rate, a mass failure reduces bank angle and height which increases bank stability, slows down retreat rate, and halts the cycle (Thorne 1982). Conversely, in excess basal capacity, the supply rate is less than the removal rate, which increases erosion rate.

1.2.2. Riparian vegetation

Riparian plants divert stream flow, modifying flow patterns. They offer resistance against the passage of water (in the channel and on the floodplain), displacing the zero-plane of velocity away from the soil surface (Thorne 1990) which results in low to negligible velocity gradient within the vegetation zone (Allen 1985a). Vegetation density is a key factor controlling velocity reduction and flow diversion (Bennett et al. 2002). The interaction between streamflow and plants creates secondary circulation patterns (Bennett 2004) and produces turbulent structures which dissipate energy from the flow (Tabacchi et al. 2000) by suppressing meso- and macro-scale eddies (Thorne 1990).

Vegetation hinders surface and in-stream sediment transport processes in several ways. In-stream vegetation decreases near-bank flow velocity and associated particle entrainment by protecting soil particles against raindrops, trapping and retaining sediment, increasing infiltration rate, and decreasing erosion rate by runoff (Abernethy and Rutherfurd 1998; Millar 2000; Rey et al. 2004; Lau et al. 2006). Fine sediments are especially likely to be trapped (Tabacchi et al. 2000). Foliage also inhibits the sub-aerial processes causing erosion in the upper reaches of a stream by minimizing soil surface weathering and by reducing sediment transfer rate from the banks to the flow (Abernethy and Rutherfurd 1998).

Plants interact with the river banks by extracting soil water through transpiration, concentrating stem flow near tree roots, and intercepting, retarding and preventing precipitation from reaching soil surface due to foliage (Tabacchi et al. 2000). They also provide mechanical reinforcement (Abernethy and Rutherfurd 1998; Millar 2000; Rey et al. 2004). Individual trees generally have a more localized effect on the river, relative to shrubs, since the latter plant type contributes both to the reduction of near-bank flow velocity and soil cohesion (Malkinson and Wittenberg 2007). Note that mature trees can lower river bank stability due to the surcharge they impose (Simon and Collison 2002), especially during episodes with abnormally high soil moisture content (Pollen-Bankhead and Simon 2010). Although soil strengthening capacity varies with plant species assemblage and moisture content, riparian vegetated strips consisting of woody and grass species are associated with greater soil strength (Simon and Collison 2002; Simon et al. 2006).

Soil moisture influences river bank stability and channel morphology. Vegetation assemblages tend to be denser at a certain distance from the river, i.e., away from inundated and drought zones (Perucca et al. 2007). A denser root network is associated with enhanced soil surface strength (Wu and Watson 1998), reduced fluvial erosion of river banks (Thorne 1990), and narrower channels (Malkinson and Wittenberg 2007). In addition to varying spatially and temporally in magnitude, the effect of root reinforcement decreases as soil moisture increases and shear strength decreases (Pollen 2007).

1.3. Research methodologies to investigate meandering processes

1.3.1. Direct observation using field and flume methods

Flow hydrodynamics and morphodynamics have been directly observed and measured in natural meandering river channels. For instance, two- (Bathurst et al. 1979; Thorne and Rais 1984; Thorne et al. 1985) and three-dimensional (Frothingham and Rhoads 2003) measurements of flow velocities in meander belts demonstrated the existence of a helical flow motion. In addition, a physics-based understanding of river bank retreat through mass wasting and of the effects of riparian vegetation on soil stability was gained through the examination of slope processes at very local scales, i.e., the scale of individual roots/tree to the scale of a river bank (Thorne 1982; Osman and Thorne 1988; Abernethy and Rutherfurd 2001; Pollen 2007).

Since the 1970s, several experiments were conducted in artificial channels with fixed, vertical sidewalls to examine the hydraulic field and equilibrium bathymetries in meandering river channels, varying channel width, substrate, sinuosity and flow discharge (e.g., Hasewaga 1983; Ferreira da

Silva and El-Tahawy 2006; Binns and Ferreira da Silva 2009; Termini 2009). This approach facilitates the observation of formative processes by permitting comprehensive measurements within a controlled and manageable laboratory environment in which time is compressed (Peakall et al. 1996; Paola et al. 2009). The development and migration of a meandering channel has been examined in large flumes containing an initially straight, deformable channel (e.g., Friedkin 1945; Federici and Paola 2003). A combination of sand and silica powder (e.g., Peakall et al. 2007) or vegetation seedling (e.g., Tal and Paola 2010) was also used to enhance soil cohesion and trigger meandering.

1.3.2. Computer modelling

Knowledge gains on lateral adjustments in natural channels have partially emerged from modelling studies undertaken at the scale of a single bank or river reach (e.g., Midgley et al. 2012; Lai et al. 2015). Analytical models are appropriate for the examination of bank retreat at local scales. For instance, the geotechnical model SLOPE/W and the groundwater flow model SEEP/W (GeoSlope International 2013a, b) can be combined to study river bank processes by computing the safety factor of a slope under various soil/moisture conditions using limit equilibrium methods. These models were used to study the timing of bank failure events relative to a flood hydrograph (Luppi et al. 2009), as well as the contribution of fluvial erosion (Darby et al. 2007) and seepage erosion (Chu-Agor et al. 2008) to bank instability.

At the scale of a river reach, the formulation of Hasegawa (1977) and Ikeda, Parker and Sawai (Ikeda et al. (1981), referred to as HIPS) and refined versions thereof (Johannesson and Parker 1989; Zolezzi and Seminara 2001; Eke et al. 2014) have been employed extensively (and are still used) to examine the long-term evolution of meandering channels (e.g., Chen and Tang 2012; Posner and Duan 2012) and the river channel – riparian vegetation interaction (e.g., Perucca et al. 2006, 2007) with a much reduced computational cost (e.g., Schwenk et al. 2015). The HIPS approach is based on the linearization of the St. Venant flow equations in which lateral bank migration rate of a single-threaded, constant width channel is a function of near-bank flow velocities (Ikeda et al. 1981). The use of HIPS models contributed to identifying the effects of planform curvature, bed topography, valley floor width and cutoff rate on meander development (Coulthard and Van de Wiel 2006). One major limitation of the HIPS model, i.e., the assumption of constant channel width, was recently addressed by Parker et al. (2011). In addition, by treating bank erosion coefficient as a stochastic variable that varies with physical bank properties, it is possible to capture the variability in planform geometries, which cannot be achieved with deterministic models (Posner and Duan 2012). At the moment, one of the primary remaining limitation of these models is that they cannot "entirely"

simulate long-term planimetric and morphological evolution due to the absence of a mathematical description of neck/chute cutoff (Chen and Tang 2012; Camporeale et al. 2013). This issue can be dealt with by assuming that a neck cutoff occurs when the distance between two segments of the channel becomes negligible (e.g., Camporeale et al. 2005). Also, sediment continuity is not met in these models and there is no in-channel topography (Coulthard and Van de Wiel 2006).

In response to some of the limitations of HIPS models, meandering processes have been integrated to cellular automata (CA) modelling framework by determining curvature radii on a cell-by-cell basis (Coulthard and Van de Wiel 2006). Due to the relatively simplified representation of flow dynamics, these models offer rapid solutions for water depth and velocity computation, and thus allows meandering processes to be examined on large spatial and temporal scales (1–100 km^2 and 1–100 years) (Coulthard et al. 2007). Early CA models suffered from a few limitations, including the impossibility to simulate meander cutoffs and downstream migration, negligence of momentum transfer in the flow equations, the weakness of the sediment deposition routine, and the need for sensitivity testing and calibration (Coulthard and Van de Wiel 2006). Some of these issues were solved in later versions of these models, and other improvements made (e.g., channel incision/aggradation, terrace formation, braided-single channel transitions) so that they became more appealing for the long-term examination of extended river reaches, whether meandering or not (Van de Wiel et al. 2007). However, many of the CA models' limitations remain.

CFD morphodynamic models, i.e., computational fluid dynamics models coupled with a sediment transport module, are increasingly employed to predict erosion and deposition zones in river channels, and examine flow hydraulics, channel morphology, and interactions between a channel and established riparian communities (e.g., Bates et al. 2005; Rinaldi et al. 2008; Tal and Paola 2010; Ham and Church 2012; Mosselman 2012). These models are almost entirely physics-based, relying on the laws of continuity and conservation of momentum to compute hydraulic conditions, and therefore, are valid across a range of scales and environments, assuming that datasets are available for calibration (Darby and Van de Wiel 2003). They were used extensively to examine flow characteristics in different contexts, including meander belts (e.g., Morvan et al. 2002; Zeng et al. 2008; Constantinescu et al. 2011; Kashyap et al. 2012) and channel confluences (e.g., Keylock et al. 2012; Constantinescu et al. 2012). Over the years, multiple physics-based hydraulic models were developed, while discrepancies in predicted flow fields were noted amongst software packages (Rameshwaran et al. 2013). Several sediment transport formulae, most of them empirical, are often coupled with the hydraulic model. For instance, Wu et al. (2000) developed bed and suspended loads transport equations which are based on rates measured in numerous natural and laboratory

channels and tested against 1859 independent data points. Researchers have started integrating deterministic slope stability algorithms in these numerical models (e.g., Jia and Wang 2001a; Darby et al. 2002; Lai et al. 2012; El Kadi Abderrezzak et al. 2016), which involves the technical challenge of combining processes operating at different scales within a single coupled model (Williams et al. 2016a). Meandering channels were successfully created from initially straight channels through numerical experiments (e.g., Sun et al. 1996; Duan et al. 2001; Crosato 2009; Jia et al. 2011; Xiao et al. 2012). In particular, Lai et al. (2012) found a good agreement with field data, which encourages the integration of bank erosion processes within 2D and 3D models. Despite recent innovations, CFD models have limited ability to account for vegetation effects on the bank erosion process.

Compatibility with finite element discretization is a topic of growing interest (e.g., Evangelista et al. (2015) followed an approach similar to the one presented in this research). The use of an adaptive mesh was suggested by Langendoen et al. (2016) as a way to minimise the number of mesh elements. The mesh adapts its structure to channel boundaries, which evolve due to erosion and accretion along river banks, maintaining distinct bank-top lines. However, the implementation of this approach is associated with excessive mesh distortion in channels with substantial lateral retreat (Lai et al. 2017) and is inapplicable to multithreaded channels. The approach shares algorithmic similarities with the HIPS formulation due to idealized bank-top lines and arbitrary bank geometry. In addition, bank evolution rate is based on excess shear stress and on an erosion-rate coefficient. Although this implementation addresses some of the aforementioned limitations of existing morphodynamic models, it nevertheless does not consider river complexity in terms of process representation and floodplain heterogeneity.

1.4. Riparian vegetation

Modelling studies seeking an understanding of channel-vegetation interactions were conducted either at high spatial resolution for short time periods, or at low spatial resolution for long periods. At the scale of a short river bank, the model BSTEM proved useful to simulate changes in matric suction and soil strength within a river bank. For example, Pollen-Bankhead and Simon (2010) used this model to demonstrate that root-reinforcement contributes to river bank stability more than evapotranspiration at all time, except during the drier months. Experiments by Thomas and Pollen-Bankhead (2010), using the same model, revealed important variations in root-reinforcement with species and location. Using another model Van de Wiel and Darby (2007) determined the effects of vegetation surcharge and root reinforcement on bank stability for varying species, vegetation position and density, and bank properties. Meanwhile, Camporeale et al. (2005) and Perucca et al.

(2006) considered 10^1–10^2 km reaches for periods of 10^3–10^5 years. A grey zone exists between these extremes (i.e., at moderate spatial and temporal resolution) in which fewer modelling studies have been undertaken.

Most CFD morphodynamic models take account of riparian vegetation to compute vertical velocity profiles (e.g., Jia and Wang (2001a) for CCHE-2D; Lang (2010) for TELEMAC-2D; Fäh et al. (2011) for BASEMENT; Olsen (2011) for SSIIM). Some models include algorithms to specifically define roughness elements that can vary across the landscape, but usually for the sole purpose of computing hydraulic conditions (Collins et al. (2004) and Iwasaki et al. (2016) are exceptions). For instance, SSIIM offers the possibility to represent hydraulic resistance as a combination of drag coefficient, diameter of stems and number of stems per cell (or per square meter) (Olsen 2011). Similarly, in TELEMAC-2D, properties of non-submerged plants are defined by the diameter and spacing of roughness elements, after which a drag coefficient is calculated using Lindner law (Lang 2010). A more comprehensive integration of vegetation through the interaction of plants with river channel evolution is still lacking within existing CFD morphodynamic models. However, it has been successfully implemented in landscape models (e.g., Collins and Bras 2004; Istanbulluoglu et al. 2004) and to some extent in an empirical vegetation model connected to an HIPS model (e.g., Perucca et al. 2006, 2007). In the latter, the contribution of vegetation to river bank erodibility was implemented by calculating vegetation density as a function of the distance to the river, the logic being that plants require water, but that they may be destroyed by the flow due to prolonged periods of flooding/drought, or by being physically removed (Perucca et al. 2006). This statistical description of vegetation evolution is restrictive since it requires an assumption regarding the ratio between the timescales of vegetation growth/decay and river evolution. Moreover, it does not allow for multiple plant species or heterogeneity in density to be defined.

1.5. Synthesis and research gaps

Our understanding of the formative biophysical conditions for river meandering as well as the medium- and long-term evolutionary mechanisms remains incomplete, although considerable progress has been achieved in the last decades (Rhoads and Welford 1991; Kleinhans 2010; Crosato et al. 2012). Despite the large number of studies on meandering processes through field, flume and modelling experiments, and the accessibility to research instruments of increased efficiency and power, inherent difficulties remain. The complexity of the natural environment, the large temporal scales of river evolution, the lack of biophysical datasets and the numerous and poorly constrained variables make river evolution difficult to observe and, needless to say, to predict in a natural context

(Paola et al. 2009). The learning experience in a controlled lab environment is challenged by scaling issues (Paola et al. 2009) and by the difficulty to create a single-thread channel (Peakall et al. 1996). Finally, the limited number of numerical models which are able to simulate geotechnical (Lai et al. 2012), riparian plant and meander cutoff (Chen and Tang 2012) processes, combined with the scarcity of datasets available for calibration, may restrain the use of computer models.

The evaluation of the knowledge gained on meandering processes can be achieved at three scales. At the local scale, there is now a thorough, quantitative understanding of these processes, due to numerous studies related to hydrodynamics, sediment transport, and vegetation-soil interactions. At large spatial and temporal scales (10^1–10^2 km and 10^3–10^5 years), knowledge is largely qualitative, but also incomplete due to the limited number of studies, to non-physics-based assumptions regarding meander cutoff, and to lack of validation. At the scale of watershed management (10^1–10^2 years) knowledge is largely missing.

Several river scientists argue that the examination of channel morphodynamics, especially of medium and long-term migration patterns, cannot be achieved using flow and sediment transport alone, but rather that it requires physics-based algorithms of bank retreat taking into account soil properties, bank geometry, riparian vegetation, and heterogeneity of floodplain soils (Lai et al. 2012; Motta et al. 2012). However, no model exists that can explicitly simulate hydraulic and sediment transport and which also include algorithms to simulate river bank failures and vegetation evolution. HIPS models have been used to examine the long-term evolution of meandering rivers (e.g., Hasegawa (1977); Ikeda et al. 1981; Johannesson and Parker 1989; Zolezzi and Seminara 2001), but the velocity-derived migration rates upon which they depend do not directly consider river bank failures, but rather lump the effects of hydraulic entrainment and mechanical failures in a single erodibility coefficient (Camporeale et al. 2005).

Meanders elongate by erosion at downstream of the apex and shorten via the creation of cutoff channels (Peakall et al. 2007). The exclusion of cutoff processes from morphodynamic models, however, limits the understanding of meander evolution to short temporal scales (Crosato et al. 2012). Previous studies have simplified the shortening process through non-physics laws (e.g., Camporeale et al. 2005; Perucca et al. 2006) and by considering that the abandoned meander bend (oxbow) disappears without leaving any morphological trace. Thus, if the efficiency of CFD morphodynamic models was improved to allow longer-term processes to operate, it is possible that no supplemental algorithm would be required to simulate neck and chute cutoffs.

Riparian vegetation should be present in any model of meander evolution due to the interaction of plants with river flow (Bennett et al. 2002) and channel (Abernethy and Rutherfurd 1998; Malkinson and Wittenberg 2007). No satisfactory implementation of vegetation has yet allowed for heterogeneous distribution of plants from multiple species over the modelling domain.

1.6. Research objectives

The overarching goal of this research is to develop a morphodynamic model that can simulate lateral retreat in river meanders at intermediate spatial (5–10 meander bends) and temporal (2–3 years) scales using physics-based algorithms, and identify key properties of bank material and riparian vegetation cover. The processes operating at these scales are seldom considered by model developers despite their clear importance for practical applications of computer modelling in fluvial investigations. The specific objectives are to:

1. Evaluate whether the simulated flow and bathymetries are significantly different amongst predictions made by some of the most widely used and recognized CFD models, and to attempt identifying the origin of discrepancies. The search for a model that is appropriate for the examination of flow hydraulics and morphodynamics in meandering channels and compatible with the goal of the research undertaken in this thesis led to this specific objective, which is addressed in Chapter 2.

2. Establish a novel approach to perform bank stability for a single- or multi-threaded river channel while being compatible with triangle meshes and computationally manageable. This includes the implementation of efficient algorithms, parallel processing, and efficient data structures suitable for vector-based spatial analysis. Most of the effort related to this objective was spent while conducting the research that led to the publications of the manuscripts presented in Appendices A–B. The 2D morphodynamic model TELEMAC-SISYPHE, relying on a two-dimensional nonlinear version of the shallow-water equations to predict flow field and sediment transport as bedload, was selected and improved to perform slope stability assessment and simulate mass wasting in a physics-based manner while taking into account mechanical plant effects.

3. Evaluate the developed coupled model against measured bank retreat rates collected along two natural river reaches of different complexities. This is covered in Appendices A–B and in Chapters 3–4.

4. Devise a method to calibrate complex morphodynamics models based on machine learning algorithms. Although these algorithms ware evaluated and used in Chapters 3–4, they are described in greater details in Chapter 4.
5. Determine the sensitivity of river bank evolution to variations in riparian biophysical context for meandering rivers with cohesive banks. The statistical approach to calibration, described in Chapters 3–4 is associated with the realization of this specific objective.
6. Verify if the sensitivity to biophysical conditions differs between river reaches. This is done in Chapter 4 by calibrating the coupled model against data acquired along two river reaches with contrasting geomorphological contexts.
7. Evaluate the approach in terms of adequacy and type of knowledge developed. A novel framework is presented in Chapter 5 as an attempt to split modelling activities into modes, each of which is related to a distinct internal structure of a system and set of evaluation criteria.

Since it is only recently that river channel-vegetation interactions were found to be critical for the prediction of river evolution, most morphodynamic modelling packages are lacking bank stability and vegetation dynamics modules. It is also fundamentally important to better simulate these processes due to the emergence of river management philosophies relying on plants to address ecological, erosion, and aesthetic issues (e.g., vegetated buffer strips, naturalization). These modules could potentially improve our knowledge of river evolution but would also likely increase modelling run time. There is thus a need to evaluate the implications of adopting a more explicit, holistic, physics-based description of bank erosion and riparian vegetation processes into a morphodynamic model to determine the gains in predictive accuracy of morphological and planform evolution, and to identify the processes or features that could be neglected in future studies.

Liaison paragraph

One of the first activities undertaken in this study consisted in identifying one or several modelling tools that could be employed to meet the overarching goal of this research. After performing a thorough theoretical comparison of models' features, I familiarized myself with a subset of these packages, along with the methods that can be used to analyse flow and sediment transport. This was done by attempting to replicate documented flume experiments over fixed and mobile beds in meandering channels. The differences found amongst predicted flow fields triggered a more profound investigation that sought to explain the origin of discrepancies and to identify the models agreeing the most with morphological datasets acquired in meandering laboratory channels. The following chapter summarizes the statistical analysis performed during this investigation, along with the main findings.

2

Sensitivity of simulated flow fields and bathymetries in meandering channels to the choice of a morphodynamic model

Yannick Rousseau, **Pascale Biron** and **Marco Van de Wiel**

Earth Surface Processes and Landforms 41(9): 1169–1184 (2016)

Abstract: Morphodynamic models are used by river practitioners and scientists to simulate geomorphic change in natural and artificial river channels. It has long been recognized that these models are sensitive to the choice of parameter values, and proper calibration is now common practice. This paper investigates the less recognized impact of the choice of the model itself. All morphodynamic models purport to simulate the same flow and sediment dynamics, often relying on the same governing equations. Yet in solving these equations, the models have different underlying assumptions, for example regarding spatial discretization, turbulence, sediment inflow, lateral friction, and bed load transport. These differences are not always considered by the average model user, who might expect similar predictions from calibrated models. Here, a series of numerical simulations in meandering channels was undertaken to test whether six morphodynamic codes (BASEMENT, CCHE-2D, NAYS, SSIIM 1, TELEMAC-2D and TELEMAC-3D) would yield significantly different equilibrium bathymetries if subjected to identical, initial flow conditions. We found that, despite producing moderately similar velocity patterns on a fixed-flat bed (regression coefficient r of 0.77 ± 0.20), the codes disagree substantially with respect to simulated bathymetries (r = 0.49 ± 0.31). We relate these discrepancies to differences in the codes' assumptions. Results were configuration specific, i.e., codes that perform well for a given channel configuration do not necessarily perform well with higher or lower sinuosity configurations. Finally, limited correlation is found between accuracy and code complexity; the inclusion of algorithms that explicitly account for the effects of local bed slope and channel curvature effects on transport magnitude and direction does not guarantee accuracy. The range of solutions obtained from the evaluated codes emphasises the need for carefully considering the choice of code. We recommend the creation of a central

repository providing universal validation cases and documentation of recognized fluvial codes in commonly studied fluvial settings.

2.1. Introduction

Morphodynamic models, i.e., computational hydraulics models coupled with a sediment transport module, are often employed to predict erosion and deposition zones in river channels, and to examine flow hydraulics, channel morphology, and interactions between a channel and established riparian communities (e.g., Bates et al. 2005; Rinaldi et al. 2008; Ham and Church 2012; Mosselman 2012). Accessibility to morphodynamic models has greatly improved since their introduction in the 1980s, with key aspects including: more detailed documentation; a broader community of users, combined with better communication platforms; low or no purchase cost; and the ability to run models on inexpensive, powerful, multiprocessing personal computers. These models are now commonly used for morphodynamic modelling in one-, two- and three-dimensions (1D, 2D and 3D) (Darby and Van de Wiel 2003).

Despite the improved accessibility to computational fluid dynamics (CFD) and morphodynamic models, investigations are generally carried out using a single modelling code. Thus, the consequences of selecting any given modelling code on river channel predictions are largely ignored. In contrast, the level of uncertainty associated with model predictions is commonly dealt with in several other scientific disciplines involving stochastic phenomena, for example in ecological modelling (Jiao et al. 2008), hydrology (Franz et al. 2010) or climate modelling, by providing a set of climate predictions from an ensemble of different models (Bates et al. 2008; Gregow et al. 2011; Fischer et al. 2012). In river-related investigations, the appropriate code should be the one that best reproduces river channel dynamics in natural systems. Because there is no a priori knowledge of which code is most appropriate for a given environmental context, model comparison studies provide useful information on the range of possible outcomes.

Although guidelines exist for modellers to determine whether results from a simulation can be deemed reliable (Roache et al. 1986; Lane et al. 2005), some of the subtleties in the models' underlying assumptions may be lost on the average model user who, given that the models are based on the same governing equations, might expect that different models, when properly calibrated, will generate very similar predictions. However, differences in sub-models, algorithms, simplifications, and other modelling options may well result in various levels of accuracy for different configurations. For example, Rameshwaran et al. (2013) used a single channel layout (a meander with medium sinuosity of 1.37) in their comparative study, but would a consistent level of accuracy of each model have been observed for a lower or higher sinuosity channel? We argue that the value of inter-comparison studies lies in the opportunity they provide to identify the most relevant algorithms and

solver options for any particular context, to determine the range of applicability of modelling codes to fluvial channel types, and to improve codes and procedures.

One of the difficulties in comparing different codes is to ensure that they are indeed comparable, i.e., that the governing equations, boundary and initial conditions, numerical mesh, etc. are identical. Since each code has its own specificities, for example on the available choice of turbulence models or sediment transport equations, bed roughness parameterisation, active layer management, etc., it is impossible to achieve perfectly identical model configurations in a comparative study. The suggested approach here is to use identical channel layout, initial flow and boundary conditions, and calibration procedure between codes.

The objectives of this study are 1) to evaluate whether different 2D and 3D morphodynamic modelling codes generate substantially divergent flow fields and equilibrium bathymetries for an identical set of imposed boundary conditions and nearly-identical set of options, sub-models and parameter values, and 2) to assess whether model performance varies with channel configuration. The accuracy of the numerical models is assessed by comparing predictions to measurements obtained in three analogue flume experiments with varying degrees of sinuosity.

2.2. Methodology

2.2.1. Numerical codes

Four 2D and two 3D morphodynamic codes are evaluated: BASEMENT v. 2.2.1021 (B_2), CCHE-2D v. 3.29.0 (C_2), NAYS v. 2.1.7.3285 (N_2), the 2D and 3D versions of TELEMAC v. 6.2 (T_2, T_3), and the 3D code SSIIM-1 v. 43 (S_3). These codes are thoroughly described in Fäh et al. (2011), Jia and Wang (2001a), Shimizu et al. (2013), Galland et al. (1991), Olsen (2011), and Janin et al. (1992), respectively for B_2, C_2, N_2, T_2, S_3 and T_3. They are selected because: 1) they each offer the possibility to simulate flow hydraulics and sediment transport processes in river channels; 2) they are widely used in fluvial-related research and in engineering applications; 3) they are well documented; and 4) they are available free of charge. Note, however, that C_2 now requires a commercial license, which was not the case when it was used for the current study. The models are used to test for significant differences in simulated flow fields, erosion/deposition patterns and accuracy levels.

In this paper, we use the term “code” to refer to the set of algorithms and solvers embedded in a modelling software package to simulate hydrodynamics and morphodynamics. The term “configuration” refers to the setup of a channel, including its dimensions, shape, substrate

characteristics and flow conditions. In this context, a "simulation" denotes a prediction of flow field and/or equilibrium bathymetry obtained by applying a given code to a given configuration.

2.2.2. Channel configurations

The six codes were compared using three sine-generated meandering channels, respectively with a low sinuosity of 1.07 (M_{low}), a medium sinuosity of 1.51 (M_{med}) and a high sinuosity of 3.70 (M_{high}) (Figure 2.1). For each channel configuration, fixed-flat and mobile beds were considered.

The meandering channel configurations are based on a series of analogue flume experiments. The experimental setup (Figure 2.1; Table 2.1), flow and boundary conditions, and generated topographies are described and mapped elsewhere: M_{low} is the numerical version of experiment ME-2 by Hasegawa (1983), with the resulting topography described in Ferreira da Silva and El-Tahawy (2006); M_{med} corresponds to the second run in Binns and Ferreira da Silva (2009); and M_{high} represents the MB-2 experiment described in Termini (2009). The ratio between bed shear stress (measured from the depth-slope product) and Shields critical shear stress ranged between 2.10 and 3.17 at the inlet (Table 2.1). All experimental data are the result of steady-state runs which lasted sufficiently long to ensure the establishment of an equilibrium bed configuration, based on a constant water surface slope and bed geometry no longer changing through time. Simulated topographic changes (for the mobile bed configurations) are compared to flume results for each numerical code. For the M_{high} configuration, water surface elevations and near-bed velocities were also available from Termini (2009). The latter were compared to the near-bed velocity in the 3D models, but not to the 2D depth-averaged models.

2.2.3. Numerical simulations

The six codes were run for the three flume meander channel configurations (Figure 2.1) under both fixed-flat and mobile bed conditions, for a total of 36 simulations. Additional simulations were launched to test the sensitivity of the studied codes to variations in key options, sub-models and parameter values.

For each flume configuration and code, a fixed-flat-bed simulation was run to adjust the elevation of the water surface at the inlet so that it is equal to the value at the outlet. This was done by varying bed roughness value (a single value selected for the entire bed) in the 2D simulations, which were similar between the codes (Table 2.2). This procedure, which is common in CFD modelling (e.g., Bates et al. 1997; Rameshwaran et al. 2013), allows to adjust the energy slope to fit experimental measurements (Vidal et al. 2007). Admittedly, there are limitations to this approach. In particular,

3D models are less sensitive to the choice of Manning's roughness value than 2D models (Lane et al. 1999; 2005). Therefore, the aforementioned calibration procedure failed with S_3 as a change in bed roughness had little effect on the energy slope. In the T_3 simulations, we were unable to configure liquid boundary conditions in a manner such that free surface elevation at the inlet adjusts

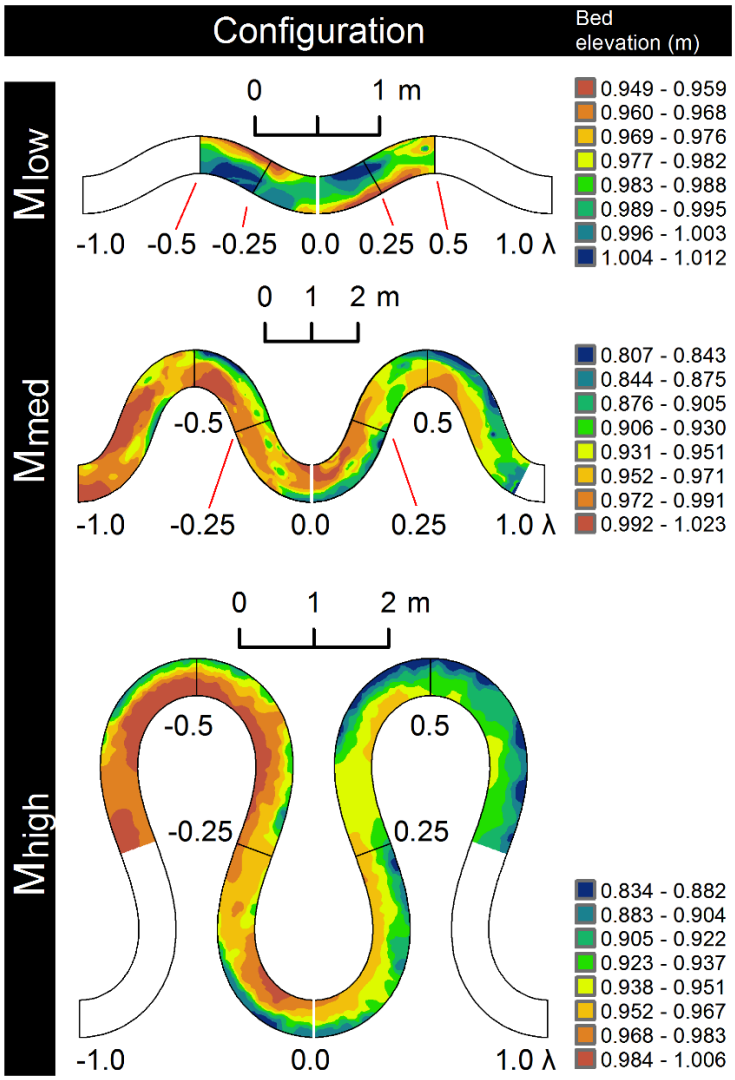

Figure 2.1. Bathymetries used during physical experiments in sinuous channels

The experiments are those of Hasegawa (1983) (M_{low},), Ferreira da Silva and El-Tahawy (2006) (M_{med}), and Termini (2009) (M_{high}. The symbol λ represents the longitudinal position of any cross-section (in terms of number of wave lengths) relative to the longitudinal channel center, where the apex is represented by $\lambda = 0$. Flow is from left to right. Note that, in the numerical simulations presented in this study, each configuration includes straight two-meter channel sections located upstream and downstream of the sinuous reach (not shown).

Table 2.1. Flow and boundary conditions for each channel configuration

Config.	*s*	*L* (m)	*B* (cm)	*H* (cm)	*B/H*	*Q* (l/s)	*S* (%)	d_{50} (mm)	*Shear stress ratio*
M_{low}	1.07	8.00	30	2.60	11.5	1.87	0.333	0.43	2.36
M_{med}	1.51	19.20	80	4.14	19.3	9.50	0.400	0.65	3.17
M_{high}	3.70	27.30	50	3.00	16.7	7.00	0.371	0.65	2.10

Each sine-generated channel consists of two waves located between two two-meter straight sections. Legend: s = sinuosity; L = total flume length; B = channel width; H = depth at inlet and outlet; Q = flow discharge at inlet; S = longitudinal slope; d_{50} = median grain size diameter. The shear stress ratio is the ratio of shear stress ($\tau = \rho g R S$, where ρ is mass density of water, g is acceleration due to gravity and R is hydraulic radius) over critical shear stress ($\tau_c = \theta_c (\gamma_s - \gamma) d_{50}$, where θ_c is taken as 0.044, γ_s is weight density of sediment in kg/m^3 and γ is weight density of water in N/m^3 and d_{50} is in m.

automatically, and thus depth is also prescribed at the inlet. As a result, the roughness coefficients used with the 3D codes in this study are those obtained by calibrating the T_2 simulations under the premises that the code T_3 is the three-dimensional version of T_2, that the range of roughness values between the 2D models is narrow, and that the parameter values of the 3D models should be as similar as possible. Another limitation is that, although identical flow conditions were selected between the modelling codes, longitudinally differences exist in predicted depth, velocity, and discharge values, especially between the 2D and 3D codes (Figure 2.S1). Computed discharges are slightly above the values set at the inlet with B_2, N_2 and T_2, but sometimes substantially different with the other codes, e.g., M_{low}-T_3, M_{high}-C_2.

For the mobile-bed simulations, the simulations started from a fixed-flat bed which was allowed to evolve to an equilibrium bathymetry throughout the simulation. Equilibrium bathymetry was assumed to be reached when the mean elevation change, within the zone between $-0.25 \leq \lambda \leq 0.25$ (Figure 2.1), became small enough that the remaining cumulative change was less than instrument resolution, assumed here equal to 1 mm, to replicate the resolution

Table 2.2. Bed roughness values of numerical models

Configuration	*Model*			
	B_2	C_2	N_2	$T_2/T_3/S_3$
M_{low}	49.50	50.50	47.94	47.67
M_{med}	38.75	39.00	38.07	38.12
M_{high}	86.00	92.18	79.94	80.12

Strickler coefficients are used in adjusting the slope of the water surface between the inlet and outlet of each channel.

of topography measurements in Binns and Ferreira da Silva (2009). For each simulation, a plot of cumulative bed elevation change against time was used to estimate the time at which the remaining change was less than the selected threshold value (Table 2.1). Note that the shape and dimension of dominant bed forms, namely pools and riffles, were stable after each mobile-bed simulation, as in the experiment of Termini (2009). Both the bed development times and the time steps varied substantially amongst the modelling codes and channel configurations, with Courant numbers ($V \cdot \Delta t / \Delta x$, where V is the flow velocity, Δt is the duration of a time step, and Δx is the cell size) generally below unity at the onset of mobile-bed simulations (Table 2.3). A Courant number below unity is recommended for good convergence of finite-difference approximations. Note that the calculated values are for average flow conditions and that the modelling code C_2 automatically altered the duration of time steps during each simulation.

Table 2.3. Simulation times, time steps and Courant numbers

Code	*Time to reach equilibrium (hours:minutes)*			*Initial time step (ms)*			*Courant number*		
	M_{low}	M_{med}	M_{high}	M_{low}	M_{med}	M_{high}	M_{low}	M_{med}	M_{high}
FL	4:00	1:22	2:30	-	-	-	-	-	-
B_2	2:31	307:47	66:30	100	100	100	0.64	0.76	1.24
C_2	125:12	131:15	102:55	10	10	10	0.06	0.08	0.12
N_2	134:17	42:19	22:01	1	1	2.5	0.01	0.01	0.03
T_2	5:15	54:08	2:41	10	10	10	0.06	0.08	0.12
S_3	43:48	27:23	99:24	100	100	100	0.64	0.76	1.24
T_3	30:42	43:08	17:01	50	100	100	0.32	0.76	1.24

Simulation time and initial duration of a time step at the onset of mobile-bed simulations, and theoretical Courant number values on rectangular beds with uniform hydraulic simulations.

2.2.4. Analysis procedure

The evaluation and description of code-code and code-flume discrepancies are derived from visual cues, measurements, and statistical analyses. A set of criteria relevant to fluvial geomorphologists, environmental engineers, ecologists and other river practitioners is employed to describe the predicted flow and equilibrium bathymetry for M_{low}, M_{med} and M_{high}. Channel bathymetries at equilibrium (M_{low}, M_{med} and M_{high}), near-bed velocity magnitudes (M_{high}), and free surface elevations (M_{high}) from the analogue flume experiments were obtained by digitizing the contour lines from the maps published by Hasegawa (1983), Binns and Ferreira da Silva (2009), and Termini (2009). To allow a comparison of simulated flow velocities between 2D and 3D codes, manual depth-averaging of velocities was done in 3D simulation by taking the value at an elevation of 0.6 times the depth

below the free surface, a method referred to as the 0.6-depth method (Rantz et al. 1982). Near-bed velocity measurements were taken at a distance of 0.8 cm above the bed in the M_{high} flume experiment over a fixed-flat bed (Termini 2009). For the comparison with 2D numerical simulations, we estimated near-bed velocities from depth-averaged values using the law of the wall for rough surfaces (Schlichting 1979), as done by S_3, with a calculated roughness height as $(26 \cdot K_{Strickler})^6$, where $K_{Strickler}$ is the Strickler roughness coefficient (Strickler 1923). The lateral slope of the free surface was estimated using a linear regression on sample points of the water surface. The bathymetries that developed during the mobile-bed runs and simulations are expressed in terms of absolute and normalized elevation values at equilibrium and in terms of normalized evolution values. Normalized elevations along a cross-section (z_n) are given by $(z - z_{min}) / (z_{max} - z_{min})$, where z = bed elevation at a node, and z_{min}, z_{max} = minimum and maximum bed elevations. This transformation removes the longitudinal bed slope. The extent of the riffles and pools that developed during the mobile-bed flume experiments was derived from a map of normalized evolutions ($\Delta_{z,n}$), given by $(\Delta_z - \Delta_{z,min}) / (\Delta_{z,max} - \Delta_{z,min})$, where Δ_z = bed evolution at any given location and $\Delta_{z,min}$, $\Delta_{z,max}$ = minimum and maximum values measured in the whole flume. Riffles were assumed to be located where $\Delta_{z,n} > 0.75$, and the pools where $\Delta_{z,n} < 0.25$. The point locations of riffles and pools of the bathymetry developed in each numerical simulation correspond to the shallowest and deepest points, respectively, derived from the thalweg and lateral bed profiles.

To avoid spatial autocorrelation problems in statistical analyses (Fortin et al. 1989), 200 test points were randomly selected for each configuration to examine discrepancies amongst and between predicted (numerical simulations) and measured (flume experiments) values. Reduced major axis regression (RMA) is used instead of ordinary least square regression to account for potential errors in both the dependent and independent variables (Hardy et al. 2003; Biron et al. 2007) and to maintain the variance of observations in our predictions (Berterretche et al. 2005). Results of RMA analyses are presented in this paper for the M_{med} but are available as supplementary material for the other two configurations (M_{low} and M_{high}). The relationships associated with a regression slope m not significantly different from 1 at a 0.05 level were identified, as evaluated using two-tailed t-tests where the null hypothesis is that regression slope is equal to 1. As recommended by Paternoster et al. (1998), t-scores were calculated using:

$$t = \frac{b_R - b_{1:1}}{\sqrt{SEb_R^2 - SEb_{1:1}^2}} \tag{2.1}$$

where SEb_R and $SEb_{1:1}$ are the standards errors associated with b_R and $b_{1:1}$, the regression coefficients of two curves. Here, b_R is the regression slope of the relationship between two datasets, and $b_{1:1} = 1$.

2.2.5. Sensitivity to mesh resolution

A computational mesh structure with a body-fitted coordinate system consisting of quadrilateral cells was employed in all simulations. A sensitivity analysis was performed to determine appropriate horizontal and vertical mesh resolutions to use for the simulations (see Supplemental Material). Three grid independence tests (Roache et al. 1986; Lane et al. 2005; Biron et al. 2007) were carried out to observe the effects of varying the number of cells in the simulation domain on flow conditions over a fixed-flat-bed for the M_{med} configuration. The procedure, evaluation criteria and results are provided as Supplemental Material (see the website of the journal in which the chapter was published). The optimal number of cells was 384 and 32, respectively in the longitudinal and transverse directions, with 6 cells in the vertical direction for the 3D codes. The same horizontal cell size was used for the other two configurations (M_{low} and M_{high}), with the same number of vertical cells for the 3D models (Table 2.4). Note that the code S_3 automatically adds one row of nodes in each dimension to better account for the effect of solid boundaries on the flow velocity profiles. Finally, despite our intention to use equal vertical cell height with the 3D models, S_3 modified the location of nodes to 0.5, 10, 30, 50, 70, 90 and 100% of flow depth. In order to keep the parameters as similar as possible between the models, the same distribution was used with T_3.

Table 2.4. Characteristics of numerical meshes

Model	Number of cells				Mean cell size (cm)		
	i	j	k	i·j·k	i	j	k
M_{low}							
B_2, C_2, N_2, T_2	161	12	1	1,932	4.99	2.50	2.60
S_3	162	13	6	12,636	4.96	2.31	0.43
T_3	161	12	6	11,592	4.99	2.50	0.43
M_{med}							
B_2, C_2, N_2, T_2	384	32	1	12,288	4.99	2.50	4.14
S_3	385	33	6	76,230	4.98	2.42	0.69
T_3	384	32	6	73,728	4.99	2.50	0.69
M_{high}							
B_2, C_2, N_2, T_2	545	20	1	10,900	5.00	2.50	3.00
S_3	546	21	6	68,796	4.99	2.38	0.50
T_3	545	20	6	65,400	5.00	2.50	0.50

Number of cells and mean cell size of the numerical meshes in the longitudinal (i), lateral (j) and vertical (k) directions.

2.2.6. Sensitivity to key model options and sub-models

Our initial intent was to use identical options and sub-models for each numerical simulation. However, this could not be fully achieved since discretization schemes, turbulence models, side wall friction laws, bed load transport formulae, and sediment inflow modes differ between codes (Table 2.5). A sensitivity analysis was thus conducted with the codes C_2, T_2, and T_3 and channel configuration M_{med} to evaluate whether eventual discrepancies in the flow field and equilibrium bathymetries could be related to differences in options and sub-models.

Spatial discretization. A single scheme is typically implemented in each morphodynamics code, namely finite element (C_2, T_2 and T_3), finite volume (B_2 and S_3) and finite difference (N_2) approaches. In T_2 and T_3, the finite volume scheme is available in scalar mode.

Shear stress and bed roughness. In all codes except S_3, shear stress along an axis *i* is described by the quadratic friction law, which is a drag coefficient formulation (see Villaret (2010) for a description), whereas S_3 relies on the law of the wall for rough surfaces, i.e., Schlichting (1979) formula, translating a user-provided roughness coefficient to a roughness height using Strickler (1923) formulae. Although bed roughness may be nonuniform in natural meandering rivers, varying with local channel curvature and sinuosity (Da Silva 1999), a single value was assigned to all mesh nodes as 1) detailed spatial variability of bed roughness values was not available for the flume experiments and 2) many modelling studies, even of natural sites, use a single roughness values, particularly for sand-bed cases (e.g., Duan and Julien 2010; Huang et al. 2014). The choice of the roughness method can affect the simulated flow field and morphodynamics. The Chézy parameterization was found to produce higher velocities, shallower channels, lower-smoother bars, and less accurate morphological predictions than the Nikuradse law (Kasvi et al. 2015). This can be explained by the fact that the former parameterization type does not consider flow velocities (Zeng et al. 2010). S_3 also ignores the terms related to the generation and dissipation of energy due to bed roughness in the governing flow equations. It is well known that the estimated shear stress values vary from one method to another (e.g., Grenier et al. 1995; Wilcock 1996; Biron et al. 2004; Pasternack et al. 2006). Assuming flow in a straight, rectangular channel with the characteristics listed in Tables 2.1 and 2.2, shear stress values predicted by the law of the wall are markedly lower (26% for T_3 and around 53% for B_2, C_2, N_2 and T_2) than those predicted by the quadratic friction law. Scatter in shear stress predictions by hydrodynamic codes was also noticed by Rameshwaran et al. (2013).

Table 2.5. Selected options, sub-models and parameter values in numerical simulations

Criteria	B_2 – BASEMENT	C_2 – CCHE-2D	N_2 – NAYS-2D	T_2/T_3 – TELEMAC	S_3 – SSIIM-1
Flow hydraulics					
Governing equations	Shallow-water	Shallow-water	Shallow-water	Shallow water (2D) Navier Stokes (3D)	Navier-Stokes
Spatial discretization[1]	FVM	FEM	FDM	FEM	FVM
Advection	Upwind	Upwind	Upwind	Upwind	Upwind
Turbulence model	None	k-ε	k-ε	k-ε	k-ε[2]
Friction law (bed)	Quadratic-Manning	Quadratic-Manning	Quadratic-Manning	Quadratic-Manning	Wall law-Manning
Friction law (walls)	Quadratic-Manning	Coefficient	None	Quadratic-Manning	Quadratic-Manning
Sediment transport					
Bed load formula[3]	TF_{WWJ}	TF_{WWJ}	TF_{MPM}	TF_{VR}	TF_{WWJ}
Magnitude=f(slope)	Van Rijn (1989) & Ikeda (1982)	Van Rijn (1989)	Hasegawa (1983) & Engelund (1974)	Koch and Flokstra (1981)	Brooks (1963)
Direction=f(slope)	Perpendicular to main flow direction	Talmon et al. (1995)	No	Koch and Flokstra (1981)	No
Direction=f(curvature)	No	Engelund (1974)	Engelund (1974)	Engelund (1974)	No
Sediment slide[4]	No	Yes	No	Yes	No
Inflow rate	Variable[5]	None	Variable[5]	Variable[5]	No

[1]Equations: finite element (FEM), finite volume (FVM), finite difference (FDM). [2]The implementation of the k-ε turbulence model in S_3 does not take account of turbulent energy and dissipation due to bed friction. [3]Valid mean grain size (d_{50}) ranges for the bedload formulae are: $2 < d_{50} < 50$mm with Meyer-Peter and Müller (1948) (TF_{MPM}); $0.2 < d_{50} < 2$mm with Van Rijn (1984) (TF_{VR}); and $0.088 < d_{50} < 28.7$mm with Wu el al. (2000) (TF_{WWJ}). [4]This algorithm ensures that no slope exceeds the angle of repose of the bed material. [5]The amount of sediment crossing the upstream boundary is equal to the amount leaving the first cell.

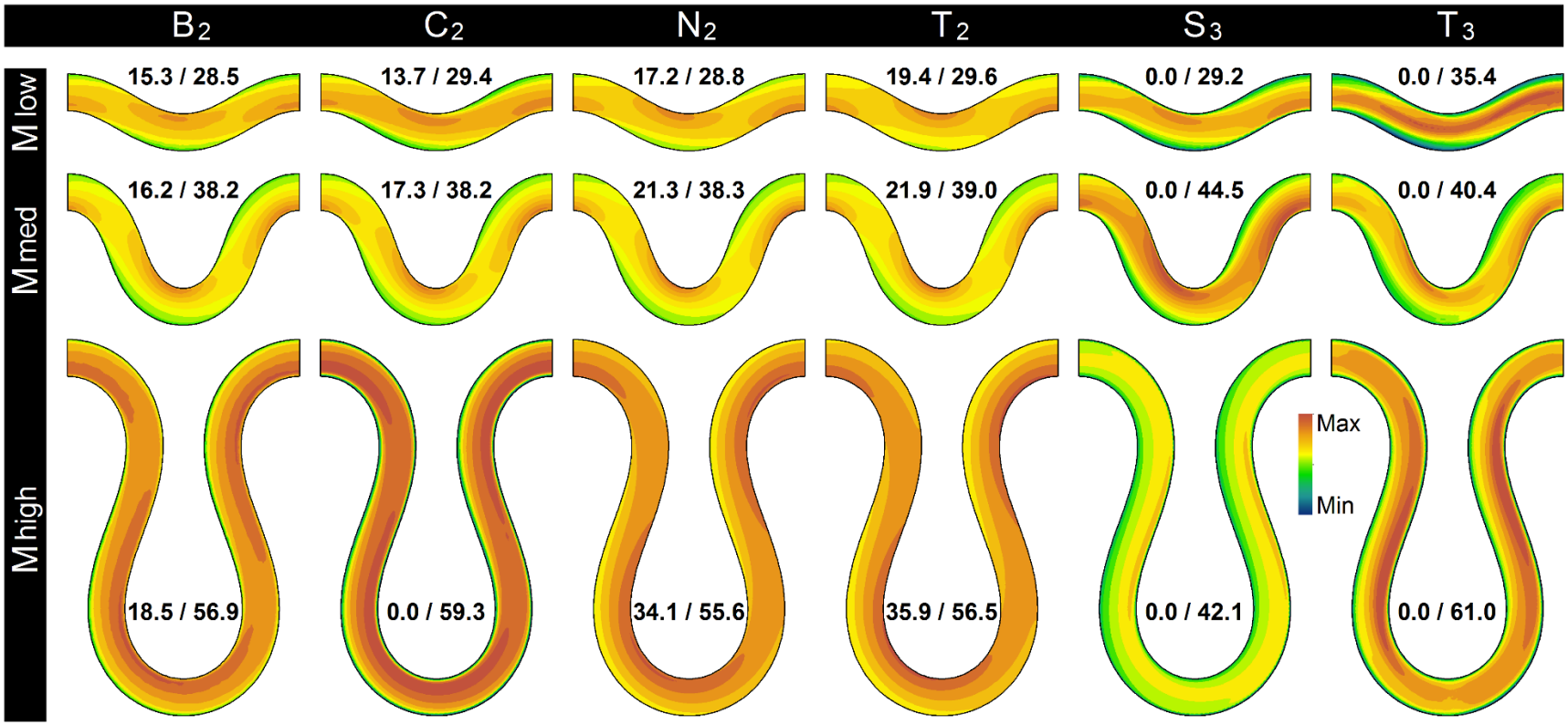

Figure 2.2. Depth-averaged flow velocity predicted by the morphodynamic models

These models are B_2, C_2, N_2, T_2, S_3 and T_3 for the fixed-flat bed simulations for **a)** M_{low}, **b)** M_{med} and **c)** M_{high}. Minimum and maximum velocities (in cm/s) are displayed with each velocity map. Note that the colour legend varies between M_{low}, M_{med} and M_{high} as it is scaled to the minimum and maximum velocities for each configuration.

Sidewall roughness. Unlike the law of the wall, the quadratic friction law does not take into account sidewall roughness. Lateral friction is nevertheless included in S_3 through the k-ε model (Versteeg and Malalasekera 1995), which results in steeper lateral velocity gradients than with T_3 due to the smooth sidewalls, and zero velocities near solid boundaries, as in T_3 (Figure 2.2). A Strickler coefficient of 100 was selected with B_2, T_2, S_3, and T_3 to represent the smooth material of the sidewalls in the analogue flume experiments (unknown for M_{low}; plywood sheet painted with epoxy paint for M_{med}; and clear Plexiglas for M_{high}). The friction law selected in C_2 simulations relies on an empirical slipness coefficient to calculate sidewall velocity strictly based on the value at the adjacent internal node. A value of 0.85 was used with all channel configurations, as recommended by Jia and Wang (2001b) for a numerical simulation with the M_{high} configuration. Although not indicated in the reference manual of N_2, sidewall friction seems to be set to total slip in N_2 due to the lack of a wall effect on lateral velocity profiles.

Turbulence closure. All codes include the k-ε turbulence closure sub-model, except B_2, which only considers molecular viscosity. Despite this, B_2 is included in this study to verify whether a code with limited representation of turbulence structure can simulate flow conditions and bathymetry in an acceptable manner. The bathymetry produced with the k-ε turbulence model exhibits wider point bars than those predicted by Smagorinsky (1963) and constant viscosity closures with a downstream tip disconnected from the sidewall and bed forms with acute delineation and great geometrical regularity (Figure 2.S2).

Bedload transport rate and direction. It is well known that some bed load transport formulae are more accurate than others in specific contexts (Batalla 1997; Martin and Ham 2005; Carmelo et al. 2013). In our simulations, we selected Wu et al. (2000) formula when available. Alternatively, the Van Rijn (1984) was selected in T_2/T_3 since it is suited to the range of grain sizes considered in this study. The evaluated codes include algorithms to consider the influence of local bed slope on transport rate (all codes) and direction (only B_2, C_2, and T_2/T_3). The effect of channel curvature on the direction of bed load motion relies on Engelund (1974) in C_2, N_2, and T_2/T_3 to estimate the upslope-inward shearing angle relative to streamline flow direction. In this equation, the angle is proportional to the ratio between flow depth and curvature radius, but the latter is calculated differently in C_2 and N_2 than in T_2/T_3. Note that this option was enabled in C_2 because simulated bathymetries were clearly incorrect when disabled. Our sensitivity analysis reveals that the Meyer-Peter and Müller (1948) formula results in a bathymetry that is almost identical to that produced by Van Rijn (1984). The simulation relying on the total load formula of Engelund and Hansen (1967) is as accurate as the other formulae,

and it best predicts the location of pools and point bars even if does not rely on a threshold stress value of particle entrainment.

Sediment inflow rate. B_2, T_2 and T_3 include an option to set the rate of sediment at the inlet equal to the outflow rate, whereas C_2 and S_3 require the inflow rate to be specified. A sediment inflow rate of 0 kg/s was specified with C_2 and S_3 since the simulations launched in S_3 did not converge when using a nonzero, constant rate (estimated with the Meyer-Peter and Müller (1948) formula, assuming a fixed-flat bed) and since it was impossible to predict the equilibrium outflow rate.

Overall, there is a good agreement amongst the bathymetries generated with the different options and sub-models (Figure 2.S2). Taking the regression coefficient as an index of similarity between two predictions, similarity is lowest between turbulence closure sub-models, i.e., k-ε vs. Smagorinsky (1963) or constant viscosity, and between sediment transport formulae, i.e., Engelund and Hansen (1967) vs. Van Rijn (1984) or Meyer-Peter and Müller (1948) (Figure 2.S3). Variations due to lateral friction, sediment inflow, and spatial discretization are less important.

2.3. Results

2.3.1. Fixed-flat bed runs

The degree of sinuosity of a meandering channel determines the phase lag between the apex of a meander belt and the location of the zone of maximum velocity, shifting upstream along the inner sidewall with the increase in sinuosity of a fixed-flat bedded channel, almost reaching the cross-over zone in highly sinuous channels (da Silva et al. 2006). Although this trend is well illustrated by S_3, the predicted high-velocity location is fairly similar between T_3 and the depth-averaged models for M_{high} (Figure 2.2). The evaluated 2D codes, and T_3 to a certain extent, predict a zone of maximum velocity just upstream of the apex, independently of sinuosity, as observed in the experiments of Xu and Bai (2013).

As expected, all codes predict a super-elevation of the free surface along the external sidewall of bends, with mean lateral slopes of 0.97 ± 0.07%, 1.04 ± 0.20% and 2.34±0.66%, respectively for M_{low}, M_{med} and M_{high}, as a result of secondary circulation (Figure 2.3). However, the degree of agreement between the codes varies with the configuration. For instance, the lateral slopes are nearly identical between the codes in M_{low}, except for T_3, which exhibits an oscillating slope, perhaps due to numerical instability. For M_{med}, the 3D codes predict lateral slopes steeper than with the 2D codes by 52% (S_3) and 30% (T_3). For M_{high}, the free surface elevation for T_3 is more in line with the 2D predictions, whereas the lateral slopes predicted by S_3 is 48% lower than that of the other codes and do not appear

to vary with meander configuration. The predictions of free surface elevations are fairly consistent between the 2D codes B_2, C_2, N_2, T_2 for M_{low} and M_{med}, (except for C_2 in M_{high}) which is to be expected since the calibration procedure consisted in adjusting the slope of the water surface between channel inlet and outlet. For the M_{high} configuration, the agreement with the flume result is also very good, with correlation coefficients of $r \geq 0.88$ (Figure 2.4). These values can be found in Figure 2.4b in the cells with white background (associated with the variable free surface elevation) at row 'FL' and columns 'r'. However, the correlation between flume and modelled near-bed velocities is lower ($r \leq 0.47$), with regression slopes much greater than unity with C_2 and T_3 (see the black cells at the row 'FL' and columns 'r' and 'm'), indicating a tendency for an overestimation of near-bed velocities by the codes (Figure 2.4). The plots associated with these relationships are shown in Figure 2.4a. For instance, the bottom-left plot presents the relationship between the free surface elevations predicted by T_3 (y-variable) against those measured during the analogue flume experiment (x-variable) for M_{high}. The top-right plot presents the same relationship for near-bed elevation values.

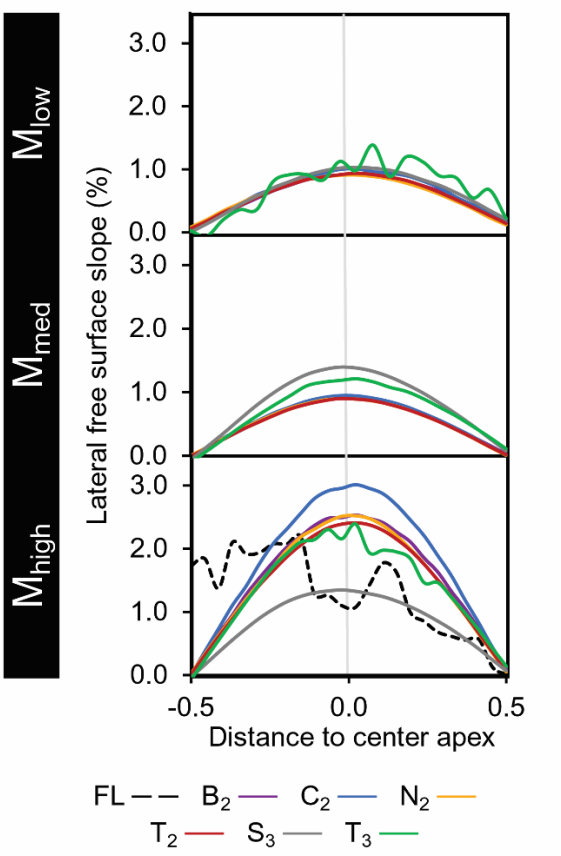

Figure 2.3. Comparison of the transverse slope of the free surface between models

Each curve corresponds to a fixed-flat bed numerical simulation along the central wave, i.e., $-0.5 < \lambda < 0.5$ in Figure 2.1, for configurations **a)** M_{low}, **b)** M_{med}, and **c)** M_{high} (FL = flume experiment).

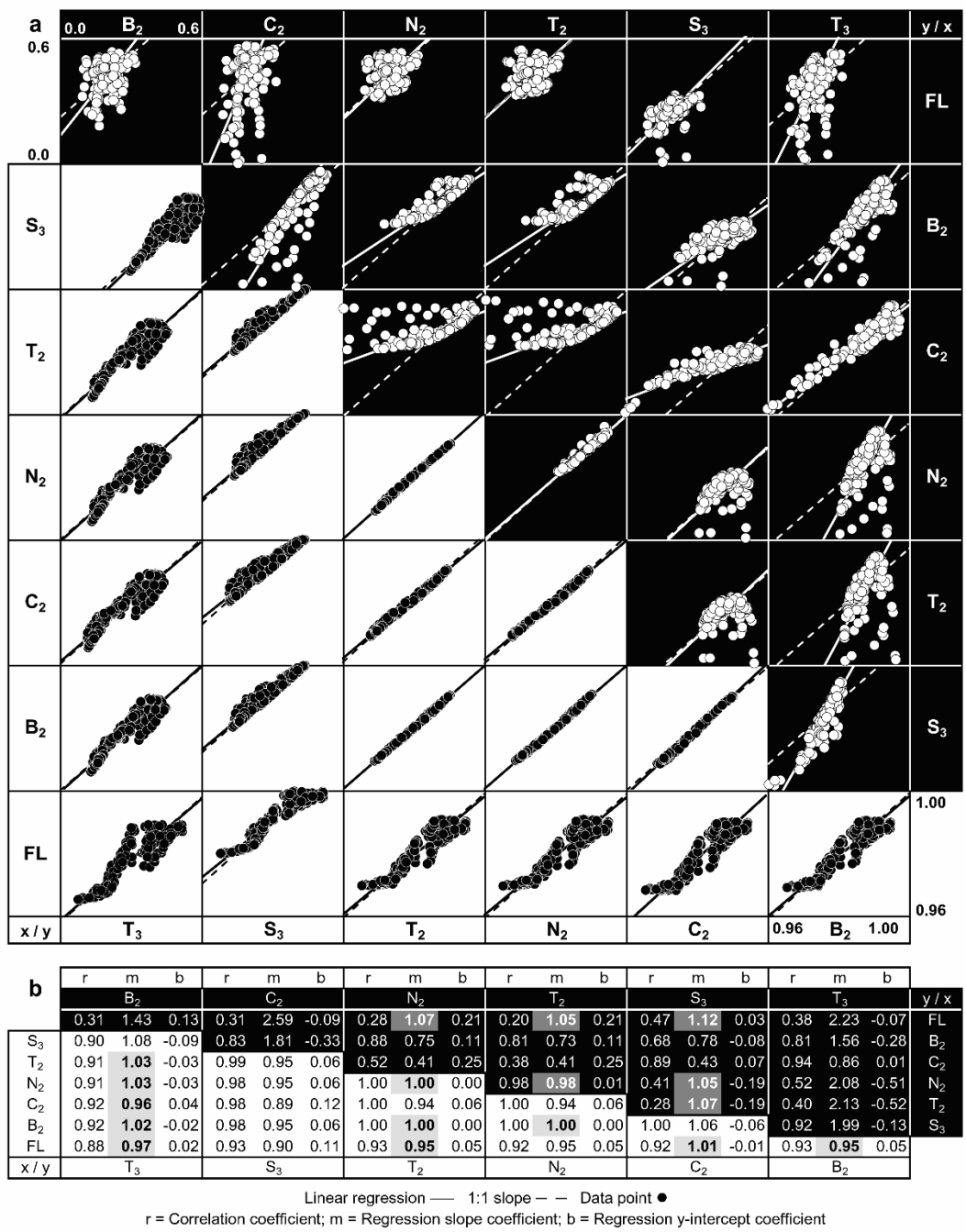

b

	r	m	b	r	m	b	r	m	b	r	m	b	r	m	b	r	m	b	
	B_2			C_2			N_2			T_2			S_3			T_3			y / x
	0.31	1.43	0.13	0.31	2.59	-0.09	0.28	**1.07**	0.21	0.20	**1.05**	0.21	0.47	**1.12**	0.03	0.38	2.23	-0.07	FL
S_3	0.90	1.08	-0.09	0.83	1.81	-0.33	0.88	0.75	0.11	0.81	0.73	0.11	0.68	0.78	-0.08	0.81	1.56	-0.28	B_2
T_2	0.91	**1.03**	-0.03	0.99	0.95	0.06	0.52	0.41	0.25	0.38	0.41	0.25	0.89	0.43	0.07	0.94	0.86	0.01	C_2
N_2	0.91	**1.03**	-0.03	0.98	0.95	0.06	1.00	**1.00**	0.00	0.98	**0.98**	0.01	0.41	**1.05**	-0.19	0.52	2.08	-0.51	N_2
C_2	0.92	**0.96**	0.04	0.98	0.89	0.12	1.00	0.94	0.06	1.00	0.94	0.06	0.28	**1.07**	-0.19	0.40	2.13	-0.52	T_2
B_2	0.92	**1.02**	-0.02	0.98	0.95	0.06	1.00	**1.00**	0.00	1.00	**1.00**	0.00	1.00	1.06	-0.06	0.92	1.99	-0.13	S_3
FL	0.88	**0.97**	0.02	0.93	0.90	0.11	0.93	**0.95**	0.05	0.92	0.95	0.05	0.92	**1.01**	-0.01	0.93	**0.95**	0.05	
x / y	T_3			S_3			T_2			N_2			C_2			B_2			

Linear regression —— 1:1 slope — — Data point ●

r = Correlation coefficient; m = Regression slope coefficient; b = Regression y-intercept coefficient

Figure 2.4. Simulated vs. measured near-bed velocities and free surface elevations.

Near-bed velocity (black background) and free surface elevations (white background) are for a fixed-flat bed for the M_{high} configuration. RMA regression is carried out on a sample of 200 points located along the central wave, i.e., $-0.5 < \lambda < 0.5$ in Figure 2.1. The dataset FL corresponds to the flume experiment by Termini (2009). Dashed lines show 1:1 agreement whereas full lines correspond to the regression slope. Values in gray cells are not significantly different from the 1:1 slope. The labels 'y/x' indicate the order of comparison, where y is the dependent variable and x the independent variable.

The regression coefficients for depth-averaged velocity magnitudes between codes reveal some similarities between the 2D codes for M_{low} and M_{med}, but less so for M_{high}, with the exception of N_2 and T_2 which are consistently very similar for all configurations (Figure 2.5). Surprisingly, a strong similarity (r = 0.72, slope not significantly different from 1) is observed between B_2 and S_3 for the M_{high} configuration, whereas this is not the case for less sinuous channels. Although the correlation between the two 3D codes is high (Figure 2.5; Figures 2.S4–6), the maximum velocity magnitude predicted by T_3 was slightly larger than the values predicted by the other codes for M_{low} (35.4 cm/s in T_3 vs. ≤ 29.2 in the other models) and M_{high} (61.0 cm/s in T_3 vs. ≤ 55.4 cm/s in the other models). However, both 3D codes predict zero velocity zones, whereas C_2 is the only 2D code to predict this (and only for M_{high}). The M_{med} configuration has the highest mean correlation coefficient (0.85),

a

C_2			N_2			T_2			S_3			T_3			y / x
r	m	b	r	m	b	r	m	b	r	m	b	r	m	b	
0.93	1.29	-0.06	0.95	0.96	0.01	0.89	0.89	0.02	0.84	2.18	-0.30	0.70	3.27	-0.56	B_2
			0.87	0.74	0.06	0.72	0.70	0.07	0.90	1.69	-0.19	0.84	2.55	-0.40	C_2
						0.96	0.94	0.01	0.71	2.28	-0.32	0.53	3.43	-0.60	N_2
									0.55	2.43	-0.36	0.35	3.66	-0.65	T_2
												0.89	1.50	-0.11	S_3

b

C_2			N_2			T_2			S_3			T_3			y / x
r	m	b	r	m	b	r	m	b	r	m	b	r	m	b	
0.99	1.01	0.00	0.97	0.92	0.02	0.95	0.91	0.03	0.83	2.06	-0.26	0.79	1.87	-0.25	B_2
			0.96	0.91	0.02	0.94	0.89	0.03	0.86	2.03	-0.26	0.82	1.84	-0.25	C_2
						1.00	0.98	0.00	0.72	2.24	-0.31	0.64	2.03	-0.30	N_2
									0.68	2.27	-0.32	0.60	2.07	-0.30	T_2
												0.96	0.91	-0.01	S_3

c

C_2			N_2			T_2			S_3			T_3			y / x
r	m	b	r	m	b	r	m	b	r	m	b	r	m	b	
0.85	1.91	-0.41	0.87	0.71	0.13	0.78	0.69	0.14	0.72	1.03	-0.15	0.82	1.76	-0.39	B_2
			0.54	0.37	0.29	0.38	0.36	0.29	0.91	0.54	0.08	0.95	0.92	-0.01	C_2
						0.98	0.97	0.01	0.44	1.44	-0.34	0.51	2.47	-0.72	N_2
									0.29	1.48	-0.35	0.38	2.54	-0.74	T_2
												0.93	1.72	-0.14	S_3

d

M_{low}			M_{med}			M_{high}			
r	m	b	r	m	b	r	m	b	Codes
0.89	0.92	0.02	0.97	0.94	0.02	0.73	0.84	0.07	2D vs. 2D
0.89	1.50	-0.11	0.96	0.91	-0.01	0.93	1.72	-0.14	3D vs. 3D
0.68	2.68	-0.42	0.74	2.05	-0.28	0.63	1.52	-0.33	2D vs. 3D
0.77	1.90	-0.22	0.85	1.53	-0.14	0.69	1.26	-0.15	Any

r = Correlation coefficient; m = Regression slope coefficient; b = Regression y-intercept coefficient

Figure 2.5. Comparison of simulated depth-averaged velocity magnitudes

This corresponds to a fixed-flat bed for a) M_{low}, b) M_{med}, and c) M_{high}. RMA regression is carried out on a sample of 200 points located along the central wave, i.e., $-0.5 < \lambda < 0.5$ in Figure 2.1. Values in gray cells are not significantly different from the 1:1 slope. d) Mean coefficient values.

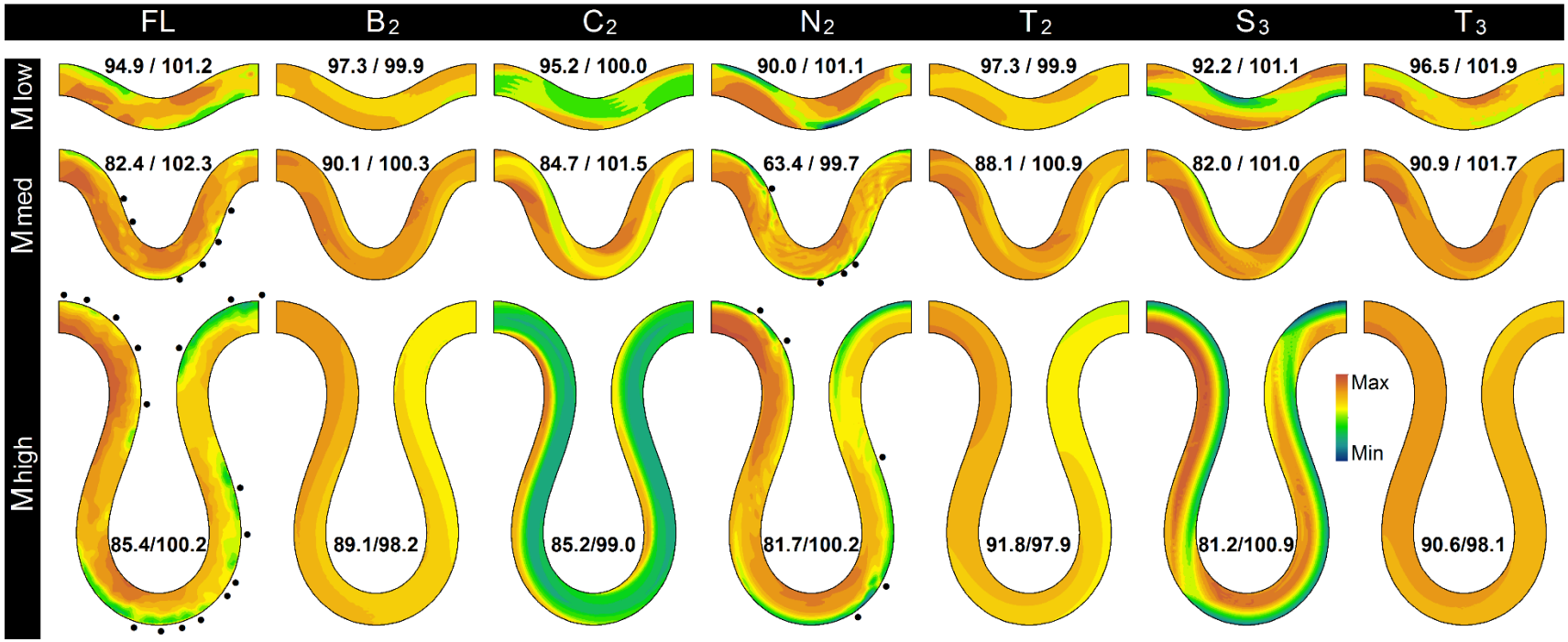

Figure 2.6. Predicted and observed bathymetries

Bathymetries were developed during numerical simulations and analogous flume experiments, i.e., on mobile bed, along the central wave, i.e., $-0.5 < \lambda < 0.5$ in Figure 1. Minimum and maximum values are displayed below each map. The measured and predicted locations of the shingle bars along the external sidewall of meander bends are indicated with black dots.

indicating more similarities between simulations for this configuration compared to lower or higher sinuosity (Figure 2.5d). We also notice a stronger agreement between codes using the same number of dimensions. For instance, the average correlation coefficient is $0.73 \leq r \leq 0.97$ for codes with same dimensionality, but it is of $0.63 \leq r \leq 0.85$ for the other code combinations.

a

	r	m	b	r	m	b	r	m	b	r	m	b	r	m	b	r	m	b	
	B_2			C_2			N_2			T_2			S_3			T_3			y / x
S_3	-0.26	-0.46	1.44	0.91	2.17	-0.29	0.54	2.11	-0.30	0.97	1.28	-0.07	0.93	2.74	-0.48	0.60	2.81	-0.44	B_2
T_2	0.65	2.05	-1.03	0.29	4.40	-3.36	0.74	**0.97**	-0.01	0.92	0.59	0.10	0.90	1.26	-0.11	0.76	1.30	-0.06	C_2
N_2	0.65	0.46	0.54	-0.10	-0.98	1.94	0.61	0.22	0.77	0.61	0.61	0.11	0.53	1.30	-0.10	0.53	1.33	-0.04	N_2
C_2	0.00	-0.77	1.73	0.81	1.65	-0.63	0.48	0.38	0.62	0.00	-1.69	2.62	0.94	2.14	-0.33	0.60	2.20	-0.28	T_2
B_2	0.03	1.90	-0.89	0.89	4.09	-3.06	0.59	**0.93**	0.07	0.26	4.17	-3.13	0.84	2.47	-1.47	0.72	**1.03**	0.06	S_3
FL	0.72	0.71	0.28	0.06	1.54	-0.54	0.68	0.35	0.64	0.85	1.57	-0.56	0.05	**0.93**	0.05	0.35	0.38	0.62	
y / x	T_3			S_3			T_2			N_2			C_2			B_2			

b

	r	m	b	r	m	b	r	m	b	r	m	b	r	m	b	r	m	b	
	B_2			C_2			N_2			T_2			S_3			T_3			y / x
S_3	0.59	0.55	0.43	0.36	1.36	-0.13	-0.07	-0.51	0.32	0.72	1.47	-0.13	0.61	1.45	-0.15	0.59	**0.96**	0.01	B_2
T_2	0.68	0.87	0.13	0.81	1.59	-0.55	0.37	0.37	0.13	0.66	**1.08**	0.01	0.73	**1.07**	-0.01	0.73	0.71	0.10	C_2
N_2	0.66	0.54	0.46	0.66	**0.97**	0.05	0.62	0.61	0.38	0.23	2.90	-0.35	0.25	2.87	-0.37	0.34	1.90	-0.14	N_2
C_2	0.69	0.47	0.52	0.71	0.85	0.17	0.85	0.54	0.45	0.50	**0.88**	0.12	0.88	**0.99**	-0.02	0.66	0.65	0.09	T_2
B_2	0.40	**1.16**	-0.15	0.77	2.09	-1.05	0.74	1.32	-0.32	0.48	2.16	-1.14	0.72	2.45	-1.43	0.71	0.66	0.00	S_3
FL	0.77	0.56	0.42	0.64	**1.02**	-0.02	0.64	0.65	0.33	0.71	**1.05**	-0.08	0.62	1.20	-0.22	0.50	0.49	0.49	
y / x	T_3			S_3			T_2			N_2			C_2			B_2			

c

	r	m	b	r	m	b	r	m	b	r	m	b	r	m	b	r	m	b	
	B_2			C_2			N_2			T_2			S_3			T_3			y / x
S_3	0.41	0.20	0.76	0.42	1.54	-0.48	0.20	1.32	-0.24	0.91	0.59	0.19	0.34	1.63	-0.44	0.72	**1.06**	-0.05	B_2
T_2	0.99	1.15	-0.14	0.41	5.65	-4.41	0.57	0.85	0.17	0.61	0.38	0.38	0.77	**1.06**	0.07	0.36	0.69	0.28	C_2
N_2	0.64	0.33	0.64	0.73	1.62	-0.59	0.64	0.29	0.68	0.24	0.44	0.30	0.62	1.24	-0.14	0.44	0.81	0.14	N_2
C_2	0.06	0.25	0.72	0.25	1.24	-0.17	0.07	0.22	0.75	-0.10	-0.77	1.63	0.48	2.79	-0.98	0.57	1.82	-0.40	T_2
B_2	0.69	**1.12**	-0.11	0.30	5.50	-4.28	0.69	**0.97**	0.02	0.20	3.40	-2.28	0.51	4.43	-3.32	0.49	0.65	0.24	S_3
FL	0.70	0.34	0.63	0.65	1.67	-0.64	0.67	0.30	0.67	0.81	**1.03**	-0.03	-0.08	-1.34	2.16	0.29	0.30	0.66	
y / x	T_3			S_3			T_2			N_2			C_2			B_2			

d

M_{low}			M_{med}			M_{high}			
r	m	b	r	m	b	r	m	b	Codes
0.78	1.29	-0.08	0.38	1.11	-0.03	0.49	0.85	0.05	2D vs. 2D
0.72	1.03	0.06	0.71	0.66	0.00	0.49	0.65	0.24	3D vs. 3D
0.72	1.89	-0.23	0.60	1.32	-0.06	0.54	1.39	-0.19	2D vs. 3D
0.75	1.59	-0.15	0.52	1.20	-0.04	0.52	1.13	-0.06	Any
0.46	1.08	-0.09	0.65	1.33	-0.32	0.34	1.43	-0.42	2D vs. 2D
-0.26	-0.46	1.44	0.59	0.55	0.43	0.41	0.20	0.76	3D vs. 3D
0.40	1.60	-0.60	0.67	1.07	-0.05	0.51	2.11	-1.04	2D vs. 3D
0.38	1.25	-0.26	0.66	1.14	-0.13	0.43	1.71	-0.67	Any

r = Correlation coefficient
m = Regression slope coefficient
b = Regression y-intercept coefficient

Figure 2.7. Parameters of RMA regression between simulated and observed flows

This compares simulated depth-averaged velocity magnitudes (black background) and bed elevations (white background) on a mobile bed for a) M_{low}, b) M_{med}, and c) M_{high}. RMA regression is carried out on a sample of 200 points located along the central wave, i.e., $-0.5 < \lambda < 0.5$ in Figure 2.1. The dataset FL corresponds to the flume experiment by Termini (2009). Dashed lines show 1:1 agreement whereas full lines correspond to the regression slope. Values in gray cells are not significantly different from the 1:1 slope. d) Mean coefficient values.

2.3.2. Mobile-bed runs

Meandering channels commonly develop a series of depositional features along the inner bank of the bend at the apex (point bars), scour zones on the opposite bank (pools), and flatter bed morphologies between consecutive pool features (riffles) (Whiting and Dietrich 1993; Blanckaert 2010). The six investigated codes indeed predict these features for the three meandering configurations

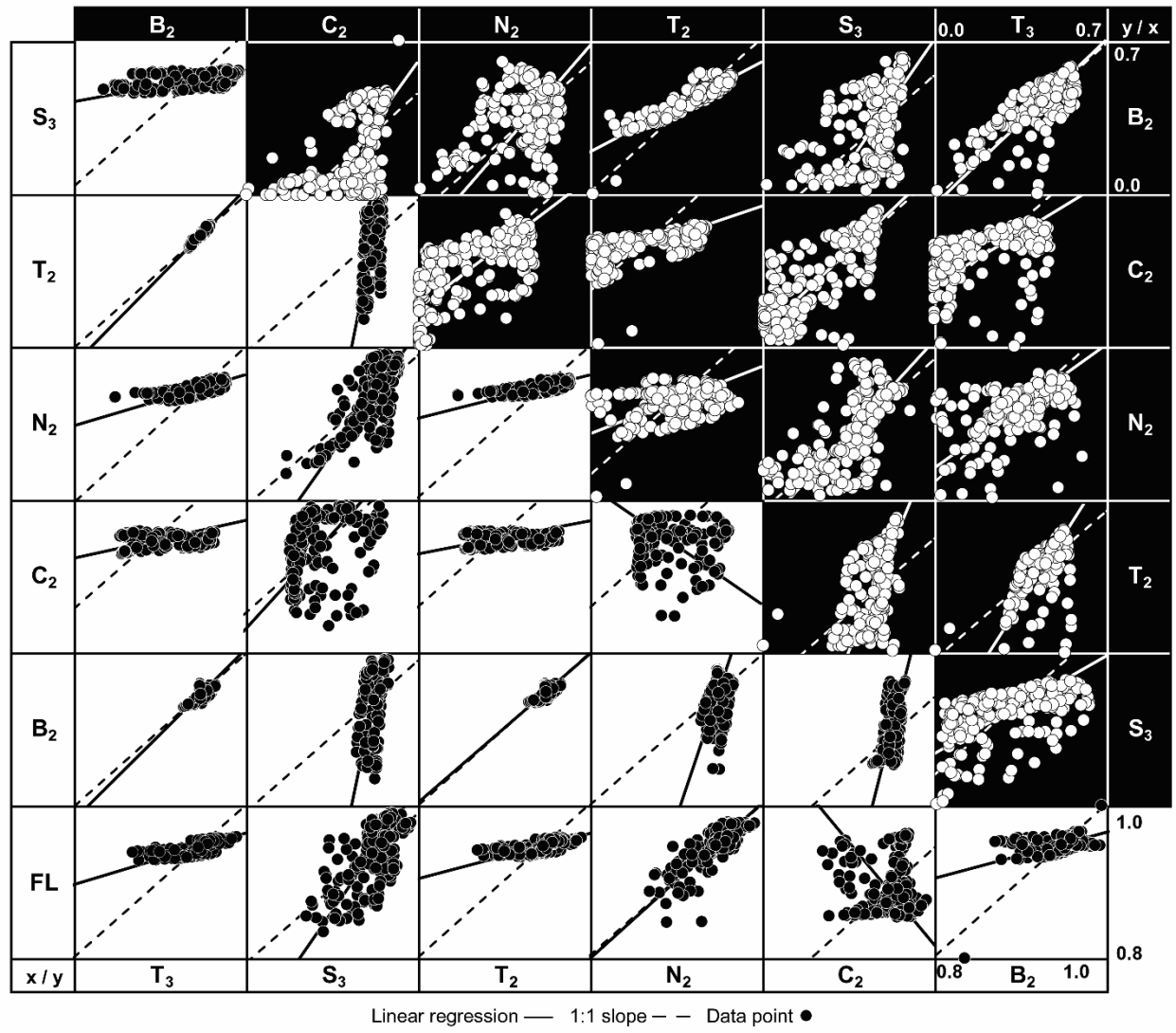

Figure 2.8. Simulated vs. measured velocity magnitudes and bed elevations

Depth-averaged velocities (black background) and bed elevations (white background) are for a mobile bed for the configuration M_{high}. RMA regression is carried out on a sample of 200 points located along the central wave, i.e., $-0.5 < \lambda < 0.5$ in Figure 2.1. The dataset FL corresponds to the flume experiment by Termini (2009). Dashed lines show 1:1 agreement whereas full lines correspond to the regression slope. Values in gray cells are not significantly different from the 1:1 slope.

(Figure 2.6). However, the location, dimensions and shape of geomorphic features differ to the extent that predictions are sometimes opposite, e.g., C_2 vs. T_2 in M_{low}. The bathymetries produced by S_3 involve a wide range of values (Figure 2.6) and are fairly accurate for M_{med} and M_{high} (Figures 2.7b–c; 2.8), which may be attributed to the selection of the Nikuradse law, although N_2 made similar predictions, but did not use Nikuradse. Velocity predictions in mobile bed simulations (Figure 2.7d) are, overall, more scattered than on fixed-flat beds (Figures 2.5d), with mean regression coefficients decreasing from $r = 0.85$ to $r = 0.52$ for M_{med} and from $r = 0.69$ to $r = 0.52$ for M_{high}. In most cases, flow fields that were similar over a fixed-flat bed such as N_2 and T_2 (Figures 2.5, with r values ≥ 0.96) are not as similar on a mobile bed ($r = 0.61$, $r = 0.23$, and $r = 0.24$, respectively for M_{low}, M_{med}, and M_{high}) (Figure 2.7a–c).

The differences between codes are even greater for bed elevations, with mean regression coefficients of $r = 0.38$, $r = 0.66$, and $r = 0.43$, respectively for M_{low}, M_{med}, M_{high} (Figure 2.7d). In addition, similar hydraulic predictions between two codes on a fixed-flat bed do not guarantee similar equilibrium morphologies on a mobile bed. For instance, B_2 and N_2 produced similar initial velocity patterns in all configurations (Figures 2.2; 2.5a–c), but their equilibrium bathymetries differ considerably (Figures 2.6; 2.7a–c). The opposite situation occurs for T_2-T_3, with different velocities leading to similar bathymetries. Finally, the degree of sinuosity affects code similarity.

Overall, the bathymetric predictions were more accurate for the M_{med} configuration. Indeed, the low accuracies obtained under C_2 and S_3 for M_{low} partially contradict the statement of Xu and Bai (2013) that uncertainty of a prediction increases with sinuosity due to greater complexity of bed morphology. Relative to the bathymetries that developed in the flume experiments, N_2 produced the best predictions for all configurations, with regression coefficients of $r \geq 0.71$ and slopes not significantly different than unity for M_{med} and M_{high} (Figures 2.7b–c; 2.8). Some models such as C_2 compare well with flume bathymetry for M_{med}, but the correlation coefficient for the other two configurations is close to zero. For B_2 and T_3, the agreement is high for both M_{low} and M_{med} in terms of the slope, but less so for M_{high}, whereas S_3 and T_2 have a similar regression slope coefficient only for M_{med}. The morphological predictions of transversal bed profiles by the codes B_2 and C_2 differ considerably than the measurements made in the flume at the apex (for M_{low}) and just upstream of the apex (for M_{med} and M_{high}) (Figure 2.9). The error is less important with the other codes, except with M_{low} for S_3, where the discrepancies are located along the sidewalls just downstream of the apex. These observations are in line with the large discrepancies in cross-sectional profiles found by Xia et al. (2013) between numerical predictions and experimental measurements in a braided natural reach.

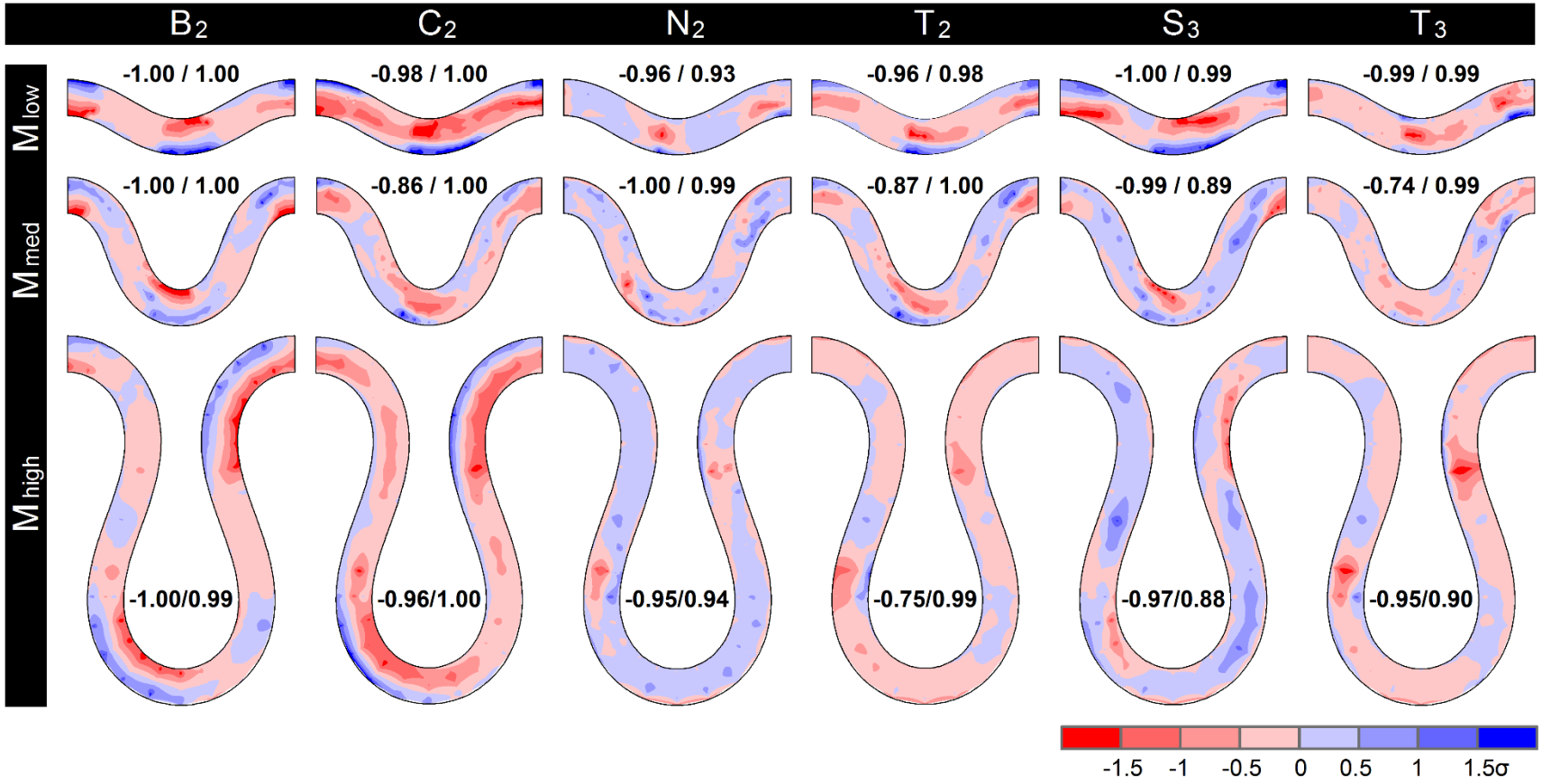

Figure 2.9. Differences between predicted and measured normalized bed elevations

This is presented in terms of number of standard deviations, σ. Minimum and maximum values are displayed beside each map.

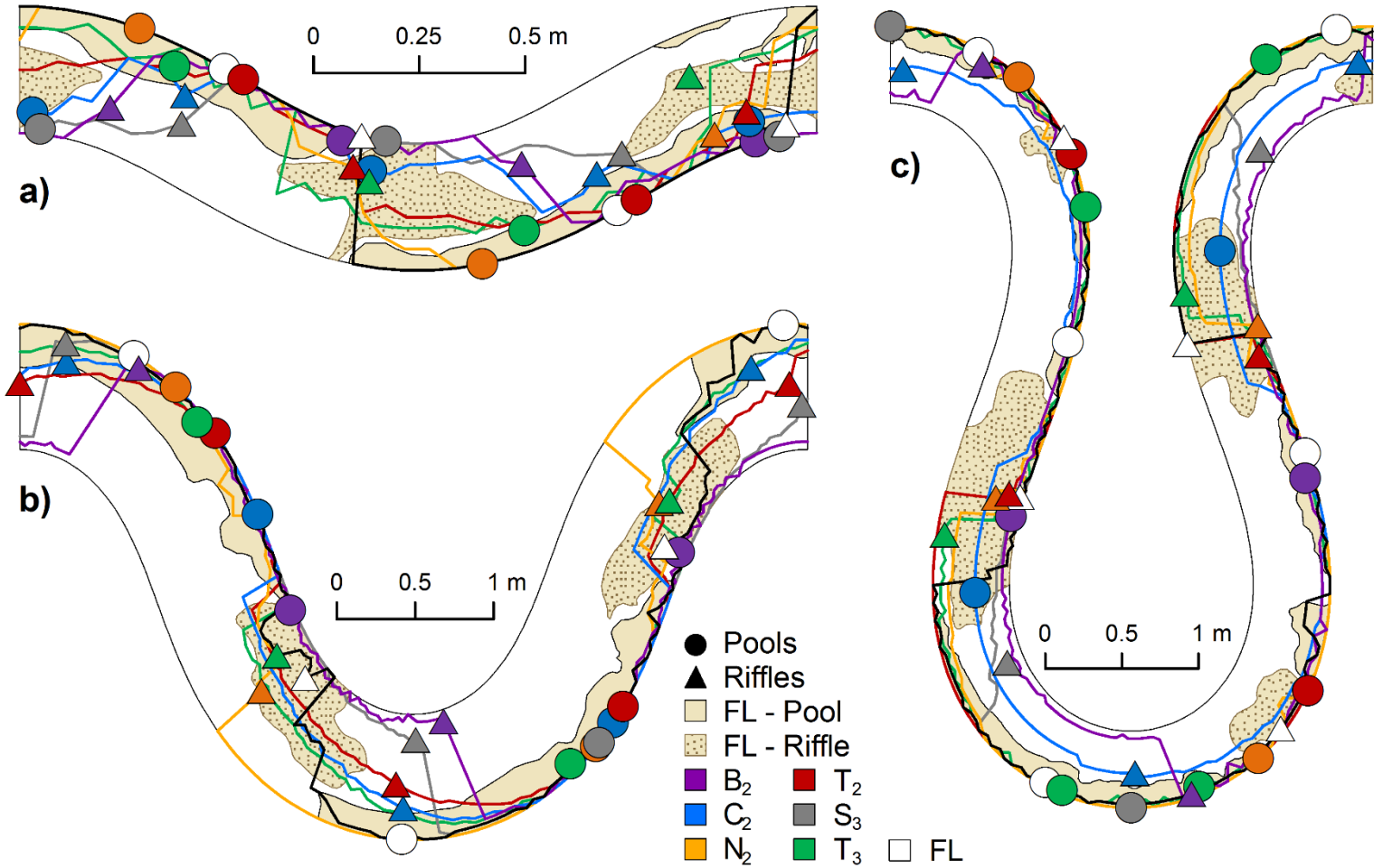

Figure 2.10. Geomorphic features formed during flume experiments and simulations

Thalweg, pools and riffles are shown along the central wave is shown, i.e., -0.5 < λ < 0.5 in Figure 2.1, for **a)** M_{low}, **b)** M_{med}, and **c)** M_{high}. Symbols represent the shallowest and deepest points, respectively, for the riffles and pools, and were derived from the longitudinal (along the thalweg) and lateral bed profiles. The full extent of the riffle and pool features is shown for the flume data only.

The location of the thalweg differs markedly between codes, with the predictions by codes B_2, C_2 (for M_{low} and M_{high}) and S_3 (for M_{low}) being the most different from the measured flume bathymetries (Figure 2.10). For example, C_2 predicts a riffle where a pool is located at the apex of the meander in M_{high}, whereas it predicts a pool in the riffle located downstream. In general, disparities between predicted morphological features increase with sinuosity. Associated with this are

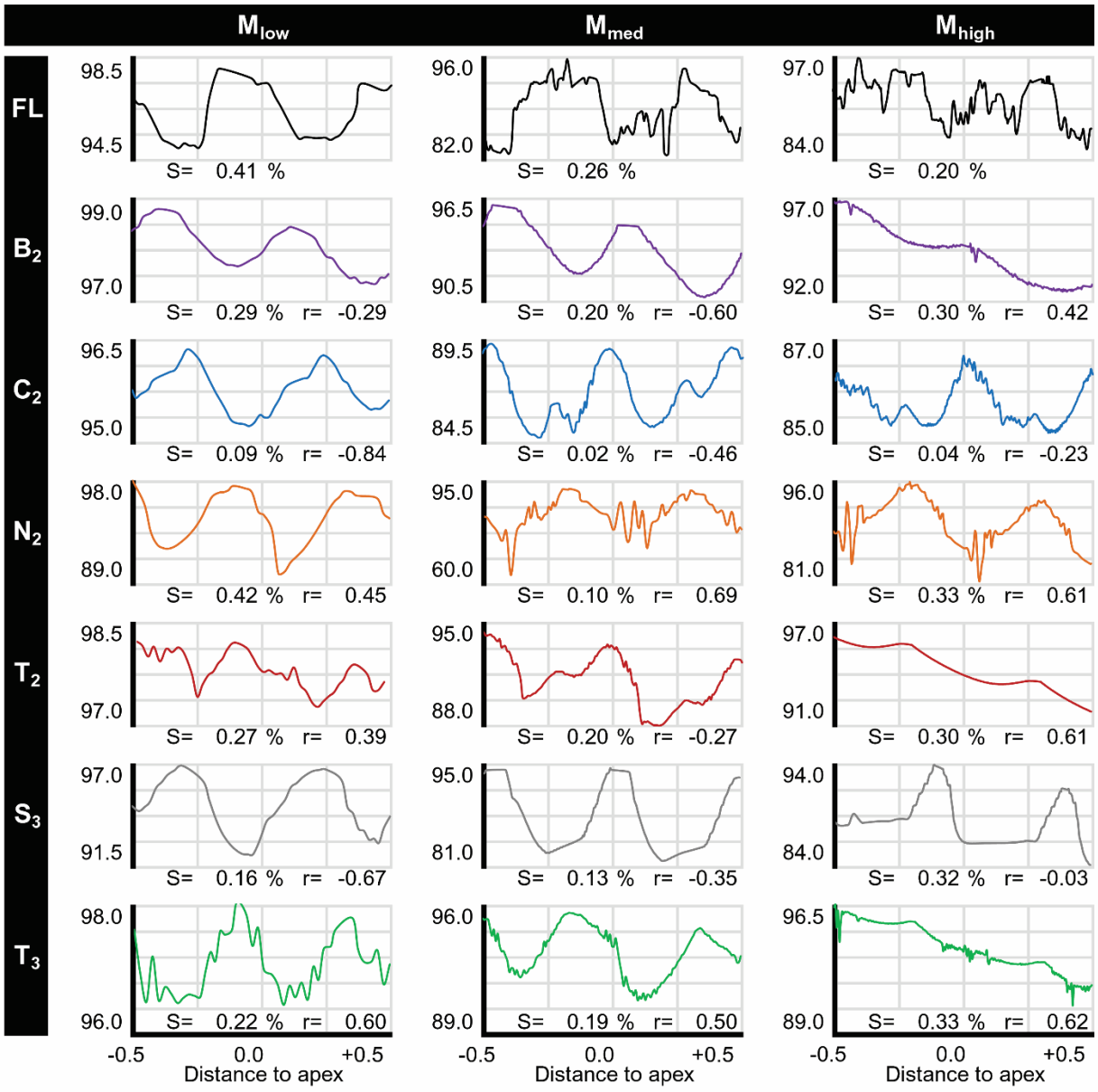

Figure 2.11. Longitudinal profiles after flume experiments and numerical simulations

Each column corresponds to one of the three meandering configurations on a mobile bed. 'S' represents the downslope longitudinal slope computed from riffle-to-riffle elevation differences. The correlation coefficient 'r' indicates the level of agreement between the predicted and measured profiles.

substantial differences in crest location, shape and wave amplitude of longitudinal profiles between the codes, but also between each code and the analogue flume experiments (Figure 2.11). The shingle bars (series of depositional lobes along the inner bank of a long bend with pools on the adjacent, outer bank) studied by Whiting and Dietrich (1993) and replicated in a flume by Ferreira da Silva and El-Tahawy (2006) and Termini (2009), although formally identified as such only in the latter study, are reproduced by N_2 for M_{med} and M_{high} (Figure 2.6). The code T_3 predicted oscillations in the longitudinal profile along the pool sections that may, instead, be artefacts of numerical instability due to abrupt increases and drops in bed elevations along the thalweg. Finally, note that N_2 and T_3 match the longitudinal flume profiles relatively well in all configurations.

2.4. Discussion

2.4.1. Model options, sub-models and calibration

Our numerical simulations could not be setup in a perfectly identical manner due to the lack of a common set of basic options and sub-models in the evaluated modelling codes (Table 2.5). Furthermore, it was simply not possible to list and consider all the features involved in each one of the analyzed simulations due to the lack of documentation on some of these features, and since the level of details included in the reference manuals varies between codes. However, sensitivity analyses revealed the limited influence of key options and sub-models on predicted bathymetries for the configuration M_{med}, and thus the variability in predictions can, at least partially, be attributed to code intricacies, such as design and implementation choices.

By ensuring that options, sub-models and parameter values are as similar as possible between the tested codes, recommended settings for a specific code may have been bypassed. In addition, in the absence of detailed hydraulic datasets, only the longitudinal slope of the water surface (e.g., velocity) was adjusted during calibration. We acknowledge that an experienced modeller would likely adjust parameter values differently for a better fit between numerical and flume experiments. However, the main aim for this study was not to numerically replicate flume experiments, but rather to provide explanations and hypotheses for observed differences in terms of hydraulic field and equilibrium bathymetries between modelling codes configured using highly similar initial flow and boundary conditions.

2.4.2. Scatter in predictions and model complexity

Substantial scatter exists in the hydraulic and morphological predictions achieved by the evaluated morphodynamic codes, the degree of accuracy varying with the modelling code, channel configuration and evaluation criterion. Scattering was especially important for M_{low} and M_{high} due to B_2 and C_2 (and S_3 for M_{low}) failing to accurately predict equilibrium bathymetries (Figure 2.7). With the configurations explored herein, T_3 would best answer a question related to low flow conditions, such as examining the habitat characteristics for aquatic species, due to its ability to predict correctly the location of the thalweg and of the geomorphic features (Figure 2.10), whilst N_2 could be useful to examine the shape of depositional bars and scour zones (Figure 2.6). A corollary to the lack of consistency in our simulations is that, since models are used in a range of contexts and disciplines, attributing ranks based on the inconsistent performance of these codes is subjective and pointless. It is also likely that the codes achieving the most accurate predictions in the current study would be less accurate under different channel, hydraulic or sedimentological configurations. A more useful exercise would consist in evaluating the range of applicability of widely used morphodynamics codes to commonly studied river types, e.g., braiding, anastomosing, meandering, and confluence. The options, sub-models and parameter values producing good agreements with datasets from flumes and natural rivers should be identified.

Further investigation helped determine why particular codes do well in a given context and poorly in another, e.g., S_3 in M_{med} and M_{high} vs. M_{low}, according to the regression coefficients for bed elevations (Figure 2.7). Even though only a small sample of modelling codes was employed in this study, it allowed to identify the options, sub-models and features of a code that are likely to enhance the accuracy of predictions in the context of a meandering river channel.

Given that secondary circulation, bed shear stress, and turbulent kinetic energy are best predicted within a three-dimensional code (Lane et al. 1999; Rameshwaran et al. 2013), it is not surprising that the hydraulic predictions obtained from the 3D codes S_3 and T_3 on a fixed-flat bed outperformed predictions from 2D codes for the configuration M_{high} (Figure 2.4). We would have expected a similar situation to occur on mobile beds due to the implicit inclusion of secondary flow and sediment circulation in the 3D codes (Rüther and Olsen 2007). However, the depth-averaged code N_2 was the most accurate for M_{low} and M_{high}, based on the regression coefficients for equilibrium bathymetries (Figure 2.7a–c). Similarly, the code T_2 was more accurate than S_3 for M_{low} and M_{high}, and as accurate for M_{med}. However, the 3D codes are expected to be more accurate than the 2D codes if suspended transport is activated due to their capacity to correctly simulate morphologies in the

presence of strong secondary currents (Ai et al. 2013; Marsooli and Wu 2014). Nevertheless, given the list of parameters selected (or imposed) for each code (Table 2.5), and considering the degree of accuracy reached in our sediment simulations, we found little evidence to support the hypothesis that increased code complexity automatically results in increased accuracy. This finding was also reported by Nicholas et al. (2012); in their study, a reduced-complexity model predicted flow field as accurately as 2D and 3D physics-based codes for a natural river reach. Similarly, Kasvi et al. (2015) revealed the preponderant role of the main two-dimensional flow in the development of a meander bend. In that case, perhaps key features of the 3D flow that are included in depth-averaged models, such as helical motion (Begnudelli et al. 2010), would be necessary to achieve accurate predictions, while others would not be essential.

Our results suggest that the effects of local bed slope and channel curvature on transport direction is not critical. The code C_2 includes these algorithms (Table 2.5) but was the least accurate amongst the evaluated codes for bed topography (Figures 2.9; 2.10). Conversely, the most accurate predictions came from N_2, which does not adjust the transport direction based on local bed slope and whose sediment slide algorithm (which ensures that any local slope does not exceed the angle of repose of the bed material) was disabled during our simulations. Similarly, the only code that does not include a turbulence model, B_2, predicts velocity patterns that are comparable to those associated with codes relying on k-ε turbulence closure. Indeed, the predicted patterns are very close to those of C_2, N_2 and T_2 on a fixed-flat bed for M_{low} and M_{med} (Figure 2.5) and are more accurate than C_2 and S_3 for bed elevations for M_{low} (Figure 2.7). However, B_2's predictions of equilibrium bathymetry are the worst for M_{med} and second worst for M_{high}, according to the regression coefficients (Figure 2.7b–c). This suggests that there may be an exception to this observation on complexity vs accuracy, and that a complex turbulence model is indeed required to adequately simulate sediment transport in more sinuous channels.

Bed shear stress and sediment transport are notoriously complex to estimate and prone to large uncertainties (Batalla 1997; Martin and Ham 2005; Carmelo et al. 2013; Rameshwaran et al. 2013). Despite this uncertainty, the codes N_2, T_2 and T_3 were fairly accurate in predicting equilibrium bathymetries measured in the three analogue flumes (Figure 2.7). The set of sub-models and algorithms included in these codes differ from those implemented in the codes B_2, C_2 and S_3. In the former, a sediment supply is present at the inlet, which allows to mimic the condition in a flume with sediment recirculation; channel curvature is estimated and used to calculate transport direction; finite elements are used instead of finite volume; and a formula other than Wu et al. (2000) is used to calculate transport rates (Table 2.5). Conversely, the presence of a sediment slide algorithm, the

consideration of wall friction and the role of bed slope on transport direction do not seem to play a critical role in achieving good predictive accuracy.

2.4.3. Uncertainty of modelling outcomes and purpose of using multiple codes

Assuming that multiple modelling codes are available to examine a phenomenon in a given context, an expert modeller would certainly be able to identify the most appropriate codes to use, based solely on experience and a list of the options and sub-models included in each code. However, assuming that multiple codes offer equivalent options, and in the absence of a validation dataset, it may be impossible to identify the code that is likely to provide the most reliable prediction. Our results suggest that the selection of a code can substantially affect simulated hydraulics and morphologies, and thus the conclusions emerging from a modelling investigation. This is especially true for the codes that include few options (e.g., C_2, N_2), and thus provide fewer opportunities to adjust parameters for a better fit between predicted and observed measurements during calibration. This issue was raised by Jowett and Duncan (2012) who reported that important discrepancies can emerge from the use of 2D and 3D codes due to the challenge of sufficiently calibrating a complex model.

Our results revealed that the accuracy of a modelling code can vary with the simulated environmental context, which suggests that model users should select a code for each specific investigation, regardless of their previous experience with codes. Although there are clear benefits in being able to use multiple codes, we acknowledge that there is a notable duplication of efforts involved in the process. However, enhanced cooperation amongst the developers of a modelling community could facilitate the development of a knowledge base regarding the applicability of fluvial models and help model users to master multiple modelling codes. For instance, single agreed-on formats could be used for basic input files such as bed topography, input flow and sediment discharges. Not only would this help a researcher or practitioner mastering a new code faster, but it would also reduce the list of required pre- and post-processing software. Although most hydrodynamic and morphodynamic models continue to use their own file formats, the International River Interface Cooperative (iRIC) has started addressing this issue by connecting a set of codes through a unique graphical user interface, which demonstrates the need for unity and collaboration in fluvial and coastal processes modelling. Finally, although a set of validation cases is included with most codes, a common set of validation cases in a central repository could serve in cross-validating and improving codes. The simulation and results files from this study are available through Supplemental Material (see the website of the journal in which the chapter was published). This

provides a first step towards building an exhaustive morphodynamic validation dataset, which hopefully will grow in the future with the addition of other codes and channel configurations.

2.5. Conclusion

A series of numerical experiments was undertaken in meandering channels with vertical sidewalls to verify whether flow hydraulics and equilibrium bathymetries would be similar between CFD-based morphodynamic modelling codes subjected to identical initial bed morphologies and very similar initial flow conditions. The numerical codes BASEMENT, CCHE-2D, NAYS, SSIIM-1, and TELEMAC-2D and -3D were used to simulate flow and sediment transport in channels (low, medium and high sinuosity) for which detailed equilibrium bathymetry is available.

Substantial discrepancies were found between the evaluated codes, and between predicted equilibrium bathymetries and observations made in analogue flume experiments. However, no code outperformed the others for all criteria and contexts considered. Indeed, codes that were performing well for a given channel configuration were in many cases not matching well flume bathymetry for a higher or lower sinuosity. This highlights the need to assess codes for more than one channel configuration.

A sensitivity analysis on key modelling options and sub-models revealed the limited influence of turbulence closure methods and bed transport formulae on simulated bed morphologies, relative to that of the choice of a code. Inter-code dissimilarities may be due to the lack of a common method to consider bed and lateral channel roughness and to estimate bed shear stress. Although we only considered a few modelling codes and channel configurations, we found no evidence that a more complex code results in more accurate predictions. In particular, the three-dimensional codes, along with those taking into account local bed slope and channel curvature, were not always accurate.

Uncertainty is an inherent consequence of numerical investigations, which existence can be attributed to process reductionism, scarcity and insufficient quality of real-world data, stochasticity of natural processes, and model structure and parameterization (Uhlenbrook and Sieber 2005; Carboni et al. 2007). The diversity of modelling codes available should be seen as an opportunity to reduce uncertainty in morphodynamic modelling by using the code that is the most appropriate for any particular context, which involves either knowing a priori which code to use, based on documented benchmark reports, or being able to discover it rapidly through a series of numerical simulations. Although we recognize that practical constraints may conflict with this recommendation, developing, documenting and sharing validation cases between models of the same

type would be a first step in this direction, as is done in this study, which gives access to the datasets as Supplemental Material (see the website of the journal in which the chapter was published). A central repository holding sample cases and documents regarding the degree of compatibility between modelling codes and channel types would certainly be useful for model users. Another important step would be for a consortium of developers to decide on a single file format to use in morphodynamic models to define cases, topographies and boundary conditions.

2.6. Supplemental material

2.6.1. Sensitivity to mesh resolution

A computational mesh structure with a body-fitted coordinate system consisting of quadrilateral cells was employed in all simulations. The sensitivity of models B_2, T_2 and S_3 to the number of horizontal cells was assessed using mesh H_A (679 cells, i.e., 97x7), H_B (3281 cells, i.e., 193x17), H_C (12,705 cells, i.e., 385x33), and H_D (49,985 cells, i.e., 769x65). The number of cells in the vertical direction was six when varying horizontal resolution in S_3. The sensitivity of T_3 to a change in vertical resolution was evaluated by launching simulations with meshes V_2, V_4, V_6, V_8, V_{10} and V_{12}, the subscript indicating the number of vertical cells.

Three grid independence tests (Roache et al. 1986; Lane et al. 2005; Biron et al. 2007) were carried out through a series of fixed-flat-bed simulations for the M_{med} configuration (Figure 2.1). The first test compared the predicted minimum and maximum flow depths and velocity magnitudes (along the x-, y- and z-axes) with the values obtained with the finest horizontal mesh H_D. A difference of less than 10% was achieved with meshes H_B (for all variables) and V_6 (except for minimum depth and velocity along the x-axis). In the second test, grid convergence indices were calculated at 200 point locations, selected randomly within the zone delimited by $-1.0 \leq \lambda \leq 1.0$ (see Figure 2.1), and compared between the mesh resolutions for the depth and velocity variables. Using meshes H_B and V_8 maximized the horizontal and vertical grid convergence indices (except for vertical velocity). In the third test reduced-major axis regression was computed for the same 200 locations, comparing flow depth and velocity predictions between mesh resolutions. A correlation coefficient larger than 0.95 was obtained for meshes H_B, H_C and H_D (all variables) and when using at least 6 vertical cells (except for velocity in the vertical direction). The horizontal and vertical mesh resolutions used to carry out the numerical experiments were those which performed well in the three tests for most codes and variables: meshes H_C and V_6.

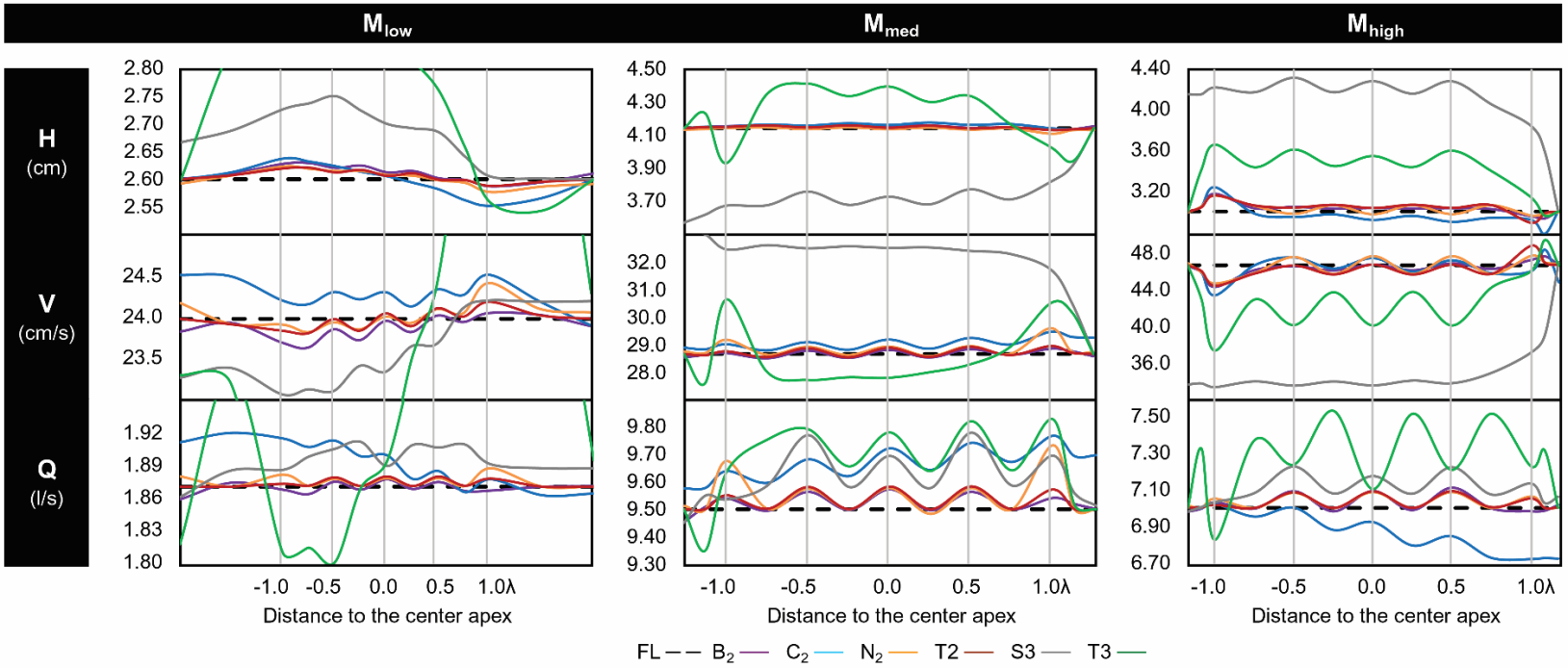

Figure 2.S1. Averaged flow depth, velocity and discharge on fixed-flat bed

This is for configurations M_{low}, M_{med}, and M_{high}. Values and depth- and width-averaged. The view was cropped in the M_{low} plots due to larger values produced by T_3, with maximum values of 2.94 cm, 30.0 cm/s and 2.30 l/s, respectively for H (depth), V (velocity), and Q (discharge); and a minimum value of 20.5 cm/s for V.

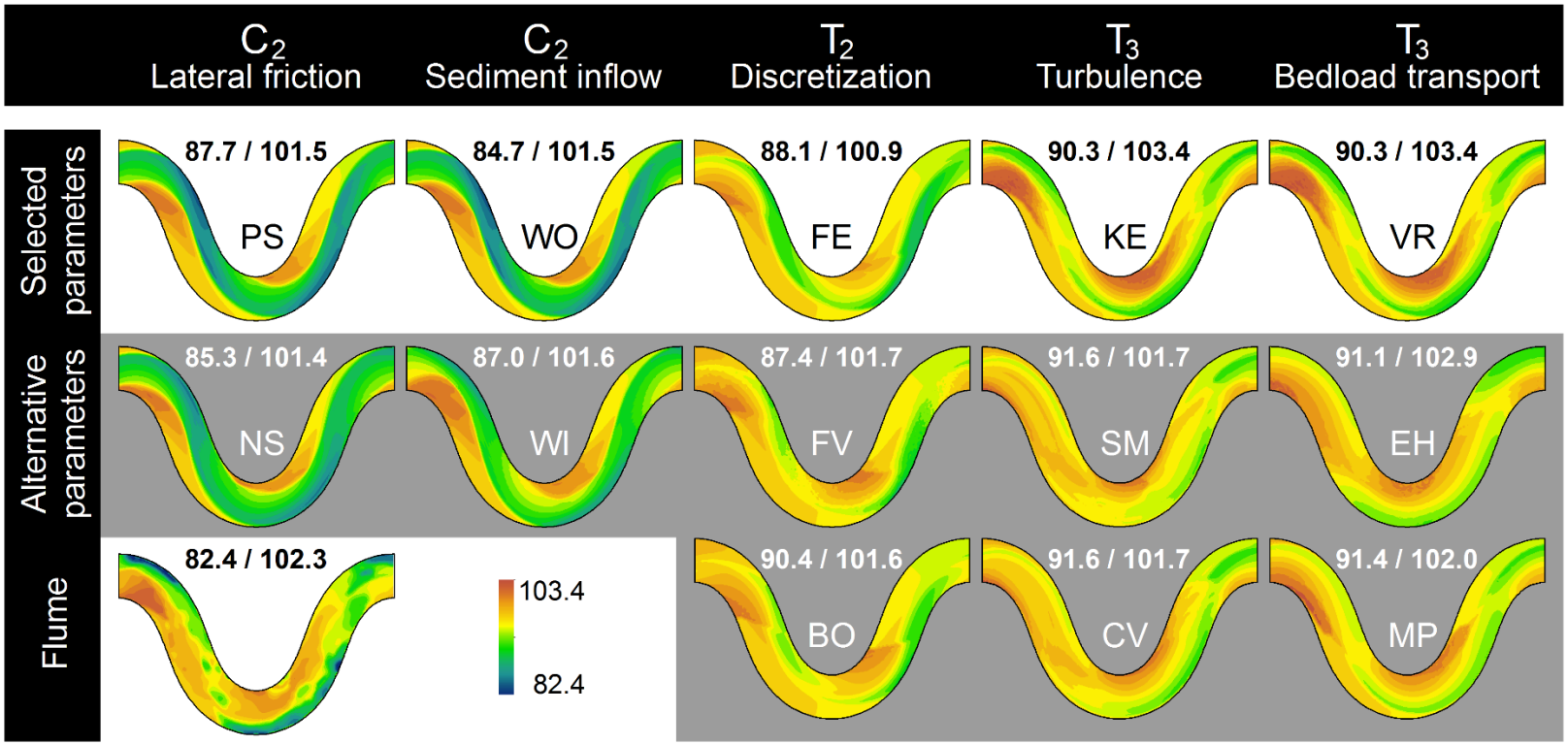

Figure 2.S2. Bathymetries predicted by the models C_2, T_2 and T_3 on a mobile bed

Results are shown for the configuration M_{med} along the central wave, i.e., $-0.5 < \lambda < 0.5$ in Figure 2.1. The predictions on the first row correspond to the settings described in Table 2.5. The subsequent rows show the bathymetries obtained by altering lateral friction, sediment inflow rate, spatial discretization, turbulence closure, or bed load transport formula. The acronyms are explained in Figure 2. The selected inflow rate is 1.66 g/m/s, which is the outflow rate simulated by C_2 at the onset of the mobile bed simulation. The map identified as FL corresponds to the analogue flume experiment. Minimum and maximum values are displayed below each map.

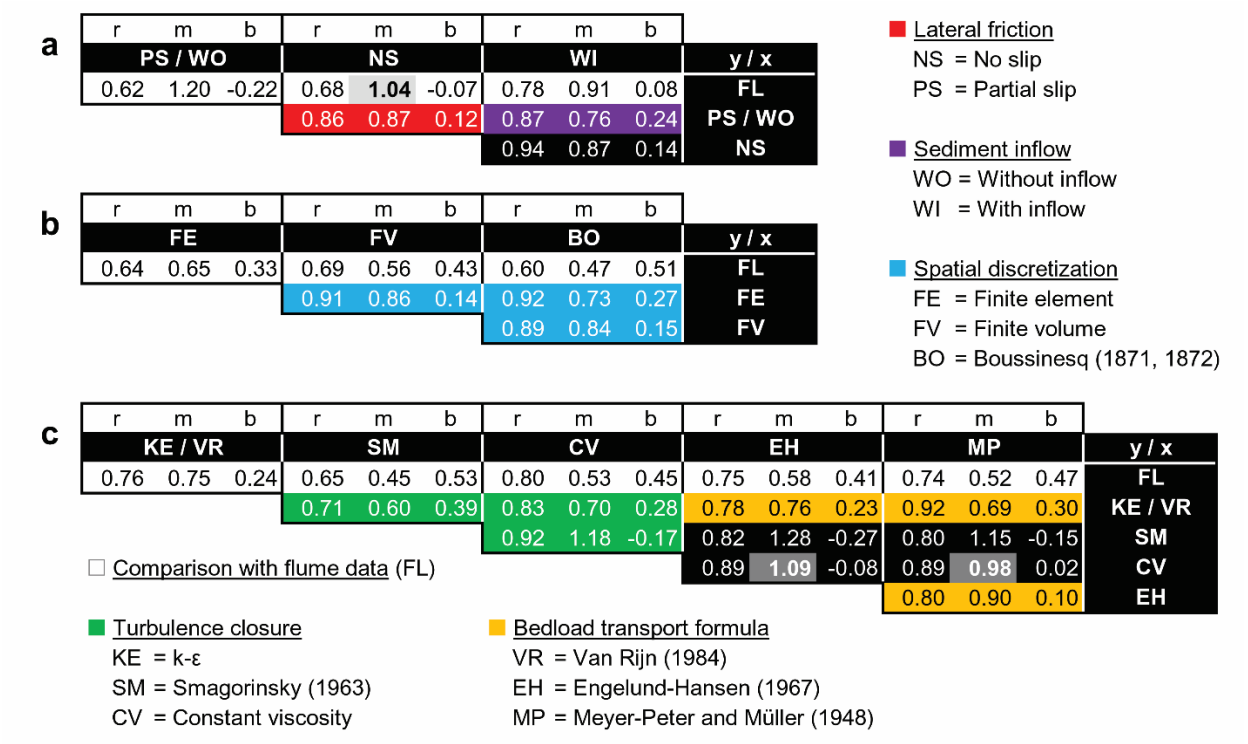

Figure 2.S3. Linear regression using the reduced major axis technique

Bed elevation values are shown for simulations on a mobile bed in **a)** C_2, **b)** T_2, and **c)** T_3 for M_{med}. The predictions using the settings described in Table 2.5 are compared to predictions obtained by altering lateral friction, sediment inflow rate, spatial discretization, turbulence closure, or bed load transport formula.

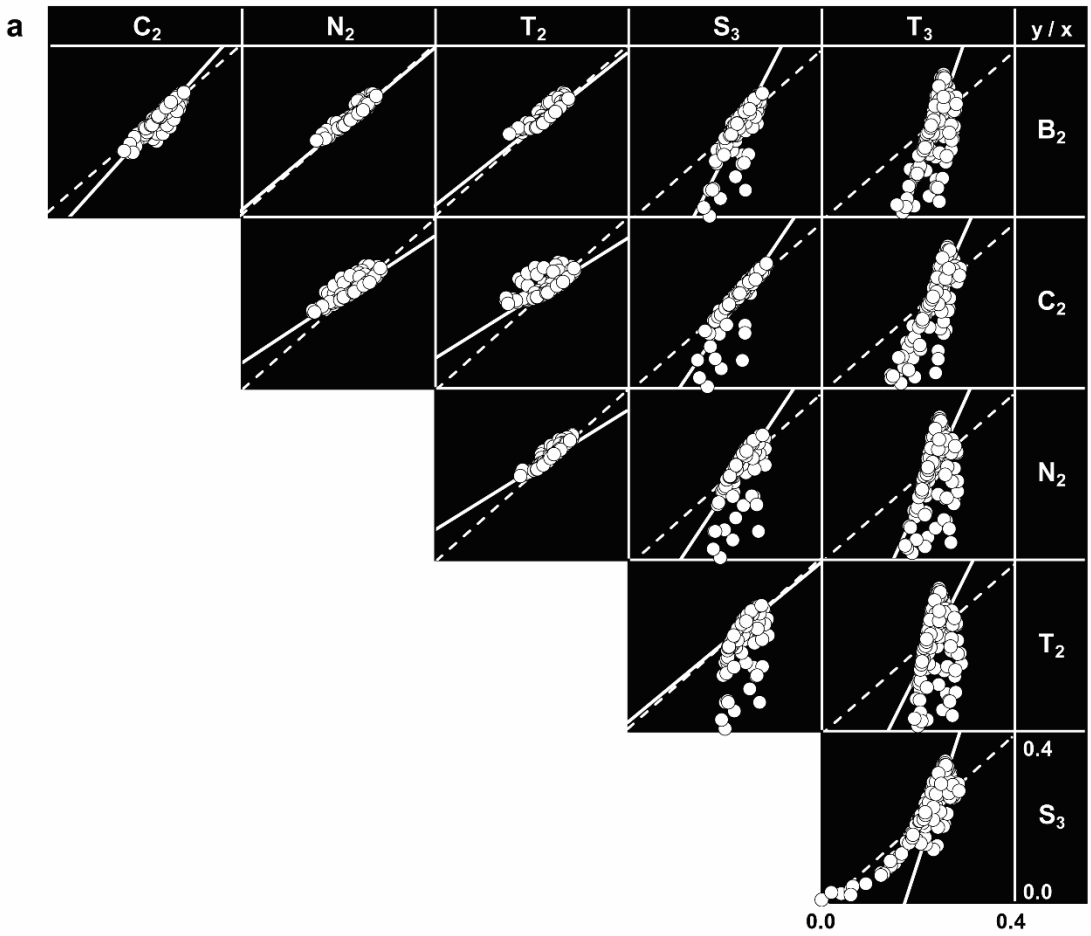

b

r	m	b	r	m	b	r	m	b	r	m	b	r	m	b	
C_2			N_2			T_2			S_3			T_3			y / x
0.93	1.29	-0.06	0.95	0.96	0.01	0.89	0.89	0.02	0.84	2.18	-0.30	0.70	3.27	-0.56	B_2
			0.87	0.74	0.06	0.72	0.70	0.07	0.90	1.69	-0.19	0.84	2.55	-0.40	C_2
						0.96	0.94	0.01	0.71	2.28	-0.32	0.53	3.43	-0.60	N_2
									0.55	2.43	-0.36	0.35	3.66	-0.65	T_2
												0.89	1.50	-0.11	S_3

Linear regression —— 1:1 slope — — Data point ●

r = Correlation coefficient; m = Regression slope coefficient; b = Regression y-intercept coefficient

Figure 2.S4. Linear regression using the reduced major axis technique

Depth-averaged velocity magnitudes are shown for simulations on a fixed bed for the M_{low} configuration. RMA regression is carried out on a sample of 200 points located along the central wave, i.e., $-0.5 < \lambda < 0.5$ in Figure 2.1. Dashed lines show 1:1 agreement whereas full lines correspond to the regression slope. Highlighted values are not significantly different from the 1:1 slope. The labels 'y/x' indicate the order of comparison, where y is the dependent variable and x the independent variable.

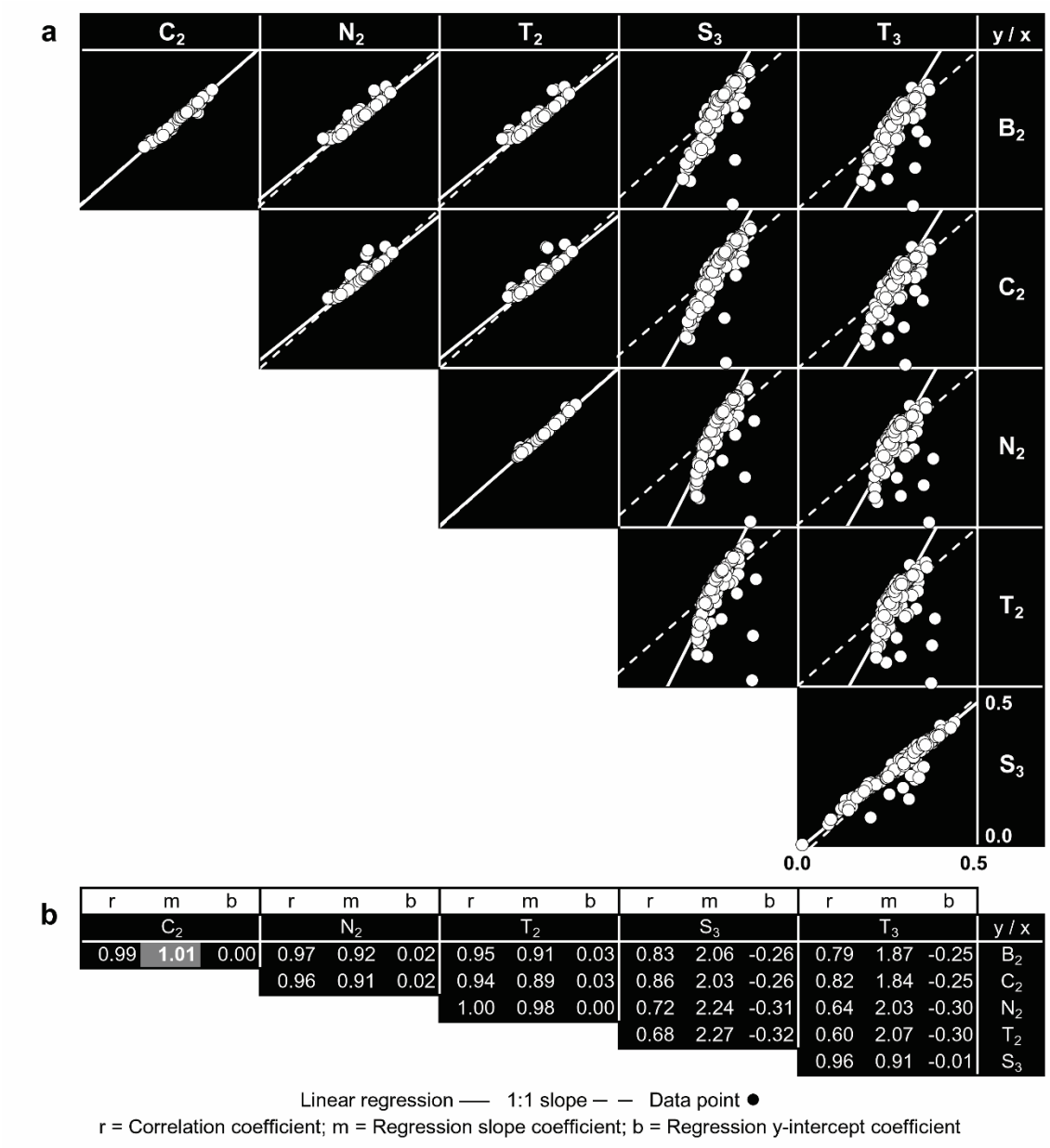

b

C_2			N_2			T_2			S_3			T_3			y / x
r	m	b	r	m	b	r	m	b	r	m	b	r	m	b	
0.99	**1.01**	0.00	0.97	0.92	0.02	0.95	0.91	0.03	0.83	2.06	-0.26	0.79	1.87	-0.25	B_2
			0.96	0.91	0.02	0.94	0.89	0.03	0.86	2.03	-0.26	0.82	1.84	-0.25	C_2
						1.00	0.98	0.00	0.72	2.24	-0.31	0.64	2.03	-0.30	N_2
									0.68	2.27	-0.32	0.60	2.07	-0.30	T_2
												0.96	0.91	-0.01	S_3

Linear regression —— 1:1 slope — — Data point ●

r = Correlation coefficient; m = Regression slope coefficient; b = Regression y-intercept coefficient

Figure 2.S5. Linear regression using the reduced major axis technique

Depth-averaged velocity magnitudes are shown for simulations on a fixed bed for the M_{med} configuration. RMA regression is carried out on a sample of 200 points located along the central wave, i.e., $-0.5 < \lambda < 0.5$ in Figure 2.1. Dashed lines show 1:1 agreement whereas full lines correspond to the regression slope. Highlighted values are not significantly different from the 1:1 slope. The labels 'y/x' indicate the order of comparison, where y is the dependent variable and x the independent variable.

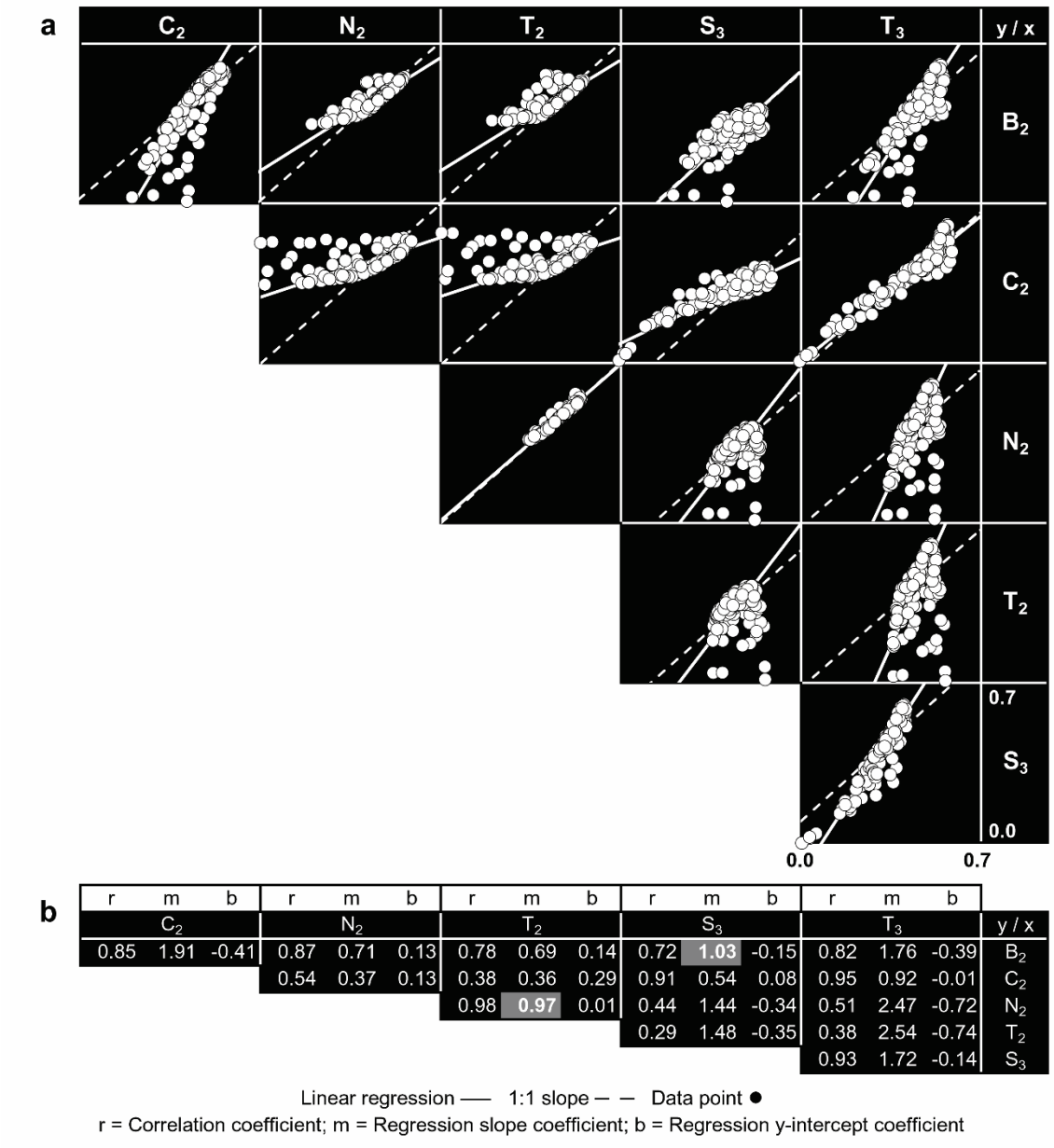

b

r	m	b	r	m	b	r	m	b	r	m	b	r	m	b	y / x
C_2			N_2			T_2			S_3			T_3			
0.85	1.91	-0.41	0.87	0.71	0.13	0.78	0.69	0.14	0.72	**1.03**	-0.15	0.82	1.76	-0.39	B_2
			0.54	0.37	0.13	0.38	0.36	0.29	0.91	0.54	0.08	0.95	0.92	-0.01	C_2
						0.98	**0.97**	0.01	0.44	1.44	-0.34	0.51	2.47	-0.72	N_2
									0.29	1.48	-0.35	0.38	2.54	-0.74	T_2
												0.93	1.72	-0.14	S_3

Linear regression —— 1:1 slope — — Data point ●

r = Correlation coefficient; m = Regression slope coefficient; b = Regression y-intercept coefficient

Figure 2.S6. Linear regression using the reduced major axis technique

Depth-averaged velocity magnitudes are shown for simulations on a fixed bed for the M_{high} configuration. RMA regression is carried out on a sample of 200 points located along the central wave, i.e., $-0.5 < \lambda < 0.5$ in Figure 2.1. Dashed lines show 1:1 agreement whereas full lines correspond to the regression slope. Highlighted values are not significantly different from the 1:1 slope. The labels 'y/x' indicate the order of comparison, where y is the dependent variable and x the independent variable.

Liaison paragraph

Two conclusions emerged from the exhaustive comparison of morphodynamic models. The first one was that some models perform significantly better than others in a meandering context. The second one was that no morphodynamic modelling software existed, or was available, that could simulate bank retreat in a physics-based manner while taking into account the mechanical effects of vegetation. However, the source code of a powerful modelling software developed by Électricité de France in the late 1980s to simulate flow and sediment transport in fluvial and coastal environments, i.e., Open TELEMAC-MASCARET, became available in 2010. Although TELEMAC is a robust, efficient and well-respected mathematical suite of solvers that was found to simulate fluvial processes fairly well in meandering planforms during the experiment corresponding to Chapter 2, it nevertheless suffered from a severe limitation with respect to the specific objectives of this thesis: the lack of a bank erosion algorithm. However, the fact that it is open source was a major asset as it permitted the modification and improvement of existing algorithms. Therefore, the decision was made to develop and integrate three modules: a geotechnical module, a riparian vegetation module, and a library of functions supporting the others with respect to spatial analysis.

The development and testing of the new modules, programmed in Fortran 90, took several years. The resulting 22,000 lines of code (35,000 lines including comments) featured many technological innovations such as physics-based bank retreat model, compatibility with single- and multi-threaded river channels, automated edge detection, multiprocessing (using MPI libraries), and a solver based on a genetic algorithm. The core principles are illustrated in Chapter 3 using a case study. Note that preliminary model testing resulted in two additional publications that are provided as Appendices A–B. The reader will find supplemental information about the capacities of the coupled model.

3

Simulating bank erosion over an extended natural sinuous river reach using a universal slope stability algorithm coupled with a morphodynamic model

Yannick Rousseau, **Marco Van de Wiel** and **Pascale Biron**

Geomorphology 295: 690–704 (2017)

Abstract: Meandering river channels are often associated with cohesive banks. Yet only a few river modelling packages include geotechnical and plant effects. Existing packages are solely compatible with single-threaded channels, require a specific mesh structure, derive lateral migration rates from hydraulic properties, determine stability based on friction angle, rely on nonphysical assumptions to describe cutoffs, or exclude floodplain processes and vegetation. In this paper, we evaluate the accuracy of a new geotechnical module that was developed and coupled with TELEMAC-MASCARET to address these limitations. Innovatively, the newly developed module relies on a fully configurable, universal genetic algorithm with tournament selection that permits it (1) to assess geotechnical stability along potentially unstable slope profiles intersecting liquid-solid boundaries, and (2) to predict the shape and extent of slump blocks while considering mechanical plant effects, bank hydrology, and the hydrostatic pressure caused by flow. The profiles of unstable banks are altered while ensuring mass conservation. Importantly, the new stability module is independent of mesh structure and can operate efficiently along multithreaded channels, cutoffs, and islands. Data collected along a 1.5-km-long reach of the semialluvial Medway Creek, Canada, over a period of 3.5 years are used to evaluate the capacity of the coupled model to accurately predict bank retreat in meandering river channels and to evaluate the extent to which the new model can be applied to a natural river reach located in a complex environment. Our results indicate that key geotechnical parameters can indeed be adjusted to fit observations, even with a minimal calibration effort, and that the model correctly identifies the location of the most severely eroded bank regions. The combined use of genetic and spatial analysis algorithms, in particular for the evaluation of

geotechnical stability independently of the hydrodynamic mesh, permits the consideration of biophysical conditions for an extended river reach with complex bank geometries, with only a minor increase in run time. Further improvements with respect to plant representation could assist scientists in better understanding channel-floodplain interactions and in evaluating channel designs in river management projects.

3.1. Introduction

Morphodynamic models have been employed for decades by researchers and practitioners to examine the evolution of alluvial river channels (e.g., Rinaldi et al. 2008; Tal and Paola 2010; Ham and Church 2012). In particular, two-dimensional nonlinear and linear models based on the shallow water equations, combined with a computational mesh that can evolve because of sediment transport, are increasingly used to determine the morphological evolution of meandering channels (Darby et al. 2002; Langendoen et al. 2016). Most of these models involve a large number of assumptions and simplifications to combine fluvial and bank erosion processes into a runnable solution, often neglecting floodplain heterogeneity in terms of morphology (Pittaluga and Seminara 2011), channel bedforms (Shen 1984; Parker et al. 2011), multithreading (Camporeale et al. 2013), sedimentology and stratigraphy (Simon et al. 2000; Malkinson and Wittenberg 2007; Lai et al. 2012), bank hydrology (Pollen 2007; Pollen-Bankhead and Simon 2010), and flow regimes. As a result, the contribution of these processes to channel evolution is poorly understood (Güneralp and Marston 2012). In addition, riparian plants that alter channel/floodplain roughness and provide mechanical soil reinforcement (Abernethy and Rutherfurd 1998; Van de Wiel and Darby 2007; Thomas and Pollen-Bankhead 2010) should be included in morphodynamic models, although this is seldom the case (Bertoldi et al. 2014). Finally, opportunities to establish spatial connections between floodplain components, for instance between hydrological processes and riparian plants (Perucca et al. 2007; Mitsch and Gosselink 2010), are often missed (Malkinson and Wittenberg 2007; Lai et al. 2012).

A few river models have been enhanced to include bank retreat algorithms (e.g., El Kadi Abderrezzak et al. 2016). The linear near-bank excess velocity approach (known as HIPS, from Hasegawa (1977) and Ikeda et al. (1981)) relies on an erodibility coefficient to lump the effects of flow, soil, and vegetation properties to bank retreat rates (see Johannesson and Parker 1989; Zolezzi and Seminara 2001; Posner and Duan 2012), thus making it impossible to isolate the specific causes for retreat, and to *entirely* simulate long-term planimetric and morphological evolution owing to the lack of analytical solution of neck/chute cutoff (Chen and Tang 2012). In addition, these models do not guarantee sediment continuity and assume a flat-bedded channel with few perturbations (Coulthard and Van de Wiel, 2006; Pittaluga and Seminara, 2011). When riparian vegetation is considered, its effect is typically limited to altering bed roughness, although a few notable exceptions exist where vegetation was connected to other floodplain processes (e.g., Collins et al. 2004; Perucca et al. 2007; Iwasaki et al. 2016). Models based on HIPS concepts do, however, have the advantage of allowing for long reaches to be simulated at relatively low computational cost (e.g.,

Schwenk et al. 2015). A few non-linear morphodynamic models have also been coupled to physically based bank erosion modules (e.g., Darby et al. 2002; Lai et al. 2012; Langendoen et al., 2016). However, several limitations remain regarding these solutions. The most severe ones are probably their incompatibility with long spatiotemporal scales (Pittaluga and Seminara 2011), the lack of physically based equations in the implemented bank stability assessment and retreat processes, and the integration of assumptions such as arbitrary bank and planform geometries (e.g., Duan and Julien 2010; Langendoen et al. 2016). The main difficulty seems associated with the inclusion of processes acting at different spatiotemporal scales compared to the shallow-water flow equations employed in the hydrodynamic models (Williams et al. 2016a).

The integration of geotechnical algorithms applicable over long river reaches in a natural environment with complex floodplain has seldom been attempted (Rousseau et al. 2014a,b; Evangelista et al. 2015). This paper presents a novel set of algorithms implemented in a new physics-based, deterministic model of channel-floodplain coevolution. The model is capable of simulating mass wasting events, including river bank failures, while also taking into account the specific biophysical context. Here, it is integrated into a two-dimensional unstructured grid morphodynamic model (TELEMAC-MASCARET), but it could also be implemented in other modelling software with relatively minor adjustments. The novel aspects included in the present modelling investigation is fivefold: (i) physics-based algorithms allowing us to parameterize lateral erosion using physical, measurable quantities; (ii) a genetic algorithm that can automatically select between rotational and translational failure mechanisms, depending on local biophysical conditions; and allow (iii) larger spatial and temporal scales than commonly employed in physics-based bank erosion modelling because of greater computational efficiency; (iv) a bank erosion module independent of mesh structure, i.e., imposing a body-fitted coordinate system is not needed; and (v) model calibration using data from a complex natural site. Furthermore, because the model includes the interaction between an alluvial river channel and its (vegetated or nonvegetated) floodplain, it is able to simulate lateral river channel adjustments that can lead to the development of meandering, wandering, or braided river planform geometries. This paper thus directly addresses the issues identified by Williams et al. (2016b, p.6639) who noted that 'Future model development efforts should be directed toward improving the realism of bank erosion processes in the model. In particular, the bank erosion scheme needs to be made independent of grid resolution and orientation.'

3.2. Overview of model components

The geotechnical and riparian vegetation modules presented here were integrated into the Open TELEAMC-MASCARET suite of mathematical solvers to include additional fluvial processes, namely lateral adjustments through mass wasting of river banks and the effects of floodplain vegetation on geotechnical stability (Rousseau et al. 2014a, b).

3.2.1. Hydrodynamics

The two-dimensional (2D) version of TELEMAC was selected to minimize computation time, although the three-dimensional (3D) version could easily be coupled to the new modules if required in future projects. The equations governing fluid motion, in their nonconservative form and Cartesian coordinates, are described in Galland et al. (1991). The Smagorinsky (1963) model was selected to consider turbulent viscosity whilst minimizing computational effort. The default advection scheme, i.e., the method of characteristics, was selected for horizontal flow velocities and depth. For boundary conditions, flow discharge and uniform velocities were imposed at the channel inlet with a free surface elevation at the outlet. In all simulations, the inlet of the flow comprised the wet nodes on the left domain side, whereas the outlet included all the mesh nodes located on the right domain side so that the outlet may adjust its location during a simulation.

3.2.2. Sediment transport and bed deformation

Sediment transport is calculated by the module SISYPHE. The Meyer-Peter and Müeller (1948) bedload formula was selected to calculate transport rates during simulations because of its compatibility with respect to sediment grain size at our field site (see below). Hiding/exposure is calculated using Egiazaroff (1965). The formulae related to the configurations considered in this study are thoroughly described in Villaret (2010). Bed evolution owing to bedload transport is calculated using the Exner equation.

The sediment transport module SISYPHE includes an algorithm that can simulate sediment slide; this was deactivated to let geotechnically stable river banks be steeper than the friction angle of sediment and, more importantly, to prevent having two modules competing for a single process. An option was enabled to include curvature effects on the direction of particle entrainment to compensate for the fact that the flow is depth-averaged. This feature was enabled in all simulations because of its relevance for the study of meandering processes. The effects of transport magnitude and direction on local topography are estimated using Koch and Flokstra (1981).

3.2.3. Lateral adjustments

The primary objective of this research was to develop an alternative methodology to simulate river bank retreat within a computational fluid dynamics (CFD) model, using a set of algorithms that is compatible with unstructured meshes, for a wide spectrum of alluvial rivers and with any modelling code offering finite element spatial discretization. This new framework relies almost completely on vector-based spatial analysis. In the generic framework, the stability submodel ignores the location of channel boundaries. Instead, it performs stability assessments across the floodplain, considering flow conditions, antecedent soil moisture, soil and sedimentological properties, and plant cover (if the vegetation module is enabled, see below). The channel planform will evolve when the banks are unstable along its boundaries.

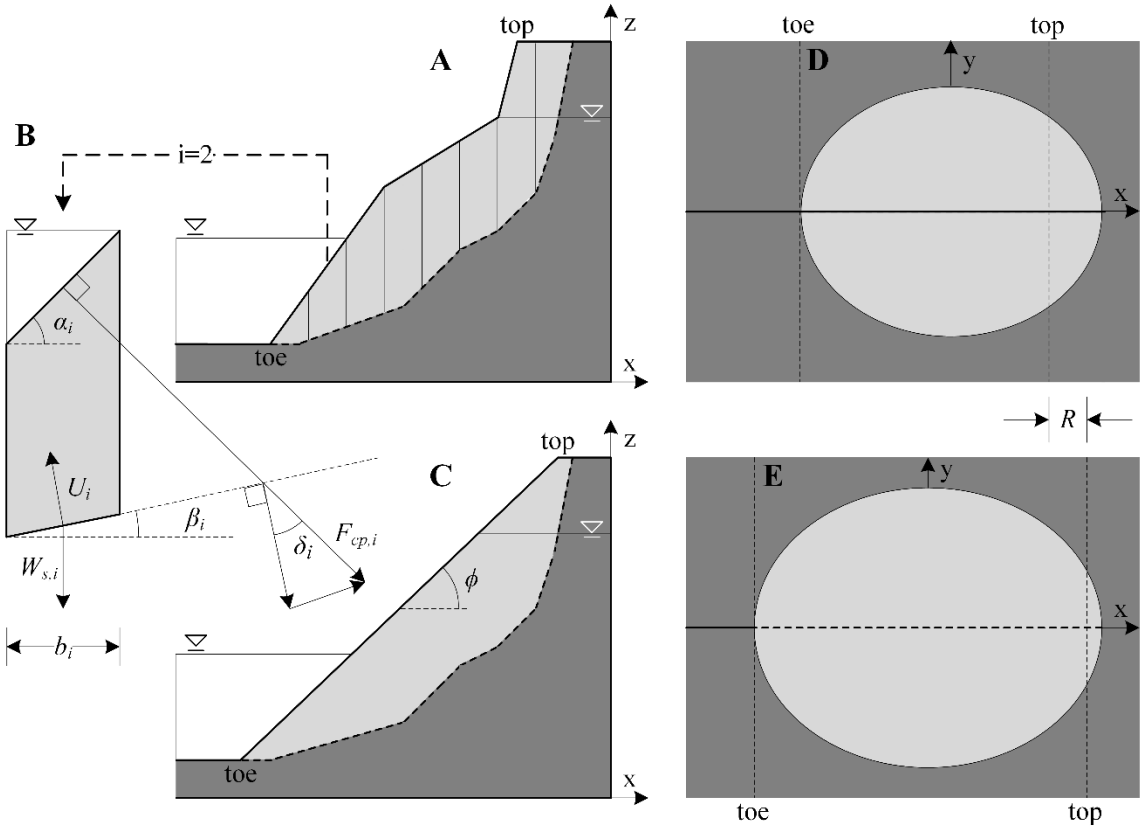

Figure 3.1. Bank slope stability assessment using Bishop's simplified method of slices

a) Initial profile, indicating stable bank region (dark gray) and failure block (light gray). **b)** Stability is calculated based on forces acting on vertical slices through the failure block (Equations 3.3–3.4). **c)** Profile following deposition of the failure block at the friction angle of the bank material. Note that this is a 2D transect of a 3D bank; the volume of the failure block in C is the same as in A. The upper limit of the failure block in C, i.e., a planar 3D surface within an elliptical zone, is adjusted to ensure that the two failure block volumes are equal. Elliptical zones affected by **d)** block failure and **e)** deposition. The character *R* indicates the distance of bank retreat.

The module is divided into five components. A landscape analysis algorithm generates a network of transects along which slope stability assessments are performed during a morphodynamic simulation (see the inset in Figure 3.1). Although this algorithm can be configured to detect potentially unstable slopes anywhere across the simulation domain, for the current study an option was enabled to perform the analysis strictly along the external river bank of meander bends through edge detection. A genetic algorithm searches for the geometry of the most likely failure profile and returns the lowest safety factor (F_s, the ratio of shear strength to shear stress – see Equations 3.3–3.4 below) encountered. The geotechnical module includes a river bank hydrology module that computes water table elevation in the river bank as a function of flow stage and hydraulic conductivity. Finally, the algorithm analyses the geotechnical stability of a river bank in search of a failure block geometry that minimizes the safety factor (during the erosion phase, the unknown is the lower extent of the failure block, represented by the dashed line in Figure 3.1a), removes the unstable failure block and deposits the material downslope at the friction angle (Figure 3.1c, also see Section 3.2.3.5 below), and updates the computational mesh nodes while ensuring mass conservation (the unknown is the upper extent of the altered unstable block during the deposition phase) (see Rousseau et al. (2014a, b) for more details). The upper extent of the post-failure block is a 3D planar surface with an elliptical shape. The mesh nodes affected by a failure are those located in the elliptical erosion and deposition zones (Figures 3.1d–3.1e) with the vertical displacement at a node inversely proportional to its horizontal distance on the stability-analysis transect.

3.2.3.1. Terrain analysis

The geotechnical model evaluates terrain stability along a large number of analysis transects carefully placed across the landscape. Each transect is oriented in the direction of the steepest ascent and adjusted in length to extend from the lowest to the highest elevation in this direction. Transect orientation is done by spinning a transect of length *trLen* around its center of mass and selecting the angle that minimizes the surface elevation's root mean square error between the points comprised in two transects located on each side of a trial transect at a distance *trLen* / 2. A smoothening stage adjusts the direction of each transect with respect to the direction of their immediate neighbours. Each transect is extended until an increase in length no longer leads to any substantial elevation change, defined by a threshold parameter (10° in our simulations) to improve efficiency, as otherwise geotechnical stability would be evaluated for very shallow banks that are unlikely to erode. Each transect is then transposed into a 2D bank profile, which is analysed for stability using the method of slices and powered by a genetic algorithm, both of which are described in detail in the following sections. By default, transects regenerate at each iteration of the geotechnical module. However,

regeneration was disabled in our simulations to facilitate the statistical comparison of retreat rates between scenarios. This strategy could be adopted because of the relatively low retreat rates and short simulations in our study. Although the location of transect centers was constant in time, each transect elongated and rotated to adjust to the evolving bank morphology.

Several options are available in the geotechnical module to define transect density, distribution pattern, and admissibility criteria, e.g., in terms of wetness/dryness and length. In the context of a study involving lateral erosion in meandering channels, the edge detection algorithm was selected; it distributes transects at equal distance along solid-liquid boundaries. Its independence of mesh structure means that it can efficiently detect river banks along multithreaded channels, cutoffs, and islands.

3.2.3.2. Genetic algorithm

Any slope stability analysis includes an algorithm that devises a set of potential slip surfaces to be evaluated for their geotechnical stability. Given a 2D geotechnical stability analysis, a solution with identifier *id* is a series of connected nodes delineating the lower limit of an unstable soil block, i.e., the dashed line in Figure 3.1a. Therefore, a solution can be described by the following vector:

$$\vec{S}_{id} = \left\{\vec{v}_1, \vec{v}_2, \ldots, \vec{v}_{n-1}, \vec{v}_n\right\} \tag{3.1}$$

where $\vec{v}_i$ is the node at rank *i* along a slip surface. The solution with the lowest F_s value is the most likely to occur.

Grid-search patterns are usually employed to list potential slip surfaces. For instance, this can be achieved by varying the location of the centre of the arc describing the shape of a circular slip surface, along with its radius. Here, a genetic algorithm with tournament selection, improved from the work of Li et al. (2010), was implemented in the geotechnical module to converge toward a critical solution more rapidly. A *child* solution is created by combining two existing solutions, *i* and *j*, such that

$$\vec{S}_{child} = \eta\vec{S}_i + (\eta - 1)\vec{S}_j \tag{3.2}$$

where η = [0,1] is a randomly generated crossover ratio. During crossover, mutation has a probability of happening, in which case a randomly selected node comprised in *child* solution is displaced. A set of matching rules, namely partner exclusivity, child count policy, and prevention of breeding between relatives, allows the variability within the pool of solutions to be optimized (Li et al. 2010). For

example, a child count policy means that two solutions S_i and S_j (a solution is a potential slip surface or the dashed line in Figure 3.1b) can produce a predefined maximum number of solutions after randomly mixing their geometrical characteristics. The lack of such a policy limits genetic variability and thus increases the time required to converge toward a stable solution, i.e., finding the failure block associated with the lowest safety factor. Finally, a user-specified migration rate dictates the probability for a solution to be created randomly rather than being the result of a crossover.

In the current context, we can define a generation as the set of n solutions that were created from an initial population. After each generation, the most critical slip surface(s) are kept, the least critical are discarded, and new randomly selected surfaces survive to the next round. The search process terminates when the most critical slip surface remains unaltered for a number of consecutive generations.

3.2.3.3. Slope stability assessment

Bishop's (1955) modified method of slices (Figure 3.1) was slightly adjusted to quantify the geotechnical stability of the soil along a transect while considering the flow's confining pressure and soil pore-water pressure. Combined with the genetic algorithm, it can produce planar, circular, and noncircular slip surfaces. Given a 2D bank profile and potential slip surface, the following set of equations must be solved by iteration:

$$F_s = \frac{\sum_{i=1}^{n} \frac{cb_i + \left(W_{s,i} + F_{cp,i} - U_i b_i\right)\tan\phi}{m_i}}{\sum_{i=1}^{n} W_{s,i}\sin\beta_i + F_{cp,i}\sin\delta_i} \tag{3.3}$$

$$m_i = \cos\beta_i + \frac{\sin\beta_i \cdot \tan\phi}{F_s} \tag{3.4}$$

where F_s = safety factor; $W_{s,i}$ = weight of soil material and groundwater in slice i out of n; U_i = the pore water pressure at the base of a slice of width b_i, basal angle β_i, and top angle α_i; δ_i = angle between the result of hydrostatic confining force and normal to failure plane; ϕ = friction angle of the soil material; and m_i = m-term in Bishop formula. Pore-water pressure is given by

$$U = \frac{\rho g}{z_{wt} - z_b} \tag{3.5}$$

where g = acceleration owing to gravity, z_{wt} = elevation of the water table, and z_b = elevation at the base of a slice. A first approximation of F_s value is done using the ordinary method of slices (Fellenius, 1927). The confined water pressure is given by

$$F_{cp,i} = W_{w,i} \cos \beta_i \tag{3.6}$$

where $W_{w,i}$ = weight of water. Any solution resulting in a safety factor lower than unity is said to be unstable and is expected to result in a slope failure.

3.2.3.4. River bank hydrology

A saturated river bank, combined with a falling flow stage, can trigger mass wasting events (Thorne 1982). To account for the lag effect between free surface and water table elevations, a simple river bank hydrology module is used to calculate water table elevation. According to this module, water table elevation (z'_{wt}) at a time $t = t_0 + \Delta t$ is given by

$$z_{wt}' = z_{fs} - \left(z_{fs} - z_{wt}\right) e^{-k\Delta_t} \tag{3.7}$$

where t_0 = time at the previous iteration, Δt = time step, $t = t_0 + \Delta t$ = time at the current iteration, z_{wt} = water table elevation at time t_0, z'_{wt} = water table elevation at time t, z_{fs} = flow surface elevation at time t_0, and k = rate of convergence of the water table elevation toward z_{fs}. The constant k is adjusted according to the hydraulic conductivity of the bank material and thus represents how quickly the water table adapts to a change in the river's flow stage. Two k-values are required per simulation: one for the rising limb of a flood hydrograph, and one for its falling limb (see values below).

3.2.3.5. Slump block removal and deposition

The slope stability analysis performed along each transect returns the side profile, i.e., the 2D curve representing the critical slip surface (Figure 3.1a). Each mesh node affected by mass wasting relocates according to its position (d_B/r_B, d_A/r_A) with respect to the boundaries of an elliptical erosion surface (Figure 3.2). The ellipse has the length of the unstable section of the analysis transect and a user-defined relative width, i.e., r_B/r_A in Figure 3.2; a value of 0.75 was selected for our simulations to cover the bank region located between a transect's immediate neighbours. A mesh node located along the edge of the ellipse is not affected by a failure. Conversely, displacement computed is greatest along the transect for each d_A/r_A value. A mesh node located within the ellipse has a vertical displacement (dz) that is computed as a linear function of the distance between the transect and the edge of the ellipse, in the direction orthogonal to the transect, i.e.,

$$dz = dz_A \cdot \frac{d_B}{r_B \sqrt{1 - \left(\frac{d_A}{r_A}\right)^2}} \tag{3.8}$$

where r_A and $r_B = r_A \cdot k_f$ = lengths of the semiaxes A and B, k_f = width-to-length ratio of all ellipses defining an erosion or deposition zone, d_A and d_B = distances from the ellipse's centre to the mesh node along each semiaxis, dz_A = elevation change at a distance d_A from the centre of the ellipse in the direction of the mesh node x along the axis A. The value of dz_A is obtained by interpolating elevation change at node x_m using the two nearest transect nodes. Mesh elements that are intersecting the transect snap to the slip surface (lower line in Figure 3.1a) after a vertical translation and/or a rotation around an axis orthogonal to the 2D profile. The volume of the unstable block is calculated by subtracting the pre- and post-failure computational meshes, assuming that the neighbouring transects are stable. The unstable slope material deposits in an elliptical zone at the toe of the slope

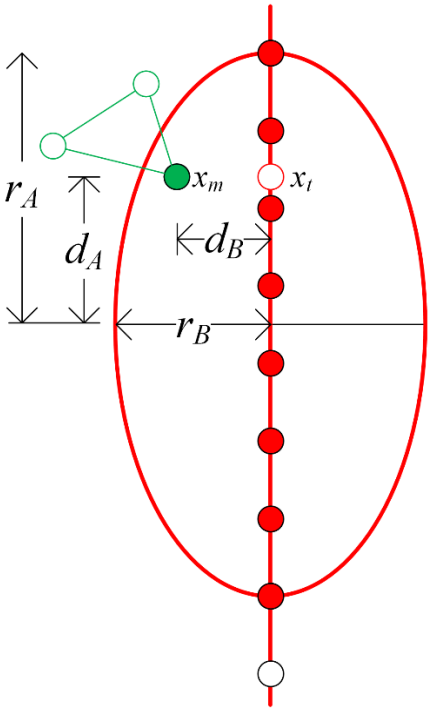

Figure 3.2. Geometry of an erosion or deposition zone

This zone is described by an ellipse (Figures 3.1d and 3.1e) with flatness r_B / r_A. Any mesh node x_m, located within the ellipse, as well as the red-filled nodes along the analysis transect are unstable. In erosion mode, the elevation change at mesh node x_m depends on the distance d_B. However, in deposition mode, the elevation of transect node x_t is assigned to mesh node x_m for each tridimensional planar surface representing a potential depositional fan surface.

at the friction angle of the bank material. An algorithm similar to the erosion algorithm is used, with one important distinction: a solver is required to ensure that the volume of eroded soil is equal to the deposited volume and thus guarantees mass conservation. Note that the elliptical zone where deposition occurs is usually not identical to the ellipse in which erosion occurs as material moves downslope during a failure.

3.2.3.6. Soil properties

In its simplest configuration mode, the geotechnical module defines bank material in terms of soil class and degree of compaction. The other relevant sedimentological parameters, i.e., mean grain size, mass density, friction angle, cohesion, and porosity, are calculated using tabular data available in NAVFAC (1986), Swiss Standard SN 670 010b (1999), and MnDOT (2015). Soil material below the water table is assumed to be saturated; it is partially saturated if fine-textured and located above the water table while being affected by capillary rise; and it is dry otherwise. Default values can be overridden by the model user. Although the module is capable of recognizing multiple soil layers, bank material was assumed to have uniform properties in our simulations.

3.2.3.7. Riparian vegetation

At each geotechnical iteration, the plant evolution module (see Rousseau et al. (2014a) for details) transfers information to the geotechnical module regarding the physiological plant properties that can influence the mechanical properties of the river bank: depth and radius of rooting zone; cohesion owing to roots; trunk height, spacing, and diameter. The plant evolution module also includes functionalities to generate a plant cover and manage plant growth. In this study, however, dry mesh nodes were covered with trees from a single species associated with a single set of physiological properties that remained constant in time.

3.3. Methodology

3.3.1. Field data

The model is evaluated against hydrological and morphological data collected along a 1.5-km-long reach of the semi-alluvial river Medway Creek, London, Ontario (Figure 3.3). Within this site, three zones were examined more closely owing to signs of previous erosion episodes; these zones will be referred to as A (transects 746–827), B (transects 352–409), and C (transects 929–954). The 20-m-wide channel is in a post-glacial valley covered by diverse assemblages of deciduous and coniferous trees, shrubs, and herbaceous species. The density of mature trees within the riparian area is higher in zone A. In zone B the tree density is noticeably lower and the proportion of shrubs

higher, perhaps because of their proximity to an area that is seasonally flooded and occupied by beavers. Zone C includes mature trees between transects 932 and 940, but grass and shrubs in the downstream transects. Bank height along the external bends typically varies between 2 and 4 m, with two bluffs substantially increasing this value locally to 20 m (Figure 3.3). This stream was selected because of the substantial observed erosion along certain banks but also because its flow has been

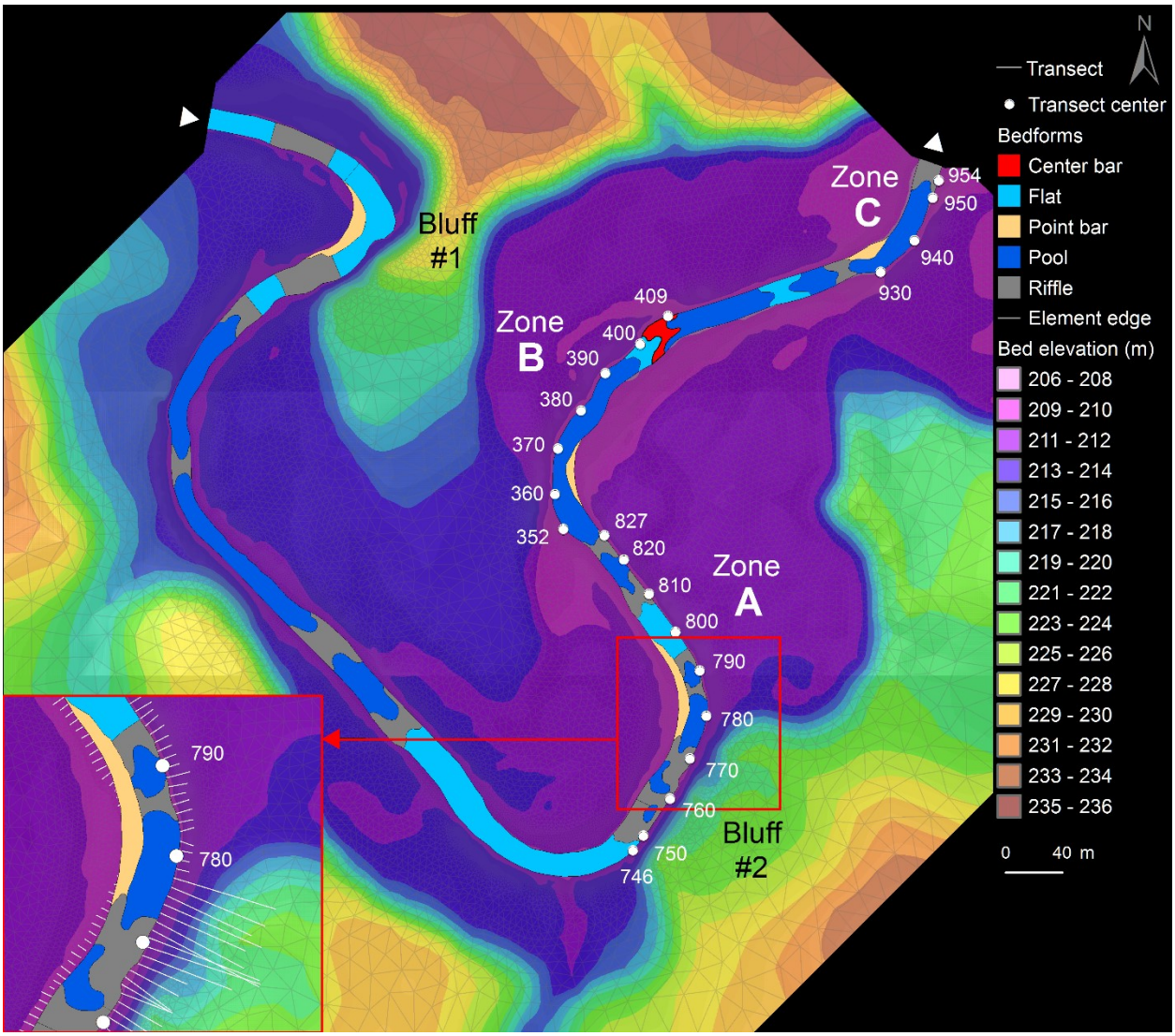

Figure 3.3. Topography of the river and floodplain at Medway Creek, London, Ontario

The outline of computational elements appears in light grey. Three zones were studied in greater detail: zone A (transects 746–827), zone B (transects 352–409), and the downstream zone C (transects 929–954). The two white arrows indicate the position of liquid boundaries and flow direction. Bedform types correspond to the locations where the substrate was sampled by N. Bergman (personal communication, 9 June 2016). Note that the center bar is partially covered with long grass and shrubs. Inset: Detail on transects that are used in slope stability assessments for zone A.

monitored for decades. Bankfull discharge (1.5-year recurrence interval, based on gauging station 02GD008 just downstream of the study reach) is about 43 m^3/s. In addition, sedimentology was examined by N. Bergman (personal communication, 8 December 2013) and rendered available for this project. Basic flow measurements (depth and velocity) were taken along the inlet and outlet cross sections of the study reach at low stage for the purpose of calibrating the flow and the energy slope prior to running numerical simulations. The difference between the predicted increase in free surface elevation at the outlet (1.58 m) from low (1.15 m^3/s) to high flow discharge (60 m^3/s) was <7% compared with data from the gauging station (1.48 m), which is an acceptable error that is not expected to have an effect on the geotechnical modelling outcome of predicted river bank failures.

Substantial efforts were put into surveying and monitoring channel morphology in this study. In November 2012, we collected over 5000 topography points of the channel bed and banks in the study reach using a differential GPS (resolution of 1 cm vertically and 1.5 cm horizontally). These points were combined with a 1-m resolution LiDAR digital elevation model (DEM) (The University of

Figure 3.4. Photographs of the most unstable river banks along the study reach

The observation period was between January 2012 and June 2015, before and after failure. The corresponding transects in Figure 3.3 are **a)** 760, **b)** 781, **c)** 807, and **d)** 393–397. White ellipses highlight trees fallen owing to bank erosion.

Western Ontario 2006) to create a DEM of the channel and floodplain. Photographs of the banks were taken after each flood with discharge $Q \geq 15$ m^3/s between February 2012 and April 2015 when the river banks were visible (e.g., no snow cover, no high flow) (Figure 3.4). A consumer-grade camera with geotagging capabilities (Canon 60D) with wide-angle lens (Canon 10–20 mm) was employed along three banks that appeared unstable. A Garmin eTrek Legend CX hand-held GPS, mounted on the camera's hot shoe, recorded the position of each photograph. Photogrammetry analysis was performed on seven photograph sets taken in zone A (Figure 3.3), corresponding to flooding events recorded between September 2013 and April 2015 (Figures 3.4, 3.5), in an attempt to estimate the amount of bank retreat in a nonintrusive way as the research site is located in a protected area. Targets were placed on six trees along unstable reaches to facilitate the analysis in the photogrammetric software Agisoft PhotoScan. Two of these trees were subject to bank failures and were evacuated by subsequent floods (Figure 3.4b), which rendered the photogrammetry analysis more tedious and less accurate than expected. Although photographs were taken in zones B and C, photogrammetry was not attempted owing to the lack of bank retreat in these zones. The photogrammetry analysis reveals a bank retreat up to 2.4 m in zone A, which is compatible with visual cues (Figure 3.4).

Data acquired by N. Bergman (personal communication, 9 June 2016) in the same study reach revealed substantial spatial variations in grain size distribution (GSD) and various bedform types (riffles, pools, bars, flats, steps, and bluffs) (Figure 3.3). Trial simulations, using a unique grain size distribution to describe bed substrate in the whole study reach, indicated the importance of varying GSD spatially. With a single curve, pools quickly filled with sediment, leading to a homogeneous longitudinal and lateral bathymetry very different from field observations. In order to simplify our

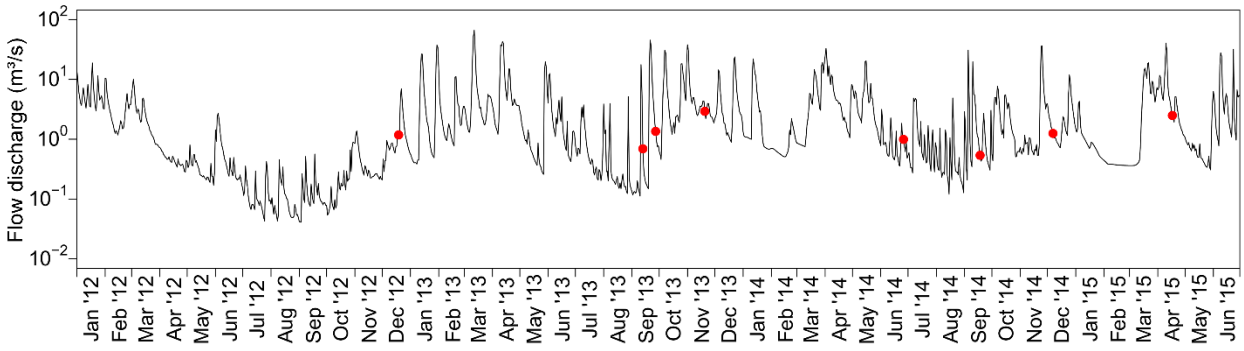

Figure 3.5. Flood hydrograph during the observation period

This period extended between January 2012 and June 2015 based on gauging station 02GD008 located just downstream of the study reach. Red dots indicate the dates where measurements of bank morphology and characterization of bank condition took place.

simulations, grain size distribution data were reorganized into three classes using the package 'rPart' (Therneau et al. 2015) in the software R (R Core Team 2013). The resulting GSD used in the simulations is presented in Table 3.1.

Table 3.1. Grain size distribution curves

Category	*Pool*		*Riffle*		*Flat*		*Step*		*Bar*	
	Size (mm)	Fraction (%)	Size (mm)	Fraction (%)	Size (mm)	Fraction (%)	Size (mm)	Fraction (%)	Size (mm)	Fraction (%)
Fine	4.1	35	20.9	27	5.0	20	20.5	17	3.0	28
Medium	66.9	43	96.6	29	57.7	43	98.1	22	63.4	49
Coarse	271.2	22	250.9	44	189.0	37	270.3	61	239.7	23

River banks exhibit three distinct soil layers along the study reach. The lower part consists of glacial till, which is buried under an equally thick sand layer and covered itself by a thin organic layer with dense root network. However, in the absence of accurate sedimentological data for our study site, and for simplicity, we set up our model with uniform textured bank material with a single layer corresponding to the USCS class ML (silt, given a mean grain size diameter of 0.0234 mm). By doing so, we hypothesize that the lower layer is more resistant than the middle and upper layers and, thus, that the till determines bank strength and retreat, which is compatible with field observations.

3.3.2. Numerical setup

3.3.2.1. Mesh generation

The size of the triangular elements of the numerical mesh varied spatially to use a higher resolution in areas most likely affected by mass wasting (along steep river banks in bends) and on the channel bed to ensure that the simulated flow was grid independent. A moderate resolution was selected for the floodplain, and a low resolution for the valley walls. Grid-independence sensitivity analyses were completed to determine the appropriate number of nodes to include in the simulation domain (Roache et al. 1986; Lane et al. 2005; Biron et al. 2007). The number of mesh nodes was 67,780 (0.09 m^2/element), 18,841 (1.20 m^2/element), 17,003 (3.67 m^2/element), and 4135 (48.69 m^2/element) respectively in the steep-bank, bed, floodplain, and valley side zones. The time step was set to 0.1 s to ensure a Courant number close to unity.

3.3.2.2. Calibration and boundary conditions

Flow: A fixed-flat-bed simulation was first run with a low flow discharge of Q = 1.15 m^3/s to adjust the elevation of the water surface at the inlet of the simulation domain to the measured inlet value at Medway Creek. This was done by varying bed roughness coefficient; a Strickler-Manning (n) value of

0.039 was selected for the entire bed. This procedure, which is common in CFD modelling (e.g., Bates et al. 1997; Rameshwaran et al. 2013), allows adjustment of the energy slope to fit experimental measurements (Vidal et al. 2007). At the field site, high-magnitude flooding events generally last a few days. For instance, a 66.2 m^3/s peak discharge occurred during a flood event that lasted nearly six days. A time-contracted γ-distributed hydrograph was therefore fitted to the gauging station data to capture the intensity and shape of this event while limiting simulation length to 12 hours. The γ equation is given by

$$Q_t = Q_0 + (Q_P - Q_0) \cdot e^m \cdot \left(t/t_P\right)^m \cdot e^{-mt/t_P} \tag{3.9}$$

where Q_t = flow discharge at time t, Q_0 = initial discharge, Q_P = peak discharge, m = shape parameter, and t_P = peak time. In all simulations, parameter values were Q_0 = 7.5 m^3/s, Q_P = 60 m^3/s, m = 4.8, and t_P = 3 h.

Sediment: A mobile-bed simulation with fixed banks and steady bankfull discharge (Q = 43 m^3/s) was run to determine the transport equations and substrate properties. The friction angle of the sediment was 36.5º, bed porosity 0.4, and mass density of sediment taken as 2650 kg/m^3. This simulation revealed a stable bed with minor adjustments over a 24-hour period. During all simulations, the sediment rate at the inlet was equal to the outlet rate.

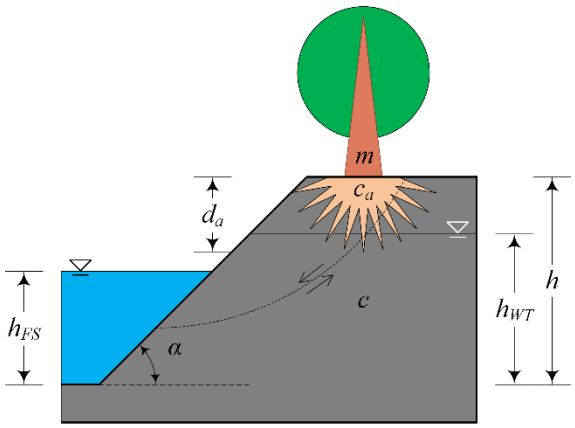

Figure 3.6. Simplified bank profile and variables for the evaluation of model behaviour

A sensitivity analysis was conducted for the following variables: bank angle (°) and height (h), soil cohesion (c), height of free surface (h_{FS}) and water table (h_{WT}), trunk mass (m), apparent cohesion owing to roots (c_a), and root crown radius (d_a). The dotted arc represents a hypothetic slip surface.

Geotechnical slope stability and vegetation: Calibration was done in three ways. First, a series of bank stability predictions along a river bank with a simple profile (Figure 3.6) was undertaken to explore model behaviour for a range of biophysical conditions, to identify the most sensitive variables, and to estimate parameter values to use in subsequent 3D simulations. For the evaluations that included vegetation effects, a single Sugar Maple (species) tree located at the bank top was considered. This tree was assumed to be positioned on the slump block, thus increasing the weight of a slump block intersecting bank top. Tree length and root radius were calculated from trunk diameter using empirical equations presented in Kenefic and Nyland (1999) and Tubbs (1977), respectively for length and radius. Wood density was assumed to be 690 kg/m^3 (Green et al. 2007). The range of parameter values considered for each sensitivity analysis (geotechnical and geotechnical-vegetation) covered those found at the field site. Owing to the nonlinearity of Equations 3.3–3.4 and stochastic behaviour of the genetic algorithm, results were analyzed using machine learning algorithms in R (R Core Team 2013). The importance of variables was quantified using the 'randomForest' package (Breiman et al. 2015), whereas classification trees were built using the

Table 3.2. Parameters of the geotechnical model

Properties of bank material	
USCS class	ML
Mean grain size (mm)	0.0234
Cohesion (kPa)	0.25
Compaction	75%
Transects	
Length (initial; minimum) (m)	5.0; 1.0
Number of nodes (initial; additional on bank top)	65; 3
Number of mesh nodes and trial angles during orientation	9; 33
Stability assessment	
Minimum block width (% of transect length)	75.0
Minimum block profile area (m^2)	$1 \cdot 10^{-2}$
Number of vertical block slices	2^5
Safety factor precision; mass balance precision (m^3)	$1 \cdot 10^{-4}$
Mass balance precision (m^3)	$1 \cdot 10^{-4}$
Genetics	
Population size	48
Number of generations (minimum; maximum)	16; 32
Number of generations without improvement (maximum)	4
Mutation rate (%)	12.5
Migration rate (%)	65.0
Options: Inbreeding; polygamy	no; no

'rPart' package (Therneau et al. 2015). In the latter analysis type, tree complexity was selected in such a way that the standard error be smaller than the error difference between consecutive levels of complexity. Second, a series of one-iteration mobile bed-and-banks simulations was completed to help determine the value of key geotechnical parameters: cohesion, USCS class, mean grain size, and compaction. The objective was to ensure that no mass failure occurs for a set of parameters representing the (low) flow conditions encountered during the week when the initial channel survey was completed. Bank stability was found to be sensitive to the four parameters with the exception of compaction. The parameter values that produced the fewest failures were selected (Table 3.2). Third, a series of 2:45 hour-simulations (corresponding to the peak values of the γ-distributed curve representing the hydrograph) were run to further examine the model's sensitivity to soil cohesion. Although the geotechnical module has the capability to calculate soil cohesion based on USCS class and degree of saturation, we note a substantial discrepancy between the range of bank cohesion values typically encountered in nature (9–67 kPa for USCS class ML) and those employed while calibrating the geotechnical module (0.25–1.50 kPa). Thus, this variable should be considered as a numerical parameter rather than an input variable, in a similar way to the roughness coefficient for hydrodynamic calibration. The high degree of compaction was assumed to match the geological past of this post-glacial environment. Regarding bank hydrology, water table elevation adjustment rates k of 0.056 and 0.018 were used respectively for the rising and falling limbs of the hydrograph. These values were obtained by fitting Equation 3.7 to data acquired by Needelman (2013) in a river bank of similar composition. The values assigned to key parameters of the genetic algorithm are provided in Table 3.2. These parameters were adjusted to minimize computation time whilst maximizing precision.

Table 3.3. Parameters varied during numerical simulations

Configuration	*Vegetation parameters*					
	a_{tree}	d_{base}	h_{tree}	m_{trunk}	d_a	c_a
HYD	-	-	-	-	-	-
SED	-	-	-	-	-	-
GTC	-	-	-	-	-	-
RVG_{SMALL}	12.5	8.7	12.1	25	1.00	0.025
RVG_{MEDIUM}	23.2	20.9	21.1	250	1.25	0.250
RVG_{LARGE}	50.3	55.7	29.8	2500	1.75	1.250

Trunk spacing is equal to twice rooting depth d_a. Legend: HYD = a hydraulic-only simulation; SED = a HYD simulation with sediment transport; GTC = a SED simulation with mass wasting; RVG = a GTC simulation with a single tree type of size specified in the subscript; a_{tree} = tree age (years); d_{base} = basal trunk diameter (cm); h_{tree} = tree height (m); m_{trunk} = trunk mass (kg); d_a = rooting depth (m); and c_a = apparent cohesion due to roots (kPa).

3.3.3. Simulations and analysis procedure

Excluding the calibration simulations, a total of six simulations were run with the biophysical parameters described listed in Tables 3.2–3.3. Physiological plant properties were varied in a way as to provide a range of stabilization power; threshold parameter values were estimated using machine learning algorithms applied to the output of geotechnical slope stability assessments along a simplified river bank profile. A high value of apparent cohesion c_a was attributed to a large, 50-year-old Sugar Maple tree, whilst the value assigned to small and medium trees was proportional to the basal trunk area of the large tree.

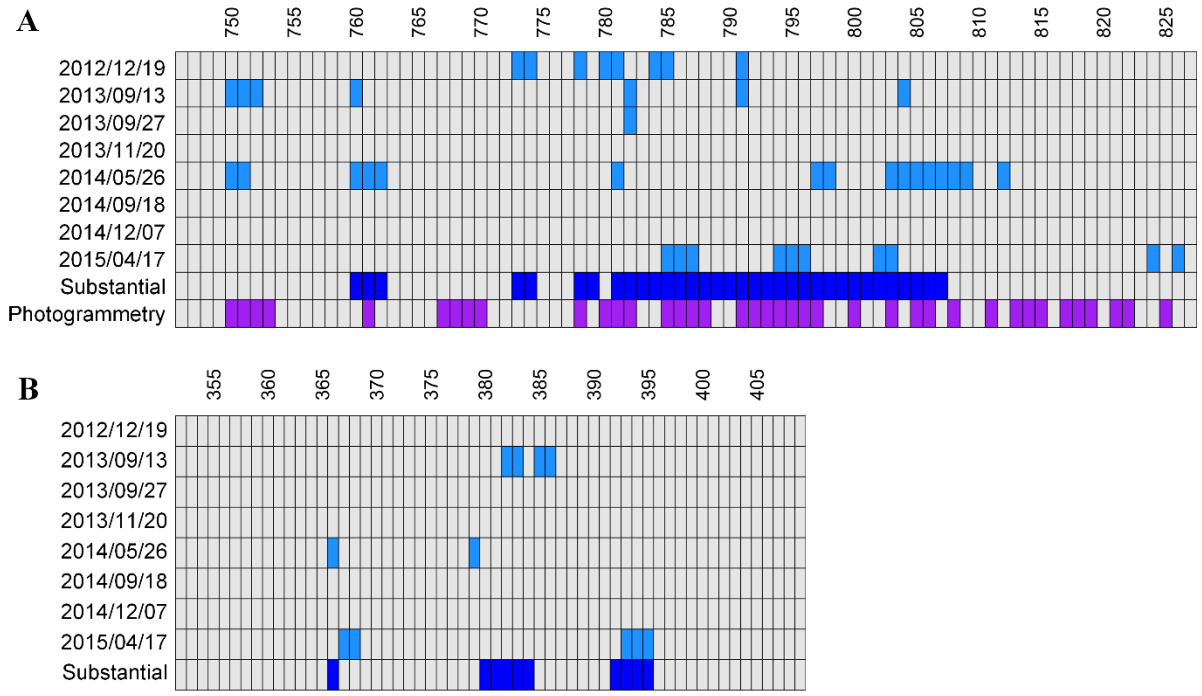

Figure 3.7. Occurrence of river bank failures along zones A and B

A light blue box corresponds to an observed geotechnical failure, based on photographs, for a specific date and transect. Dark blue boxes correspond to substantial total retreat (≥0.1 m²) during the observation period, i.e., between 19 December 2012 and 17 April 2015, and include fluvial and geotechnical processes that led to the removal of bank material along a transect. Purple boxes indicate transects where retreat was detected by photogrammetry for the same period (provided for zone A only).

3.4. Results

3.4.1. Field observations

A total of 25 flooding events with a magnitude of $Q \sim 15$ m^3/s or above were recorded during the study period (2012–2015) (see Figure 3.5). The largest number of bank failures were noticed on 26 May 2014, following a winter that included six floods with peak discharge varying between 14.4 and 33.0 m^3/s and after receiving 45.3 mm of rain, and on 17 April 2015 (associated with 18.9 and 40.3 m^3/s floods). Zone A was subject to a larger number of failures (42) than zone B (11) (Figure 3.7), whereas a single minor failure occurred along transect 953 of zone C on 20 November 2013 (not shown). Photogrammetry analysis performed for zone A of the study reach reveals a bank retreat up to 2.4 m in the eroded areas (purple column in Figure 3.7). Assuming that bank evolution occurred where calculated retreat rates were ≥10 cm, the accuracy of photogrammetric measurements, relative to field observations, was 61%; this low value is owing to a low number of benchmarks. In addition, riparian vegetation is responsible for false positives downstream of transect 812. The accuracy climbs to 76% when excluding these transects. Nevertheless, the magnitude of retreat rates is comparable to visual observations made in the field.

3.4.2. Accuracy quantification and evaluation

In order to facilitate the comparison of numerical simulations with morphological changes observed at the field site, the accuracy of each prediction was quantified using Youden's (1950) index:

$$J = SN + SP - 1 = \frac{TP}{TP + FN} + \frac{TN}{TN + FP} - 1 \tag{3.10}$$

where SN = sensitivity, SP = specificity, TP = number of true positive, TN = number of true negatives, FP = number of false positives, and FN = number of false negatives. This rating method provides a constant range of indices, between 1.0 (correct prediction for every transect) and -1.0 (wrong prediction for every transect), which facilitates the comparison of predictive accuracy amongst configurations and river reaches. In our analysis, an error of one transect spacing (~3.5 m) is tolerated, which means that a prediction contributes to TP if a failure was observed along a given transect or along its directly neighbouring transects.

3.4.3. Effects of model components

3.4.3.1. Hydraulics

Given the scoring system described above, using maximum bed shear stress along a channel cross section as an indicator of bank evolution is not very successful. Indeed, using a threshold value of 25 Pa results in Youden's indices of -0.28 and -0.15 respectively for zones A and B (rows HYD in Figure 3.8). This threshold value was selected because it maximizes the overall accuracy of hydraulic simulations. Very few failures are correctly predicted (true positives), and several are incorrectly predicted (false positives).

3.4.3.2. Sediment transport

The result of the simulation with bedload transport only, i.e., with the geotechnical and vegetation modules disabled, reveals a fairly stable channel with changes located primarily along channel margins. Nevertheless, looking at the total volume of displaced material, we note an initial adjustment of bed morphology during the first iteration of the simulation followed by a slow evolution rate that is proportional to flow discharge during the rising and falling limbs of the

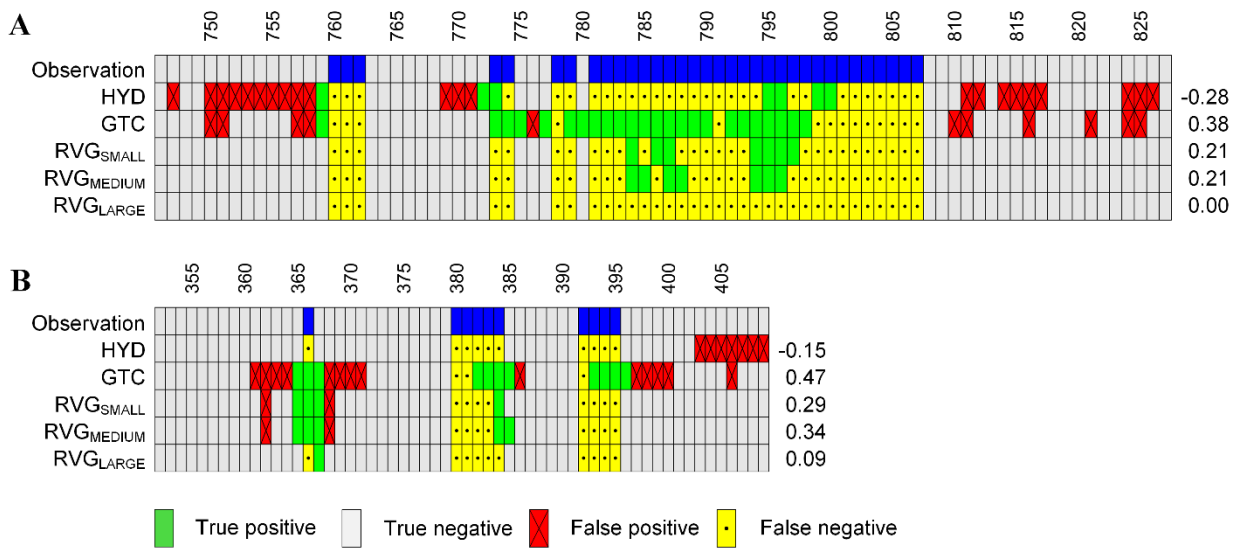

Figure 3.8. Comparison of bank failures observed within the study reach

The observation period extended between January 2012 and June 2015 to numerical predictions. The *x*-axis labels correspond to the transects shown in Figure 3.3 for zones A and B. Zone C is not shown owing to the lack of substantial bank retreat through mass wasting during the observation period. The values on the right side of each table correspond to Youden's index attributed to each numerical prediction, calculated using Equation 3.10. The observation row corresponds to the substantial row in Figure 3.7. HYD = a hydraulic-only simulation; GTC = a simulation with sediment transport and mass wasting; RVG = a GTC simulation with a single tree type of size specified in the subscript. The subscripts SMALL, MEDIUM, and LARGE refer to tree size (see Table 3.3 for the physiological properties of plant cover).

hydrograph. Insignificant bathymetric changes, combined with rapid channel stabilization, indicate that the coupled morphodynamic model TELEMAC-2D-SISYPHE, i.e., without geotechnical algorithms, is unlikely to simulate lateral retreat in our study reach.

3.4.3.3. Geotechnical processes

Simulations with different parameter sets were run to evaluate the sensitivity of the coupled geotechnical model to key parameters. For instance, doubling the adjustment rate of the water table elevation results in very similar erosion patterns. However, a rise in water table elevation within the river bank is required to create mass wasting in the upper bluff area. Although a steady low flow discharge of 7.5 m^3/s is sufficient to trigger the retreat of low banks, a peak discharge of 60 m^3/s, i.e., similar to the maximum value recorded during the observation period (66.2 m^3/s on 12 March 2013), when combined with a γ-shaped hydrograph curve, improves fit with observations. In particular, a flow discharge of 60 m^3/s affects the tall bluff (transects 746–762 in Figure 3.3) and increases the length of the eroded bank subject to mass wasting (transects 778–807 in Figure 3.8a). Similarly, soil cohesion values of 0.25, 0.50, and 1.00 kPa were evaluated, with a value of 0.25 kPa resulting in the best match with field observations.

Enabling the geotechnical module results in much improved predictions of retreat location compared to using a threshold bed shear stress value. This is reflected in the calculated accuracy values, i.e., Youden's indices of 0.38 (GTC) vs. -0.28 (HYD) in zone A, and 0.47 vs. -0.15 in zone B (Figure 3.8b). Despite the presence of several false positives, configuration GTC correctly predicts the location of the river banks where acute erosion was observed in the field (row GTC in Figure 3.8). Two of the most unstable bank regions along zone A are correctly identified (Figures 3.4a–b). The model may not be able to identify transects 799–807 (Figures 3.4c and 3.8a) because most failures along this bank occurred only once the upstream 50-m region had retreated substantially, i.e., after 18 floods with a magnitude of at least 15 m^3/s over a period of 1.5 years (Figure 3.7). Although configuration GTC results in the largest number of true positives, it also involves several false positives between transects 810–825 (Figure 3.8a). This may be explained by the fact that the presence of riparian vegetation is only indirectly, partially accounted for with an adjustment of soil cohesion in configuration GTC.

3.4.3.4. Riparian vegetation

The vegetation module developed for this study influences the degree of bank stability by increasing soil cohesion (up to a certain depth under soil surface, depending on plant physiology) and by increasing the mass of a slump block (tree species only). These mechanical actions in turn affect

friction forces along the slip surface (e.g., dashed line in Figure 3.1a), stabilizing or destabilizing a river bank, depending on bank geometry and local biophysical conditions.

All three configurations involving vegetation, i.e., RVG_{SMALL}, RVG_{MEDIUM}, and RVG_{LARGE}, induce a drastic reduction in the number of failures (false positives and true positives) relative to the basic geotechnical scenario (row GTC in Figure 3.8). Configurations with small and medium trees result in Youden's indices lower than that of the GTC configuration in zone A. Although this difference is less important in zone B, configurations RVG_{SMALL} and RVG_{MEDIUM} fail to predict the correct extent of the large unstable zone (transects 778–807 in Figure 3.8a) and the occurrence of failures in the top of the bluff (Figure 3.4a and transects 760–762 in Figure 3.8a). In addition, the largest failure (in volume) recorded in zone B during the observation period is not predicted by the model (transects 392–395 in Figure 3.8b). This may be caused by the increased stability in the model that was using trees, whereas at the field site for this zone shrubs are present. The scenario with the largest trees almost completely eliminated bank instabilities, with a progression in mechanical reinforcement with an increase in tree size. Although vegetation considerably reduces the number of failures and volume of displaced floodplain material, it does not necessarily reduce the mean failure volume (Table 3.4). For instance, 151 failures produced a total displacement of 41.1 m^3 in zone C under the RVG_{MEDIUM} configuration, whereas a single failure displaced 18.3 m^2 under RVG_{LARGE}. Therefore, vegetation cover triggers a nonlinear response that seems to be exacerbated by complex river bank geometry, combined with the stochastic nature of the genetic algorithm. Nonlinearity is expected to increase even more with spatiotemporal variations in sedimentology and in plant physiology and assemblage.

Table 3.4. Number of failures and absolute volume change in zones A, B, and C

Configuration	*Number of failures*			*Volume change (m^3)*		
	A	*B*	*C*	*A*	*B*	*C*
SED	-	-	-	17.3	7.6	15.9
GTC	590	199	108	3316.7	352.8	45.7
RVG_{SMALL}	199	100	166	64.1	255.5	65.2
RVG_{MEDIUM}	108	94	151	51.9	138.3	41.1
RVG_{LARGE}	0	6	1	12.2	12.3	18.3

Zone A corresponds to transects 746–827, zone B to transects 352–409, and zone C to transects 929–954 (Figure 3.3). Legend: SED = a hydraulic simulation with sediment transport; GTC = a SED simulation with mass wasting; RVG = a GTC simulation with a single tree type of size specified by the subscript.

3.4.4. Timing and magnitude of bank retreat

Neglecting soil displacement occurring at the onset of simulations (which may be attributed to bed adjustment with respect to flow dynamics), the SED configuration produces displacement rates matching the shape and phase of the γ-distributed hydrograph, with maximum values reaching 1.3, 0.6, and 1.4 m^3/15-min period respectively for zones A, B, and C (Figure 3.9). Activating the

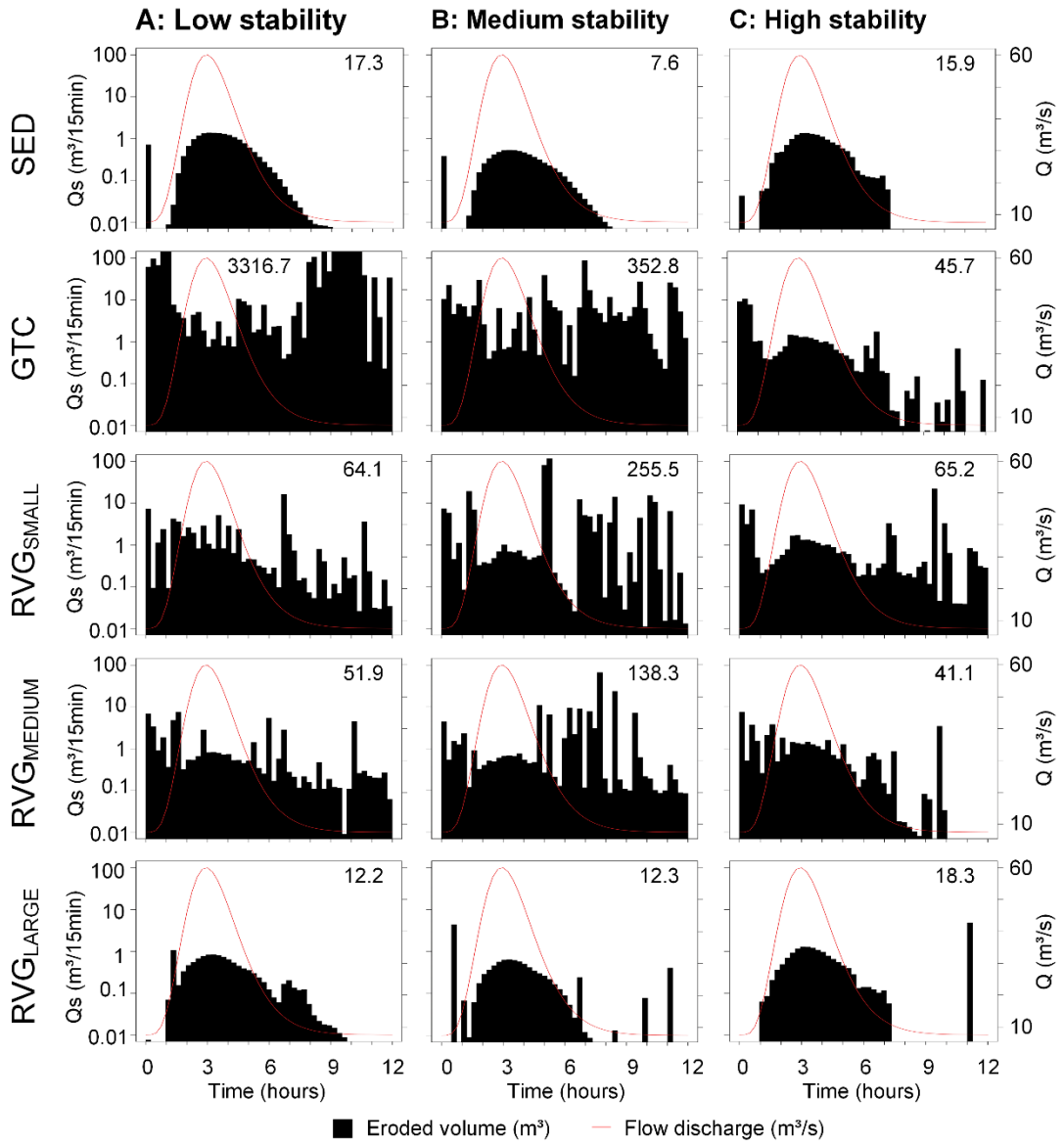

Figure 3.9. Predicted floodplain material displacement and flow discharge

Primary and secondary *y*-axes correspond to Q_s and Q. Columns correspond to zones A (low bank stability), B (medium bank stability), and C (high bank stability) in Figure 3.3. In-plot annotations are the cumulative, simulated displaced volumes (m^3).

geotechnical module alters the timing of mass wasting and total volume of displaced soil material, and produces a complex signal emerging from the overlap of bedload entrainment and mass wasting processes. Although we note similar patterns in the geomorphic response to the 12-hour flood event amongst zones and amongst configurations (Figure 3.9), displacement occurs primarily near the end of the falling limb, i.e., when flow discharge has returned to preflood magnitude. The lag between flow and soil displacement peaks seems to be caused by the indirect consideration of soil hydraulic conductivity in the geotechnical modules, which is done by defining water table convergence coefficients. The similarity in response between zones A and B (Figures 3.9–3.10) may be attributable to similarities in bank geometry, height, and cover along unstable transects. In particular, zone C has a lower tree density than zones A and B and does not exhibit three distinctive soil strata. Finally, note

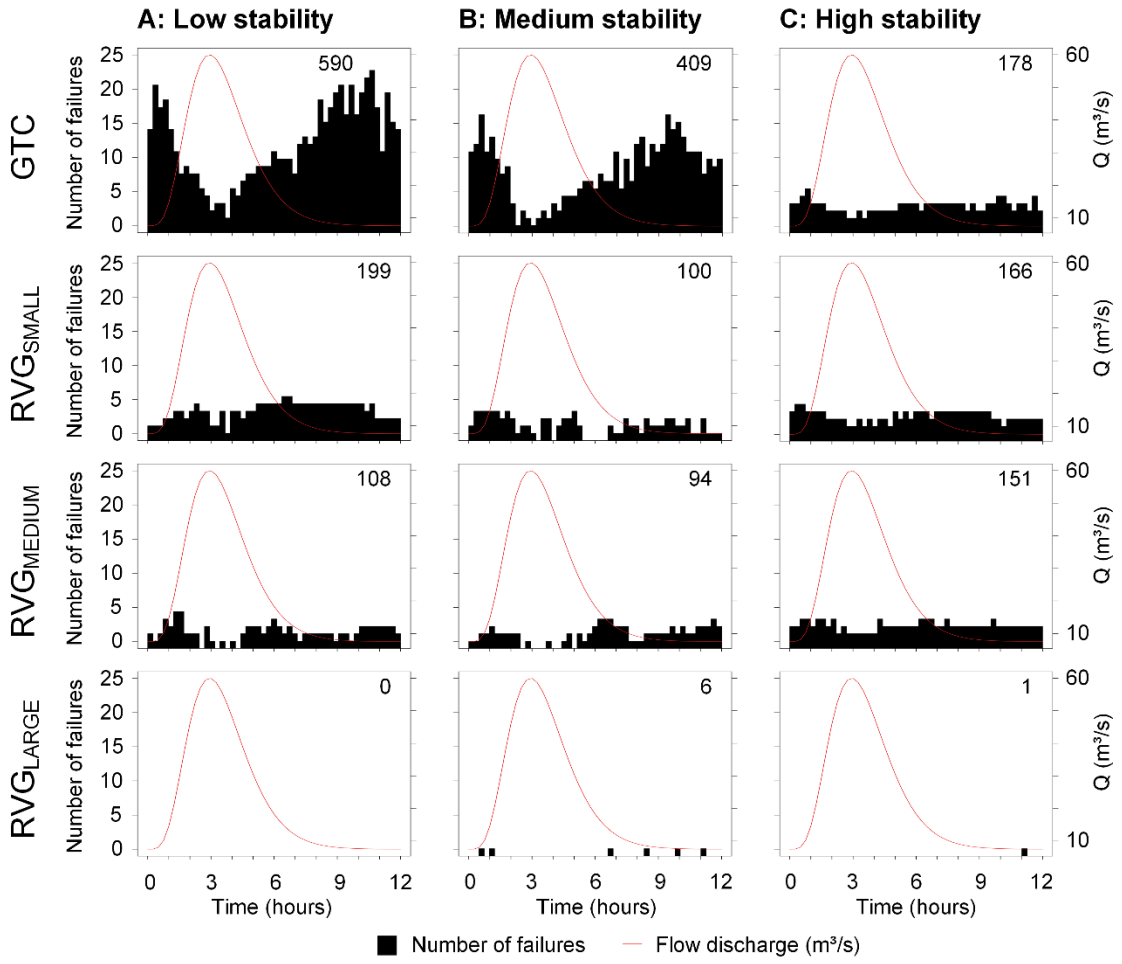

Figure 3.10. Predicted number of failures and flow discharge

Primary and secondary *y*-axes correspond to the number of failures and *Q*. Columns correspond to zones A (low bank stability), B (medium bank stability), and C (high bank stability) in Figure 3.3. In-plot annotations are the total number of simulated failures.

that a substantial reduction in the number of failures does not automatically translate into a substantial reduction in the volume of displaced soil material (e.g., Figure 3.9 vs. Figure 3.10).

The volume of displaced soil material is inversely proportional to the maturity of the vegetation cover, which demonstrates the substantial contribution of physiological plant properties on channel dynamics (Figure 3.9). Small and medium trees reduce the incidence of mass wasting in zones A and B but have very little effect in zone C (Figure 3.10). Note that a patch of young trees provides enough soil reinforcement to substantially reduce the number of failures. The timing of displaced material in configuration RVG_{LARGE} is similar to the timing in SED, with the distinction that vegetation slightly reduces soil displacement rate (Figure 9). This may be attributed to the increase in friction caused by the presence of riparian vegetation on river banks, which highlights the importance of including flow-vegetation interaction.

3.5. Discussion

This research confirms that a morphodynamic model lacking a dedicated geotechnical component is unable to simulate lateral adjustments in a meandering channel with cohesive banks. In our simulations, the sediment transport module alone predicts little bank retreat for a study reach that was observed to be unstable. In addition, using a threshold bed shear stress value appears to be a weak predictor for the location of bank failures (row HYD in Figure 3.8).

Lateral erosion processes have been included into fluvial models using various approaches and comparing them directly with the modules presented here is not straightforward, particularly as very few have attempted to simulate complex natural cases (e.g., Van de Wiel and Darby 2004). Bishop's (1955) method of slices, used here to quantify river bank stability, was also employed in other fluvial studies, but often with the intent of examining the geotechnical stability at the river bank and reach scales, not connecting it to a hydraulic model (e.g., Van de Wiel and Darby 2007; Langendoen and Simon 2008; Midgley et al. 2012). A few models consider geotechnical soil properties in the calculation of retreat rates, but these are generally kept constant during a simulation. For instance, the incipient collapse angle is not affected by flow stage in Asahi et al. (2013).

A major advantage of our model is the integration of a river bank hydrology module and the consideration of spatial variations in soil moisture within the bank during stability evaluations. Furthermore, it allows the complexity of natural rivers to be fully represented, whereas most other models impose idealized bank profiles (e.g., Eke et al. 2014; Langendoen et al. 2016) and planform geometries (e.g., Crosato 2007). Several of these implementations assume (without enforcing) mass

conservation during bank retreat and, by doing so, ignore the role of basal control on river bank stability (Thorne 1982). However, retreat models incorporating a deposition algorithm exist (e.g., Van de Wiel and Darby 2004; Dulal et al. 2010).

A major advantage of the proposed model is its genetic algorithm, which selects the failure mechanism (rotational or translational) as it determines the extent of the slump block. This feature is particularly relevant to the study of meandering river channels, which develop in cohesive floodplains (Anderson and Anderson 2010), as rotational failures tend to be associated with cohesive soils (Thorne 1982). Conversely, most existing bank retreat formulations assume noncohesive soils, and therefore translational failures. The consideration of biophysical conditions (e.g., soil composition and moisture, flow stage, water table elevation, plant cover) by the genetic algorithm is also compatible with the episodic nature of bank retreat in natural rivers (Abernethy and Rutherfurd 1998; Pollen-Bankhead and Simon 2010). Therefore, existing morphodynamic models, often generating geometrically idealized meandering planforms, may not apply to complex river environments.

Bank retreat along Medway Creek was discontinuous in time, space, and magnitude during the observation period (Figures 7–8). These irregularities are fairly well simulated by our model, which seems to suggest the necessity to include a sophisticated geotechnical algorithm in morphodynamic models for improved applicability to natural rivers. The proposed modelling approach, which is more detailed and physics-based than previous implementations in the description of salient processes, therefore reduces the gap between theory and practical applications for complex river environments by integrating vector-based geospatial treatment, not only in data surveying as Güneralp and Marston (2012) suggest but at the heart of the modelling algorithm.

The integration of physics-based stability equations also facilitates the fragmentation of river bank erosion into distinct processes (e.g., fluvial and geotechnical), forces (e.g., hydrostatic pressure, pore-water pressure, slump block weight), and components (e.g., riparian plants). Fragmentation, which is one of the key novelties of the proposed morphodynamic modelling approach, enables to examine causal relationships, with parameter values defined in terms of distinct, ideally measurable, physical quantities. Existing planform meander models, including the HIPS formulation (Hasegawa 1977; Ikeda et al. 1981), simulate lateral retreat as a function of excess near-bank shear stress or excess velocity (e.g., Güneralp et al. 2012; Zolezzi et al. 2012), which prevents the direct manipulation of variables influencing lateral erosion.

A similar observation can be made regarding the inclusion of plant effects. Most existing models indirectly consider vegetation (but see Van de Wiel and Darby (2004, 2007) for a simplified physics-based approach) by increasing the threshold stream power required to initiate sediment transport (e.g., Murray and Paola 2003) or by altering bed roughness based on plant physiology and arrangement, which reduces near-bed velocities (e.g., Crosato and Saleh 2011), or by attributing an added cohesion value owing to presence of roots while ignoring surcharge effect (e.g., Eaton and Giles 2009). Fuzzy concepts have also been used to lump, quantify, and integrate the stabilization effects of riparian plants. Modifying bank erodibility based on biomass density (e.g., Camporeale et al. 2013) allows to relate planform patterns to biomass density and vegetation growth rate (Perucca et al. 2007). However, this numerical, immaterial, and partially subjective conceptualization of floodplain vegetation limits the application of these models to real-world investigations as biomass does not unambiguously translate into a set of measurable physiological plant properties or alterations of soil strength.

By fragmenting geotechnical and vegetation processes and forces, the model presented in this paper facilitates the identification of causes of bank failure. However, the current version of the model fails to recognize the normal range of cohesion values associated with soil and roots in nature, which indicates that it is not yet capable of accounting for the overall complexity of the natural environment, although the overall approach constitutes a step in this direction.

Describing fluvial processes using physically correct equations considerably increases run time, and therefore, severely limits the spatiotemporal scales that can be investigated. The inclusion of the nonlinear version of the shallow-water equations and quantification of geotechnical stability based on a limit equilibrium method, combined with the selection of appropriate cell size and time step to ensure numerical stability and the validity of predictions (e.g., grid-independence testing using Biron et al. (2007); Courant number below unity), contribute to this situation. Despite the activation of parallel processing and the use of a genetic solver for the geotechnical computations, each simulation took ~4.5 days to run on a computer equipped with double hex-core processors. As an indication, the coupled model spent 18.0%, 69.5%, and 12.5% of its time in the hydraulic, sediment, and geotechnical modules respectively. Thus, further improvements in algorithmic efficiency are needed for river scientists and practitioners to employ the type of model presented here to perform simulations over long spatiotemporal scales.

In this study, and for the sake of efficiency, we explored parameter sensitivity using machine learning algorithms on a series of one-iteration simulation results and identified threshold values for

key parameters. Such short trial simulations helped to identify the range of reasonable parameter values but did not allow for the interaction between processes and the full spectrum of combinations of biophysical conditions to be taken into account. This may explain why activating the vegetation module enhances stability more drastically than expected, leading to less accurate predictions than a strictly geotechnical simulation. The outcome may have differed with a sophisticated calibration/fitting method capable of determining soil and apparent (owing to roots) cohesion values maximizing correlation between observed and predicted failures.

The proposed bank retreat approach differs from previous implementations in its enhanced applicability to complex natural river environments, as most geotechnical models simulating river banks failures are limited in scale to a few tens of meters (e.g., Thomas and Pollen-Bankhead 2010; Midgley et al. 2012), whilst morphodynamic models mainly focus on flume-size channels with noncohesive banks (e.g., Langendoen et al. 2016) and assume nonvegetated floodplains (e.g., Pittaluga and Seminara 2011; Asahi et al. 2013). Therefore, with a few exceptions such as the model developed by Lai et al. (2015), it is one of the very few models that can accurately predict bank erosion episodes at a scale relevant to the management and restoration of river reaches. Validating the meandering planform properties and dynamics predicted by pseudo-empirical approaches is often limited to a coarse comparison of behavioural evolutionary traits against those visible in historical aerial photographs (e.g., Camporeale et al. 2005; Perucca et al. 2007; Duan and Julian 2010) or against data sets from analogue flume experiments (e.g., Duan et al. 2001; Rüther and Olsen 2007). Conversely, the fairly subtle planform changes associated with physics-based models are not necessarily detectable on airborne imagery. Although a sophisticated, physics-based model applicable to natural vegetated rivers provides more detailed mechanistic information related to river bank erosion processes, it also requires exhaustive data measurements for parameterization and validation, which are seldom available.

3.6. Conclusion

New geotechnical and vegetation modules were developed and coupled to the hydrodynamic module TELEMAC-2D and sediment transport module SISYPHE to create a universal and more physics-based representation of the evolution of alluvial river channels at the kilometer scale. The agreement between observed and predicted river bank failures in our simulations is encouraging, and comparison with field data revealed a marked improvement in bank failure predictions when adding the geotechnical module, albeit with limited gain in accuracy when adding the vegetation module.

The main novelty of the developed modules is the possibility to parameterize lateral erosion using physical, measurable quantities such as geotechnical soil properties (texture, cohesion, compaction, and porosity) and physiological plant properties (wood density, trunk diameter and length, and root strength and depth). Importantly, and innovatively, the geotechnical evaluations are done independently of the hydrodynamic mesh, which allows single- or multithreaded alluvial river types of any scale (flume, stream, and river) to be studied for cohesive and noncohesive soils, with or without aquatic or terrestrial plants. The consideration of a floodplain rather than strictly a channel allows us to consider palaeochannels and to include the effects of mass wasting events occurring away from the channel, for instance, along valley walls. Furthermore, the effect of soil water content, in particular the effects of the imbalance between free surface and water table elevations during a flooding event, is an important addition to the model as it is recognized as critical to river bank stability. Finally, the use of a fully configurable genetic algorithm with tournament selection keeps runtimes close to those of a morphodynamic model lacking a lateral erosion algorithm while allowing to efficiently locate planar, circular, and noncircular slip surfaces through a single algorithm. Our solution addresses some of the critiques of existing morphodynamic models such as the lack of physics in lateral erosion algorithms, the omission of mass wasting and vegetation processes, and their incapacity to consider multithreaded channels.

To enhance the applicability of the developed model for river-related management issues, future developments should focus on improving the physical representation of vegetation, in particular, with respect to the cohabitation of multiple individuals and species in a single simulation cell, a situation that is usually encountered in a natural setting. An adaptive mesh, such as the one built by Langendoen et al. (2016), would also likely be more efficient for physics-based 2D and 3D models. Most importantly, there is a serious need for accessible time series of biophysical, hydraulic, topographic, and sedimentological data sets to calibrate and validate models such as ours. As highlighted by Rousseau et al. (2016), creating a central repository providing universal validation cases for morphodynamic modelling would be extremely valuable.

Liaison paragraph

The developed coupled model was calibrated using data from a natural river to evaluate its ability to accurately simulate bank retreat. The model agreed with the observations despite minimal efforts put into calibration and despite the complexity of the river channel considered with respect to sedimentology and vegetation cover. Questions then emerged regarding the capacity of the model to be calibrated for a different site. Assuming this can be achieved, parameter values would logically need to vary substantially between reaches associated with distinctive geomorphological contexts. In addition, the relative importance between key parameters may differ. These reflections and hypotheses triggered the numerical experiment described in the following chapter. This experiment can be distinguished from the previous one in that a more thorough calibration procedure was followed, and that vegetation was excluded from the analysis to focus on geotechnical properties of the bank material.

4

Comparing the sensitivity of bank retreat to changes in biophysical conditions between two contrasting river reaches using a coupled morphodynamic model

Yannick Rousseau, **Pascale Biron** and **Marco Van de Wiel**

Water 10(4): 518 (2018)

Abstract: Morphodynamic models of river meandering patterns and dynamics are based on the premise that the integration of biophysical processes matching those operating in natural rivers should result in a better fit with observations. Only a few morphodynamic models have been applied to natural rivers, typically along short reaches, and the relative importance of biophysical parameters remains largely unknown in these cases. Here, a series of numerical simulations were run using the hydrodynamic solver TELEMAC-2D, coupled to an advanced physics-based geotechnical module, to verify if sensitivity to key biophysical conditions differs substantially between two natural meandering reaches of different scale and geomorphological context. The model was calibrated against observed measurements of bank retreat for a 1.5-km semi-alluvial meandering reach incised into glacial till (Medway Creek, Ontario, Canada), and an 8.6-km long sinuous alluvial reach of the St. François River (Quebec, Canada). The two river reaches have contrasting bed and bank composition, and they differ in width by one order of magnitude. Calibration was performed to quantify and contrast the contribution of key geotechnical parameters, such as bank cohesion, to bank retreat. Results indicate that the sensitivity to key geotechnical parameters is dependent on the biophysical context and highly variable at the sub-reach scale. The homogeneous sand-bed St. François River is less sensitive to cohesion and friction angle than the more complex Medway Creek, flowing through glacial-till deposits. The latter highlights the limits of physics-based models for practical purposes, as the amount and spatial resolution of biophysical parameters required to improve the agreement between simulation results and observations may justify the use of a reduced complexity modelling approach.

4.1. Introduction

Despite increasing reliance on numerical modelling to simulate flow hydraulics, sediment transport and bank erosion in rivers (Rinaldi et al. 2008; Tal and Paola 2010; Ham and Church 2012; Langendoen et al. 2016), several challenges remain when investigating natural channels. These are attributed to the complexity and spatial heterogeneity of processes related to soil properties, bank morphology, hydrology and riparian vegetation (Lai et al. 2012; Motta et al. 2012).

Knowledge gains on lateral adjustments in natural channels have often emerged from studies undertaken at the scale of a single bank or river reach (e.g., Midgley et al. 2012; Lai et al. 2015). The manner in which findings are presented in these studies may give the impression that alluvial river channels are affected in a similar way by external forces, independently of their scale and biophysical context. For instance, generalizations have been made such as soil cohesion increasing river bank stability (Peakall et al. 2007; Tal and Paola 2010) or vegetation stabilizing banks due to mechanical reinforcement (Abernethy and Rutherfurd 1998; Millar 2000; Rey et al. 2004). On the contrary, the surcharge imposed by mature trees on a river bank can have a destabilizing effect (Simon and Collison 2002), in particular during the falling limb of a hydrograph (Pollen-Bankhead and Simon 2010). However, because each finding likely applies to limited river contexts similar to the one from which they were drawn, the relative importance of biophysical variables may in fact differ considerably between river channels (Parker et al. 2008). Given the diversity of soil characteristics and heterogeneity of the floodplain with respect to biophysical conditions (Güneralp and Marston 2012), there is an urgent need to develop tools that can be used with ease to evaluate the evolution of a diversity of alluvial and semi-alluvial river reaches (Güneralp et al. 2012).

In the last 10–15 years, several laboratory studies have examined the role of vegetation on increased cohesion in meander formation (e.g., Tal and Paola 2007; Braudrick et al. 2009; Van Dijk et al. 2013). Previous laboratory studies also used cohesive substrate, such as clay (e.g., Friedkin 1945; Schumm and Khan 1971; Smith 1998). However, most modelling (e.g., Asahi et al. 2013; Langendoen et al. 2016) and flume-based studies (e.g., Van Dijk et al. 2012; Ferreira da Silva and Ebrahimi 2017) on meandering rivers involve sand bed and banks, whereas the meandering process typically occurs in cohesive floodplains (Anderson and Anderson 2010). In particular, the mechanisms responsible for the development of meandering channels in a laboratory channel (e.g., Tal and Paola 2010) may differ from those observed in nature, even if these channels share similar physiological traits. In addition, model validation is often achieved broadly with respect to visual elements captured using airborne imagery such as channel planform and dynamics (e.g., Perucca et

al. 2007; Duan and Julien 2010), with only a few modelling parameters representing the broad characteristics of soil and vegetation cover. For instance, bank material can be attributed an erodibility coefficient (Perucca et al. 2007) while plants are represented by a density value. The problem of how transferrable findings obtained at a given scale for a particular river type are to other channels remains scarcely documented. For example, are the key physical parameters contributing equally to bank stability in all river contexs? Very few studies have attempted to calibrate a model against data from a natural river channel/floodplain to help answer this question (Mosselman (1998), Darby et al. (2002), and Evangelista et al. (2015) being exceptions) and none, to the best of our knowledge, have compared parameter values between river channels. This could be attributed to weaknesses in the physics behind meander dynamics models which do not take into account channel morphology (including bars) and vegetation (Pittaluga and Seminara 2011). It may also be related to the substantial computational power required by these models (Hervouet 2000) and to the scarcity or incompleteness of field datasets owing to limitations in financial resources, time, available technologies, and data accessibility (Oreskes and Belitz 2001; Mulligan and Wainwright 2013). This is particularly the case for bank retreat models (Nelson et al. 2003).

River bank retreat involves a sequence of processes operating simultaneously at different timescales (Nelson et al. 2003; Darby et al. 2007). For example, bend migration process is generally associated with periods that are much larger than that of the flow (Williams et al. 2016). Indeed, river banks are subject to slow transformations involving tension cracking (Thorne and Tovey 1981), basal erosion by the flow (Thorne 1982) and riparian vegetation cover (Abernethy and Rutherfurd 2000; Pollen-Bankhead et al. 2009) and assemblage (Simon and Collison 2002). Bank failures occur as soon as bank strength drops below a critical value. From a modelling point of view, this duality is challenging, and it has been addressed by at least two contrasting approaches. A linear framework, relying on near-bank excess velocity and an empirical representation of bank resistance (known as the HIPS formulation, from Hasegawa (1977) and Ikeda et al. (1981)), makes it possible to examine channel dynamics at long spatio-temporal scales (e.g., Schwenk et al. 2015). However, the consideration of basic flow and soil properties (velocity, cohesion), combined with the lack of a groundwater hydrology model and the impossibility to take into account complex channel and floodplain bathymetry (Parker et al. 2011; Pittaluga and Seminara 2011) are serious limitations when analysing lateral retreat along natural river channels (Güneralp and Marston 2012). A second popular approach is the use of enhanced computational fluid dynamics (CFD) models (e.g., Darby et al. 2002; Lai et al. 2012; Langendoen et al. 2016). The primary limitations of this approach are that it is computationally demanding and applicable to short spatio-temporal scales. They are also usually

designed for curvilinear meshes (e.g., Duan et al. 2001; Jia et al. 2011), which often prevents their use with multithreaded channels (Camporeale et al. 2013).

This paper compares the sensitivity of river bank retreat to geotechnical parameter values between two natural river channels of different scale and geomorphological contexts in Quebec and Ontario (Canada). Both modelling investigations are undertaken with the hydrodynamic solver TELEMAC-2D (Riadh et al. 2014) and sediment transport solver SISYPHE (Tassi and Villaret 2014) from the suite open TELEMAC-MASCARET (EDF-R&D 2018) v7.0. They which were coupled to a physics-based geotechnical module that considers a broader set of soil properties than commonly included in most bank erosion models (Rousseau et al. 2017). This research is based on three methodological novelties, (i) the use of a coupled CFD-geotechnical numerical model to examine the morphodynamics of a multithreaded river reach at the km scale, (ii) the use of sedimentological and bathymetric data to calibrate models of river bank retreat, and (iii) the inclusion of groundwater hydrology into a coupled CFD-geotechnical numerical model and study. These lead to two main novel applications, (i) the identification of a set of biophysical conditions that fit observations of bank retreat for two different natural river channels, and (ii) a comparison of simulated bank retreat evolution between two natural river channels of different scales and geomorphological contexts.

4.2. Methodology

4.2.1. Study sites

Two contrasting fluvial environments with field observations on bank retreat are examined in this study (Figure 4.1a). The river reaches differ in terms of geological and geomorphological history, type of channel, spatial scale, and bank composition. The two sites were selected based on the availability of data against which to validate modelling outcomes.

The first site is the downstream 8.6-km reach of the alluvial St. François River (SF hereafter), St. François-du-lac (Quebec, Canada), near its confluence with the St. Lawrence River (Figure 4.1). A 3.4-km secondary branch forms an island within this reach. The primary branch has a sinuosity of 1.22. This channel has a bankfull (2-year return period) discharge of 1227 m^3/s and a bankfull width of ~151 m when combining both branches. The longitudinal bed slope is around 0.04% in the main branch, and therefore markedly smaller than for MC. The nature and lateral extent of riparian vegetation cover varies according to land use and to the occurrence of recent bank erosion episodes. A few banks were stabilized with riprap to protect roads near the island on both sides of the river. A narrow riparian zone consisting of an assemblage of herbaceous plants, shrubs and immature trees

is present next to agriculture lands. The trees were able to reach late succession stages in areas with less human impact near the deltaic area, near the downstream end of the island, and along the upstream left bank. A thorough analysis of the geotechnical properties of bank material reveals a sandy soil with several sandy silt, silty sand and silt layers (Tremblay 2012); the silt material has a mean grain size of 0.075 mm. Mean grain size of the bed is 0.3 mm (Verhaar et al. 2010). The average recorded retreat rates in the two bends downstream of the confluence were 1.53 and 1.13 m/year between September 2008 and 2010; these values are lower than the average of 3.53 and 2.07 m/year between 1964–2008 (Tremblay 2012). Channel bathymetry was surveyed with a DGPS (C. Boyer, personal communication, 2012). A total of 22,934 topographic points were acquired along 91 cross-sections, with an average distance of ~140 m between two consecutive cross-sections. Bed elevation

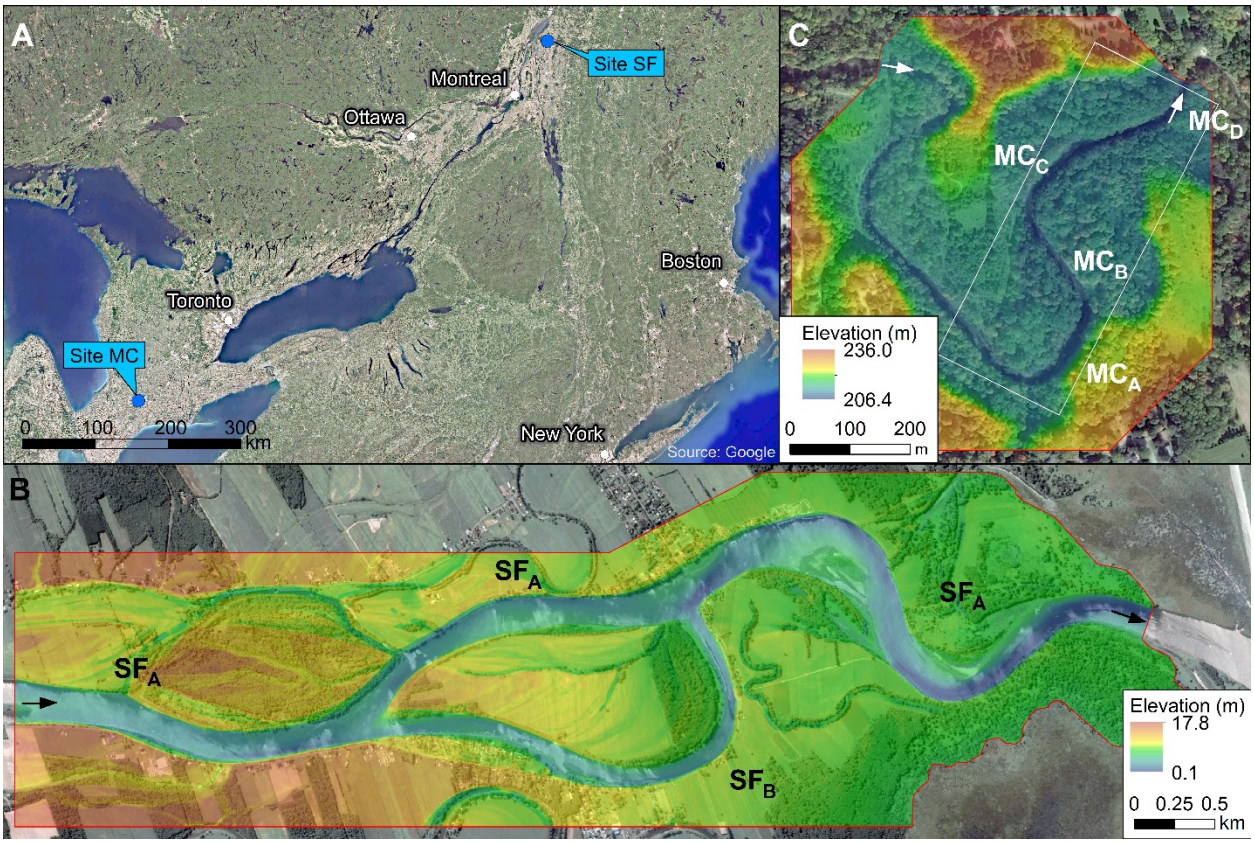

Figure 4.1. Field sites

a) Location map showing the two study sites. Numerical domain of **b)** the St. François River (herein referred as SF) (Quebec; 72.908762°W, 46.103081°N), near its confluence with the St. Lawrence River and **c)** a sinuous reach along Medway Creek (herein referred as MC) (Ontario; 81.289621°W, 43.008107°N). The white rectangle corresponds to the area presented in Figures 4.6b and 4.7b. Arrows indicate flow direction. Elevation values are relative to mean sea level. Subscripts identify sub-reaches.

values were interpolated linearly in the downstream direction. Floodplain topography was defined based on 194,631 LiDAR points acquired in 2001 and combined to the bathymetry dataset to create a DEM. The SF river banks were also surveyed in the spring and fall of 2009 and 2010 to identify the nature of bank retreat.

The second site is a 1.5-km long reach of the semi-alluvial river Medway Creek (MC hereafter), London (Ontario, Canada) (Figure 4.1c). The study reach has a sinuosity of 2.31 and is located in a post-glacial valley covered by different assemblages of deciduous and coniferous trees, shrubs, and herbaceous species. The lower bank soil layer consists of glacial till is buried under a thick sand layer covered with a thin organic layer. Bed substrate comprises gravel, sand and till patches. The mean grain size of the unconsolidated material is 103.7 mm, although substantial variations exist between geomorphic units. Bankfull discharge, based on data collected at a gauging station just downstream of the study reach, is 43 m^3/s, which corresponds to a channel width of ~20 m. Longitudinal bed slope is 0.27%. Further details on this site are available in (Rousseau et al. 2017). Over 5000 topographic points of the channel bed and banks were acquired in the study reach using a high-resolution DGPS instrument in November 2012. This manual technique is appropriate for the acquisition of morphological data in a channel with vegetated banks as plants and large woody debris create visual obstructions. These points were combined with 1-m resolution LiDAR data (University of Western Ontario 2006) to create a Digital Elevation Model (DEM) of the channel and floodplain. The field site was visited before and after each flood (>15 m^3/s) between 2012 and 2015 to determine changes in morphology and vegetation cover along four sub-reaches of interest, herein referred to as **A**, **B**, **C** and **D** (Figure 4.1c). The geometric properties of these sub-reaches are presented in (Table 4.1).

Table 4.1. Channel and bank morphology

Site	*Sub-reach*	*Side*	*Length (km)*	*Bank height (m)*		*Bank angle (°)*		*Bed width (m)*	
				Range	*Mean*	*Range*	*Mean*	*Range*	*Mean*
SF	A	Left	8.66	0.9–8.8	5.0	1.9–18.1	7.4	124.3–392.4	210.9
	A	Right		1.0–10.3	5.3	1.0–10.3	5.3		
	B	Left	3.42	1.1–8.6	3.5	1.4–11.7	5.9	64.5–160.4	107.3
	B	Right		1.9–8.7	5.0	4.8–21.3	9.9		
MC	A	Right	0.09	2.1–11.8	8.4	19.6–38.4	30.6	11.4–18.5	14.1
	B	Right	0.17	1.4–12.8	3.8	17.6–67.2	26.5	7.7–14.4	11.0
	C	Left	0.19	1.1–5.0	2.6	11.8–29.5	21.1	5.5–20.7	11.6
	D	Right	0.09	1.3–3.4	2.4	14.9–32.5	25.2	13.4–18.9	15.6

Sites SF and MC, and associated sub-reaches are shown in Figure 4.1.

4.2.2. Model description

Physics-based geotechnical algorithms were coupled to the hydrodynamic module TELEMAC-2D and to the sediment transport module SISYPHE to include river bank retreat due to mass wasting. Only the basic features of the model are provided in this section. Further details are available in (Rousseau et al. 2017).

The hydrodynamic model TELEMAC-2D, which is described in (Galland et al. 1991) was set up with Smagorinsky (1963) formula to simulate turbulence while minimizing runtime. The default advection scheme (method of characteristics) is used to determine flow velocities and depth. The bed load is enabled using Meyer-Peter and Müller (1948) equation included in the sediment transport module SISYPHE (described in Villaret (2010)). The effects of local topography on transport magnitude and direction are taken into account using Koch and Flokstra (1981) equation.

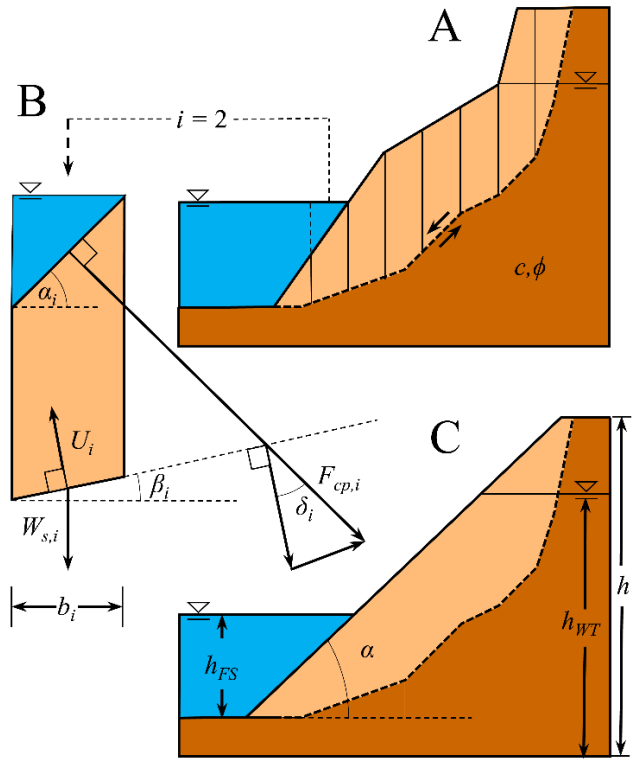

Figure 4.2. Representation of a slump block in the model

a) Fragmentation of slump block into slices during bank stability assessment with Bishop's simplified method of slices. The dotted arc represents a hypothetic slip surface. **b)** Stability is calculated by analysing the forces acting on slice base, namely pore-water pressure, confining pressure exerted by the flow and soil weight. Variables are included in Equations 4.1–4.3. **c)** Bank profile following deposition of the failure block at the friction angle of the bank material. In this study, this simplified bank profile also serves in representing bank geometry during the comparison of model behaviour between the SF and MC reaches.

The developed geotechnical module is powered by a genetic algorithm similar to the one proposed by Li et al. (2010) and relies on Bishop (1995) slope stability equation:

$$F_s = \frac{\sum_{i=1}^{n} \frac{cL_i + \left(W_i + F_{cp,i}\cos\delta_i - U_i\right)\tan\phi}{m_i}}{\sum_{i=1}^{n} W_i \sin\beta_i + F_{cp,i}\sin\delta_i} \tag{4.1}$$

$$m_i = \cos\beta_i + \frac{\sin\beta_i \cdot \tan\phi}{F_s} \tag{4.2}$$

where F_s = safety factor; c = soil cohesion; L_i = length of slice base i out of n; W_i = weight of soil material and groundwater; $F_{cp,i}$ = confining pressure exerted by the flow; δ_i = angle between the result of hydrostatic confining force and normal to failure plane; U_i = hydrostatic uplift force due to pore water pressure at slice base, basal angle β_i, ϕ = friction angle of the soil material; and m_i = m-term (Figure 4.2).

A river bank hydrology model calculates water table elevation (z_{wt}) at time t using

$$z_{wt}(t) = z_{fs}(t) - \left[z_{fs}(t) - z_{wt}(t_0)\right]e^{-k(t-t_0)} \tag{4.3}$$

where t_0 = previous time, z_{fs} = flow surface elevation at time t_0, and k = rate of convergence of the water table elevation toward z_{fs}. The constant k is adjusted according to the hydraulic conductivity of the bank material, and thus represents the rapidity by which water table adapts to a change in flow stage. Two k-values are required: one for the rising flow stage, and one for the falling stage.

4.2.3. Numerical setup

4.2.3.1. Simulated flows

The largest flow discharge to be recorded at each site during the observation period was selected for subsequent numerical simulations. A verification was made to ensure that the selected flow discharges were indeed associated with bank retreat. Although flood hydrographs vary in magnitude, duration and shape in nature, simple single-peak hydrological events were used in numerical simulations to limit the level of complexity as morphodynamic modelling results are known to be affected by a large number of variables Rousseau et al. (2016). The duration of simulations was substantially reduced, relative to the duration of natural events being simulated, to limit simulation times.

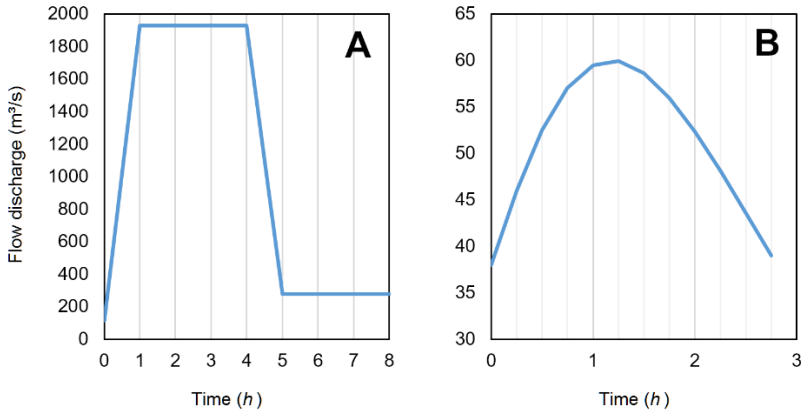

Figure 4.3. Hydrographs imposed to the coupled models during numerical simulations These correspond to **a)** site SF and **b)** site MC.

The numerical simulations analyzed in this study did not use the flood hydrographs recorded at the examined field sites due to the extended period of time over which observations took place (two and three years, respectively for sites SF and MC). A flood with a peak discharge of 1928 m^3/s, recorded on the St. François River at Hemming-Falls gauging station (ID 02OF002; Water Office, Environment Canada), occurred between 24 September and 15 October 2010. It corresponds to a return period of ~22 years. The single peak hydrograph was compressed in time to become an 8-h simulation in which peak discharge is reached between t = 1 h and t = 4 h (Figure 4.3). The 3-h peak discharge is essential owing to the substantial amount of time required for a new hydrodynamic equilibrium to be reached following a change in imposed flow discharge (travel time from inlet to outlet is large due to the long channel combined with low average velocity) (Table 4.2). For Medway Creek, the shape of the hydrograph is approximated using a γ function. Peak discharge is 60 m^3/s, i.e., similar to the maximum value recorded during the observation period (66.2 m^3/s on 12 March 2013), and event duration is 2.75 h (Figure 4.3). The selected discharge corresponds to a return period of ~2.5 years.

4.2.3.2. Mesh generation

The geotechnical module requires a large number of mesh nodes near river banks to allow for sediments eroded from the bank to deposit following a mass wasting event and correctly distinguish pre- and post-failure bank morphologies (Rousseau et al. 2017). Mesh resolution is slightly reduced in the areas that are unlikely to be affected by mass wasting, i.e., near channel center, and away from river banks on the floodplain (Table 4.3). Varying node density allows to minimize the total number of mesh nodes, and thus simulation time; this is essential to perform calibration on a complex model as it often requires to run large numbers of numerical simulations. Therefore, a triangular mesh

structure was built using the software BlueKenue (CHC 2011). The software creates nodes using a dynamic moving front algorithm, connects them using unconstrained Delaunay triangulation, and smoothens the mesh with a Laplacian algorithm.

For MC, elevation values from the DEM were assigned to a mesh structure that includes very small triangular elements (0.22 m^2) along unstable steep banks, small elements (0.87 m^2) along channel centerline, medium-size elements (2.16 m^2) in the riparian zone, and large ones (up to 10.83 m^2) away from the channel on the floodplain. The same strategy was adopted for SF, with the exception that a greater variety of element sizes was used to ensure smooth transitions between small elements along river banks (1 m^2) and larger ones near channel center (25 m^2) and on floodplain (100 m^2).

Table 4.2. Hydraulics conditions at each site during the simulated floods

Site	*t*	*B*	*H*	*V*	*Q*	*Fr*	S_0 (%)	τ_0
SF	0.00	224.77	1.69	0.31	116	0.08	0.003	0.50
	4.00	579.14	3.43	0.97	1928	0.17	0.039	13.12
	8.00	357.43	2.14	0.36	277	0.08	0.013	2.72
MC	0.00	17.70	0.61	0.60	38	0.25	0.274	16.39
	1.25	35.11	1.16	1.04	60	0.31	0.270	30.72
	2.75	30.62	1.07	0.99	39	0.31	0.274	28.76

Legend: t = simulation time (h), B = channel width (m), H = flow depth (m), V = flow velocity (m/s), Q = flow discharge (m^3/s), $Fr = V / (g\ H)^{0.5}$, Froude number, S_0 = longitudinal slope of free surface (%), and $\tau_0 = \rho\ g\ R\ S$ = bed shear stress (N/m^2) (ρ is mass density of water, g is gravitational acceleration and R is hydraulic radius). For site SF, H and V are the average flow depth and velocity values for all points with $H > 0.01$ m, and $B = Q / (H\ V)$.

4.2.3.3. Calibration and boundary conditions

Flow

Calibrating the model requires free surface elevation data at the inlet and outlet of the simulation domain. The method employed to measure free surface elevation values varied between field sites, as explained below. Following this, numerous hydraulic-only simulations were run with varying bed roughness values to adjust the energy slope so that it matched field measurements (Vidal et al. 2007).

For SF, the calibration procedure was based on the analysis of high-resolution aerial photographs and hydrometric data. Flow width at the inlet was measured using an aerial photograph and was associated with the flow discharge recorded by the upstream Hemming-Falls gauging station (ID 02OF002) on the day the photograph was taken (Q = 791.6 m^3/s on 18 March 2016). A theoretical Manning's n bed roughness value of 0.0352 was calculated from flow conditions and cross-section

geometry, which allowed to build a stage-discharge rating curve and impose an unsteady flow discharge and level at the inlet. Near the outlet of the simulation domain, free surface elevation is markedly affected by the level of the St. Lawrence River. Historical hydrometric data (Q = 174.6 m^3/s) from the Sorel gauging station (ID 02OJ022), located ~20 km upstream along the St. Lawrence River, combined with a second aerial photograph taken on 14 August 2009, was used to estimate free surface elevation (based on flow width) at the outlet of the simulation domain during the event that occurred on 24 September 2009.

For MC, flow measurements (depth and velocity) were taken along the inlet and outlet cross sections of the study reach at low flow discharge (1.15 m^3/s). A Manning bed roughness coefficient of n = 0.0153 produced an energy slope matching field conditions. This roughness value, combined with known cross-section morphology, were used to estimate water surface elevation at the outlet for larger discharge values. The anticipated difference in free surface elevation between low discharge (1.15 m^3/s) and simulated peak flow discharge (60 m^3/s) was 1.58 m. It compares well with the difference of 1.48 m recorded at a gauging station located 1.1 km downstream (ID 02GD008); considering the large longitudinal bed slope in this reach (4.17 m over 1.5 km).

The selected bed roughness values contrast with those obtained from a qualitative approach (e.g., Arcement and Schneider 1989). For instance, Manning's n bed roughness coefficient at site SF is expected to be ~0.032. The model may require a slightly higher value due to the flow resistance created by the St. Lawrence River, located at the downstream end of the SF river. In the case of MC, the roughness value estimated using the methodology described in (Arcement and Schneider 1989). is ~0.043. Determining bed roughness during calibration is based on the best adjustment with measured water levels. Differences between this numerical approach and qualitative estimations are therefore expected.

Table 4.3. Simulation meshes

Site	*Element area (m^2)*				*Nodes*	*Elements*	*Area (km^2)*	*Time step (s)*
	Channel	*Bank*	*Bank top*	*Floodplain*				
SF	10.83–4.33	1.08	4.33	21.65–43.30	158,097	315,915	12.42	0.5
MC	0.86	0.16	5.00	25.00	107,761	215,284	0.43	0.1

Geotechnical analysis

The geotechnical calibration procedure comprised two steps and was applied to each one of the fluvial environments examined. The first step consisted in running a series of bank stability evaluations, assuming a straight bank profile (Figure 4.2c), to explore the model behaviour for a range of river bank dimensions (height and angle) and hydrological conditions (free surface and water table elevations) that can be encountered at the two field sites (row 'General' under 'Tree classification' in Table 4.4). The same procedure was followed with mass density (ρ) and friction angle (ϕ) parameter values set to known values for these sites (rows 'SF' and 'MC' under 'Tree classification' in Table 4.4). This calibration, which is using a simple bank geometry, served in the identification of key geotechnical parameters, in the estimation of threshold parameter values leading to a safety factor near unity, and in creating a statistical model representing geotechnical processes for the two environments examined. The procedure is performed using machine learning algorithms, namely random forest (Breiman et al. 2015) and tree classification (Therneau et al. 2015)

Table 4.4. Parameter values employed during calibration

Site	α	h	h_{FS} & h_{WT}	c	ρ	ϕ	*Soil compaction*
Geotechnical stability model (without bank retreat)							
General	10, 20, 30, 40, 50, 60, 70, 80	1, 2, 3, 4, 5, 7.5, 10, 12.5	0.25, 0.50, 0.75	0, 0.00025, 0.0005, 0.001, 0.0025, 0.005, 0.01, 0.025, 0.05, 0.1, 0.25, 0.5, 1 2.5, 5	1550, 1750, 2000, 2250, 2500	10,20, 30,40	0, 0.5, 1
SF	20, 30, 40, 50, 60, 70, 80	1, 2, 3, 4, 5, 7.5, 10, 12.5	0.25, 0.50, 0.75	0.01, 0.025, 0.050, 0.100, 0.250, 0.5, 1, 2.5, 5	1950	9.2	0, 0.5, 1
MC	40, 50, 60, 70, 80				2100	40	
Coupled model (with bank retreat)							
SF	N.A.	N.A.	N.A.	0.125, 0.250, 0.375, 0.5, 1, 2.5, 5	1950	5, 10, 15, 20, 25	0.75
MC					2100	25, 30, 35, 40, 45	

Legend: α = bank angle (°), h = bank height (m), h_{FS} and h_{WT} are proportions of h, respectively for free surface and water table elevations, c = cohesion (kPa), ρ = soil mass density (kg/m^3), ϕ = friction angle (°) of bank material, soil compaction is minimal at 0 and maximum at 1. N.A. = Non-applicable.

(see Section 4.2.5). Here, random forest is employed to quantify variable importance. The binary tree-like structure resulting from tree classification is organized such that a splitting criterion (at any given node, based on the values associated with a variable with respect to the optimal threshold value) separates the data from its leaves and splits it into two sets, maximizing the increase in homogeneity from the node to its children. Here, the homogeneity of bank profiles with respect to safety factors is quantified using the Gini index. In addition to revealing divides and threshold values, a classification tree provides the frequency of occurrence of each leaf. In a second step, a three-dimensional calibration was performed using combinations of the two most influential parameters identified in the first step, i.e., soil cohesion, c, and friction angle, ϕ (Table 4.5). Additional simulations were run while varying soil density ρ to verify if this could result in improved fit.

This calibration strategy was selected to restrain the number of simulations to run with the coupled model. It is acknowledged that testing a larger number of combinations of parameters values would likely lead to a better fit with experimental data, but it would also be very time consuming in a context where each simulation takes several days to run (e.g., over 5 days for most the simulations presented here). In addition, this paper does not seek to accurately replicate the location and extent of bank failures, but rather to evaluate whether two contrasting fluvial environments are affected similarly by key biophysical conditions. This is why the model was calibrated without being validated. The calibration process therefore had a single purpose: demonstrate that parameters can be adjusted to fit observations.

4.2.4. Bank retreat and fitness

Transects placed at a regular interval longitudinally along each reach (at each 100.0 m and 3.2 m, respectively for sites SF and MC) were employed to classify bank locations in terms of stability;

Table 4.5. Parameter sets and values

c	ϕ					
	5	10	20	30	35	40
	ρ = 1950			ρ = 2100		
0.125	SF_{01}	SF_{02}	SF_{03}	MC_{01}	MC_{02}	MC_{03}
0.250	SF_{04}	SF_{05}	SF_{06}	MC_{04}	MC_{05}	MC_{06}
0.375	SF_{07}	SF_{08}	SF_{08}	MC_{07}	MC_{08}	MC_{08}
0.500	SF_{10}	SF_{11}	SF_{12}	MC_{10}	MC_{11}	MC_{12}

Legend: c = cohesion (kPa), ϕ = friction angle (º) of bank material, and ρ = soil mass density (kg/m^3). Subscript correspond to identifiers of parameter sets for sites SF and MC.

the categories employed were: stable, eroded by fluvial processes, eroded by geotechnical processes, and eroded by a combination of fluvial and geotechnical processes. For SF, the anthropogenically-protected river banks that did not undergo any change were excluded from the analysis.

This study does not seek to replicate the bank retreat rates observed along sites MC and SF but to identify the location of retreating river banks. The model is said to be successful, or to agree with an observation of river bank failure, if it predicts a retreat distance larger than a threshold value at a given transect. The selected threshold distances were set to 0.1 m for MC (0.5% of channel width) and to 5.0 m for SF (3.3% of channel width). River banks that have undergone a shorter retreat were considered stable. Note that the threshold value for SF corresponds to the actual average long-term retreat rate (see Section 2.1). For MC, in the absence of long-term historical data, the threshold value was selected because it maximizes the overall fit between observed and simulated retreat distances.

The fitness of a parameter set (all locations combined along the studied reach) with respect to bank retreat is quantified using confusion matrices and an alteration of Youden's (1950) *J* index:

$$J = SN \quad \text{(if only failures are predicted)} \tag{4.4a}$$

$$J = SP - 1 \quad \text{(if no failure is predicted)} \tag{4.4b}$$

$$J = SN + SP - 1 \quad \text{(otherwise)} \tag{4.4c}$$

$$SN = TP \,/\, (TP + FN) \tag{4.5}$$

$$SP = TN \,/\, (TN + FP) \tag{4.6}$$

where SN = sensitivity, SP = specificity, TP = number of true positive, TN = number of true negatives, FP = number of false positives, and FN = number of false negatives. Positive refers to the occurrence of a bank failure, whereas a negative refers to the lack of a failure. This rating method provides a constant range of indices, between 1.0 (correct prediction for every transect) and -1.0 (wrong prediction for every transect), which facilitates the comparison of fitness amongst sites and parameter sets. For the purpose of facilitating the interpretation of results, *TP* and *TN* were combined to indicate an agreement (or fit); the same was done with *FP* and *FN* to indicate a disagreement.

In the context of the present study, the overall similarity between observed and simulated retreat rates, all transects combined, is referred to as model fitness or agreement. The term accuracy could have been used if independent calibration and validation sets had been used as part of the modelling procedure. This is not the case here: the modelling experiment consisted in calibrating two models, one at each site, to determine the circumstances under which banks are unstable and

describe differences in the influence of biophysical parameters between the models. The lack of a validation dataset implies that the models were not used to perform predictions. Therefore, the terminology employed reflects this situation. However, the metric employed here, Youden's *J* index is compatible with both fitness or accuracy assessment.

4.2.5. Sensitivity analysis using tree classification

Tree classification was performed (within the software R (The R Foundation 2018) v4.1 and with the package rPart (Therneau et al. 2015)) to build a visual representation of the combinations of parameter values (e.g., cohesion, compaction, heights of bank, friction angles) leading to similar safety factors, to identify key geotechnical variables, and to quantify the importance of each parameter. The set of rules behind a tree constitutes a statistical model. A simple straight slope with uniform bank material and spatial scales similar to the ones considered in this study was considered for this purpose (Figure 4.2c). A first tree was built by analyzing river bank stability for the geotechnical and geometric properties encountered at the two field sites combined. Two additional trees were built (i.e., one for SF and one for MC) while imposing measured site-specific biophysical conditions. Here, each parameter set is narrowed down to the range of morphological and geotechnical conditions present at the associated field site. Therefore, the values of variables ϕ and ρ were set to those measured on site, and thus, were kept constant.

The calibration strategy based on tree classification was selected to restrain the number of simulations to run with the coupled model. It is acknowledged that testing a larger number of combinations of parameters values would likely lead to a better fit with experimental data, but it would also be very time consuming in a context where each simulation takes several days to run (e.g., over five days for most the simulations presented here). In addition, this paper does not seek to accurately replicate the location and extent of bank failures, but rather to evaluate whether two contrasting fluvial environments are affected similarly by key biophysical conditions. This is why the model was calibrated without being validated. The calibration process therefore had a single purpose: demonstrate that parameters can be adjusted to fit observations.

4.3. Results

The presentation of results is done in three steps. In Section 4.3.1, the decision trees representing bank stability at both field sites are described, which allows to see the emergence of key parameters. Note that these trees were built (see Section 4.2.5) by considering a large number of combinations of bank geometries and biophysical conditions (Figure 4.2c), and running the geotechnical stability

model (without bank retreat) to evaluate the stability of each combination. In Section 4.3.2, decision trees are used to evaluate bank stability along transects, each of which is represented by a simplified geometry (Figure 4.2c). In Section 4.3.3, numerical simulations are run within the coupled hydraulic-sediment-geotechnical model (with bank retreat) for twelve combinations of parameter set values.

4.3.1. Identification of key geotechnical parameters

The trees built using the rPart package algorithm were simplified to keep only one instance per sequence, along with its frequency. Looking at the general tree (SF and MC sites combined), the most frequent sequence is c-ϕ-α-h, which includes 33% of stability assessments in this sample (Figure 4.4). The other frequent sequences are c-ϕ-ρ (23%), c-ϕ-α (17%) and c-ϕ-α-ρ (16%). Note that c-ϕ is present in 94% of sequences, whereas h_{FS} only influences the safety factor for 3% of the sample. Similarly, *soil compaction* and h_{WT} are not present in any sequence. Overall, the most important variables are h, α, c and ϕ (column 'General' in Table 4.6). Therefore, given that h and α are imposed by bank geometry at the field sites, and that h_{FS} and h_{WT} depend on flow conditions, c and ϕ are the geotechnical parameters that the model is most sensitive to.

Site-specific classification trees (Figure 4.5) are subsets of the 'general' tree that is summarized in Figure 4.4. In addition, all variable sequences, with the exception of c-α-h-h_{FS}, are present in both classification trees, and are arranged identically. Similarly, the relative importance of the variables is

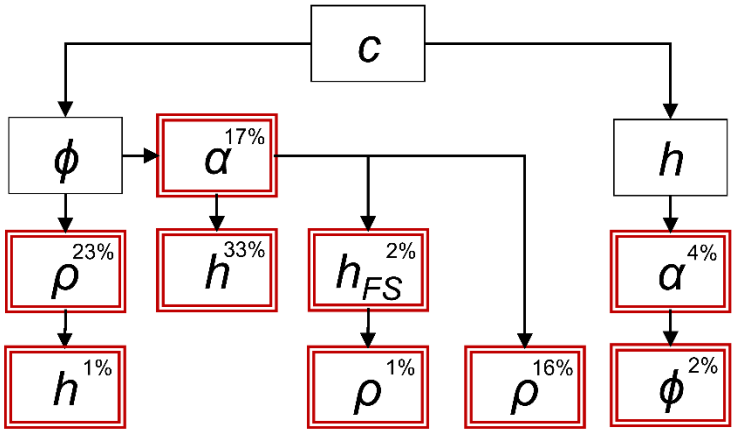

Figure 4.4. Simplified tree classifications considering all parameter combinations

This shows all decision paths leading to a similar safety factor. Each rectangle is associated with a decision along a path. Each red rectangle is a terminal node along a decision path. Percentages indicate the occurrence of the path within the dataset.

similar between sites (columns SF and MC in Table 4.6). However, the frequency of sequences differs slightly. For instance, there are fewer instances of the *c*-*α*-*h* sequence with site SF, which is compensated by a greater number of *c*-*α*-h_{FS} and *c*-*h*-*α*. Therefore, h_{FS} appears to have a greater control on bank stability at the SF site, and *h* is less influential, relative to the other parameters.

This calibration, which is based on parameter values related to geotechnical processes, suggests that bank retreat patterns along two contrasted river channels are expected to be similar. However, it is not clear whether this similarity will remain when taking into account sediment transport and complex channel bathymetries within morphodynamic simulations. This is tested in Section 4.3.3. But first, the achievable fit, based on tree classification, is examined with respect to each study site.

4.3.2. Evaluation of river bank stability based on tree classification

The rules behind the condensed decision trees presented in Figure 4.4 were used to evaluate the stability of river banks along St. François River and Medway Creek within the studied reaches, based on a simplified representation of bank morphology, i.e., according to bank height (*h*) and angle (*α*) only (Figure 4.2c). The calculations were performed on the observed geometries and bathymetries. This required to *a priori* extract *h* and *α* (Table 4.1) at each transect (Figure 4.6). The free surface

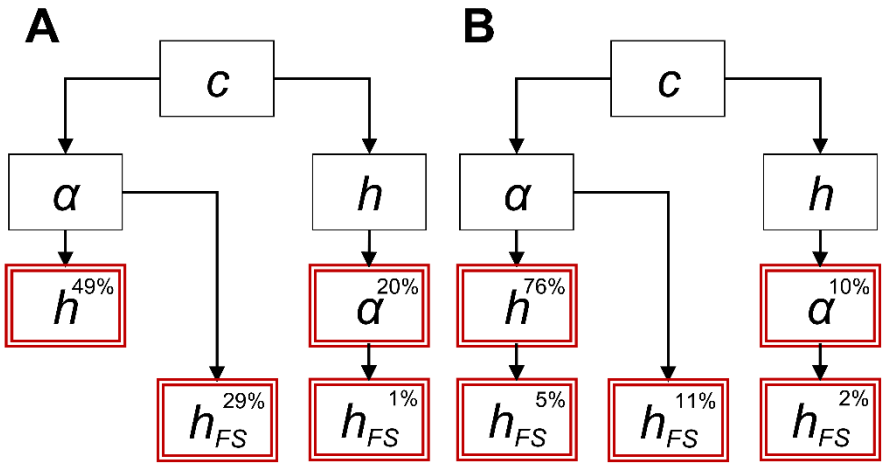

Figure 4.5. Simplified tree classifications considering a subset of parameter combinations

This shows decision paths using fixed values of density (ρ) and friction angle (ϕ) based on field data for **a)** MC, where ρ = 2100 kg/m^3 and ϕ = 40° and **b)** SF sites, where ρ = 1950 kg/m^3 and ϕ = 9.2°. Each rectangle is associated with a decision along a path, e.g., $c \leq 2.5$ kPa for the MC site. Each red rectangle is a terminal node along a decision path. Percentages indicate the occurrence of the path within the dataset. For instance, 76% of decision paths related to the MC site have the sequence *c*-*α*-*h*. Soil compaction was assumed to be equal to 0.75.

elevation (h_{FS}) values employed were those calculated by a hydraulic model (sediment transport and geotechnical processes disabled), whereas water table elevation (h_{WT}) was assumed to be equal to h_{FS}.

Table 4.6. Importance of parameters expressed as Gini indices

Parameters	*Site*		
	General	*SF*	*MC*
Morphological			
h	2806.9	103.0	93.9
α	1923.8	63.6	70.7
h_{FS}	216.1	9.1	6.9
h_{WT}	80.7	6.4	3.5
Geotechnical			
c	1899.5	154.6	115.8
ϕ	1552.6	-	-
ρ	182.4	-	-
compaction	84.4	9.0	3.5
Sample size	388,800	17,280	17,280

Parameters represents biophysical conditions and bank dimensions. The Gini index is the mean decrease in impurity, which measures how well the trees included in a forest split a dataset. A large index indicates great importance. Note that the indices (importance) can be compared between variables, but not between the different samples (i.e., General, MF and MC). Legend: α = bank angle (°), h = bank height (m), h_{FS} and h_{WT} are proportions of h, respectively for free surface and water table elevations, c = cohesion (kPa), ρ = soil mass density(kg/m^3), ϕ = friction angle (°) of bank material, k_{ASC} and k_{DESC} = water table adjustment rates with respect to free surface elevation, respectively for the rising and falling limbs of the hydrographs.

The best fit (with a Youden's J = 23.3%) is obtained with c = 1.0 kPa and ϕ = 10° at the SF site (Table 4.7). The fit drops to J = 19.0% with c = 0.5 kPa. The ϕ-value is compatible with the soil samples analysis performed by Tremblay (2012) (ϕ = 9.2°). For the MC site, the best agreement (J = 26.6%) occurs with c = 0.1 kPa and ϕ = 30°, when considering the whole reach. However, other combinations of parameters c and ϕ also result in a good agreement between simulated and observed failures, e.g., c = 1 kPa and ϕ = 20° (J = 21.9%), or c = 2.5 kPa and ϕ = 10° (J = 15.3%). The largest ϕ-value is compatible with the steep banks present at the field site and with the properties of highly cohesive soils. However, there are important differences in the level of agreement between sub-reaches **A**, **B**, **C** and **D** (Table 4.7). The best agreement (J = 47.0%) is obtained in sub-reach **B** (with c = 0.1 kPa and ϕ = 30°). The worst agreement is found in reach **A** (Youden's J = 0% with any c-ϕ combination) and is barely acceptable in sub-reach **C** (J = 8.3%) with c = 0.5 kPa and ϕ = 10°. In sub-reach **D**, the agreement is also poor, with the highest Youden's J (0.0%) with high friction angle (ϕ = 40° and

c = 0.1 kPa) or high cohesion (c = 2.5 kPa and ϕ = 20°) (Figure 4.7). Note that the parameter ρ did not influence fitness, although it affected the safety factor values along a few analysed transects.

Although the overall fitness is fairly similar between SF (23.3%) and MC (26.6%), the range of combinations resulting in the best agreement with field observations is narrower for SF ($0.5 \leq c \leq 1$ kPa and ϕ = 10°) than it is for MC (a few combinations within $0.1 \leq c \leq 2.5$ kPa and $10 \leq \phi \leq 30$° kPa).

4.3.3. Simulation of lateral erosion within the coupled model

4.3.3.1. St. François River

The strongest fit with observations of lateral erosion along the banks of the SF channel (J = 50.2%) is obtained with parameter set SF_{03} (Table 4.8), with a moderate friction angle (ϕ = 20°) and low cohesion (c = 0.125 kPa). This is similar to the soil texture at the field site (sand with ϕ = 9.2°). Most sets agree about the instability of the left meander bend downstream of the confluence (transects ~60–70 in box A_L of Figure 4.8). Good agreement is observed, to a limited extent, with respect to the

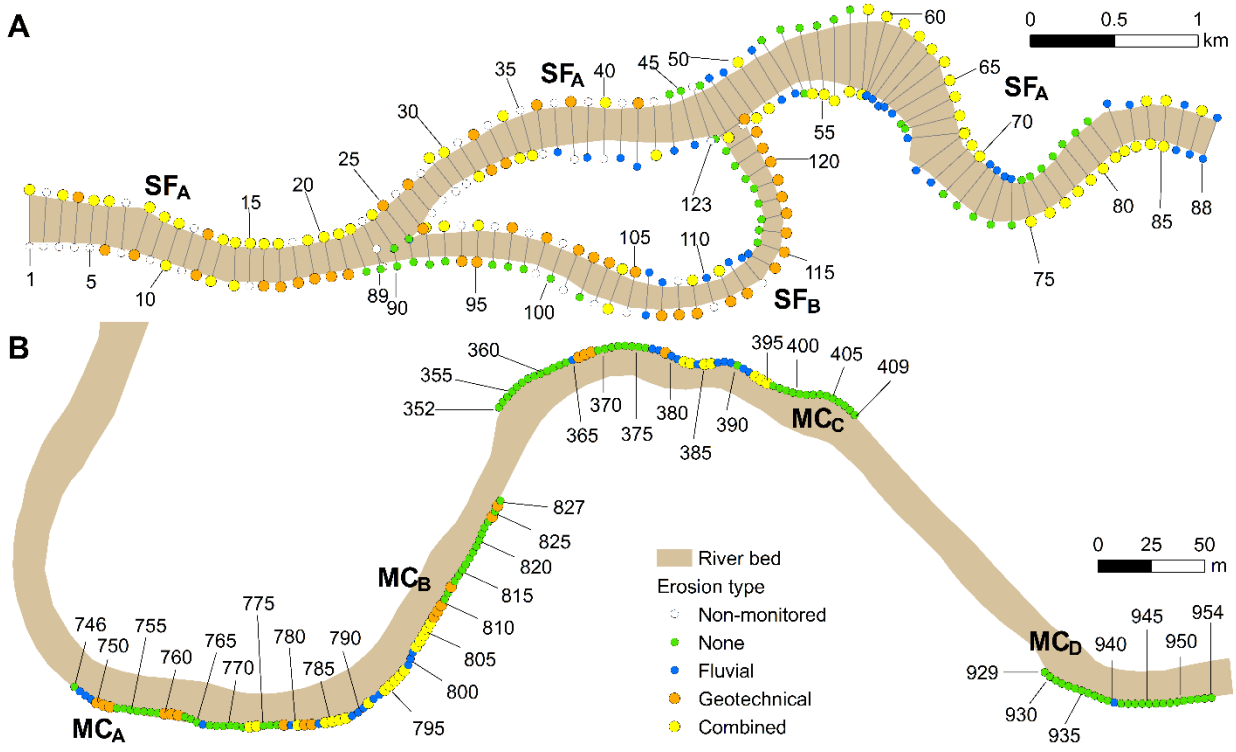

Figure 4.6. Observed bank erosion mechanism along river banks

This is shown for sites **a)** SF and **b)** MC. Numbers refer to transect identifiers. For SF, sub-reaches **A** and **B** include transects 1–88 and 89–123, respectively. MC includes sub-reaches **A** (transects 746–774), **B** (transects 775–827), **C** (transects 352–409) and **D** (transects 929–954).

instability of the second meander bend (transects ~75–80 in box A_R of Figure 4.8), despite a few false negatives at transects ~70–74. The agreement seems stronger along the internal and external river banks in acute bends (transects 29–42, 60–69, 75–83 and 107–123 in Figure 4.7a). However, the longitudinal extent of the unstable banks at these locations is greater than observed at the field site, e.g., see transects 57–58, 71–74 and 106. Finally, the most important discrepancy is found along the right bank near the bifurcation.

Table 4.7. Fitness of the geotechnical stability models (without bank retreat)

Site	*Sub-reach*	ϕ	*c*					
			0.10	0.25	0.50	1.00	2.50	5.00
SF		10	0.0	**15.1**	**19.0**	**23.3**	-2.3	0.0
		20	-2.3	-2.3	-2.3	0.0	0.0	0.0
		30–40	0.0	0.0	0.0	0.0	0.0	0.0
MC	A	10–40	0.0	0.0	0.0	0.0	0.0	0.0
	B	10	0.0	0.0	0.0	0.0	**34.6**	-12.0
		20	0.0	0.0	0.0	**35.2**	-0.1	-0.1
		30	**47.0**	-0.1	-0.1	0.0	0.0	0.0
		40	0.0	0.0	0.0	0.0	0.0	0.0
	C	10	0.0	0.0	**8.3**	0.4	**4.6**	0.0
		20	0.4	0.4	0.4	-21.3	0.0	0.0
		30	-8.8	0.0	0.0	0.0	0.0	0.0
		40	0.0	0.0	0.0	0.0	0.0	0.0
	D	10	0.0	-100.0	-96.2	-96.2	-92.3	**0.0**
		20	-96.2	-96.2	-96.2	-57.7	**0.0**	0.0
		30	-57.7	**0.0**	**0.0**	**0.0**	0.0	0.0
		40	**0.0**	0.0	0.0	0.0	0.0	0.0
	B, C, D	10	0.0	0.0	5.0	3.3	**15.3**	2.1
		20	3.3	3.3	3.3	**21.9**	1.7	1.7
		30	**27.5**	1.7	1.7	0.0	0.0	0.0
		40	0.0	0.0	0.0	0.0	0.0	0.0
	A, B, C, D	10	0.0	0.0	4.0	2.5	**19.6**	2.3
		20	9.9	9.9	9.9	**22.5**	1.6	1.6
		30	**26.6**	1.6	1.6	0.0	0.0	0.0
		40	0.0	0.0	0.0	0.0	0.0	0.0

Simplified bank geometries are assumed. Values are expressed in terms of Youden's *J* indices. Maximum values are identified in bold. A simple geometry (such as shown in Figure 4.2) is assumed with the dimensions provided in Table 4.1. The location of each sub-reach is shown in Figure 4.6. Legend: c = soil cohesion (kPa) and ϕ = friction angle (°) of soil material.

4.3.3.2. Medway Creek

The best overall fit, when combining sub-reaches **A**, **B**, **C** and **D**, are associated with lower cohesion (c = 0.125 kPa) and high friction angle (35° ≤ ϕ ≤ 40°) (Table 4.9). This is compatible with the steep-angled banks of the semi-alluvial MC that are weakened by cracks and bioturbation. Two combinations of the parameters c, ϕ and ρ also result in a good agreement between simulations and field observations, i.e., parameter sets MC_{02}, MC_{06} and MC_{11} (Table 4.5). The enhanced bank stability owing to a high cohesion (from MC_{06} to MC_{11}) is compensated by a decrease in ϕ to maintain the level of agreement. A similar observation can be made for set MC_{09} (Table 4.9); the level of agreement is maintained by decreasing ρ (from 2100 to 1900 kg/m^3) to compensate for a reduction in c (from 0.500 to 0.375 kPa). The model is very sensitive to the value of all three variables and selecting the parameter value c is particularly critical; with ϕ = 40°, any c-value ≥ 1 results in no mass failure. In addition, the agreement is stronger when ϕ = 35° is selected in combination with 0.125 ≤ c ≤ 0.5 kPa (MC_{11}); selecting a lower or higher ϕ-value adversely affect the fit. Finally, conversely to the

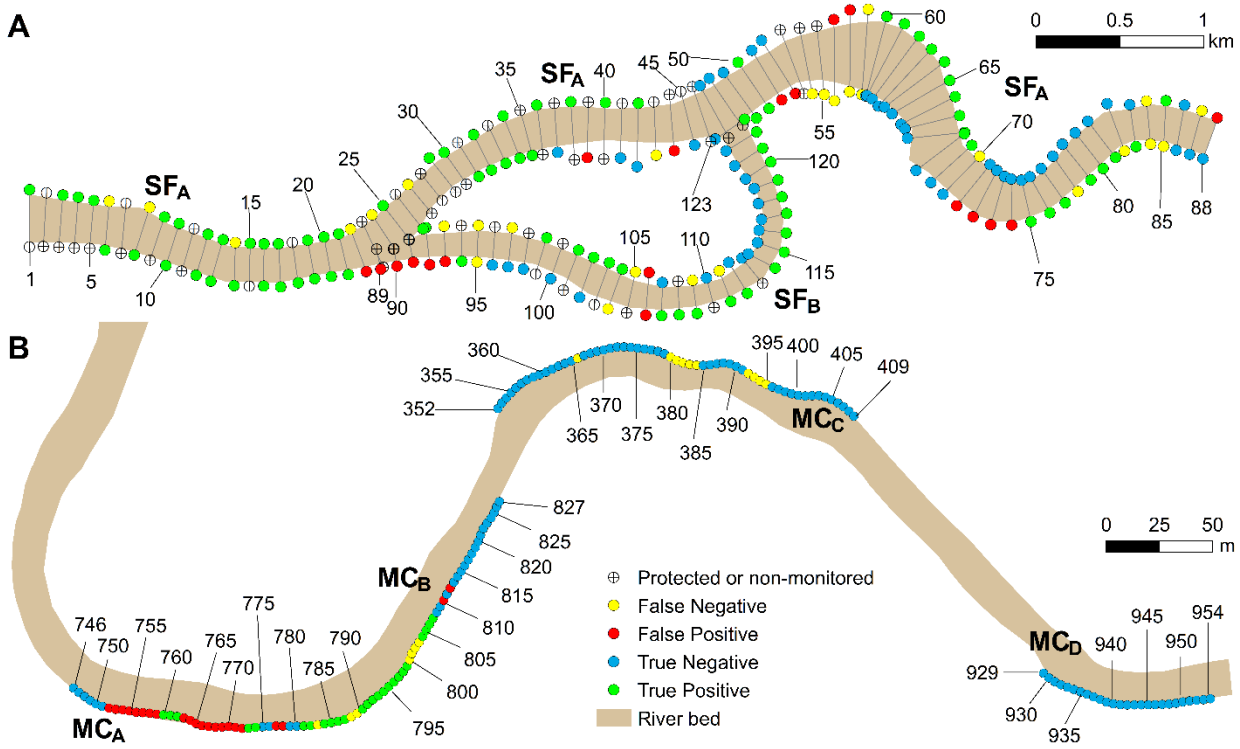

Figure 4.7. Simulated bank evolution along river banks

This shows he fitter parameter set at each site, i.e., **a)** parameter set SF_{04} (Tables 4.5, 4.8), and **b)** parameter set MC_{10}, MC_{05}, MC_{12} and extra set (c = 1 kPa; ϕ = 40°; ρ = 2100 kg/m^3) (Tables 4.5, 4.9), respectively for sub-reaches **A** (transects 746–774), **B** (transects 775–827), **C** (transects 352–409) and **D** (transects 929–954). Numbers refer to transect identifiers. Numbers refer to transect identifiers. For SF, sub-reaches **A** and **B** include transects 1–88 and 89–123, respectively.

observations made for site SF, the model is sensitive to variations in ρ; overall, Youden's index drops when increasing ρ.

Model's performance with respect to any given parameter set varies substantially with the sub-reach considered (Table 4.9). Looking at the overall fit hides disagreements within sub-reaches **A**, **C** and **D**. Indeed, the agreement is only good in sub-reach **B** (for all scenarios) and **A** (for MC_{07} and MC_{10}). For instance, parameter set MC_{05} (c = 0.25 kPa, ϕ = 35°) results in the best fit in sub-reach **B**, but is one of the worst parameter sets in sub-reach **D**. In the latter reach, the strongest agreements are obtained with $c \geq 1$ kPa and ϕ = 40°. Similarly, c ≥ 0.50, $\phi \geq 40°$ and $\rho \geq 2000$ kg/m^3 are required to maximize agreement in sub-reach **C**. This seems to indicate a spatial variation in geotechnical properties along the channel. This could be explained, at least partially, by the lack of consideration of the impact of vegetation and sedimentological layers in the model (see discussion section).

Sub-reach **A** differs from the other sub-reaches due to much higher banks (20 m, relative to 2–4 m elsewhere). The fit varies between J = -62.5% and +25.0% in this sub-reach (Table 4.8). The best agreements are obtained with ($0.125 \leq c \leq 0.375$ kPa, ϕ = 35°) and (c = 0.50 kPa, ϕ = 40°, ρ = 2000 kg/m^3). A slight increase in parameter value can substantially alter fit, e.g., increase in ϕ by only 5° between parameter sets MC_{02} and MC_{03}, which indicates that the model is very sensitive to geotechnical parameter values in this sub-reach. This variation could also be explained by the fact that the sum of *TP* and *TN* is very low (box A_R in Figure 4.9). In contrast, the range of fitness values is lower in sub-reaches **B** and **C**.

4.3.3.3. Sensitivity

The SF model is more sensitive to changes in ϕ than in c (Table 4.8). The standard deviation (σ) of mean (μ) Youden's J is 0.9% for c values, compared to 16.1% for ϕ values. The first value is obtained by calculating μ at each row, and calculating the standard deviation of the mean values. The second value is obtained by doing the same with columns. For site MC, σ is equal to 3.6% for

Table 4.8. Fitness of the calibrated coupled model (with bank retreat) for site SF

c	ϕ		
	5	10	20
0.125	7.1	30.9	**50.2**
0.250	15.5	31.3	48.2
0.375	15.9	30.4	44.9
0.500	16.8	35.7	40.0

Values are expressed in terms of Youden's J indices. Maximum value is identified in bold. Legend: c = cohesion (kPa), ϕ = friction angle (º) of bank material, and ρ = soil mass density (1950 kg/m^3).

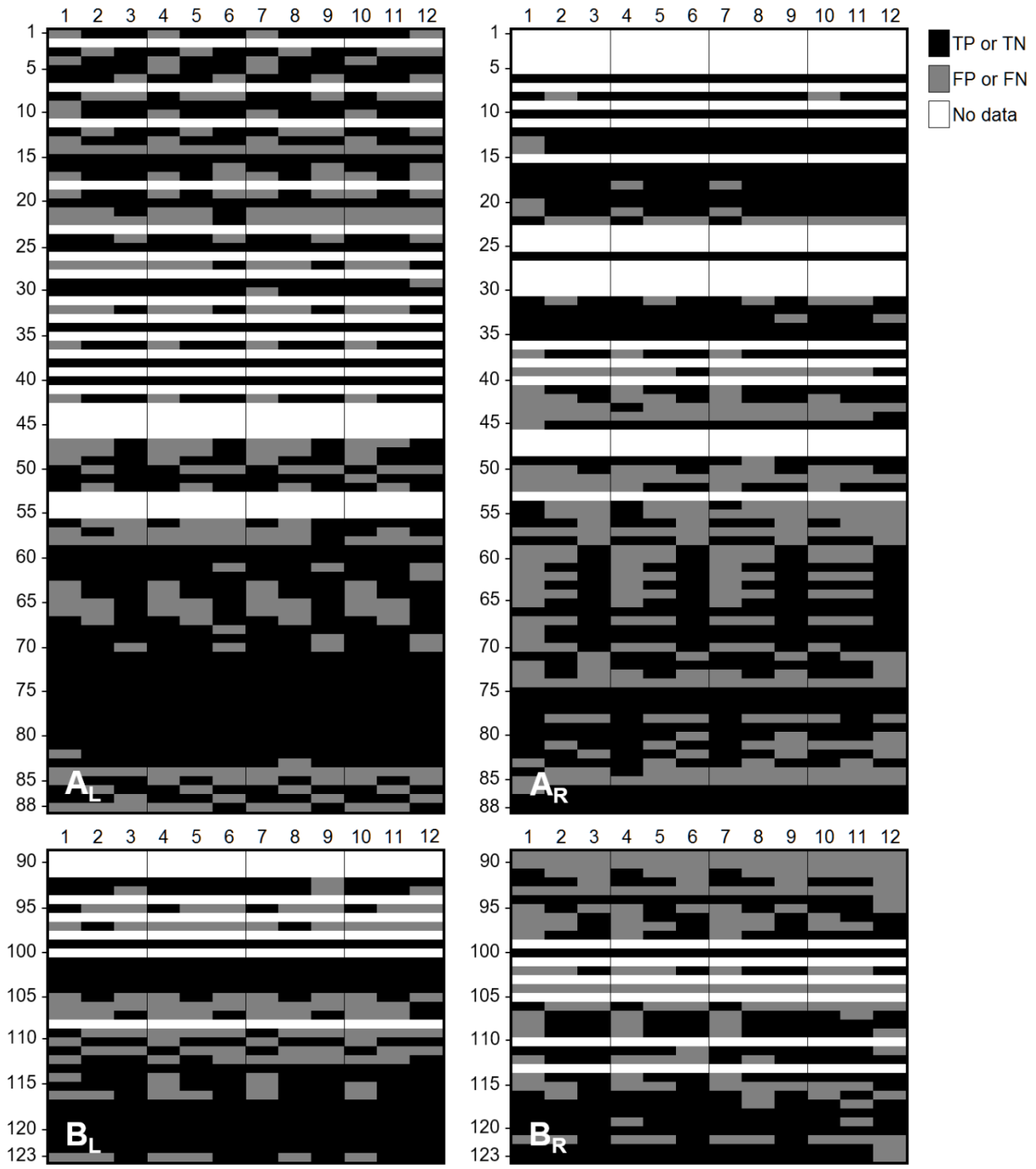

Figure 4.8. Agreement with observations for SF based on the confusion matrix

FN = false negative, FP = false positive, TN = true negative, and TP = true positive. Rows indicate channel transects (see Figure 4.6), columns indicate parameter sets (see Table 4.5). White rows correspond to unmonitored transects. The subscript corresponds to the river side (L = left; R = right).

Table 4.9. Fitness of the calibrated coupled model (with bank retreat) for site MC

Sub-reach	c	ϕ		
		30	35	40
A	0.125	-23.3	0.8	-59.2
	0.250	-15.0	0.8	-6.7
	0.375	20.8	0.8	-46.7
	0.500	**25.0**	-43.3	-62.5
B	0.125	27.4	39.0	39.6
	0.250	16.5	**58.7**	44.3
	0.375	16.7	24.8	33.2
	0.500	5.6	40.2	14.5
C	0.125	-32.1	-19.2	-10.4
	0.250	-23.3	-12.5	-6.3
	0.375	-19.2	-8.3	-4.2
	0.500	-10.8	-8.3	**0.0**
D	0.125	-69.2	-65.4	-38.5
	0.250	-73.1	-53.8	-34.6
	0.375	-61.5	-34.6	-30.8
	0.500	-42.3	-38.5	**-19.2**
B, C, D	0.125	11.3	21.9	28.4
	0.250	5.1	**30.1**	22.1
	0.375	8.4	19.5	16.0
	0.500	9.2	22.5	9.2
A, B, C, D	0.125	5.3	16.7	13.7
	0.250	0.7	**22.5**	14.7
	0.375	7.1	13.0	4.4
	0.500	8.1	9.8	-3.5

Values are expressed in terms of Youden's *J* indices. Maximum values are identified in bold.
Legend: c = cohesion (kPa), ϕ = friction angle (º) of bank material, ρ = soil mass density (2100 kg/m^3), and J = Youden's index. The location of each sub-reach is shown in Figure 4.6.

c values, compared to 5.4% for ϕ values, when considering all sub-reaches of site MC. The same trend is observed for individual sub-reaches **B**, **C** and **D**. However, sensitivity to ϕ is more important, with σ being equal to 11.2% for c values, compared to 23.7% for ϕ values.

4.3.4. Geotechnical stability model versus coupled model

A better agreement is obtained for SF with the coupled model (J = 50.2%; Table 4.8) than with the geotechnical stability model (J = 23.3%; Table 4.7). The optimal parameter values are also slightly different with ϕ = 10° and c = 1.0 kPa for the geotechnical stability model (Table 4.7), relative to ϕ = 20° and c = 0.125 kPa for the coupled model (Table 4.9). For MC, the best fits are similar with respect

to Youden's index and optimal parameter values between the two model types. The indices are J = 26.6% without bank retreat (Table 4.7) and J = 22.5% with bank retreat (Table 4.8). The optimal parameters are ϕ = 30° and c = 0.1 kPa for the model strictly evaluating bank stability compared to ϕ = 35° and c = 0.25 kPa for the bank retreat model. However, the fit is relatively poor in sub-reach **A** with the geotechnical stability model for all values of ϕ and c *(J = 0.0%; Table 4.7)*, which is less the case with the coupled model (maximum J = 25.0%; Table 4.8), although most indices are negative. However, the fit is stronger with the geotechnical stability model in sub-reach **C** (maximum J = 8.3% compared to 0.0%).

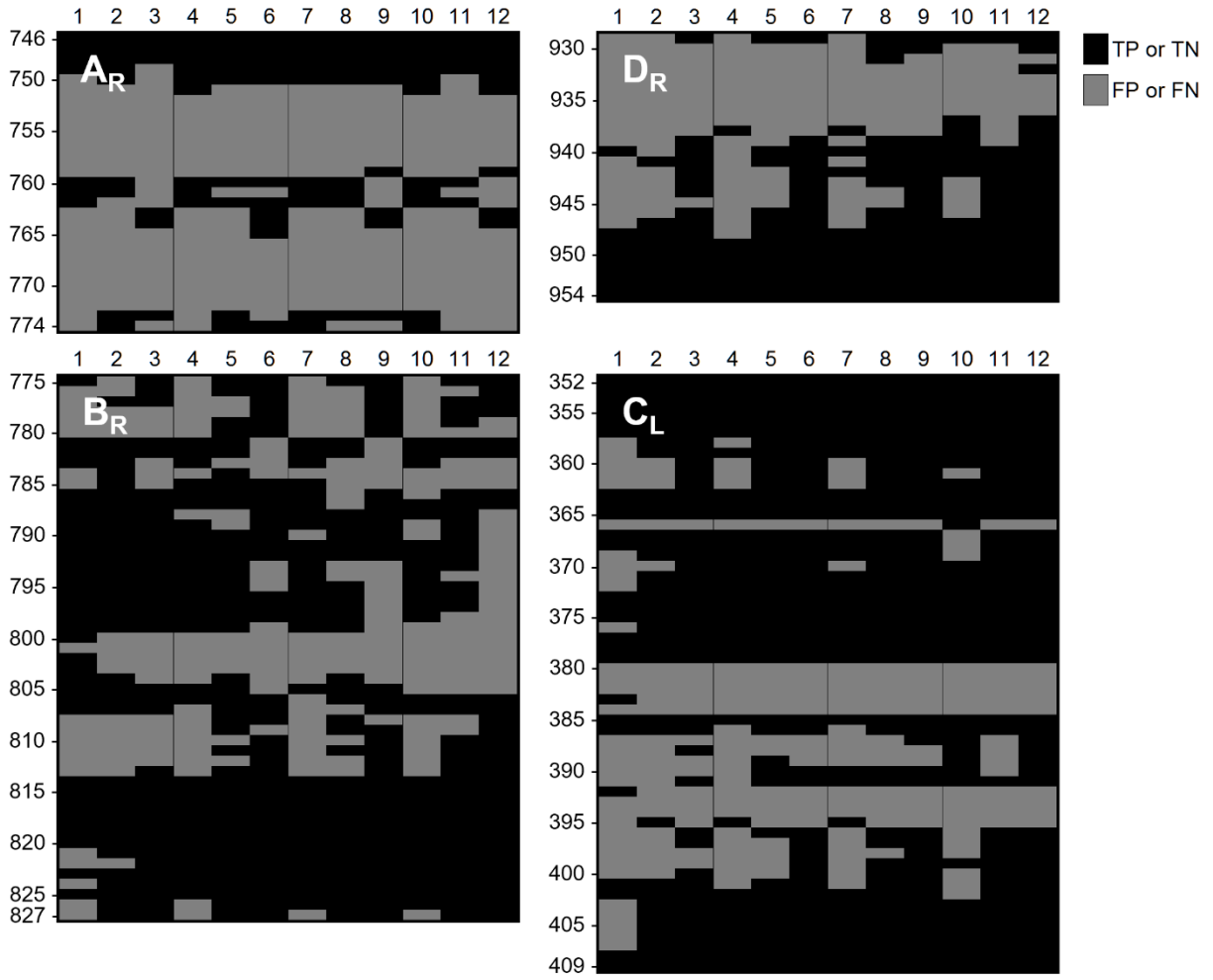

Figure 4.9. Agreement with observations for MC based on the confusion matrix

FN = false negative, FP = false positive, TN = true negative, and TP = true positive. Rows indicate channel transects (see Figure 4.6), columns indicate parameter sets (see Table 4.5). The subscript corresponds to the river side (L = left; R = right).

4.4. Discussion

The two conceptual novelties of this study are the identification of a set of biophysical conditions that fit observations of bank retreat for two different natural river channels, and a comparison of simulated bank retreat between two natural river channels of different scales and geomorphological contexts.

The fact that the biophysical parameter values producing the best fit between observed and simulated bank retreat at site MC varies between sub-reaches suggests a variation in bank material composition over a relatively short distance. Indeed, each sub-reach at MC exhibits distinctive texture and layering (Figure 4.10). In sub-reach **B**, a sandy layer overlays glacial till, which also forms the channel bed. In sub-reach **D**, sediments are more thoroughly mixed vertically. Conversely, the analysis of two soil columns by Tremblay (2012) revealed a vertical profile consisting primarily of sand, but separated by a few silty sand, sandy silt and silt layers. The greater uniformity of bank material in the latter case may explain that a stronger fit was obtained for SF (J = 50.2 in Table 4.9) than for MC (J = 22.5 in Table 4.8). Note that the presence of sedimentary strata was not considered in the model. The cohesion values that maximize model fit with river bank evolution at study sites are at least one order of magnitude lower than those commonly encountered in nature despite the fact that the model's ability to quantify stability was *a priori* tested against known problems of translational and rotational failures. For instance, Tremblay (2012) measured a cohesion of 13 kPa at the toe of a bank at SF (for a silty sample), which is ~100 times larger than the value associated with the parameter set that produced the best fit (Table 4.9). This seems to indicate that the model, even if it is physics-based, does not take into account a number of aspects of natural river banks that contribute to bank failures. The analysis of relatively homogeneous soil samples free of tension cracks in a laboratory may overestimate the overall strength of bank material found in nature. Finally, the fact that the observed lateral retreat corresponds to a timescale (2 and 3 years, respectively for SF and MC) much larger than the simulation time (8 and 2.75 h, respectively for SF and MC) may explain why a reduced cohesion value is required for the simulation outcome to fit observations.

A marked difference in the cohesion value that maximizes fit was noted between MC sub-reaches (Tables 4.7–4.8). This may, at least partially, be attributed to the mechanical effects of the plant cover, which are lumped into the soil cohesion parameter. The model did not introduce spatial variations in soil characteristics; cohesion was identical at all nodes but varied between simulations. In natural rivers, the vertical variation in root density is such that the apparent cohesion is greater in the upper soil layer for several species (Abernethy and Rutherfurd 2001; Pollen-Bankhead and

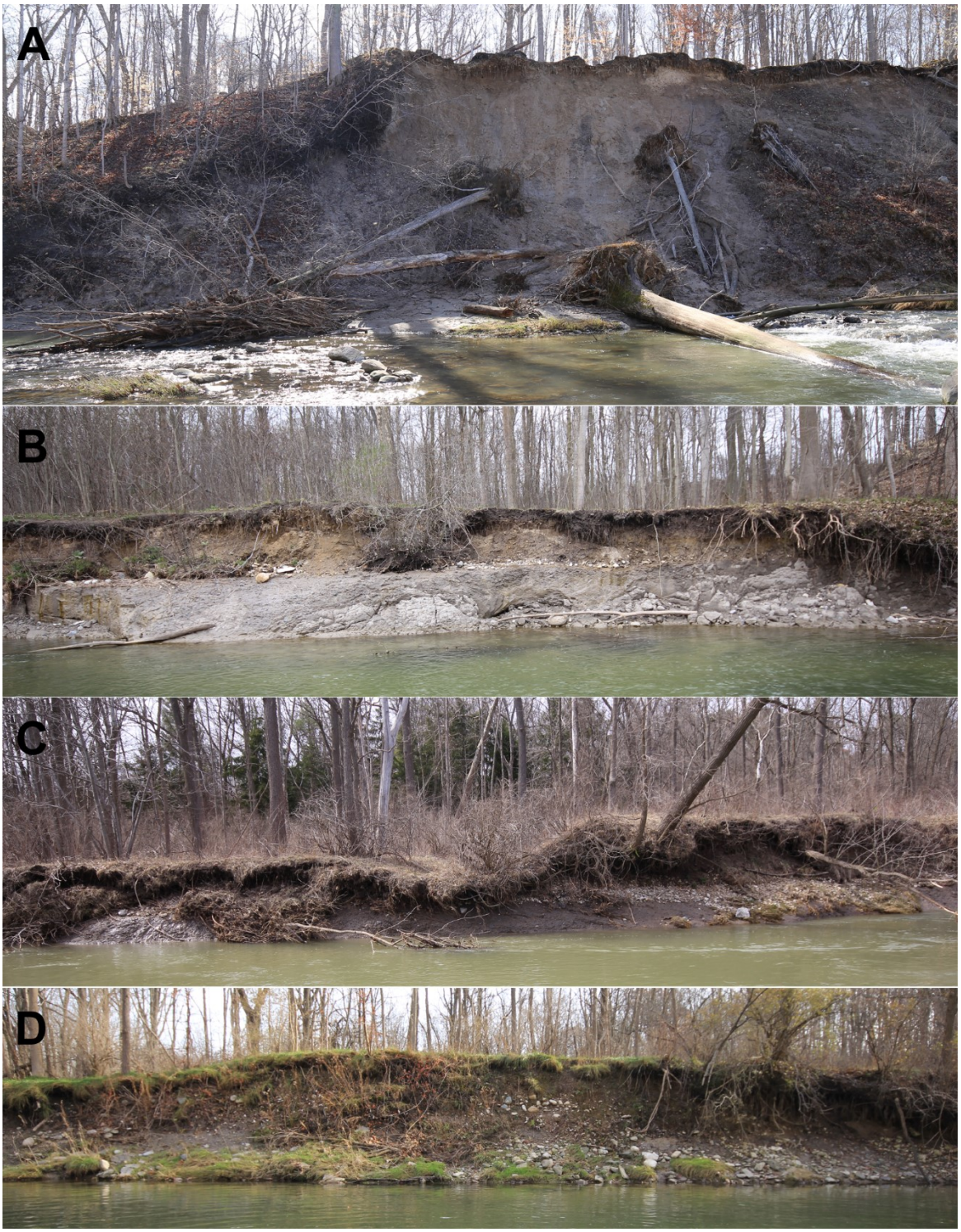

Figure 4.10. Photographs taken along Medway Creek banks

Sub-reaches **A** (transects ~782–760), **B** (transects ~792–786), **C** (transects ~380–388), and **D** (transects ~939–932) (Figure 4.6).

Simon 2009), whereas the distribution of plant species and assemblage introduces a horizontal variation in soil strength, even assuming homogeneous soil material (Simon and Collison 2002). The most unstable sub-reach at MC is **B**; it is densely vegetated but associated with the lowest cohesion value (Table 4.8). At this location, the removal of vegetation by floods, combined with the surcharge imposed by mature trees seem to have triggered bank retreat. Conversely, sub-reach **D** is associated with the highest cohesion and friction angle (Table 4.8), perhaps owing to a vegetation stand consisting of herbaceous plants and young trees (Figure 4.10d), offering enhanced cohesion for little surcharge. However, an exposed bank section (upstream of the location shown in Figure 4.10d) was very stable during the observation period. Therefore, riparian vegetation seems to have a greater effect on bank stability in sub-reach **B**, even if it is less than 500-m away from sub-reach **D**. Similarly, spatial variations in root reinforcement may be responsible for the large number of false positives obtained in sub-reach **A** of site MC (transects 752−772). This steep bluff is topped by mature trees that may prevent its collapse. Failures have been observed in this area (Figure 4.10), but they are usually limited in extent to the area around a tree trunk falling off the bluff. For this sub-reach, the parameter set associated with the strongest agreement indicates that soil is moderately cohesive (c = 0.5) in this sub-reach, compared to sub-reaches **B** and **D**.

A better fit with observations is obtained by associating a set of parameter values to each river bank segment or floodplain patch with homogeneous biophysical conditions (soil characteristics, vegetation assemblage, etc.). For instance, the best overall fitness climbs from J = 22.5% to 41.8% for MC when considering the best parameter set at each sub-reach (**A**, **B**, **C** and **D**). For SF, Youden's J only increases by 5.3% when varying parameter values spatially, which suggests more homogeneous soil characteristics at SF field site, relative to MC. The suggestion to integrate floodplain heterogeneity into planform evolution models (Güneralp et al. 2012) would not only serve in improving the fit between observations and simulation results but would make the model more independent of input parameter values; the parameter set would remain valid throughout a simulation. However, care is required to avoid overfitting a model, which would otherwise compromise its capacity to be validated against a second dataset. Here the possibility of overfitting comes from the fact that soil cohesion, despite the physics-basis of the model, still represents the combined effect of at least two components, namely soil and vegetation. This model characteristic would render the model less representative of the system with time if vegetation cover was to change. More work on complex river systems such as MC is needed to determine if, for practical purposes, a reduced complexity modelling approach would be more appropriate; it may not be

realistic to attempt gathering biophysical data at the level of details required to obtain an acceptable fit.

Downstream conditions also differ between the sites. Both the inlet and outlet of the MC site are directly related to flow discharge. However, although the free surface at the inlet of SF is also related to the imposed flow discharge, the second half of the reach depends on the level of the St. Lawrence River in which the SF river drains. The selected free surface elevation at the outlet of this domain corresponds to the elevation recorded at a gauging station during the simulated event. During the observation period, a large number of combinations of inlet-outlet free surfaces have been encountered, but a single one of these combinations is examined in this study. We acknowledge that the differences in imposed hydrographs and boundary conditions between sites SF and MC, arising from the differences in scale and location of the sites compared, may affect results. However, free surface elevation (h_{FS}) and water table elevation (h_{WT}) were found to be less influential than geotechnical parameters (Table 4.6). It is thus unlikely that selecting a different event would have led to significantly different results. In addition, a good fit was obtained with respect to bank retreat for site SF.

One of the most important limitations of the coupled model is that it assumes that water table adjusts solely as a function of variations in the free surface of the flow. By doing so, it neglects the fact that banks may be fully saturated. This situation may explain the presence of false negatives between transects 380–395 at site MC. The area north of sub-reach **C** is partially submerged during the spring due to snowmelt, and a pond drains to the river by the remnants of a meander bend that was abandoned prior to 1942 (entering the floodplain at transects 377–384 and exiting at transects 403–410 and beyond) (Figures 4.6, 4.10c). It is quite possible that the disagreement between simulated and observed failures in this area be attributed to the lack of a physics-based hydrological component that can be set up to consider realistic water table elevations across the floodplain. The presence of vegetation at the field site during failure events could have been detrimental when the soil was saturated, the mechanical effects of plants being outweighed by hydrological effects, as suggested by (Simon and Collison 2002). Therefore, the fact that soil moisture content did not vary longitudinally along the bank according to preferential groundwater flows in the coupled model may have contributed to overestimating bank stability.

Calibrating a morphodynamic model can be time consuming, and detailed field data on bank retreat are seldom available. The integration of a geotechnical module, combined with large uncertainty regarding the value of geotechnical parameters to be used for a field site, renders the

process more tedious as a larger number of trial simulations needs to be run to adjust model outcomes to observations. Here, a statistics-assisted calibration based on tree classification was completed to determine the range of parameter values leading to a safety factor near unity. Similar agreements were obtained with the geotechnical stability model (without bank retreat) and coupled model (with bank retreat) (see Section 4.3.4), which seem to indicate that initial channel bathymetry and biophysical conditions can be sufficient to estimate the location of bank retreat, without the need to consider hydrodynamics and sediment transport. However, caution is required as these two model types generated slightly different parameter values (see Section 4.3.4). This difference could be attributed to the lag effect between water table and free surface elevations and to the consideration of complex bank morphologies by the coupled model. In contrast, water table elevation is equal to the free surface elevation, and bank profile is always straight with the geotechnical model. The coupled model also allows for one or several subsequent failures to occur in different portions of the slope. A potential application of machine learning algorithms would be to allow the geotechnical module to recognize and use the rules emerging from a decision tree directly into a coupled model. This would substantially reduce computation time. The module would remain partially physics-based as the rules would have been pre-established using the geotechnical module.

4.5. Conclusion

This study sought to identify the most sensitive parameters in a morphodynamic model capable of taking into account mass wasting in a physics-based manner, and to verify whether the sensitivity to key geotechnical parameters differs between two contrasting fluvial environments. Our results indicate that lateral erosion is very sensitive to soil cohesion and friction angle, and to a lesser extent, to mass density of the bank material. A few combinations of these parameters resulted in a good agreement between simulation results and field observations, particularly in the alluvial St. François River case, where biophysical parameters of river banks and floodplain are more homogeneous. However, the agreement with field observations, and thus sensitivity, varies substantially from a parameter set to another, between sub-reaches, and between the two study sites. Sensitivity was also greater in some sub-reaches of the more complex semi-alluvial channel of Medway Creek.

The secondary objective was to devise a calibration method adapted to morphodynamic modelling that requires running as few simulations as possible. A pre-calibration phase, which used tree classification, and based on the assumption that the combined selected parameters values must bring the safety factor near unity, was used to estimate parameter values that are likely to result in an agreement with field observations. An iterative process was then used to run morphodynamic

simulations within the coupled model, each time slightly varying the value of key geotechnical parameters in order to explore model behaviour and to improve fit with observations.

The primary implication of the substantial degree of sensitivity found at both field sites is that morphodynamic models must account for spatial variations in geotechnical properties along a channel and must be reductionist enough to describe the complexity of the fluvial environment that they represent. For a highly complex semi-alluvial channel incised in glacial till such as Medway Creek, it may be unrealistic to achieve this level of reductionism, and a reduced-complexity modelling approach may be considered. For less complex alluvial systems such as the St. François River, the model employed in this study possesses these desirable characteristics, in particular, its physical base and ability to manipulate geotechnical variables to better represent bank material. In all cases, allowing to vary geotechnical properties across the floodplain should be the next step to improve morphodynamic models.

Liaison paragraph

A substantial proportion of the effort invested in this research went into the design and implementation of a novel modelling approach that can be used to fill knowledge gaps regarding lateral retreat mechanisms in alluvial and semi-alluvial river channels. The lack of a suitable model that could be used to address these gaps at the onset of this research triggered the development of a new modelling approach and software. The large amount of data required to configure the complex model developed raises questions about its usefulness and about the nature of the knowledge that can emerge from its use. The investigations described in this thesis consisted in calibrating models for three laboratory-size meandering channels and two natural river reaches. Yet, models are often used, or known to be relevant, to forecast the future state of a system. This narrow perspective only partially applies to the context of this research. The coupled model comprises five sub-models, i.e., the hydraulics, sediment transport, geotechnical, riparian vegetation and groundwater hydrology modules, each of which involves a distinctive modelling procedure and sub-system. Therefore, determining the usefulness of the modelling software employed in this research, or of any other similar software employed to examine fluvial processes, is not straightforward as it depends on the nature of the inquiry, on data availability for the site of interest, on spatiotemporal scales, and on the modelling procedure. The following chapter breaks down the modelling exercise into a sequence of distinct modes whose recognition can only contribute to the determination of model adequacy with respect to the examination of a given phenomenon. The modules forming the coupled model are used as examples to illustrate the epistemological framework developed; these are compared with equivalent algorithms that are present in similar fluvial and bank retreat models.

5

Predicting, explaining and exploring with computer simulations in fluvial geomorphology

Eric Desjardins, **Marco Van de Wiel** and **Yannick Rousseau**

Earth-Science Reviews (accepted pending revisions on 11 April 2018)

Abstract: This paper contributes to the epistemology and methodology of computer simulations, focussing especially on examples from geomorphology. The first part of our analysis presents a general framework within which to interpret and evaluate the adequacy of simulations models pursuing three epistemic purposes (or modes): prediction, explanation, and exploration. The second part of the paper applies this framework to a case in fluvial geomorphology. This application enables further specification of the three modeling modes and shows how they can work together in the inquiry of natural phenomena. Finally, our analysis looks briefly at the path-dependent nature of model building, which highlights the importance of historical contingencies in model development.

5.1. Introduction

Computer simulations have become an important tool in natural sciences over the last decades, especially in domains investigating complex phenomena that prove difficult to track and control in lab or field experiments. Hitherto, discussions about this type of modelling have approached a number of epistemological and methodological issues. These range from whether simulation modeling is as a special and distinct form of experimentation (Humphreys 1994, 2009; Lenhard 2007; Frigg and Reiss 2009), to questions of (partial) autonomy of simulation models from theory (Morgan and Morisson 1999; Winsberg 2010), to the contribution to scientific understanding by way of representing (Winsberg 2015), predicting (Oreskes et al. 1994; Parker 2010), explaining (Cartwright 1983; Bokulich 2011, 2013) and exploring (Lenhard 2007; Gelfert 2016), and, to name one more, how purposes should play a role in model evaluation (Parker 2011).

The following analysis contributes to this rich and growing literature on the epistemology and methodology of computer simulations by integrating the latter two subjects, i.e., the different ways in which simulation modeling contributes to scientific understanding and what are the criteria for model evaluation. Parker's (2011) pragmatic position about model evaluation offers a good entry point to explain the relation between understanding and evaluation. She says: "[i]t is the adequacy-for-purpose of a model that should be the target of model evaluation and testing: the question is not whether a scientific model is true … but whether it is adequate for the purposes for which it is to be used" (Parker 2011, 1). The first part of the following analysis provides a general conceptual framework within which to interpret three well-recognized epistemic purposes: prediction, explanation, and exploration. These purposes are interpreted as different modes of scientific understanding that need to be specified in the context of computer simulation. Although the literature on these general epistemic purposes is becoming increasingly rich, the different accounts do not always agree on definitions, and the delineation of some functions remains difficult and blurry at time. Our framework focuses on general procedural and inferential features of simulation modelling, which enables a specific and straightforward conceptual distinction between each mode as well as an elaboration of some of the basic adequacy criteria for each of them.

The second part of the paper applies the framework using an example from fluvial geomorphology. This application permits a more fine-grained explication of all three modes and at the same time exemplifies how they can work together in a series of model-based investigations of a natural phenomenon. The resulting discussion corroborates Bokulich's (2013) thesis that different (families of) models have different affordances, which can lead to a division of cognitive labour in

scientific inquiry. Our analysis focusses on the former aspect and demonstrates that, under the framework developed in the first section, a given model can realize different purposes with different degrees of adequacy. Finally, we look at the broader context of inquiry in the evaluation of computer simulations, emphasizing the role of historical dependencies between models, and how this phenomenon reinforces the adequacy-for-purpose thesis.

5.2. Three modes of simulation and their general adequacy conditions

Researchers relying on computer simulations to undertake a scientific investigation implicitly adopt one of three modelling modes (Table 5.1). These three modes have different inferential methodologies, and thus offer different opportunities and challenges in characterizing and studying target systems.

5.2.1. Predictive mode

In predictive modelling (Table 5.1a), the researcher seeks to ascertain the future state of one or several metrics of the target system (S) captured by the model. The researcher thus sets the external factors (E)[1], the initial state (S_0), the interacting set of processes (P), and formulates these in a computation model to predict the future state (S_t) of the relevant metrics. The adequacy of predictive modelling is determined through the predictive accuracy of the model, i.e., by the models' ability to accurately predict the relevant metrics for S_t within a reasonable degree of error. It is possible however that a prediction cannot be verified (if the target system is difficult of access or if the predictions are for a very distant future, or if the conditions S_0 or E never arose). Therefore, predictive adequacy is not always testable. However, to be predictively adequate, it is not necessary that the variables and processes implemented in the model capture the causal structure of the target system. A model that produces the right results for the wrong reasons can still be predictively adequate, as long as it can reliably inform the user about the future value of key metrics. Note also that the degree of predictive adequacy can vary. For instance, a model that has been calibrated and validated for a range of possible environmental conditions would tend to be a more adequate tool for predictions than a model which has only been calibrated and validated on a limited set of environmental

[1] The concept of "external" is linked to the studied system, but also to the way in which components are represented in the model. Fluvial models, for example, represent rivers as channels transporting water and sediment due to gravitational force, but impose factors such as water discharge and riparian vegetation. The integration of new algorithms in existing modelling packages can result in internalizing factors by extending the set of recognized processes and metrics.

conditions. This is discussed further in Section 5.2.2.

Table 5.1. Three modelling modes

A) Predictive	**B)** Explanatory	**C)** Exploratory
	i-	i-
	ii-	ii-
	iii-	iii-

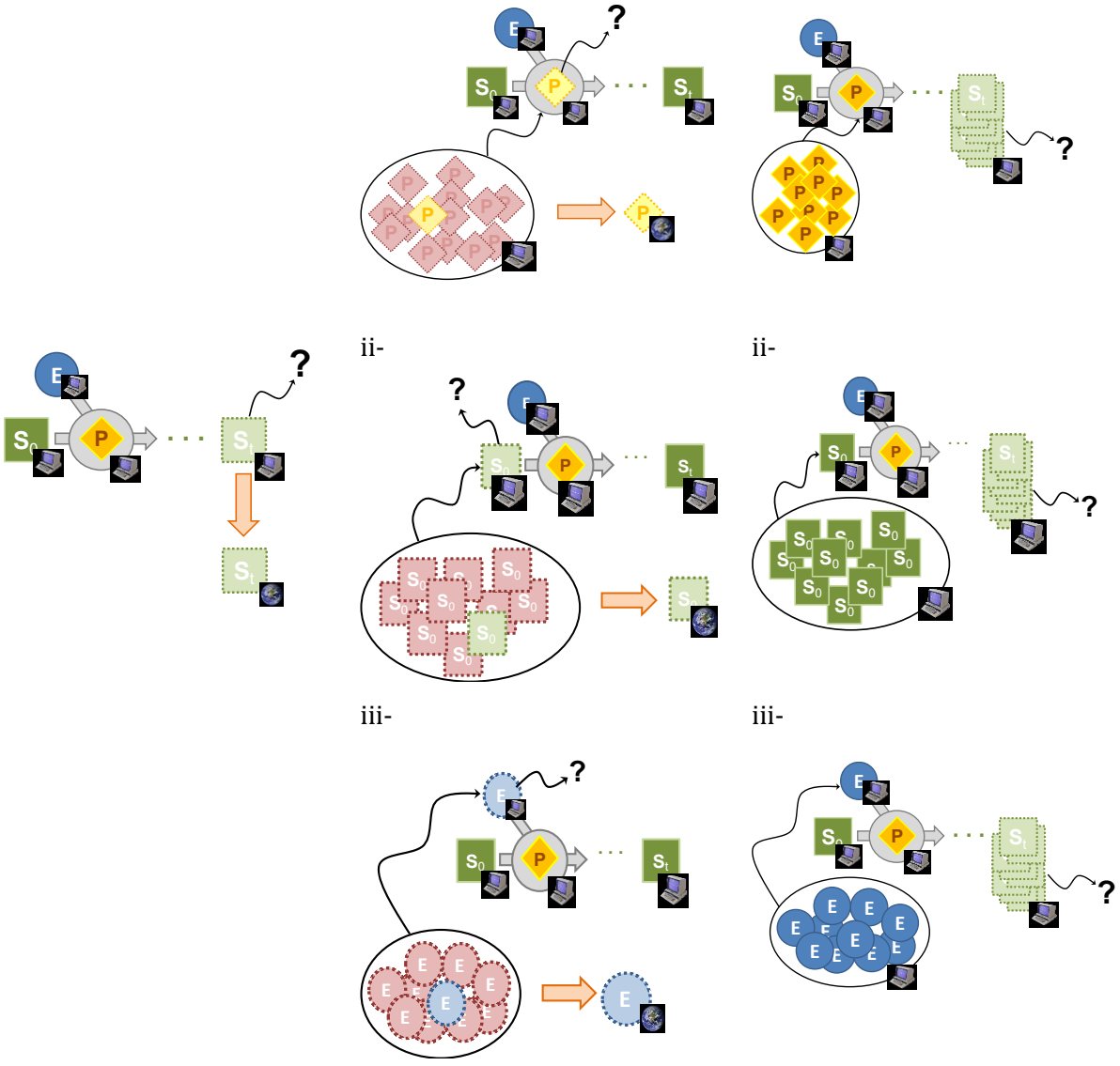

Each mode involves a few components: external factors (*E*) affecting a set of interacting processes (*P*), and the initial (S_0) and final (S_t) states of the system. The computer and earth icons indicate if a component exists *in silico* or *in mundo*. The question marks indicate what the researcher wants to know. The straight-fat arrow corresponds to the aspect of the world that is understood if the simulation effort is successful.

5.2.2. Explanatory mode

In explanatory modelling (Table 5.1b), the researcher is interested in understanding why or how a target system gets to be *in a known state*. For example, a researcher might observe patterns in sediment size distribution in a given river type and seek to discover the origins and causes of these patterns. For instance, in the context of a meandering river, particles tend to be finer on point bars (Anderson and Anderson 2010) than in riffles (Church and Jones 1982). To explain this situation, the researcher could use a computer code and vary the model configurations (set of S_0, P, E) until the successful simulation of the observed distribution. Table 5.1b-i illustrates an experimental scenario in which the researcher tries to identify the processes and the process interactions that yield a specific known outcome. Given data on a system's state at two points in time and on the external influences on the system during the period of interest, but a lack of information regarding the processes that are responsible for the change in system state, a modeller can run a series of numerical simulations, enabling, disabling or adding processes, changing parameter values and tweaking the nature of process interactions, to find a subset of processes and interactions that *can possibly* yield the observed final state. The inference, then, is that the successful formulation of P, given S_0 and E, is representative of how the target system *might* work internally. In other words, explanatory computer modelling provides how-possibly explanations.[2] Note however that various versions of explanation can be obtained by manipulating different aspects of the model, such as trying different initial states (Table 5.1b-ii) or changing parameters for external factors (Table 5.1b-iii). Researchers use one version over another by considering where the uncertainty lies.

In morphodynamic modelling, it is quite common to vary P, along with associated parameter values, while keeping E constant. For instance, although sedimentological properties can be obtained through surveying, and precipitation obtained from the nearest weather station, the selected sediment transport formulae (type and parameters) needs to be adjusted to fit the dynamics of the target system's bed. In terms of the framework proposed, the values for S_0 and E might be relatively well known, but due to uncertainty about the active processes and their interaction, the explanation would be stated in terms of processes. On the other hand, when the uncertainty lies principally within external conditions or past states, as might be the case for example in paleo-environmental reconstructions, then the explanation is an inference about the production of a given outcome from selected initial conditions or external factors, a problem also known as postdiction.

[2] For a good analysis of the difference between how-possibly and how-actually explanation in the context of computer models, see Bokulich (2014).

A basic and minimal requirement for adequacy under the explanatory mode is the model's capacity to agree with the observed phenomenon. In this context, it is important not to confound adequacy with precision. The nature of the explanation will at least depend on the research question and on the algorithms comprised in the modelling solution. For instance, the outcome of a modelling exercise could be a qualitative description of a system, e.g., increase or decrease in river bank stability as a function of key external forces, timing of bank retreat in respect to a flood hydrograph, or channel enlargement or narrowing due to colonization by riparian vegetation. Alternatively, a greater precision may be preferred in other circumstances, e.g., stream temperature at low flow during summer, biodiversity index of the macroinvertebrates community, or patterns in landscape topography. In all cases, the model could be equally adequate. A model could be perfectly adequate for the examination of a phenomenon, e.g., river channel migration, without necessarily being able to simulate the recorded bank retreat rate of a given river. Explanatory adequacy thus depends on the level of description sought rather than on the amount of details provided (see Bokulich (2014, 334) for a similar view).

The capacity to simulate an observed phenomenon (i.e., an observed system state or system behaviour) is a necessary condition for explanatory adequacy, but it is a minimal and sometimes insufficient requirement. To achieve a greater degree of explanatory adequacy, the model should also include the key constituents, processes and interactions that are hypothesized to govern the target system. This second requirement, that we could call representativity, can be further specified in two ways. First, the processes admitted into the model should be present (or at least believed to be possibly present) in the target system. Second, the way and extent to which each process affects model variables should reflect the hypothesized interactions amongst components in the target system. For example, if a researcher wants to explain sedimentological changes on a river bed over a decade, it would generally be adequate to use a model that includes features and processes related to hydrological regimes, sedimentology, and riparian vegetation. However, if the river is also affected by additional anthropogenic processes, e.g., gravel mining, then the researcher would provide a more adequate explanation if the model also included this human-driven process.

It is worth noting that calibration constitutes a form of explanation that is used in most, if not all, modelling investigations. Calibration is the optimization of model parameters, which typically influences the strength and interaction of simulated processes (P), to "best explain" an observed state S_t of the system. In practice this is achieved by adjusting the model's parameters to minimize the discrepancies between simulated and observed metrics at the final state of the system, which results in a localized explanation, i.e., one that applies to the specific case being examined. However, this

procedure does not necessarily lead to the identification of causalities. Indeed, different calibrated models can fit the same target system, and it is possible that multiple distinct model configurations (set of processes P and parameters) result in the same system state S_t (a condition known as equifinality; see Section 5.2.4 for further details on this). Nevertheless, the successful calibration of a model involves at least one possible, and hopefully plausible, set of parameter values that explains an observed phenomenon.

5.2.3. Exploratory mode

The third and final mode, exploratory modelling (Table 5.1c), is arguably the most experimental of all three.[3] Here, the researcher is not interested in finding or explaining a particular final state S_t, but instead, is seeking *to explore a set of model configurations* for sensitivities, divergences, plausible ranges, existence of spatial and temporal patterns or trends, existence of thresholds, etc. As it was the case with the explanatory mode, it is possible to explore a system's behaviour by fluctuating initial states (S_0), external factors (E), and processes (P) (Figure 5.1c). The key aspect that distinguishes the two modes, however, is the fact that an explanation involves matching known components from a target system, whereas exploration evaluates the simulated future states S_t of a system, based on different S_0, P and E sets, which are not necessarily associated with a target system. As highlighted by Larsen et al. (2014), the capacity to manipulate model components makes computer-based exploration similar to experiments that seek for causality. It enables the examination of a system with initial or environmental conditions different than those commonly observed in nature, thereby exploring counterfactuals that can enable the formulation of hypotheses and improve our understanding of causal mechanisms responsible for the emergence of systemic properties. However, unlike Larsen et al. (2014), our framework does not limit exploratory modelling to that role. Nor does it imply that exploration must be realized by simplifying and leaving out physical details. The exploration mode is thus essentially analysing the simulation outputs collectively in search of overarching properties that might emerge from all the simulated S_t.

Although exploration using a calibrated model allows to evaluate the impacts of hypothetical perturbations on a known target system, it is important to note that exploring, in our framework, does not involve an assessment of the goodness of fit between simulated datasets and a measured

[3] Several philosophers of science conceive of computer simulations as a form of inquiry that resembles experimental investigations (e.g., Dowling 1999; Hugues 1999; Winsberg 2003, 2009; Parker 2009). We are sympathetic to this viewpoint, but engaging with this debate would distract us from our main objective.

state in a target system. As such, this mode is perhaps the most susceptible to be seen as mere frivolity; a numerical computation of hypothetical idealization. However, this would be an oversimplification. Research using exploratory computer simulations often imports knowledge obtained from empirical observations, and it can be an important step toward a better understanding of unexpected features of natural phenomena (Gelfert 2016; Lenhard 2007; Winsberg 2009; Larsen et al. 2014). Moreover, certain activities involving exploratory modelling have a clear practical value and are much less in danger of becoming mere computational curiosities. For example, sensitivity analysis, i.e., the process of assessing variability in outputs with respect to changes in parameter values, is a form of exploratory modelling that can identify the key factors affecting a system's behaviour. This information can play a crucial role in reducing uncertainty of the modelling exercise as a whole (e.g., orienting field work efforts towards the most sensitive variables) and in guiding policy making (e.g., fixing limits on greenhouse gas emissions that have the most severe effects on climate change).

Due to the diversity of exploration possibilities and contexts, it is rather difficult to provide a complete list of adequacy conditions for the exploratory mode. Two general and universal criteria are manipulability and tractability. Manipulability can be ambiguous. In the context of this paper, it simply means the capacity to configure a computer model in such a way as to gain some understanding of the model's limits and capabilities, and ultimately of the target system's behaviour. The second criterion, tractability, refers to the ability to trace the origins of interesting dynamics or patterns in the simulated system, such that they can be attributed to specific S_0, P or E. Thus, a model that enables different kinds of changes (e.g., qualitative, quantitative, and incremental) or a model in which researchers can integrate heterogeneity while maintaining tractability and analysability of outputs will have a greater exploratory potential. As implied by Larsen et al.'s (2014) analysis, simpler models may fair better at this task, but it does not mean that exploration cannot be performed with complex models as well.

Gelfert (2016, Ch.4) identifies four purposes of exploratory modelling: 1) starting point for future inquiry, 2) proof-of-principle demonstration, i.e., a proof that a target can be represented or that a certain kind of behavior could be produced, 3) generation of potential explanations, and 4) assessment of suitability of target, i.e., adjusting one's conception of a target phenomenon by modifying various parameters or the range of initial conditions. Our framework presents exploration under a different light than Gelfert does, and thus, not all of these purposes count as exploration for us. For instance, examining a system's behaviour (Gelfert's second purpose) would qualify as explanatory under our framework. Gelfert suggests that a model-based explanation is potential, and

thus exploratory, when there is no theory under which the model can be subsumed. Our framework is independent of such any top-down/bottom up considerations. Moreover, since all simulation-based explanations are merely potential (i.e., how-possible) in our framework, the kind of distinction used by Gelfert loses its meaning in our framework. Under the criteria established in Section 5.2.2., modeling remains explanatory as long as there is a step in the process where the modeller engages in a selection process for a model (or model configuration) that can produce an outcome that matches a known dataset. This said, exploration can be a step that many modellers take before engaging in an explanatory mode (as exemplified in Section 5.3.1).

Table 5.2. Adequacy criteria for modelling modes and relevance of equifinality per criterion

Mode	*Adequacy criteria*	*Relevance of equifinality*
Predictive	Accuracy: capacity to correctly predict the value or trend of a metric.	Not an issue. May be an indicator of robustness.
Explanatory	Accuracy: capacity to produce a model output that fits an observed metric.	Not an issue.
	Representativity: ability of a model to capture the (hypothesized) relevant processes of a phenomenon.	Needed to simulate multiple realizability. Makes explanations "how possibly" rather than "how actually."
Exploratory	Manipulability: capacity to intervene on a computer model to produce diverse analyzable model outputs.	Not an issue.
	Tractability: capacity to relate the model output to a parameter value(s) and/or modelling options.	Established causalities may not be bidirectional. Needed in sensitivity analysis.

5.2.4. Equifinality and adequacy

Equifinality, i.e., the situation where a given simulation output S_t is compatible with multiple model configurations (i.e., multiple combinations of S_0, E and P) (Beven 2006), is commonly seen as a problematic phenomenon in modeling. However, this verdict is in fact too simplistic. Whether or not equifinality is a problem depends largely on the modelling mode. Equifinality is certainly likely to be perceived as problematic by model users during explanatory modelling, as it may suggest multiple how-possible explanations. Recall the fictive situation mentioned earlier where a researcher wants to explain the transformation of a river's morphology in a complex urban environment, and can do

so by adopting either of two strategies: by including only natural processes, or by also including human-induced processes such as gravel mining. It might well be that both of these process configurations (*P*) would lead to acceptable realization of the simulated final state S_t, albeit likely with different parameter values for the selected processes. This situation is likely to occur when modelling complex phenomena, with the implication that it can compromise the representativity condition of adequacy (Table 5.2). This essentially renders simulation-based explanations how-possibly explanations.

Procedures have been devised to deal with explanatory equifinality (Beven and Freer 2000). A modeller can compare model configurations that lead to a unique outcome, and decide which one(s) provide(s) plausible explanations, given the knowledge and data available for the target system. This can involve taking additional measurements on the target system to eliminate implausible solutions, i.e., parameter sets (or values) that do not contribute to the observed change in state of a given system, thereby increasing representativity and trustworthiness (Morton 1993). In situations where relevant metrics are inaccessible, modelers must rely on theoretical knowledge, common sense, or reliable proxies, which does not necessarily reduce adequacy, but can affect the trust in the model's explanatory capacity. In many cases, tracking the source of equifinality can provide insights into the mechanisms forming the target system, as well as into its attributes. Ideally, the retained model configuration must include the most relevant processes and interactions, but also the fewest *ad hoc* parameters.

Note, however, that despite the epistemic problem arising because of explanatory equifinality, being able to produce the same outcome from multiple model configurations can be an asset when the target system is itself subject to multiple realizability. For instance, it is possible for two very similar landscapes to occur at two different locations, without having been affected by the same types of forces (Cruslock et al. 2010). In this case, equifinality is needed to provide two adequate explanations.

In exploratory modelling the occurrence of equifinality may affect tractability by blurring the relations between predicted geomorphic features and input parameters. The implications of this issue are tightly related to the objectives of the modelling exercise. For instance, if a modeller seeks to define causal relationships, then the conceptual model emerging from an exploratory modelling exercise may not be appropriate for any given application due to the existence of many-to-one relations. In other circumstances, equifinality can be an emergent property of the modelled system, e.g., a convergence on similar (or identical) outcomes can describe a pattern or trend in the system

dynamics. Alternatively, during a sensitivity analysis, equifinality could reveal the insensitivity of certain parameters or the existence of self-regulatory mechanisms, forcing a large number of model configurations to converge to well-defined potential outcomes. In both situations, the model user or researcher benefits from this information. Overall, since manipulability is independent of equifinality, the modelling investigation always leads directly to conclusions without affecting trustworthiness, which cannot be said for the explanatory mode.

Finally, under the predictive mode, the consequences of equifinality are probably not as serious, for two reasons. First, a model is predictively adequate if it reliably informs the user about the future value of key metrics; the details of the exact mechanisms that produced a final state are of secondary importance, which renders equifinality less relevant. Second, and arguably more fundamentally, predictive modelling involves running a single simulation, whereby a specific combination of S_0, P and E are given and a single prediction for S_t is obtained. Hence, equifinality is not even arising in predictive mode. Stochastic modeling provides a possible exception, in which case the presence of equifinality (under stochastic multiple runs with identical configurations) is an indicator of the robustness of the prediction.

It is, of course, possible to run multiple individual predictive models (e.g., scenario planning, where different S_0 or E are considered), at which point convergent predictions basically indicate an insensitivity to the variation in scenarios. Alternatively, one could run multiple predictive simulations using the same S_0 and E with different models (i.e., different P), at which point identical predictions basically indicate a robustness of the models and help establishing trust in the assessments of various scenarios. This is not commonly done in geomorphology, but in the context of climate change, for example, most models included in the fifth IPCC report agree that "human activities caused more than half of the observed increase in global mean surface temperature from 1951 to 2010" (Bindoff et al. 2013, p.869)[4]. The high degree of confidence in this claim is in part due to multiple independent models (i.e., different representations of implementations P) supporting such attribution. In this case, equifinality between the models helps building trust in a potential future system state.

[4] Note that the agreement here is about the claim that anthropogenic forcing is responsible for more than 50% of the observed increase since the last 60 years. This does not mean that all models agree about how many degrees are attributed to human activities.

5.2.5. Summary

The typology presented above provides a general and abstract account of some of the most basic types of scientific understanding as pursued in simulation modeling. Specifically, it shows that computer simulations can, in their own way, be involved in the general epistemic objectives of predicting, explaining and exploring. Although we do not claim to exhaust all goals, many specific modelling objectives would, nevertheless, fall under one of these three simulation modes (or epistemic purposes). More importantly, looking at computer simulations as experiments undertaken under different investigative modes permits a more practice-oriented and fine-grained analysis of their purposes and adequacy.

5.3. Applying the framework to fluvial geomorphology

Using an example from fluvial geomorphology, we will now apply the framework developed in the previous section to relate each one of the three modes it comprises to common modelling activities. Our analysis will demonstrate how a given model can have different adequacy for different purposes and the corollary, that developing a model to achieve a certain type of understanding can affect its ability to perform other modes. These findings are in line with Bokulich's (2013) division of cognitive labour thesis. Depending on the nature of a modelling investigation, a user may not necessarily engage with all modes of modelling, or may encounter them in a different order than presented in the preceding section. In Sections 5.3.2–5.3.4 we present them in the order in which they were chronologically encountered in a specific modelling investigation.

5.3.1. Origin and purpose of numerical modelling in fluvial geomorphology

Knowledge on river dynamics in geomorphology has traditionally been obtained from field observations (Rhoads and Thorn 1996), and more recently, from controlled lab experiments within downscaled physical models (e.g., Pyrce and Ashmore 2005; Tal and Paola 2010). Gaining general knowledge about rivers from field observations presents numerous challenges. Due to centuries of evolution through various forces and processes acting at different spatiotemporal scales, natural rivers and floodplains exhibit highly irregular morphology and heterogeneous distribution of basic components (e.g., soil, water, plants). Moreover, anthropogenic activities have contributed to reshaping the planet's surface and, in many instances, have directly or indirectly altered the characteristics of the river channels and drainage networks, thus adding multiple confounding variables and blurring the phenomena of interest. Earth scientists also face additional difficulties

such as the presence of feedback loops and nonlinearities dissimulating causal relations, and evidence being wiped out with time (Cox 2007; Phillips 2006).

Due to these constraints, geomorphologists increasingly employ computer models to create virtual abstractions of the components and processes affecting channel dynamics (Coulthard and Van de Wiel 2012; Van de Wiel et al. 2016). Several different modelling strategies have been envisioned and implemented to address a range of research questions pertaining to a diversity of river phenomena and contexts. In this section, the focus will be on the use of numerical morphodynamics models[5] comprising mathematical algorithms to simulate 1) water motion in an open channel, 2) sediment transport along its bed, and 3) bank retreat due to mass wasting. River meandering processes, as well as other alluvial river types, can be examined using this family of models (Duan et al. 2001; Shimizu et al. 2009; Lai et al. 2012). The discussion is oriented toward the epistemic aspects related to a recent adaptation of the TELEMAC-MASCARET[6] suite of solvers that sought to include a physics-based description of river bank retreat processes while considering the mechanical properties of soil and plants (Rousseau et al. 2014a, b) (Figure 5.1). The original TELEMAC-MASCARET package comprises several modules, including Telemac-2D, which is a fluid dynamics solver, and SISYPHE, which is a collection of algorithms describing sediment entrainment and transport caused by moving fluid.

The adapted modelling code permits the coexistence of multiple types of process descriptions. Overall, processes are described in terms of fundamental physical laws, such as conservation of mass and momentum for flow, or the balance of physical forces acting on a river bank (Bishop 1955). In a few instances, however, they are based on empirical observations made in natural and artificial river channels, e.g., most of the sediment transport formulae are empirically based, and the physiological properties of riparian vegetation are based on measurements taken from a very small sample of species and individuals (Tubbs 1977; Kenefic and Nyland 1999). Also, as with many mathematical models, idealizations were introduced.

For example, despite physics-based slope stability assessment and conservation of mass during bank transformation (following the collapse of an unstable bank), the model represents post-failure bank surface geometry as a planar surface oriented from the horizontal at an angle that is specific to the bank material; this greatly simplifies the natural phenomenon, especially in the case of a

[5] This family of models rely on the shallow-water equations for fluid motion, i.e., a 2D simplification of Navier-Stokes equations, combined with formula for sediment transport.

rotational failure, which usually results in the accumulation of soil material at bank toe in a natural context. In addition, the model is difficult to use with large-shallow channels due to algorithmic limitations. Finally, note that the new modules were added into an existing modelling package, i.e., TELEMAC-MASCARET. This decision, motivated by financial, time, and strategic constraints, significantly affected algorithmic choices when developing the new modules, but most importantly, imposed restrictions on model applicability – as indicated below.

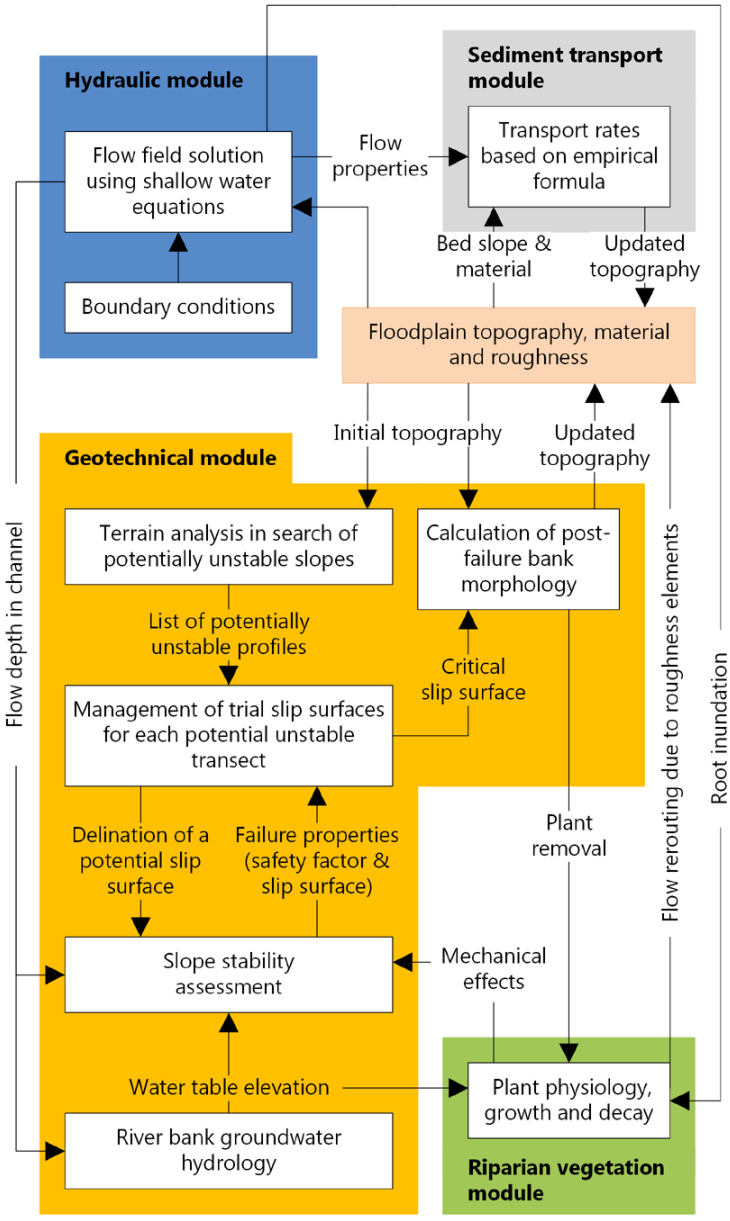

Figure 5.1. Modules and sequence of steps in the morphodynamic model

5.3.2. Exploratory mode

The expansion to the morphodynamic model was developed with the intent to *explore* the contribution of key biophysical factors (especially those related to soil composition) and hydrological regimes on the morphological evolution of an alluvial, single- or multi-threaded river system, at the spatial scale of a few hundred meters and at the temporal scale of a flooding event. Note however that this exploration is accompanied by a form of explanation; prior to exploration the researcher must also make sure that the augmented model can produce the right type of outcome, i.e., morphological evolution of a meandering river. This could be compared to Gelfert's (2016) "proof-of-principle". Once it has been demonstrated that a model is capable of representing the relevant type of target system, a sensitivity analysis, i.e., the evaluation of the relative influence on the observed phenomenon of model processes and factors, constitutes the primary form of exploration that is taking place in this inquiry. Sensitivity analyses allow researchers to gain insight into the behaviour of the model itself (Legleiter et al. 2011), while enabling the formulation of hypotheses regarding natural analogues (Loheide and Booth 2011; Nassar 2011). Furthermore, this exercise can help planning and prioritizing field data collection activities by identifying the factors that deserve a greater level of attention (Newham et al. 2003; Kuta et al. 2010). In the case of the coupled model analysed here, multiple simulations have been launched, and their results analyzed, to test the modelling software and functionalities, to define thresholds in parameter values, and to identify the most sensitive parameters. For instance, the model was found to be very sensitive to geotechnical properties of the bank material, in particular to soil cohesion, and species assemblage (Rousseau et al. 2014b).

What makes the coupled model, i.e., TELEMAC-MASCARET combined with the geotechnical and riparian vegetation modules, an adequate tool to explore the morphodynamics of meandering river channels? Recall that the basic requirements for exploratory adequacy are the ability to *manipulate* in the right way and *trace* the effects of interventions, thereby gaining a better knowledge of the model's limits and capabilities. The fact that the manipulations of the model and simulation configurations required to undertake a sensitivity analysis were possible demonstrates a degree of exploratory adequacy of the model.

The tractability of the model can assist the researcher in elaborating new hypotheses on river morphodynamics that could not be formulated and tested using previously existing morphodynamic models. For example, hypotheses emerging from the relationship between established plant types/species (defined in terms of measurable physiological traits) and channel planform and

morphology, or the possibility to define plant cover in detail, renders the model adequate for use in a large range of studies.

Several other qualities make the augmented model adequate for exploration. First, its universal (or non-context specific) character means that it can be applied to a wide range of alluvial river types, although it is most relevant to those evolving in at least partially cohesive soils (Rousseau et al. 2014b). More broadly, context-specificity does not preclude exploration, but it can limit the range of processes considered by the researchers. Second, the adequacy of this model to explore is derived from using formulae and algorithms that are known to be effective and reliable. For example, integrating a genetic algorithm to minimize run time is recognized as an adequate approach to improve efficiency (Li et al. 2010). Third, strategic decisions taken during the software planning and development stages, which influenced the computer code's structure, added flexibility by permitting incremental spatial variations for a large number of biophysical parameters, thereby enabling the simulation of irregular patterns found in nature. These strategic decisions also made it possible to bring corrections, alterations, and expansions of the code, such as the three-dimensional flow and coastal wave propagation modules mentioned above.

5.3.3. Explanatory mode

Let us now consider the same model serving an explanatory role. Recall that explanation, per the proposed framework, is accompanied by two basic requirements: 1) hypothesized representativity of the processes and conditions involved in the behavior of a target system, and 2) agreement between model outputs and known outcome states of this system. More formally, it should be possible to identify a set of processes P and external factors E (i.e., parameters and boundary conditions) producing a known system state S_t from a known initial state S_0 over a period of time t. Alternatively, the goal may be to find an unknown initial state S_0, given E and P, or to find an unknown E, given S_0 and P. The model described in Figure 1 meets both requirements. It can be broken down into key biophysical components and mechanisms. Moreover, the attributes in the model are associated with measurable physical quantities. It is also possible to find at least one combination of biophysical mechanisms and parameter values leading to an agreement between observed and simulated state S_t. Hitherto, the model has been calibrated and validated against datasets from flume configurations (artificial laboratory channels) and a natural semi-alluvial river. For instance, the locations of retreated river banks along Medway Creek, Ontario, a 20-meter wide reach of a semi-alluvial stream, were reasonably well predicted after calibrating the model against field observations made over a period of 3.5 years (Figure 2). The model output does not perfectly match observations

(e.g., false negatives between transects 760–762 and 798–807; Figure 2a). This mismatch could be attributed, at least partially, to a process *P* that is present in the target system, i.e., impacts of riparian vegetation, but ignored in the simulation that produced the outcome shown in Figure 2. However, despite its limited adequacy to simulate bank erosion along a vegetated river reach, the model correctly identifies most of the unstable bank locations (e.g., the three unstable zones along the second monitored river bank were detected (Figure 2b)).

Matching the heterogeneity found in the natural world can be a challenge for the researcher trying to explain a phenomenon by using a simulation model. The lack of heterogeneity in both the input and output of most planform evolution models has received criticism (Güneralp et al. 2012). It has been suggested that this issue could partially be solved by integrating groundwater and vegetation dynamics components in existing modelling packages (Bertoldi et al. 2014). Although the model presented in this section contains several assumptions and idealizations, it nevertheless contains the two key processes deemed essential for producing the right type of irregularity. The added modules allow spatial variations in plant cover and does not impose any geometrical restriction on planform migration. Not only has this strategy proven appropriate after the successful calibration-validation of the coupled model against a morphological dataset from a short river reach (Rousseau et al. 2014a, b), but it also favors the development of irregular morphologies typically found in natural channels. Broadly speaking, the model produces the right kind of resemblance with the target system, which is an important indicator of representation adequacy (Mäki 2011, 57).

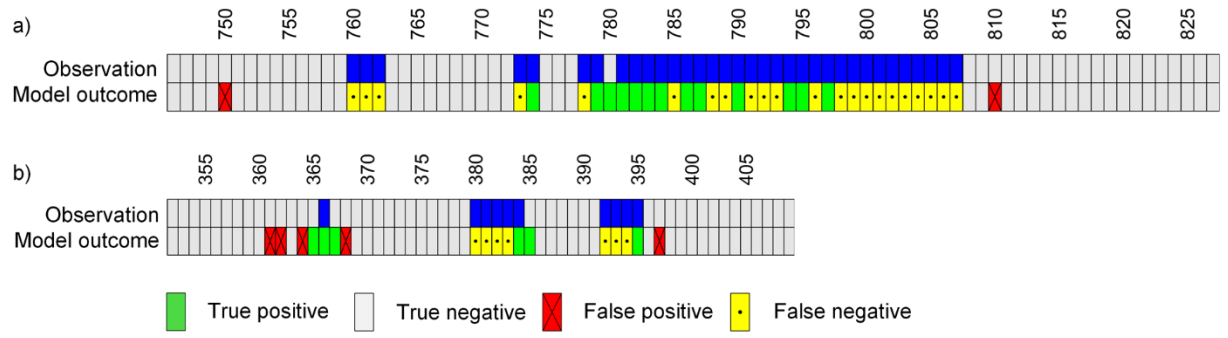

Figure 5.2. Observed and simulated bank failures

This presents a comparison of bank failures observed along two river banks of Medway Creek, London, Ontario between January 2012 and June 2015. The labels along the x-axis correspond to locations along each river bank. The distance between adjacent locations is 3.3 meters. A bank failure prediction was considered correct if it occurred within a distance of one location from the location associated with an observed prediction. This is the case for transects 365, 367, 385, and 780.

Trust in the model's adequacy to explain channel evolution processes is also affected by several external factors. TELEMAC has been employed, improved, and evaluated in a range of contexts over an extended time period (Bates et al. 1997; Corti and Pennati 2000; Sun et al. 2010; Langendoen et al. 2016), which gives a high level of trust in its adequacy. Because of the addition of new algorithms, the level of confidence in the new augmented model is not as high; but this could be improved after calibration and validation against datasets from a diversity of alluvial river types and spatial scales, where cohesion due to the occurrence of a fine-textured soil or of a riparian vegetation cover plays a role. However, very few comprehensive morphological datasets exist at the moment to achieve this ambitious objective; this situation can introduce uncertainty in parameter estimation, and thus decrease model reliability (Samadi et al. 2009). The large number of factors and parameters comprised in the model, combined with context-dependent data requirements and scarce datasets that can take a diversity of forms, further increases this challenge. For instance, records on physiological traits, hydrological and mechanical properties of riparian plants are rather thin, and are not always available for the soil and ecological conditions of interest.[7] Therefore, trust in river morphodynamics model seems to be affected by a variety of circumstances external to the modelling exercise, including technology, time, and financial constraints.

5.3.4. Predictive mode

The augmented model has not yet been used in predictive mode. Given the current state of technology and computational capacity, the primary consequence of integrating geotechnical and vegetation processes into a river morphodynamics modelling package that rely, to a large extent, on physics-based algorithms, is that simulations are limited to short spatiotemporal scales. Even with substantial improvements in computational power, the model presented in this section may not produce realistic landscapes during long-term simulations due to propagation errors (Kleinhans et al. 2005). Some researchers were able to study long-term river evolution using variants of this model type, but only by making choices that significantly limit the representativity and explanatory potential of their model. For example, they must represent river environments as rather homogeneous channels with simplified transportation and sedimentological properties, describe physical processes in fewer than three dimensions (Lane et al. 1999; Wu et al. 2004), lump erosion processes into an erodibility coefficient (Camporeale et al. 2005), ignore the floodplain or assume that it is lacking elements such as topography, secondary channels (Abad and Garcia 2006), or hydraulic and mechanical effects of

[7] For examples of studies that provide plant properties for riparian species see Abernethy and Rutherfurd (2001), Simon and Collison (2002), Pollen (2007), or Adhikari et al. (2013).

riparian vegetation on the flow and geomorphic processes (Bertoldi et al. 2014). The fact that simulations involve simplifications is known territory, but it does not mean that all value is lost. As discussions about exploration often highlight, the value of a model is often heuristic in that the simplification of a system can still provide insights into future research and field data requirements (Oreskes et al. 1994; Gelfert 2016). Furthermore, one must recognize that, under special circumstances, e.g., forecasting the impacts of the anthropogenic climate change on a river network's form and organisms, the predictive mode may be the only means available to foresee the future state of a system, and to inform the decisions made by competent management authorities (Verhaar et al. 2011).

Note, however, that models that are only adequate for short-term predictions can nonetheless be relevant to examine practical questions of fluvial channel designs and management. The previous generation of morphodynamic models, which only included basic fluvial processes, have been employed to evaluate the technical effectiveness of instream hydraulic structures, i.e., artificial structures put in place as a mitigation measure against bank erosion (Matsuura and Townsend 2004; Minor et al. 2007), to improve navigation (Jia et al. 2009; Huang and Ng 2007), or to enhance fish habitat (Boavida et al. 2011). Predictions were based solely on flow hydraulics (Haltigin et al. 2007), or were able to simulate sediment dynamics (Minor et al. 2007). Due to a recent shift in the type of river management/restoration interventions toward the use of less invasive procedures, it is expected that the augmented model studied in this section, as well as a variety of similar morphodynamic models, will soon serve in scenario planning involving riparian vegetation.

5.4. Looking more broadly at the context of inquiry

It is tempting, while developing adequacy criteria for different modelling modes, to think of models in isolation from the broader context of inquiry. However, like any other theory-building activity in science, computer modelling involves several decisions over multiple stages and takes place in a complex network of interacting agents and institutions engaged in research. These interactions, combined with many contextual factors (e.g., technical abilities and knowledge of model users, level of documentation, hardware, financial and time constraints), can affect the product developed, the way states and processes are described, and the researchers' judgement about model's suitability. In other words, deciding whether a given model is the right tool for the job is not only an internal affair based on epistemic adequacy criteria. The social and historical background, i.e., research and modeling inquiries that happen elsewhere and those that took place in the past, can also shape the decision landscape. In this section, we discuss a type of model-to-model interaction that can influence

researchers' judgement while deciding whether a tool is adequate or not.

A model is typically the result of an historical process involving incremental developments that are constrained by a pre-established structural framework.[8] The fluvial modelling example we used in Section 5.3 illustrates this situation. The TELEMAC modelling software was introduced in the early 1990s (Galland et al. 1991) and has become increasingly popular in the modeling community following the release of its code to the public domain. Developers gradually introduced new modules and coupled them to existing code to improve representativity. Many modellers and industries have adopted TELEMAC-MASCARET, not only based on its trustworthiness, but also due to the much greater costs involved in learning, implementing, or developing an alternative model. Rather than reinventing the wheel, model users typically tinker and sometimes add functionalities to an established set of algorithms. So, existing models are not as independent of previous models as they may appear.

The integration of additional processes and features in an existing model impose constraints on subsequent algorithmic developments. For instance, the way in which a TELEMAC-compatible mesh holds biophysical quantities, i.e., within vertices using a finite element discretization scheme, is different from the way in which the same information is organized in a cellular automata model type, i.e., in a grid with rectangular, orthogonal cells (Van de Wiel et al. 2007; Coulthard et al. 2013). Therefore, the implementation of the same process in both models, based on a common theoretical understanding of a natural phenomenon, could take different forms. Similarly, simulating river bank retreat within the former model type can be quite cumbersome. The implementation in TELEMAC-MASCRET of a universal algorithm of bank retreat by Rousseau et al. (2014a,b) was accomplished by only permitting vertical adjustments. Conversely, Langendoen et al. (2016) integrated an adaptive grid algorithm to improve resolution near water boundaries (i.e., nodes can relocate horizontally as well), but limited the applicability of the resulting model to single-threaded channels. Both implementations relied on different strategies to deal with TELEMAC's legacy, which resulted in distinct sets of experimental limitations. These

[8] See Winsberg (2009, pp.109–110) for a discussion of the historical nature of climate models.

examples show that the decisions adopted by a group of experts responsible depends on a series of past contingencies. The same theoretical understanding and the same modeling starting point can lead to divergent modeling strategies.

This phenomenon of path dependence has received a lot of attention in the economical (e.g., Arthur 1994; David 1985, 2007), political (e.g., Pierson 2004), and biological realms (e.g., Jacob 1977; Gould 1989; Beatty and Desjardins 2009; Desjardins 2011). In the latter contexts, path dependence has often been used to explain why certain social institutions and evolutionary strategies are suboptimal. Cultural and biological evolutions do not proceed by selection of what is best, but by piling up and tinkering with strategies that work, i.e., strategies that are merely adequate. This viewpoint applies to modelling as well. Completely rewriting and streamlining a code requires a massive time-investment with minimal immediate pay-off. On the short-term, it is more effective to tinker with an existing model, even though the result is an ever-monstrous code and an ever-greater impediment to doing the overhaul. This type of sub-optimality and historical constraints are further reasons for approaching model evaluation in terms of adequacy and reliability instead of focusing (exclusively) on the semantic category of truth.

5.5. Conclusion

Computer models are useful fictions that can serve various purposes, the most famous of which are forecasting future states of a system and identifying key influences in a target system. As such, they should be evaluated in terms of adequacy for a purpose. The above paper presented three important modeling purposes/modes: prediction, explanation, and exploration. It also identified some of the main adequacy conditions for each mode. In brief, a model is adequate under the predictive mode if there is (or would be) a fit between simulated data set and yet-to-be-measured metric on target system. Under the explanation mode, adequacy has two dimensions. First, a model is minimally adequate when it is capable to yield some known specified outcome (either general qualitative or more specific metric). Trust in the ability to explain a phenomenon is typically increased if a modelling software can fit a wide number of environmental contexts. Second, a greater degree of explanatory adequacy is achieved if a model is also representative, i.e., the ways in which the processes/initial conditions/external factors are implemented in the model capture features of the target system. Finally, a model is adequate to explore if a user can integrate and manipulate parameters to perform various types of analyses that provide understanding of model capabilities,

thresholds, and limitations. Such improved understanding will typically require tractability as well.

As shown using an example from fluvial geomorphology, these three modelling modes are not completely independent. In practice, many modelling projects involve each of the different modes of modelling at different stages of inquiry. We saw that exploration is often a precursor to explanation, and the confidence one has in the ability of a model to produce relevant information through exploration could be boasted by the verification of a somewhat surprising prediction. Moreover, these modes can work together at different stages of inquiries. A common, although not necessary, progression could be: investigate model dynamics (explore), then calibrate parameters (explain observed measurements), and finally investigate the future state of a system for a given scenario (predict). Finally, our analysis of the broader context of inquiry reveals the path-dependent nature of model building, and thus provides another reason to believe that models can only be adequate rather than truthful. If model building is a path-dependent process, where decisions of the past impose some constraints on what and how models are built today, then looking at the history of a given modelling tradition can help us to understand the direction of modelling practices by different communities of modellers.

6

Discussion and conclusion

The overarching goal of this research was to develop a morphodynamic model that can simulate bank retreat in vegetated floodplains at intermediate spatiotemporal scales using physics-based algorithms, and thus that can be used to identify key biophysical controls on the meandering process. The main steps required to achieve the specific research objectives were to select a model, alter its code to include geotechnical algorithms, monitor the evolution of bank morphology along two natural reaches, elaborate a statistics-based methodology to quantify model fitness, and calibrate models against observed bank retreat observations. This research also provided a good opportunity to reflect on the epistemology of the modelling approach, and on its adequacy to support research and practical applications related to bank retreat and river meandering.

6.1. Novelties

During the last ~10–15 years, several morphodynamic models have been developed and used to simulate meander evolution. Although these models allowed good progress in our understanding of the broad controls on meander planform dynamics, the lack of flexibility regarding mesh structure, combined with the lack of physics in the implementation of bank retreat algorithms, may have, at least partially, limited real-life applications of these models. The proposed modelling approach fills some of these gaps and enables gains in knowledge at intermediate spatiotemporal scales.

Although the research described in this thesis examines lateral retreat in meandering reaches, the implemented geotechnical algorithm was developed with the intent of making the computations independent of mesh structure to ensure compatibility with single- and multi-threaded river channels while keeping track of paleo-channels. Only few studies have attempted this (Evangelista et al. (2015), El Kadi Abderrezzak et al. (2016), Langendoen et al. (2016) being exceptions so this is a major contribution of this thesis). The coupled model features an empirical bank hydrology sub-model and can take account of the mechanical effects of riparian vegetation on bank stability. The integration of vector-based spatial analysis allowed to detect flow boundaries and scan the terrain in

search of slopes along which to perform stability assessment and retreat. The configurable, stochastic genetic algorithm does not only reduce calculation time compared to the grid-pattern search method, but allows for planar, circular and non-circular slip surfaces to form, with conservation of mass being respected during river bank failures. Finally, the implemented data structure, along with multiprocessing, limits the increase in computation time that results from the inclusion of new processes.

In addition of the effort put into the design and creation of the geotechnical and riparian vegetation modules, a substantial amount of time was invested into the integration of objectivity at each stage of this research. For instance, a slight modification of Youden (1950)'s index was employed to quantify the resemblance between observed and simulated bank retreat occurrences (see Chapters 3–4). This score can represent predictive accuracy as well as goodness of fit during calibration. Machine learning algorithms were employed whenever appropriate. An example is the use of tree classification to facilitate calibration with the identification of key parameters and of a range of possible values. Finally, the geotechnical model relies on spatial analysis concepts to detect solid boundaries, analyze topography, and convert parts of the 3D mesh into 2D profiles (see Appendices A–B). The proposed approach differs from previous ones by blending multiple types of analysis and technical solutions.

6.2. Findings

A comparison of six modelling codes allowed to identify those that can accurately simulate flow hydraulics and bed evolution in meandering river channels (see Chapter 2). Larger discrepancies than expected were found in flume-sized channels, considering that the models were configured with nearly identical boundary conditions, mesh structures and turbulence models. This corroborated the findings of Rameshwaran et al. (2013) obtained based on simulation results from four hydraulic modelling software. Variations in bed roughness and bed shear stress equations can affect transport rates, and thus simulated equilibrium bathymetries. However, limited sensitivity to key options was found, which indicates that the differences in predictions are attributed to code intricacies, such as design and implementation choices. In addition, the analysis demonstrated that model complexity, e.g., 2D/3D, turbulence closure, consideration of local bed slope, does not necessarily improve predictive accuracy. The best model to use in a modelling investigation depends on the specific environment examined, but information about the range of applicability of fluvial models is not available. In our case, TELEMAC-2D was selected to examine lateral retreat, because it performed well in meandering channels with fixed sidewalls and could be modified to include new algorithms.

The coupled model served three purposes. First, the model was calibrated against data from two natural river reaches to demonstrate its ability to fit observations (see Chapters 3–4). Machine learning algorithms were employed to estimate parameter values and to determine their relative importance. The first site (Medway Creek) featured stratified banks with glacial till at the bank toe and sand in the upper bank region. The agreement with observed retreat rates was satisfactory in one of the four sub-reaches considered, but less so elsewhere. At a second site (St. François River), which exhibited more uniform conditions, the agreement was stronger and spatially more uniform. The disagreement at the former site seemed to be caused by heterogeneity with respect to groundwater hydrology and soil composition, which was not implemented in the model. Second, the model was used during preliminary testing to analyse the sensitivity of biophysical conditions to lateral retreat using one-iteration simulations (see Appendices A–B). Soil texture was found to affect the number of failures and total eroded area, with stability being the greatest for banks consisting of fine sand or clay. Vegetation type and species exerted an important control on bank stability as well, although varying the composition of plant assemblage had little effect on stability. When imposing a flood hydrograph, soil cohesion and friction angle were by far the most influential parameters. Third, calibrating the model to fit observations made along two natural river reaches highlighted model sensitivity to the geomorphological context. In particular, flow stage had a greater influence on bank retreat in the wider river reach, which featured more uniform biophysical conditions. In addition, the more complex site of Medway Creek is subject to equifinality as a few combinations of a few parameter sets can lead to equally good fit. The sensitivity of bank retreat to the type of river reach suggests a specificity of the knowledge developed, and thus highlights the need for caution when transferring conceptual models and empirical relationships between river reaches.

6.3. Future development

The developed CFD-based geotechnical model identifies key biophysical parameters with respect to river bank retreat in alluvial and semi-alluvial river channels, but more importantly, it is an example of an approach that can be used to make connections between specific river geomorphological contexts and developed channel planforms and morphologies. It highlights the challenges emerging from the simulation of bank retreat for a complex, heterogeneous floodplain, and the need to develop fluvial models that are suitable for the study of complex river channels at intermediate spatiotemporal scales. In this research, the agreement seemed limited by the assumed homogeneity of soil properties for one of the two natural reaches examined. Although the developed model allows to vary spatially soil properties to represent soil properties with enhanced precision, we should

question if this is a viable strategy considering the scarcity of geotechnical and morphological datasets. Therefore, it is quite possible that the approach followed needs to be adjusted to enhance its applicability, or that alternative approaches such as that proposed by reduced-complexity models (Brasington and Richards 2007), be more appropriate in the case of highly complex fluvial environments. The model presented in this thesis can nevertheless be employed to identify the processes that could be omitted or simplified in subsequent models.

The coupled model suffers from the same limitation as its parents CFD model, which is to be limited in use to short spatiotemporal scales. This contrasts with the long time period over which meandering processes operate. Time compression was used in this study to get around this limitation (see Chapters 3–4) with an assumed correspondence between observed bank retreat over a period of several years and the hydrograph of a single hydrological event that caused bank retreat. The strategy employed worked fairly well with the shorter Medway Creek reach, but required a substantial manipulation of the imposed hydrograph for the longer and flatter St. François River reach considered (see Section 4d.2.3.1). Several additional strategies (e.g., parallel processing and a genetic algorithm; see Chapter 3) were used to reduce computation time; such features may become essential components of contemporary numerical models. In this study, machine learning algorithms strictly contributed to model calibration (see Chapter 4). These algorithms could also be integrated directly into morphodynamic models as a physics-based statistical model of bank retreat, which would reduce computation time.

Finally, a diversity of strategies was employed over the last decade to simulate lateral retreat and meandering processes (e.g., improvements of the linear HIPS formulation (Eke et al. 2014), integration of stochasticity (Posner and Duan 2012), implementation of an adaptive mesh (Langendoen et al. 2016) that would be exempt from mesh distortion in channels with substantial bank retreat (Lai 2017) (this could be solved by using a fractal design), coding of a universal genetic algorithm (see Chapter 3), integration of machine learning into the modelling process (see Chapter 4)). Combining these strategies and others, borrowed from disciplines that are not necessarily associated with fluvial geomorphology, could well be the key to improving fluvial models.

References

Abad JD, García MH (2006) RVR Meander: A toolbox for re-meandering of channelized streams. *Comput Geosci 32*: 92–101.

Abernethy B, Rutherfurd ID (1998) Where along a river's length will vegetation most effectively stabilise stream banks? *Geomorphology 23*: 55–75.

Abernethy B, Rutherfurd ID (2000) The effect of riparian tree roots on the mass-stability of riverbanks. *Earth Surf Proc Land 25*: 921–937.

Abernethy B, Rutherfurd ID (2001) The distribution and strength of riparian tree roots in relation to riverbank reinforcement. *Hydrol Proc 15*: 63–79.

Adhikari AR, Gautama MR, Yub Z, Imadaa S, Acharya K (2013) Estimation of root cohesion for desert shrub species in the Lower Colorado riparian ecosystem and its potential for streambank stabilization. *Ecol Eng 51*: 33–44.

Ai C, Jin S, Xing Y (2013) The influence of suspended load on 3D numerical simulation of flow and bed evolution in a meandering channel bend. *J Hydraul Eng 139*: 450–455.

Allen JRL (1985a) Sliding, rolling, leaping and making sand waves. In *Principles of Physical Sedimentology* (pp. 55–79). Caldwell, New Jersey: The Blackburn Press.

Allen JRL (1985b) Winding down to the sea. In *Principles of Physical Sedimentology* (pp. 91–100). Caldwell, New Jersey: The Blackburn Press.

Anderson RS, Anderson SP (2010) Rivers. In *Geomorphology: The Mechanics and Chemistry of Landscapes* (pp. 380–421). Cambridge, UK: Cambridge University Press.

Arcement GJ, Schneider VR (1989) Guide for selecting Manning's roughness coefficients for natural channels and floodplains (U.S. Geological Survey water-supply paper 2339). Department of the Interior, U.S. Geological Survey, Denver, United States.

Arthur B (1994) Increasing returns and path dependence in the economy. USA: University of Michigan Press.

Asahi K, Shimizu Y, Nelson J, Parker G (2013) Numerical simulation of river meandering with self-evolving banks. *J Geophys Res – Earth Surf 118*(1–2): 1–22.

Batalla RJ (1997) Evaluating bed-material transport equations using field measurements in a sandy gravel-bed stream, Arbúcies River, NE Spain. *Earth Surf Proc Land 22*: 121–130.

Bates BC, Kundzewicz ZW, Wu S, Palutikof JP. 2008. Climate Change and Water. Technical Paper of the Intergovernmental Panel on Climate Change. IPCC Secretariat: Geneva.

Bates PD, Anderson MG, Hervouet J-M, Hawkes JC (1997) Investigating the behaviour of two-dimensional finite element models of compound channel flow. *Earth Surf Proc Land 22*: 3–17.

Bates PD, Lane SN, Ferguson RI (2005) Computational Fluid Dynamics: Applications in Environmental Hydraulics, Wiley, New York.

Bathurst JC, Thorne CR, Hey RD (1979) Secondary flow and shear stress at river bends. *J Hydr Eng Div – ASCE 105*: 1277–1295.

Beatty J, Desjardins E (2009) Natural selection and history. *Biol Philoso 24*(2): 231–246.

Begnudelli L, Valiani A, Sanders BF (2010) A balanced treatment of secondary currents, turbulence and dispersion in a depth-integrated hydrodynamic and bed deformation model for channel bends. *Adv in Water Resources 33*: 17–33.

Bennett A (2004) Effects of emergent riparian vegetation on spatially averaged and turbulent flow within an experiment channel. In Bennett SJ, Simon A (Eds.) *Riparian vegetation and fluvial geomorphology* (pp. 29–41). Washington, DC: American Geophysical Union.

Bennett SJ, Pirim T, Barkdoll BD (2002) Using simulated emergent vegetation to alter stream flow direction within a straight experimental channel. *Geomorphology 44*: 115–126.

Bernhardt ES, Palmer MA, Allan JD, Alexander G., Barnas K, Brooks S, Carr J, et al. (2005) Ecology – Synthesizing US river restoration efforts. *Science 308*: 636–637.

Berterretche M, Hudak AT, Cohen WB, Maiersperger T K, Gower ST, Dungan J (2005) Comparison of regression and geostatistical methods for mapping Leaf Area Index (LAI) with Landsat ETM+ data over a boreal forest. *Remote Sens Environ 96*: 49–61.

Bertoldi W, Siviglia A, Tettamanti S, Toffolon M, Vetsch D, Francalanci S (2014) Modeling vegetation controls on fluvial morphological trajectories. *Geophys Res Lett 41*: 7167–7175.

Beven K (2006) A manifesto for the equifinality thesis. *J Hydrol 320*(1): 18–36.

Beven K, Freer J (2001) Equifinality, data assimilation, and uncertainty estimation in mechanistic modelling of complex environmental systems using the GLUE methodology. *J Hydrol 249*: 11–29.

Bindoff NL, Stott PA, AchutaRao KM, Allen MR, Gillett N, Gutzler D, Hansingo K, Hegerl G, Hu Y, Jain S, Mokhov II, Overland J, Perlwitz J, Sebbari R, Zhang X (2013) Detection and attribution of climate change: from global to regional. In Stocker TF, Qin D, Plattner G-K, Tignor M, Allen SK, Boschung J, Nauels A, Xia Y, Bex B, Midgley PM (Eds.) *Climate change 2013: The physical science Basis. Contribution of working group I to the Fifth Assessment Report of the Intergovernmental panel on climate change*. Cambridge, United Kingdom and New York, USA: Cambridge University Press.

Binns AD (2006) "Time-evolution and stability of the bed in sine-generated meandering streams: An experimental study." MSc thesis, Queen's University, Kingston, Canada.

Binns A, Ferreira da Silva A (2009) On the quantification of the bed development time of alluvial meandering streams. *J Hydraul Eng – ASCE 135*(5): 350–360.

Birch CPD (1999) A new generalized logistic sigmoid growth equation compared with the Richards growth equation. *Ann Bot – London 83*: 713–723.

Biron PM, Haltigin TW, Hardy RJ, Lapointe MF (2007) Assessing different methods of generating a three-dimensional numerical model mesh for a complex stream bed topography. *Int J Comput Fluid D 21*(1): 37–47.

Biron PM, Robson C, Lapointe MF, Gaskin SJ (2004) Comparing different methods of bed shear stress estimates in simple and complex flow fields. *Earth Surf Proc Land 29:* 1403–1415.

Biron PM, Haltigin TW, Hardy RJ, Lapointe MF (2007) Assessing different methods of generating a three-dimensional numerical model mesh for a complex stream bed topography. *Int J Comput Fluid D 21*(1): 37–47.

Bishop AW (1955) The use of the slip circle in the stability analysis of slopes. *Géotechnique 5*(1): 7–17.

Blanckaert K (2010) Topographic steering, flow recirculation, velocity redistribution, and bed topography in sharp meander bends. *Water Resour Res 46*: W09506.

Boavida I, Santos JM., Cortes RV, Pinheiro AN, Ferreira MT (2011) Assessment of instream structures for habitat improvement for two critically endangered fish species. *Aquat Ecol 45*(1): 113–122.

Bokulich A (2011) How scientific models can explain. *Synthèse 180*(1): 33–45.

Bokulich A (2013) Explanatory models versus predictive models: reduced complexity modeling in geomorphology. In *EPSA11 Perspectives and foundational problems in philosophy of science* (pp. 115–128). Springer International Publishing.

Bokulich A (2014) How the tiger bush got its stripes: 'How possibly' vs. 'how actually' model explanations. *The Monist 97*(3): 321–338.

Boussinesq J (1872) Théorie des ondes et des remous qui se propagent le long d'un canal rectangulaire horizontal, en communiquant au liquide contenu dans ce canal des vitesses sensiblement pareilles de la surface au fond. *J Math Pures Appl 17*:55–108.

Boussinesq JV (1871) Théorie générale des mouvements qui sont propagés dans un canal rectangulaire horizontal. *CR Acad Sc 73*: 256–260.

Bras RL, Tucker GE, Teles V (2003) Six myths about mathematical modeling in geomorphology. In Wilcock PR, Iverson RM (Eds.) *Prediction in geomorphology* (pp. 63–79). American Geophysical Union: Washington, DC.

Brasington J, Richards K (2007) Reduced-complexity, physically-based geomorphological modelling for catchment and river management. *Geomorphology 90*: 171–177.

Braudrick CA, Dietrich WE, Leverich GT, Sklar LS (2009) Experimental evidence for the conditions necessary to sustain meandering in coarse-bedded rivers. *P. Nat. Acad. Sci. USA 106*: 16936–16941.

Breiman L, Cutler A, Liaw A, Wiener M (2015) randomForest - Classification and regression based on a forest of trees using random inputs [computer software]. R package version 4.1–10.

Bridge J (2003) Rivers and floodplains: forms, processes, and sedimentary record. Oxford, UK: Blackwell Publishing.

Brooks HN (1963) Discussion of "Boundary shear stresses in curved trapezoidal channels" by AT Ippen, PA Drinker. *J Hydr Eng Div – ASCE 89*:327–333.

Camporeale C, Perona P, Porporato A, Ridolfi L (2005) On the long-term behavior of meandering rivers. *Water Resour Res 41*(12): W12403.

Camporeale C, Perucca E, Ridolfi L, Gurnell AM (2013) Modeling the interactions between river morphodynamics and riparian vegetation. *Rev Geophys 51*(3): 379–414.

Carboni J, Gatelli D, Liska R, Saltelli A (2007) The role of sensitivity analysis in ecological modelling. *Ecol Model 203*(1–2): 167–182.

Carmelo J, Murillo J, García-Navarro P (2013) Numerical assessment of bed-load discharge formulations for transient flow in 1D and 2D situations. *J Hydroinform 15*(4): 1234–1257.

Cartwright N (1983) How the laws of physics lie. Oxford: Clarendon Press.

CHC (2011) Blue Kenue Reference manual. Canadian Hydraulics Centre: Ottawa, Canada.

Chen D, Tang C (2012) Evaluating secondary flows in the evolution of sine-generated meanders. *Geomorphology 163–164*: 37–44.

Chu-Agor ML, Wilson GV, Fox GA (2008) Numerical modeling of bank instability by seepage erosion undercutting of layered streambanks. *J Hydraul Eng – ASCE 13*(12): 1133–1145.

Church M (1992) Channel morphology and typology. In: Calow P, Petts GE (Eds.) *The river's handbook: hydrological and ecological principles* (pp.126–143). Oxford: Blackwell.

Church M, Jones D (1982) Channel bars in gravel-bed rivers. In Hey RD, Bathurst JC, Thorne CR (Eds.) *Gravel-bed rivers* (pp. 291–325). New York: John Wiley & Sons.

Cleland CE (2001) Historical science, experimental science, and the scientific method. *Geology 29*(11): 987–990.

Collins DBG, Bras RL, Tucker GE (2004) Modeling the effects of vegetation-erosion coupling on landscape evolution. *J Geophys Res 109*: 1–11.

Constantinescu G, Koken M, Zeng J (2011) The structure of turbulent flow in an open channel bend of strong curvature with deformed bed: insight provided by detached eddy simulation. *Water Resour Res 47*: W05515.

Constantinescu G, Miyawaki S, Rhoads B, Sukhodolov A (2012) Numerical analysis of the effect of momentum ratio on the dynamics and sediment-entrainment capacity of coherent flow structures at a stream confluence. *J Geophys Res 117*: F04028.

Corti S, Pennati V (2000) A 3-D hydrodynamic model of river flow in a delta region. *Hydrol Process 14*(13): 2301–2309.

Coulthard TJ, Hicks DM, Van de Wiel MJ (2007) Cellular modelling of river catchments and reaches: Advantages, limitations and prospects. *Geomorphology 90*: 192–207.

Coulthard TJ, Neal JC, Bates PD, Ramirez J, de Almeida GAM, Hancock GR (2013) Integrating the LISFLOOD-FP 2D hydrodynamic model with the CAESAR model: implications for modelling landscape evolution. *Earth Surf Proc Land 38*(15): 1897–1906.

Coulthard TJ, Van de Wiel MJ (2006) A cellular model of river meandering. *Earth Surf Proc Land 31*: 123–132.

Coulthard TJ, Van de Wiel MJ (2012) Modelling river history and evolution. *Phil Trans R Soc A 370*: 2123–2142.

Cox NJ (2007) Kinds and problems of geomorphological explanation. *Geomorphology 88*: 46–56.

Crosato A (2007) Effects of smoothing and regridding in numerical meander migration models. *Water Resour Res 43*: W01401.

Crosato A (2009) Physical explanations of variations in river meander migration rates from model comparison. *Earth Surf Proc Land 34*: 2078–2086.

Crosato A, Desta FB, Cornelisse J, Schuurman F, Uijttewaal WSJ (2012) Experimental and numerical findings on the long-term evolution of migrating alternate bars in alluvial channels. *Water Resour Res 48*: W06524.

Crosato A, Saleh MS (2011) Numerical study on the effects of floodplain vegetation on river planform style. *Earth Surf Proc Land 36*: 711–720.

Cruslock EM, Naylor LA, Foote YL, Swantesson JOH (2010) Geomorphologic equifinality: A comparison between shore platforms in Höga Kusten and Fårö, Sweden and the Vale of Glamorgan, South Wales, UK. *Geomorphology 114*: 78–88.

Culmann C (1866) Grafische Statik, Zurich, Switzerland.

Da Silva AMAF (1999) Friction factor of meandering flows. *J Hydraul Eng 125:* 779–783.

Da Silva AMF, El-Tahawy T, Tape W (2006) Variation in flow pattern with sinuosity in sine-generated meandering streams. *J Hydraul Eng 132*(10): 1003–1014.

Darby SE, Alabyan AM, Van de Wiel MJ (2002) Numerical simulation of bank erosion and channel migration in meandering rivers. *Water Resour Res 38*(9): W1163.

Darby SE, Gessler D, Thorne CR (2000) Computer program for stability analysis of steep, cohesive riverbanks. *Earth Surf Pro Land 25*: 175–190.

Darby SE, Rinaldi M, Dapporto S (2007) Coupled simulations of fluvial erosion and mass wasting for cohesive river banks. *J Geophys Res 112*: F03022.

Darby SE, Van de Wiel MJ (2003) Models in fluvial geomorphology. In Kondolf GM, Piégay H (Eds.) *Tools in fluvial geomorphology* (pp. 503–537). West Sussex, England: John Wiley & Sons, The Atrium, Southern Gate, Chichester.

David PA (1985) Clio and the Economics of QWERTY. *The American economic review 75*(2): 332–337.

David PA (2007) Path dependence: a foundational concept for historical social science. *Cliometrica 1*(2): 91–114.

DeBarry PA (2004) Hydrogeomorphology. In *Watersheds: processes, assessment and management* (pp. 92–113). Hoboken, New Jersey: John Wiley & Sons.

Desjardins E (2011) Historicity and experimental evolution. *Biol Philos 26*(3): 339–364.

Dowling D (1999) Experimenting on theories. *Sci Context 12*(02): 261–273.

Duan JC, Julien PY (2010) Numerical simulation of meandering evolution. *J Hydrol 391*: 34–46.

Duan JG, Wang SSY, Jia YF (2001) The applications of the enhanced CCHE2D model to study the alluvial channel migration processes. *J Hydraul Res 39*(5): 469–480.

Dulal KP, Kobayashi K, Shimizu Y, Parker G (2010) Numerical computation of free meandering channels with the application of slump blocks on the outer bends. *J Hydro Environ Res 3*: 239–246.

Duncan M, Wright S (2005) Soil strength and slope stability. Hoboken, NJ: John Wiley & Sons.

Eaton BC, Giles TR (2009) Assessing the effect of vegetation-related bank strength on channel morphology and stability in gravel-bed streams using numerical models. *Earth Surf Proc Land 34*: 712–724.

EDF-R&D (2018, April 5) *open TELEMAC-MASCARET*. Retrieved from http://www.opentelemac.org

Egiazaroff IV (1965) Calculation of non-uniform sediment concentrations. *J Hyd Eng Div ASCE 91*: 225–248.

Eke E, Parker G, Shimizu Y (2014) Numerical modeling of erosional and depositional bank processes in migrating river bends with self-formed width: morphodynamics of bar push and bank pull. *J Geophys Res Earth Surf 119*: 1455–1483.

El Kadi Abderrezzak, Die Moran A, Tassi P, Ata R, Hervouet J-M (2016) Modelling river bank erosion using a 2D depth-averaged numerical model of flow and non-cohesive, non-uniform sediment transport. *Adv Water Resour 93*: 75–88.

Engelund F (1974) Flow and bed topography in channel bend. *J Hydraul Div – ASCE 100*(NHY11): 1631–1648.

Engelund F, Hansen E (1967) A monograph on sediment transport in alluvial streams. Teknisk Forlag, Denmark.

Evangelista S, Greco M, Iervolino M, Leopardi A, Vacca A (2015) A new algorithm for bank-failure mechanisms in 2D morphodynamic models with unstructured grids. *Int J Sediment Res 30*: 382–391.

Fäh R, Müller R, Rouselot P, Vetsch D, Volz C, Vonwiller L, Veprek R, and Farshi D (2011) System Manuals of BASEMENT Version 2.2. Retrieved from Swiss Federal Institute of Technology Zurich, Laboratory of Hydraulics, Glaciology and Hydrology (VAW): http://www.basement.ethz.ch

Federici B, Paola C (2003) Dynamics of channel bifurcations in noncohesive sediments. *Water Resour Res 39*(6): 1162.

Fellenius W (1927) Statistical analysis of earth slopes and retaining walls considering both friction and cohesion and assuming cylindrical sliding surfaces. W. Ernst und Sohn, Berlin, Germany (in German).

Ferreira da Silva AM, Ebrahimi M (2017) Meandering morphodynamics: insights from laboratory and numerical experiments and beyond. *J Hydraul Eng 143*(9): 03117005.

Ferreira da Silva AM, El-Tahawy C (2006) Location of hills and deeps in meandering streams: an experimental study. In Ferreira RML, Alves ECTL, Leal JGAB, Cardoso AH (Eds.) *River flow* (pp. 1097–1106). Taylor & Francis Group: London.

Fischer AM, Weigel AP, Buser CM, Knutti R, Künsch HR, Liniger MA, Schär C, Appenzeller C (2012) Climate change projections for Switzerland based on a Bayesian multi-model approach. *Int J Climatol 32*(15): 2348–2371.

Florsheim JL, Mount JF, Chin A (2008) Bank erosion as a desirable attribute of rivers. *Bioscience 58*(6): 519–529.

Fortin MJ, Drapeau P, Legendre P (1989) Spatial autocorrelation and sampling design in plant ecology. *Vegetatio 83*: 209–222.

Franz KJ, Butcher P, Ajami NK (2010 Addressing snow model uncertainty for hydrologic prediction. *Adv Water Resour 33*(8): 820–832.

Fredlund D, Krahn J, Pufahl D (1981) The relationship between limit equilibrium slope stability methods (Vol. 3, pp. 409–416). Presented at the International Conference on Soil Mechanics and Foundation Engineering, Stockholm, Sweden.

Friedkin J (1945) A laboratory study of the meandering of alluvial rivers. US Waterways Experiment station: Vicksburg.

Frigg R, Reiss J (2009) The philosophy of simulation: hot new issues or same old stew? *Synthese. 169*(3): 593–613.

Frothingham KM, Rhoads BL (2003) Three-dimensional flow structure and channel change in an asymmetrical compound meander loop, Embarras River, Illinois. *Earth Surf Proc Land 28*: 625–644.

Galland J-C, Goutal N, Hervouet J-M (1991) TELEMAC: A new numerical model for solving shallow water equations. *Adv Water Resour 14*(3): 138–148.

Gelfert A (2016) How to do science with models: a philosophical primer. Springer briefs in philosophy New York: Springer.

Geo-Slope International (2001a) SEEP/W for Finite Element Seepage Analysis, Version 5, User Manual. Calgary, Alberta.

Geo-Slope International (2001b) SLOPE/W for Slope Stability Analysis, Version 5, User Manual. Calgary, Alberta.

Goh, A. (1999). Genetic algorithm search for critical slip surface in multiple-wedge stability analysis. *Can Geotech J 36*(2): 382–391.

Gould SJ (1989) Wonderful life: The Burgess Shale and the nature of history. New York: W.W. Norton.

Green DW, Winandy JE, Kretschmann DE (2007) Mechanical properties of wood. In: The Enyclopedia of wood [technical report]. U.S. Department of Agriculture. Skyhorse Publishing, New York.

Gregow H, Ruosteenoja K, Pimenoff N, Jylhä K (2011) Changes in the mean and extreme geostrophic wind speeds in Northern Europe until 2100 based on nine global climate models. *International J Climatol 32*(12): 1834–1846.

Grenier RR Jr, Luettich RA Jr, Westerink JJ (1995) A comparison of the nonlinear frictional characteristics of two-dimensional and three-dimensional models of a shallow tidal embayment. *J Geophys Res 100*(C7): 13,719–13,735.

Groves DG, Lempert RJ (2007) A new analytic method for finding policy-relevant scenarios. *Global Environ Chang 17*(1): 73–85.

Grüne-Yanoff T, Weirich P (2010) The philosophy and epistemology of simulation: A review. *Simulat Gaming 41*(1): 20–50.

Güneralp I, Abad JD, Zolezzi G, Hooke J (2012) Advances and challenges in meandering channels research. *Geomorphology 163–164*: 1–9.

Güneralp I, Marston RA (2012) Process-form linkages in meander morphodynamics: bridging theoretical modeling and real world complexity. *Prog Phys Geog 36*(6): 718–746.

Haltigin TW, Biron PM, Lapointe MF (2007) Three-dimensional numerical simulation of flow around stream deflectors: The effect of obstruction angle and length. *J Hydraul Res 45*(2): 227–238.

Ham D, Church M (2012) Morphodynamics of an extended bar complex, Fraser River, British Columbia. *Earth Surf Proc Land 37*: 1074–1089.

Hardy RJ, Lane SN, Ferguson RI, Parsons DR (2003) Assessing the credibility of a series of computational fluid dynamic simulations of open channel flow. *Hydrol Process 17*: 1539–1560.

Hasegawa K (1977). Computer Simulation of the Gradual Migration of Meandering Channels. In *Proceedings of the Hokkaido Branch Japan Society of Civil Engineering* (pp. 197–202). Japan Society of Civil Engineering, Tokyo, Japan. (In Japanese)

Hasegawa K (1983) Hydraulic research on planimetric forms, bed topographies and flow in alluvial rivers. Ph.D. thesis, Hokkaido University, Sapporo, Japan.

Hervouet J-M (2007) Hydrodynamics of free surface flows modelling with the finite element method. Chichester, West Sussex, England: Wiley.

Howard AD (1996) Modelling channel evolution and flood-plain morphology. In Anderson MG, Walling DE, Bates PD (Eds.) *Floodplain processes* (pp. 15–62). Chichester, John Wiley & Sons.

Huang J, Greimann BP, Randle TJ (2014) Modelling of meander migration in an incised channel. *Int J Sediment Res 29*: 441–453.

Huang SL, Ng C-O (2007) Hydraulics of a submerged weir and applicability in navigational channels: Basic flow structures. *Int J Numer Meth Eng 69*(11): 2264–2278.

Hughes R (1999) The Ising model, computer simulation, and universal physics. In Morgan M, Morrison M (Eds.) *Models as mediators* (pp.97–145). Cambridge: Cambridge University Press.

Humphreys P (1994) Numerical experimentation. In: Humphreys P (Ed.) *Patrick Suppes: Scientific philosopher 2* (pp.103–121). Boston: Kluwer.

Humphreys P (2009) The philosophical novelty of computer simulation methods. *Synthese 169*(3), 615–626.

Ikeda S (1982) Lateral bed-load transport on side slopes. *J Hydr Eng Div – ASCE 108*(11): 1369–1373.

Ikeda SG, Parker G, Sawai K (1981) Bend theory of river meanders: 1. Linear development. *J Fluid Mech 112*: 363–377.

Istanbulluoglu E, Tarboton DG, Pack RT, Luce CH (2004) Modeling of the interactions between forest vegetation, disturbances, and sediment yields. *J Geophys Res – Earth Surf 109*(F1): F01009.

Iwasaki T, Shimizu Y, Kimura I (2016) Numerical simulation of bar and bank erosion in a vegetated floodplain: A case study in the Otofuke River. *Adv Water Resour 93*: 118–134.

Jacob F (1977) Evolution and Tinkering. *Science 196*(4295): 1161–1166.

Janin JM, Lepeintre F, Pechon P (1992) TELEMAC-3D: a finite element code to solve 3D free surface flow problems (HE-42/92.07). Électricité de France, Laboratoire National d'Hydraulique: Chatou, France.

Jia Y, Scott S, Xu Y, Wang SSY (2009) Numerical study of flow affected by bendway weirs in Victoria bendway, the Mississippi River. *J Hydraul Eng 135*(11): 902–916.

Jia Y, Wang SSY (2001a) CCHE2D: Two-dimensional hydrodynamic and sediment transport model for unsteady open channel flows over loose bed (NCCHE-TR-2001-1). Retrieved from the University of Mississippi, National Center for Computational Hydroscience and Engineering: http://www.ncche.olemiss.edu/

Jia Y, Wang SSY (2001b) CCHE2D: Verification and validation tests documentation (NCCHE-TR-2001-2). National Center for Computational Hydroscience and Engineering, University of Mississippi.

Jia Y, Zhang Y, Wang SSY (2011) Simulating bank erosion process using a depth averaged computational model. In: *Proceedings from the 7th IAHR Symposium on River, Coastal and Estuarine Morphodynamics*. Beijing, China.

Jiao Y, Neves R, Jones J (2008) Models and model selection uncertainty in estimating growth rates of endangered freshwater mussel populations. *Can J Fish Aquat Sci 65*(11): 2389–2398.

Johannesson H, Parker G (1989) Linear theory of river meanders. In Ikeda S, Parker G (Eds.) *River meandering* (pp. 181–214). Water Resour Monogr, vol. 12. AGU: Washington, D. C.

Jowett IG, Duncan MJ (2012) Effectiveness of 1D and 2D hydraulic models for instream habitat analysis in a braided river. *Ecol Eng 48*: 92–100.

Kamphuis JW, Gaskin PN, Hoogendoorn E (1990) Erosion tests on four intact Ontario clays. *Can Geotech J 27*: 692–696.

Kashyap S, Constantinescu G, Rennie CD, Post G, Townsend R (2012) Influence of channel aspect ratio and curvature on flow, secondary circulation, and bed shear stress in a rectangular channel bend. *J Hydraul Eng 138*(12): 1045–1059.

Kasvi E, Alho P, Lotsari E, Wang Y, Kukko A, Hyyppä H, Hyyppä J (2015) Two-dimensional and three-dimensional computational models in hydrodynamic and morphodynamic reconstructions of a river bend; sensitivity and functionality. *Hydrol Process 29*:1604–1629.

Kenefic L, Nyland RD (1999) Sugar Maple height-diameter and age-diameter relationships in an uneven-aged northern hardwood stand. *Northern Journal of Applied Forestry 16*(1): 43–47.

Keylock CJ, Constantinescu G, Hardy RJ (2012) The application of computational fluid dynamics to natural river channels: eddy resolving versus mean flow approaches. *Geomorphology 179*: 1–20.

Kleinhans M (2010) Sorting out river channel patterns. *Prog Phys Geog 34*: 287–326.

Kleinhans MG, Buskes CJJ, de Regt HW (2005) Terra incognita: explanation and reduction in earth science. *Int Stud Phil Sci 19*(3): 289–317.

Koch FG, Flokstra C (2–7 February 1981) Bed level computations for curved alluvial channels. At *XIXth Congress of the International Association for Hydraulic Research*: New Delhi, India.

Kuta RW, Annable WK, Tolson BA (2010) Sensitivity of field data estimates in one-dimensional hydraulic modeling of channels. *J Hydraul Eng 136*(6): 379–384.

Lai YG (2017) Modeling stream bank erosion: practical stream results and future needs. *Water 9*: 950.

Lai YG, Thomas RE, Ozeren Y, Simon A, Greimann BP, Wu K (20–24 May 2012) Coupling a two-dimensional model with a deterministic bank stability model. In *Proceedings from the ASCE World Environmental and Water Resources Congress* (pp. 1290–1300). Albuquerque, New Mexico, USA.

Lai YG, Thomas RE, Ozeren Y, Simon A, Greimann BP, Wu K (2015) Modeling of multilayer cohesive bank erosion with a coupled bank stability and mobile-bed model. *Geomorphology 243*: 116–129.

Lane SN, Bradbrook KF, Richards KS, Biron PM, Roy AG (1999) The application of computational fluid dynamics to natural river channels: Three-dimensional versus two-dimensional approaches. *Geomorphology 29*: 1–20.

Lane SN, Chandler JH, Porfiri K (2001 Monitoring river channel and flume surfaces with digital photogrammetry. *J Hydraul Eng 127*:871–877.

Lane SN, Hardy RJ, Ferguson RI, Parsons DR (2005) A framework for model verification and validation of CFD schemes in natural open channel flows. In: Bates PD, Lane SN, Ferguson RI (Eds.) *Computational Fluid Dynamics: applications in environmental hydraulics*. Wiley: New York, 169–192.

Lang P (2010) TELEMAC modelling system – TELEMAC-2D software v6.0 user manual. Retrieved from Électricité de France, Recherche et développement, Open TELEMAC-MASCARET: http://www.opentelemac.org

Langendoen EJ, Mendoza A, Abad JD, Tassi P, Wang D, Ata R, Abderrezzak KEk, Hervouet J-M (2016) Improved numerical modelling of morphodynamics of rivers with steep banks. *Adv Water Resour 93*: 4–14.

Langendoen EJ, Simon A (2008) Modeling the evolution of incised streams. II: Streambank erosion. *J Hydraul Eng 134*(7): 905–915.

Larsen L, Thomas C, Eppinga M, Coulthard T (2014) Exploratory modeling: extracting causality from complexity. *EOS 95*(32): 285–292.

Lau JK, Lauer TE, Weinman ML (2006) Impacts of channelization on stream habitats and associated fish assemblages in East Central Indiana. *Am Midl Nat 156*(2): 319–330.

Legleiter CJ, Kyriakidis PC, McDonald RR, Nelson JM (2011) Effects of uncertain topographic input data on two-dimensional flow modeling in a gravel-bed river. *Water Resour Res 47*: W03518.

Lenhard J (2007) Computer simulation: The cooperation between experimenting and modeling. *Philos Sci 74*(2): 176–194.

Levins R (1966) The strategy of model building in population biology. *Am Sci 54*(4): 421–431.

Li Y-C, Chen Y-M, Zhan TLT, Ling D-S, Cleall PJ (2010) An efficient approach for locating the critical slip surface in slope stability analyses using a real-coded genetic algorithm. *Can Geotech J 47*: 806–820.

Loheide SP, Booth EG (2011) Effects of changing channel morphology on vegetation, groundwater, and soil moisture regimes in groundwater-dependent ecosystems. *Geomorphology 126*(3–4): 364–376.

Lohnes R, Handy R (1968) Slope angles in friable loess. *J Geol 76*: 247–258.

Luppi L, Rinaldi M, Teruggi LB, Darby SE, Nardi L (2009) Monitoring and numerical modelling of riverbank erosion processes: A case study along the Cecina River (central Italy). *Earth Surf Proc Land 34*: 530–546.

Mäki U (2011) Models and the locus of their truth. *Synthese 180*: 47–63.

Malkinson D, Wittenberg L (2007) Scaling the effects of riparian vegetation on cross-sectional characteristics of ephemeral mountain streams: a case study of Nahal Oren, Mt. Carmel, Israel. *Catena 69*(2): 103–110.

Martin Y, Ham D (2005) Testing bedload transport formulae using morphologic transport estimates and field data: Iower Fraser River, British Columbia. *Earth Surf Proc Land 30*(10): 1265–1282.

Marsooli R, Wu W (2014) Three-dimensional numerical modeling of dam-break flows with sediment transport over movable beds. *J Hydraul Eng 141*:04014066.

Matsuura T, Townsend R (2004) Stream-barb installations for narrow channel bends - A laboratory study. *Can J Civ Eng 31*(3): 478–486.

Meyer-Peter E, Müller R (1948) Formulae for bed-load transport. At *2nd IARH Congress*. Stockholm: Sweden.

Micheli ER, Kirchner JW, Larsen EW (2004) Quantifying the effect of riparian forest versus agricultural vegetation on river meander migration rates, Central Sacramento River, California, USA. *Riv Res Appl 20*: 537–548.

Midgley TL, Fox GA, Heeren DM (2012) Evaluation of the bank stability and toe erosion model (BSTEM) for predicting lateral retreat on composite streambanks. *Geomorphology 145–146*, 107–114.

Millar RG (2000) Influence of bank vegetation on alluvial channel patterns. *Water Resour Res 36*(4): 1109–1118.

Minnesota Department of Transportation (MnDOT) (2015) Pavement design [technical report]. Office of materials and road research, Minnesota, United States.

Minor B, Rennie CD, Townsend RD (2007) 'Barbs' for River Bend Bank Protection: Application of a three-dimensional numerical model. *Can J Civ Eng 34*: 1087–95.

Mitsch WJ, Gosselink JG (2010) Wetlands, 3rd ed. John Wiley & Sons: New York, NY.

Moriasi DN, Arnold JG, Van Liew MW, Bingner RL, Harmel RD, Veith TL (2007) Model evaluation guidelines for systematic quantification of accuracy in watershed simulations. *Trans Asabe 50*(3): 885–900.

Morton A (1993) Mathematical models: questions of trustworthiness. *Brit J Phil Sci 44*(4): 659–674.

Morvan H, Pender G, Wright NG, Ervine DA (2002) Three-dimensional hydrodynamics of meandering compound channels. *J Hydraul Eng 128*(7): 674–682.

Mosselman E (1998) Morphological modelling of rivers with erodible banks. *Hydrol proc 12*: 1357–1370.

Mosselman E (2012) Modelling sediment transport and morphodynamics of gravel-bed-rivers. In Church MA, Biron P, Roy AG (Eds.) *Gravel bed rivers: processes, tools, environments* (pp. 101–115), John Wiley & Sons: New York.

Motta D, Abad JD, Langendoen EJ, Garcia MH (2012) A simplified 2D model for meander migration with physically-based bank evolution. *Geomorphology 163–164*: 10–25.

Mulligan M, Wainwright J (2013) Modelling and model building. In Wainwright J, Mulligan M (Eds.) *Environmental modelling: finding simplicity in complexity* (pp 7–73). Wiley, New York.

Murray AB, Paola C (2003) Modelling the effect of vegetation on channel pattern in bedload rivers. *Earth Surf Proc Land 28*: 131–143.

Naiman RJ, Fetherson KL, McKay SL (1998) Riparian forests. In Naiman RJ, Bilby RE (Eds.) *River ecology and management* (pp. 289–323). New York, NY: Springer-Verlag.

Nassar MA (2011) Multi-parametric sensitivity analysis of CCHE2D for channel flow simulations in Nile River. *J Hydro Environ Res 5*(3): 187–195.

Naval Facilities Engineering Command (NAVFAC) (1986) Design manual version 7.2 – Foundations and earth structures [technical report no. SN 0525-LP-300-7071]. Alexandria, Virginia.

Needelman M (2013) Évaluation du rôle des milieux humides dans l'espace de liberté par l'étude de la connectivité nappe-rivière [Master's thesis]. Université du Québec à Montréal, Montréal, Canada.

Nelson JM, Bennett J, Wiele SM (2003) Flow and sediment-transport modeling. In Kondolf GM, Piégay H (Eds.) *Tools in fluvial geomorphology* (pp. 539–576) Wiley: New York, USA.

Newham LTH, Norton JP, Prosser IP, Croke BFW, Jakeman AJ (2003) Sensitivity analysis for assessing the behaviour of a landscape-based sediment source and transport model. *Environ Model Softw 18*: 741–751.

Nicholas A (2013) Morphodynamic diversity of the world's largest rivers. *Geology 41*(4): 475–478.

Nicholas AP, Sandbach SD, Ashworth PJ, Amsler ML, Best JL, Hardy RJ, Lane SN, Orfeo O, Parsons DR, Reesink AJH, Sambrook Smith GH, Szupiany RN (2012) Modelling hydrodynamics in the Rio Paraná, Argentina: An evaluation and inter-comparison of reduced-complexity and physics based models applied to a large sand-bed river. *Geomorphology 169–170*: 192–211.

Nielsen M (1996) Lowland stream restoration in Denmark. In: A Brookes, FD Shields (Eds.) River channel restoration: Guiding principles for sustainable projects (pp. 269–289). Chichester, England: John Wiley & Sons.

Olsen NRB (2011) Three-dimensional numerical model for simulation of sediment movements in water intakes with multiblock option – User's manual. Retrieved from The Norwegian University of Science and Technology, Department of Hydraulic and Environmental Engineering: http://folk.ntnu.no/nilsol/ssiim/

Oreskes N, Belitz K (2001) Philosophical issues in model assessment. In Anderson MG, Bates PD (Eds.) *Model validation: perspectives in hydrological science* (pp. 23–41). Wiley: New York.

Oreskes N, Shrader-Frechette K, Belitz K (1994) Verification, validation, and confirmation of numerical models in the earth sciences. *Science 263*(5147): 641–646.

Osman AM, Thorne CR (1988) Riverbank stability analysis. I: Theory. *J Hydraul Eng 114*(2): 134–150.

Paola C, Straub K, Reinhardt L (2009) The "unreasonable effectiveness" of stratigraphic and geomorphic experiments. *Earth-Sci Rev 97*: 1–43.

Parker WS (2009) Does matter really matter? Computer simulations, experiments, and materiality. *Synthese 169*(3): 483–496.

Parker WS (2010) Predicting weather and climate: Uncertainty, ensembles and probability. *Studies in History and Philosophy of Science Part B: Studies in History and Philosophy of Modern Physics 41*(3): 263–272.

Parker WS (2011) Scientific models and adequacy-for-purpose. In *Modern Schoolman: A Quarterly Journal of Philosophy – Proceedings of the 2010 Henle Conference on Experimental & Theoretical Knowledge 87*(3–4): 285–293.

Parker G, Shimizu Z, Wilkerson GV, Eke EC, Abad JD, Lauer JW, Paola C, Dietrich WE, Voller VR (2011) A new framework for modeling the migration of meandering rivers. *Earth Surf Proc Land 36*: 70–86.

Parker C, Simon A, Thorne CR (2008) The effects of variability in bank material properties on riverbank stability: Goodwin Creek, Mississippi. *Geomorphology 101*: 533–543

Pasternack GB, Gilbert AT, Wheaton JM, Buckland EM (2006) Error propagation for velocity and shear stress prediction using 2D models for environmental management. *J Hydrol 328*: 227–241.

Paternoster R, Brame R, Mazerolle P, Piquero A (1998) Using the correct statistical test for the equality of regression coefficients. *Criminology 36*: 859–866.

Peakall J, Ashworth P, Best J (1996) Physical modelling in fluvial geomorphology: Principles, applications and unresolved issues. In Rhoads BL, Thorn CE (Eds.) *The Scientific Nature of Geomorphology – Proceedings of the 27th Binghamton Symposium in Geomorphology* (pp. 221–253). New York, NY: John Wiley & Sons.

Peakall J, Ashworth PJ, Best JL (2007) Meander-bend evolution, alluvial architecture, and the role of cohesion in sinuous river channels: a flume study. *J Sediment Res 77*: 197–212.

Perucca E, Camporeale C, Ridolfi L (2006) Influence of river meandering dynamics on riparian vegetation pattern formation. *J Geophy Res – Biogeosciences 111*(G1): G01001.

Perucca E, Camporeale C, Ridolfi L (2007) Significance of the riparian vegetation dynamics on meandering river morphodynamics. *Water Resour Resear 43*: W03430.

Pham TV, Fredlund DG (2003) The application of dynamic programming to slope stability analysis. *Can Geotech J 40*(4): 830–847.

Phillips JD (2006) Evolutionary geomorphology: thresholds and nonlinearity in landform response to environmental change. *Hydrol Earth Syst Sc 10*: 731–742.

Pierson P (2004), Politics in time: history, institutions, and social analysis. Princeton, N.J.: Princeton University Press.

Pittaluga M, Seminara G (2011) Nonlinearity and unsteadi-ness in river meandering: A review of progress in theory and modelling. *Earth Surf Proc Land 36*: 20–38.

Pollen N (2007) Temporal and spatial variability in root reinforcement of streambanks: Accounting for soil shear strength and moisture. *Catena 69*: 197–205.

Pollen-Bankhead N, Simon A (2010) Hydrologic and hydraulic effects of riparian root networks on streambank stability: Is mechanical root-reinforcement the whole story? *Geomorphology 116*: 353–362.

Pollen-Bankhead N, Simon A, Jaeger K, Wohl E (2009) Destabilization of streambanks by removal of invasive species in Canyon de Chelly National Monument, Arizona. *Geomorphology 103*(3): 363–374.

Posner AJ, Duan JG (2012) Simulating river meandering processes using stochastic bank erosion coefficient. *Geomorphology 163–164*: 26–36.

Press WH, Flannery BP, Teukolsky SA, Vetterling WT (1992) Numerical recipes in Fortran 77: the art of scientific computing, 2nd ed. Cambridge University Press, p. 214.

Pyrce RS, Ashmore PE (2005) Bedload path length and point bar development in gravel-bed river models. *Sedimentology 52*(4): 839–857.

Rameshwaran P, Naden P, Wilson CAME, Malki R, Shukla DR, Shiono K (2013) Inter-comparison and validation of computational fluid dynamics codes in two-stage meandering channel flows. *Appl Math Model 37*(20–21): 8652–8672.

Rantz SE et al. (1982) Measurement and computation of streamflow. Water Supply paper No. 2175: Vols. 1 and 2. U.S. Geological Survey: Washington, D.C.

Rameshwaran P, Naden P, Wilson CAME, Malki R, Shukla DR, Shiono K (2013) Inter-comparison and validation of computational fluid dynamics codes in two-stage meandering channel flows. *Appl Math Model 37*(20–21): 8652–8672.

R Core Team (2013) R: A language and environment for statistical computing. R Foundation for Statistical Computing, Vienna, Austria.

Rey F, Ballais J-L, Marre A, Rovéra G (2004) Role of vegetation in protection against surface hydric erosion. *C R Geosci 336*(11): 991–998.

Rhoads BL, Welford MR (1991) Initiation of river meandering. *Prog Phys Geog 15*: 127–156.

Rhoads BL, Thorn CE (1996) Observation in geomorphology. In Rhoads BL, Thorn CE (Eds.) *The scientific nature of geomorphology* (pp. 21–56). Chichester, England: John Wiley & Sons.

Riadh A, Goeury C, Hervouet J-M (2014) Telemac modelling system: TELEMAC-2D software v7.0 User's manual. Recherche et développement, Électricité de France: Chatou, France.

Richards K (2004) Sediment transport processes. In *Rivers: form and process in alluvial channels* (pp. 90–121). Caldwell, New Jersey: The Blackburn Press.

Rinaldi M, Mengoni B, Luppi L, Darby SE, Mosselman E (2008) Numerical simulation of hydrodynamics and bank erosion in a river bend. *Water Resour Res 44*(9): W09428.

Roache PJ, Ghia KN, White FM (1986) Editorial policy statement on the control of numerical accuracy. *J Fluid Eng-T ASME 108*: 2.

Rousseau YY, Van de Wiel MJ, Biron PM (2014a) Integration of a geotechnical model within a morphodynamic model to investigate river meandering processes. In Schleiss AJ, De Cesare GD, Franca MJ, Pfister M (Eds.) *River flow 2014 – International conference on fluvial hydraulics* (pp.1127–1133), Lausanne, Switzerland. CRC Press/Balkema; London, UK.

Rousseau YY, Biron PM, Van de Wiel MJ (2014b) Implementation of geotechnical and vegetation modules in TELEMAC to simulate the dynamics of vegetated alluvial floodplains. In Bertrand O, Coulet C (Eds.) *TELEMAC User conference* (pp.169–177), Grenoble, France. ARTELIA Eau & Environnement; Grenoble, France.

Rousseau YY, Biron PM, Van de Wiel MJ (2016) Sensitivity of simulated flow fields and bathymetries in meandering channels to the choice of a morphodynamic model. *Earth Surf Proc Land 41*(9): 1169–1184.

Rousseau YY, Biron PM, Van de Wiel MJ (2017) Simulating bank erosion over an extended natural sinuous river reach using a universal slope stability algorithm coupled with a morphodynamic model. *Geomorphology 295*: 690–704.

Rüther N, Olsen NRB (2007) Modelling free-forming meander evolution in a laboratory channel using three-dimensional computational fluid dynamics. *Geomorphology 89*(3–4): 308–319.

Rykiel EJ (1996) Testing ecological models: the meaning of validation. *Ecol Model 90*: 229–244.

Samadi A, Amiri-Tokaldany E, Darby SE (2009) Identifying the effects of parameter uncertainty on the reliability of riverbank stability modelling. *Geomorphology 106*: 219–230.

Schlichting H (1979) Boundary-layer theory, 7th Edition, trans. by J. Kestin. McGraw-Hill: New York and London.

Schumm SA, Khan HR (1971) Experimental study of channel patterns. *Nature 233*: 407–409.

Schwenk J, Lanzoni S, Foufoula-Georgiou E (2015) The life of a meander bend: Connecting shape and dynamics via analysis of a numerical model. *J Geophys Res – Earth Surf 120*: 690–710.

Seminara G (2006) Meanders. *J Fluid Mech 554*: 271–297.

Shen HW (1984) Examination of present knowledge of river meandering. In: Elliot, C.M. (Ed.) *River Meandering – Proceedings of the Conference Rivers '83*. American Society of Civil Engineers, New Orleans, New York, pp. 1008–1012.

Shimizu Y, Giri S, Yamaguchi S, Nelson J (2009) Numerical simulation of dune − Flat bed transition and stage-discharge relationship with hysteresis effect. *Water Resour Res 45*: W04429.

Shimizu Y, Inoue T, Hamaki M, Iwasaki T (2013) Nays2D solver manual. iRIC Project.

Sidle RC, Pearce AJ, O'Loughlin CL (1985) Hillslope stability and land use. *American Geophysical Union – Water Resource Monograph* 11: 63–65

Simon A, Bennett SJ, Neary VS (2004) Riparian vegetation and fluvial geomorphology: Problems and opportunities. In Bennett SJ, Simon A (Eds.) *Riparian vegetation and fluvial geomorphology* (pp. 1–10). Washington, DC: American Geophysical Union.

Simon A, Collison AJC (2002) Quantifying the mechanical and hydrologic effects of riparian vegetation on streambank stability. *Earth Surf Proc Land 27*: 527–546.

Simon A, Curini A, Darby SE, Langendoen EJ (2000) Bank and near-bank processes in an incised channel. *Geomorphology 35*: 193–217.

Simon A, Pollen N, Langendoen E (2006) Influence of two woody riparian species on critical conditions for streambank stability: Upper Trukee River, California. *J Am Water Resour As 42*(1): 99–113.

Smagorinsky J (1963) General circulation experiments with the primitive equations. *Monthly Weather Review 91*: 99–164.

Smith CE (1998) Modeling high sinuosity meanders in a small flume. *Geomorphology 25*: 19–30.

Strickler A (1923) Beiträge zur Frage der Geschwindigkeitsformel und der Rauhigkeitszahlen fur Ströme, Kanäle und Geschlossene Leitungen, Berna.

Sun T, Meakin P, Jossang T, Schwarz K (1996) A simulation model for meandering rivers. *Water Resour Resear 32*(9): 2937–2954.

Sun X, Shiono K, Rameshwaran P, Chandler JH (2010) Modelling vegetation effects in irregular meandering river. *J Hydraul Resear 48*: 775–783.

Swiss Standard SN 670 010b (1999) Characteristic coefficients of soils [technical report]. Association of Swiss Road and Traffic Engineers.

Tabacchi E, Lambs L, Guilloy H, Planty-Tabacchi A-M, Muller E, Décamps H (2000) Impacts of riparian vegetation on hydrological processes. *Hydrol Proc 14*: 2959–2976.

Tal M, Paola C (2010) Effects of vegetation on channel morphodynamics: Results and insights from laboratory experiments. *Earth Surf Proc Land 35*: 1014–1028.

Talmon AM, Van Mierlo MCLM, Struiksma N (1995) Laboratory measurements of the direction of sediment transport on transverse alluvial-bed slopes. *J Hydraul Res 33*(4): 495–517.

Tassi P, Villaret C (2014) Sisyphe v6.3 User's manual. Recherche et développement, Électricité de France: Chatou, France.

Termini D (2009) Experimental observations of flow and bed processes in large-amplitude meandering flume. *J Hydraul Eng 135*(7): 575–587.

The R Foundation (2018, April 4) The R Project for statistical computing. Retrieved from: https://www.r-project.org

Therneau T, Atkinson B, Ripley B (2015) rPart - Recursive partitioning for classification, regression and survival trees [computer software]. R package version 4.1-10.

Thomas RE, Pollen-Bankhead N (2010) Modeling root-reinforcement with a Fiber-Bundle Model and Monte Carlo simulation. *Ecol Eng 36*: 47–61.

Thompson DM (2006) Did the pre-1980 use of in-stream structures improve streams? A reanalysis of historical data. *Ecol Appl 16*: 784–796.

Thorne CR (1982) Processes and mechanisms of river bank erosion. In: Hey RD, Bathurst JC, Thorne CR (Eds.) *Gravel-bed rivers* (pp. 227–270) New York, NY: John Wiley & Sons.

Thorne CR (1990) Effects of vegetation on riverbank erosion and stability. In: Thorne CR (Ed.) *Vegetation and erosion* (pp. 125–144). New York, NY: John Wiley & Sons.

Thorne CR, Rais S (1984) Secondary current measurements in a meandering river. In: Elliot CM (Ed.) *River meandering – Proceedings of the conference rivers* (pp. 675–686) American Society of Civil Engineers: New York.

Thorne CR, Tovey NK (1981) Stability of composite river banks. *Earth Surf Proc Land 6*(5): 469–484.

Thorne CR, Zevenbergen LW, Pitlick JC, Rais S, Bradley JB, Julien PY (1985) Direct measurements of secondary currents in a meandering sand-bed river. *Nature 315*(6022): 746–747.

Tremblay M (2012) Caractérisation de la dynamique des berges de deux tributaires contrastés du Saint-Laurent: Le cas des rivières Batiscan et Saint-François. Master's thesis, Université de Montréal, Canada.

Tubbs CH (1977) Root-crown relations of young Sugar Maple and Yellow Birch. Research Note NC-225. USDA Forest Service.

Uhlenbrook S, Sieber A (2005) On the value of experimental data to reduce the prediction uncertainty of a process-oriented catchment model. *Environ Modell Softw 20*: 19–32.

University of Western Ontario (2006) Light Detection and Ranging (LIDAR) (Last Pulse) digitation elevation model [computer file].

Van de Wiel MJ, Coulthard TJ, Macklin M, Lewin J (2007) Embedding reach-scale fluvial dynamics within the CAESAR cellular automaton landscape evolution model. *Geomorphology 90*: 283–301.

Van de Wiel MJ, Darby SE (2004) Numerical modeling of bed topography and bank erosion along tree-lined meandering rivers. In: Bennett SJ, Simon A (Eds.) *Riparian vegetation and fluvial geomorphology* (pp. 267–282). American Geophysical Union: Washington, DC.

Van de Wiel MJ, Darby SE (2007) A new model to analyse the impact of woody riparian vegetation on the geotechnical stability of riverbanks. *Earth Surf Proc Land 32*: 2185–2198.

Van de Wiel MJ, Rousseau YY, Darby SE (2016) Modelling in fluvial geomorphology. In Kondolf GM, Piégay H (Eds.) *Tools in fluvial geomorphology 2nd edition* (pp. 383–411). Oxford: Wiley-Blackwell.

Van Dijk WM, Van de Lageweg WI, Kleinhans MG (2012) Experimental meandering river with chute cutoffs. *J Geophys Res 117*(F3).

Van Rijn LC (1984) Sediment transport, part I: bed load transport. *J Hydraul Eng 110*(10): 1431–1456.

Van Rijn LC (1989) Handbook: sediment transport by current and waves (H 461). Delft Hydraulics: Netherlands.

Verhaar PM, Biron PM, Ferguson RI, Hoey TB (2010) Numerical modelling of climate change impacts on Saint-Lawrence River tributaries. *Earth Surf Proc Land 35*(10): 1184–1198.

Verhaar PM, Biron PM, Ferguson RI, HoeyTB (2011) Implications of climate change in the twenty-first century for simulated magnitude and frequency of bed-material transport in tributaries of the Saint-Lawrence River. *Hydrol Proc 25*: 1558–1573.

Versteeg HK, Malalasekera W (1995) Turbulence and its modelling. In *An introduction to computational fluid dynamics* (pp. 41–84). Pearson Education Limited: Essex, England.

Vidal J-P, Moisan S, Faure J-B, Dartus D (2007) River model calibration, from guidelines to operational support tools. *Environ Modell Softw 22*: 1628–1640.

Villaret C (2010) SISYPHE 6.0 User manual (H-P73-2010-01219-FR). National hydraulic and environment laboratory, EDF R&D: Chatou, France.

Weihaupt JG (1974) Possible origin and probably discharges of meandering channels on planet Mars. *J Geophys Res 79*(14): 2073–2076.

Whiting PJ, Dietrich WE (1993) Experimental studies of bed topography and flow patterns in large-amplitude meanders. *Water Resour Res 29*(11): 3615–3622.

Whitlow R (1995) Stability of slopes. In *Basic soil mechanics 2* (pp. 346–393). New York, NY: John Wiley & Sons.

Wilcock PR (1996) Estimating local shear stress from velocity observations. *Water Resour Res 32*: 3361–3366.

Williams RD, Brasington J, Hicks DM (2016a) Numerical modelling of braided river morphodynamics: review and future challenges. *Geography Compass 10*(3), 102–127.

Williams RD, Measures R, Hicks DM, Brasington J (2016b) Assessment of a numerical model to reproduce event-scale erosion and deposition distributions in a braided river. *Water Resour Res 52*: 6621–6642.

Winsberg E (2003) Simulated experiments: Methodology for a virtual World. *Philos Sci 70*(1): 105–125.

Winsberg E (2009) A tale of two methods. *Synthese 169*(3): 575–592.

Winsberg E (2015) Computer simulations in science. In Edward N. Zalta (Ed.) *The Stanford encyclopedia of philosophy (Summer 2015 Edition)*. Retrieved from: http://plato.stanford.edu/archives/sum2015/entries/simulations-science/

Wu W, Vieira DA, Wang SSY (2004) One-dimensional numerical model for nonuniform sediment transport under unsteady flows in channel networks. *J Hydraul Eng 130*(9): 914–923.

Wu W, Wang SSY, Jia Y (2000) Nonuniform sediment transport in alluvial rivers. *J Hydraul Res 38*(6): 427–434.

Wu TH, Watson A (1998) In situ shear tests of soil blocks with roots. *Can Geotech J 35*(4): 579–590.

Xia J, Wang Z, Wang Y, Yu X (2013) Comparison of morphodynamic models for the Lower Yellow River. *J Am Water Resour As 49*(1): 114–131.

Xiao Y, Shao X-J, Wang H, Zhou G (2012) Formation process of meandering channel by a 2D numerical simulation. *Inter J Sed Res 27*: 306–322.

Xu D, Bai Y (2013) Experimental study on the bed topography evolution in alluvial meandering rivers with various sinuousnesses. *J Hydro Environ Res 7*: 92–102.

Youden WJ (1950) Index of rating diagnostic tests. *Cancer 3*: 32–35.

Zeller J (1967) Meandering channels in Switzerland. *International J Hydrol Sci 75*: 174–186.

Zeng J, Constantinescu G, Blanckaert K, Weber L (2008) Flow and bathymetry in sharp open-channel bends: experiments and predictions. *Water Resour Res 44*: W09401.

Zeng J, Constantinescu G, Weber L (2010) 3D calculations of equilibrium conditions in loose-bed open channels with significant suspended sediment load. *J Hydraul Eng 136*:557–571.

Zhu D-Y (2001) A method for locating critical slip surfaces in slope stability analysis. *Can Geotech J 38*(2): 328–337.

Zolezzi G, Seminara G (2001) Downstream and upstream influence in river meandering. Part 1. General theory and application to overdeepening. *J Fluid Mech 438*: 183–211.

Zolezzi G, Luchi R, Tubino M (2012) Modeling morphodynamic processes in meandering rivers with spatial width variations. *Rev Geophys 50*: RG4005.

Appendix A

Integration of a geotechnical model within a morphodynamic model to investigate river meandering processes

Yannick Rousseau, **Marco Van de Wiel** and **Pascale Biron**

River Flow: 1127–1133 (2014)

Abstract: Despite significant progress made in the research conducted to understand the morphodynamics of meandering rivers using computer models, a number of challenges and limitations remain with respect to simulating lateral river channel adjustments. In particular, some biophysical processes critical to bank erosion (e.g., related to soil and vegetation) are often neglected or oversimplified, proxy variables such as flow velocity are used to predict lateral migration rates, non-physical assumptions are frequently made to simulate channel cut offs, and channel and floodplain processes are commonly studied separately. The objective of this paper is not to address all of these issues, but to present a new geotechnical model that was integrated into a numerical morphodynamic model to include lateral erosion due to mass wasting. The model accounts for floodplain morphology and river bank hydrology, without compromising computational efficiency. The integrated geotechnical component includes a set of physics-based rules to quantify slope stability across the simulation domain. It is managed by a fully configurable universal genetic algorithm with tournament selection to efficiently calculate the spatial extent of block slumps whose slip surface profile is allowed to be planar, circular or irregular. This module is compatible with any type of mesh structure, making it suitable for the investigation of the dynamics of single- and multi-threaded river channels. Following bank failure, the fine material is assumed to be immediately entrained by the flow, whereas the coarse fraction is deposited along the formally unstable slope at the friction angle of the bank material. By keeping track of floodplain topography, and not solely of channel morphology, the model allows for preferential pathways to develop on the valley floor, which may affect both the direction and rate of channel migration.

A.1. Introduction

A.1.1. Meander dynamics

The characteristics of the flow field and sediment transport patterns in meandering river channels are fairly well understood due to the observations made over decades in flume, field and numerical experiments. For instance, instrumental measurements (e.g., Bathurst et al. 1979; Thorne and Rais 1984; Thorne et al. 1985; Frothingham and Rhoads 2003) and numerical simulations (e.g., Morvan et al. 2002) both demonstrated the existence of a helical flow in meander bends. The dynamics of planform development and evolution, however, remains less clear.

The irregularity of meander planform observed in nature is puzzling (Güneralp and Marston 2012) and corresponds to the knowledge gaps on river meandering processes. Processes and features deemed complex have historically been left out of the equation in studies pertaining to meander morphodynamics, at best assuming uniformity in the environmental conditions. The effects of heterogeneity and spatiotemporal variability in the floodplain conditions on planform evolution and on biophysical feedbacks are largely ignored (Güneralp et al. 2012; Güneralp and Marston 2012). But, more generally, there is a notable paucity of knowledge related to the feedbacks between channel morphodynamics and floodplain patterns and processes (Pittaluga and Seminara 2011; Güneralp and Marston 2012).

A.1.2. Morphodynamic modelling

River meandering morphodynamics has been studied using numerical models for many years (e.g., Ikeda et al. 1981). While certain features typical of this type of river planform were reproduced to a certain extent, some issues remain. Firstly, the idealized meander bends developed through numerical simulations depart from those observed in nature, the latter being fairly irregular (Shen 1984). This may be partly explained by the fact that many numerical models of meandering rivers focused on the initiation of channel meandering in the virtual environment (e.g., Duan et al. 2001; Asahi et al. 2013). It may also indicate that the available models are not holistic enough to take account of all the important features of the natural environment in which meandering rivers develop and evolve.

Secondly, the physics and river geometry are often greatly simplified to allow for simulations to run for longer temporal scales, with the consequence that important processes are not taken into account. As an example, although process simplification is required to study the long-term evolution of meandering rivers, the HIPS formulation (see Ikeda et al. 1981; Johannesson and Parker 1989;

Zolezzi and Seminara 2001) lumps the effects of hydraulic entrainment and mechanical bank failures into a single erodibility coefficient without physically describing the geotechnical processes that are responsible for lateral channel migration (Camporeale et al. 2005). The role of riparian vegetation in modifying river bank erodibility is generally not included in morphodynamic models (Malkinson and Wittenberg 2007). Other features that are challenging to deal with in a meandering model are the chute and neck cut offs, for which no analytical solution exists (Chen and Tang 2012). Finally, as a consequence of the geometrical constraints imposed by model design choices, a flat floodplain deprived from paleochannels is often assumed as the environment on which the single-threaded meandering channel will migrate. This prevents the creation of preferential pathways within an alluvial valley.

Most of the aforementioned issues could be addressed by more sophisticated models of bank retreat (Camporeale et al. 2005; Motta et al. 2012). In addition, developing and employing hybrid models that employ both reductionist and holistic approaches could help identifying patterns in the co-evolution of the river channel and floodplain (Güneralp et al. 2012). Finally, designing models in which the key features of a meandering river's environment can develop would certainly unlock the potential for morphodynamic models to tackle research questions related to the long-term evolution of these rivers (Crosato et al. 2012).

A.1.3. Challenges and opportunities

The morphodynamic simulations achieved within computational fluid dynamics (CFD) models are computationally intensive and commonly require a significant amount of time to complete due to the non-simplified set of equations governing the flow and to the finer spatial and temporal scales generally considered. An additional set of equations describes spatially-varied fluvial erosion. The consideration of lateral migration from a physically-based perspective (e.g., using the principles of limit equilibrium to evaluate slope stability) within a CFD model adds to the computational burden and discourages the use of such an integrated modelling solution to study the evolution of a river channel over long temporal scales.

There are nevertheless multiple reasons motivating the choice of a CFD model to examine river morphodynamics. Firstly, more powerful computers and more efficient models are now readily accessible and provide new opportunities to tackle complex river dynamics questions. Secondly, the current state of technology already makes it possible to devise a number of experiments aiming to better understand morphodynamic processes in a model that minimizes geometrical restrictions, is able to represent the 3D helical flow, and can deal with both in-channel and overbank flow (Howard

1996; Pittaluga and Seminara 2011; Güneralp and Marston 2012). This, in turn, would help developing hypotheses on the controls on river meandering (e.g., sedimentology, hydrological regime) and on the biophysical interaction of the river channel and floodplain (e.g., channel morphology vs. effects of bank and floodplain vegetation on the hydraulic field and mechanical soil reinforcement).

A bank migration module was designed and implemented within a CFD model by Duan et al. (2001) and Darby et al. (2002), to simulate bank advance and retreat along alluvial channels in a more realistic manner. Similarly, by developing a model that can simulate bank erosion, bank failures, point bar accretion and channel cutoffs, Asahi et al. (2013) explained the evolution in sinuosity and width of a meandering river, and examined the effects of flow magnitudes on the physiological characteristic of the developed river planform and channel bars. The fact that a greater number of modelling tools now integrate bank erosion as a physically-based process is likely to increase the number of studies using CFD to investigate morphodynamic problems.

A.1.4. Research objectives

This paper describes a physics-based, deterministic morphodynamic model that was developed to examine some of the questions and hypotheses related to river morphodynamics, which are difficult to tackle using existing meandering models due to the structural restrictions they impose on the simulation domain. In particular, this new model allows to simulate lateral river channel adjustments that can lead to the development of a meandering river planform geometry.

A.2. Model description

This section describes the geotechnical module that was developed and integrated into the hydraulic solver suite TELEMAC-MASCARET. This new module is divided into five components (Figure A.1). A *landscape analysis* algorithm (Section A.2.1) generates a network of transects along which slope stability assessments are performed during a morphodynamic simulation. This algorithm detects slopes anywhere across the simulation domain, and not strictly along the external river bank of meander bends. A *genetic algorithm* (Section A.2.2) searches for the geometry of the most likely failure profile along each transect. Another algorithm performs *slope stability assessment* (Section A.2.3) to obtain the safety factor associated with any potential failure profile. The geotechnical module also includes a *river bank hydrology manager* (Section A.2.4) that computes water table elevation in the floodplain, near the river bank. Finally, a *slump block analyzer removes* the unstable slump blocks, *deposits* the material downslope and *updates* the computational mesh (Section A.2.5).

These components work together to assess the geotechnical stability of a river channel and floodplain described by a triangular irregular network (TIN), subject to specific river flow conditions (free surface elevation), to include sediment transport through mass movement in addition to transport by fluvial processes.

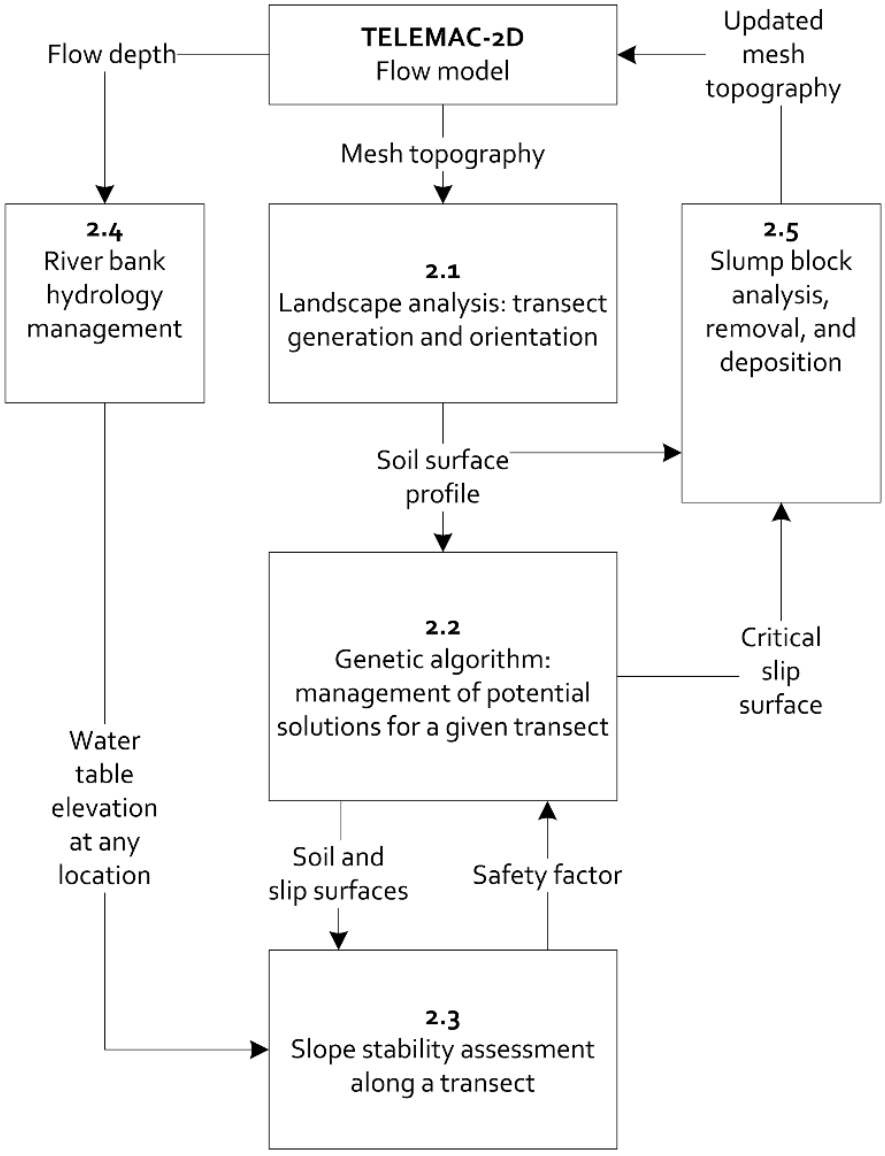

Figure A.1. Components of the geotechnical modules and coupling with TELEMAC

A.2.1. Landscape analysis

The geotechnical module presented in this paper was developed and coupled with TELEMAC to enable the examination of single- and multi-threaded channel dynamics within a CFD model as well as to provide a more holistic modeling tool for investigating the interactions between channel and floodplain processes.

The selected design, in particular the independence of the landscape stability assessment algorithm in respect to the computational mesh, allows geotechnical failures to occur at any location across the landscape. This fundamental feature of the module contrasts with the strategy implemented in most bank erosion models, where a body-fitted coordinate system is used to describe the bathymetry of a single-threaded channel, whilst the floodplain lacking topography and not considering the impact of previous erosion and deposition events (i.e., ignorance of paleo- and ephemeral channels). In these models, a stability assessment is achieved at each cross-section (corresponding to the longitudinal axis), which greatly simplifies stability assessment, but imposes constraints on the mesh structure, which renders the inclusion of complex floodplain processes challenging.

At each iteration of the geotechnical module, horizontal transects are generated, and spaced evenly along the x- and y-axes of the computational mesh. The length of transects, their spacing, and the number of points forming each one are specified by the user, albeit the module automatically adjusting transect length according to the location of domain boundaries. Following this, each transect is rotated until pointing in the direction of steepest ascent. This operation is necessary to avoid underestimating the gradient of hillslopes, and thus not properly detecting geotechnical instabilities. Finally, the length of each transect is adjusted by removing or adding nodes at both extremities until the computational mesh profile associated with the transect is monotonically increasing or decreasing, e.g., rising from channel bed to bank top (Figure A.2).

To improve computational efficiency, the geotechnical model can be configured to consider only those transects that are entirely submerged, entirely dry, or partially dry, i.e., located at the edge of the flow. This option is relevant to the investigation of landscapes in which the dry areas are assumed to be geotechnically stable. An example illustrating the outcome of the transect generation and orientation procedure for an entire simulation domain is given in Figure A.3.

A.2.2. Genetic algorithm

A critical slip surface, i.e., the interface between a block slump and the underlying more stable soil material, is commonly located using a grid search strategy. This procedure searches for the slip surface producing the lowest safety factor within a slope, considering a set of trial surfaces obtained by gradually varying geometrical characteristics. The genetic algorithm with tournament selection described in Li et al. (2010) was selected and implemented to maximize the efficiency of the slip search process. The aim was to design a single algorithm that would consider different slip surface shapes, namely planar, circular and non-circular, and which thus includes the mechanisms of mass movement resulting in the translation and rotation of the soil material. The current algorithm, however, imposes a monotonic slope to the critical slip surface, a constraint that will be removed in a subsequent version of the module.

The genetic algorithm is based on the theory of natural selection, whereby an optimal solution is allowed to 'evolve' out of a set of randomly chosen initial population of solutions. Each potential solution has a genetic makeup consisting of the points defining its geometry, such that a solution $\vec{S}$ with identifier *id* is represented by the vector:

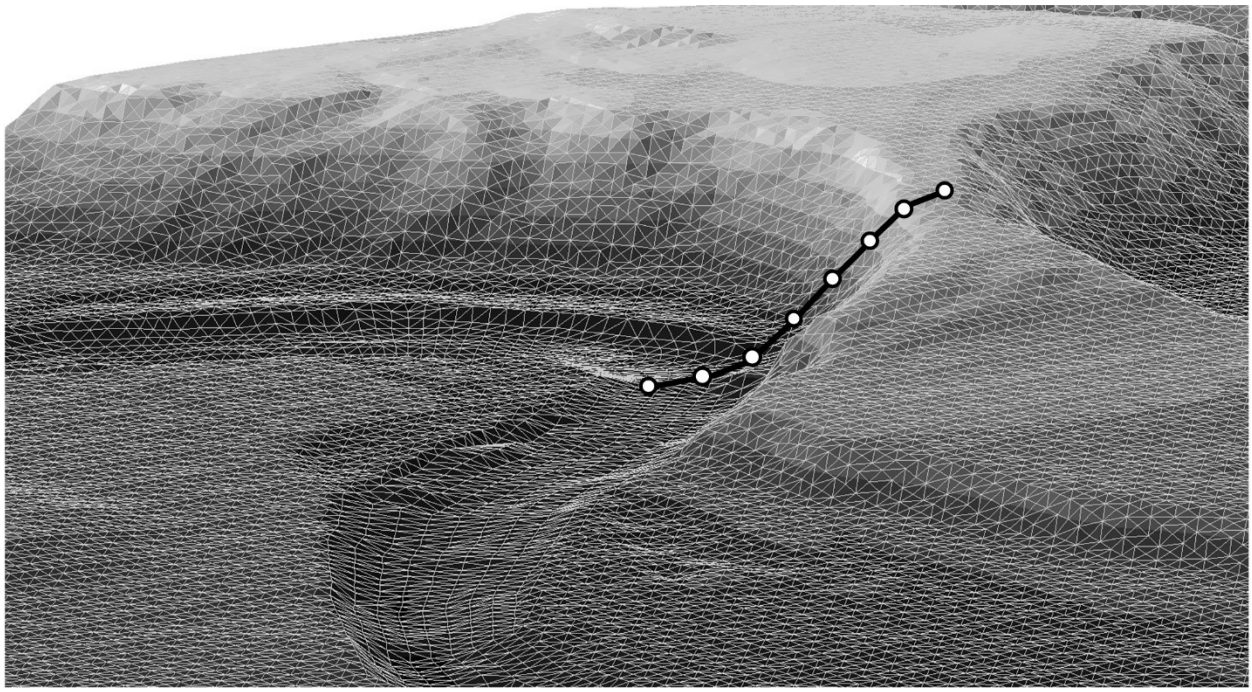

Figure A.2. Bird's-eye view of the computational mesh

It features a transect that consists of height nodes placed along a river bank for which a geotechnical analysis is to be performed.

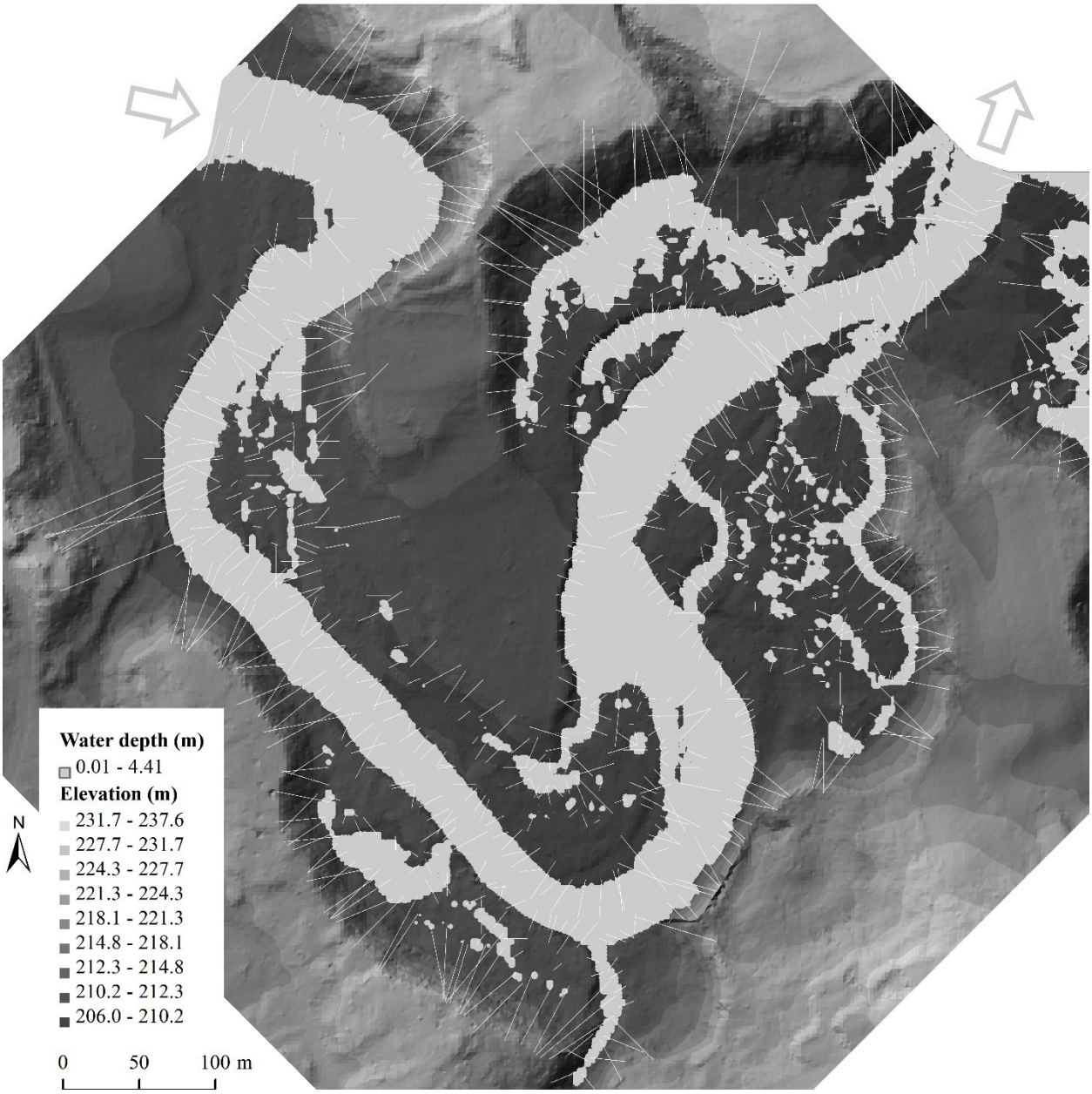

Figure A.3. Transect generation and orientation procedure

This is performed for a short reach comprised in the valley of the semi-alluvial Medway Creek, London, Canada. The topographic dataset is a combination of data acquired using LiDAR (floodplain) and centimeter-level differential GPS (main river channel) technologies. Flow depth is predicted with TELEMAC-2D and corresponds to a discharge of $70m^3/s$ (recurrence interval of 4.2 years). In this reach, mean channel width is 20m. The arrows indicate the location of the inlet and outlet, and flow direction. A horizontal spacing of 0.71 times the transect length (16m) is employed, which ensures a complete coverage of the landscape in the stability analysis. Only the partially submerged transects are shown.

$$\vec{S}_{id} = \{\vec{v}_1, \vec{v}_2, ..., \vec{v}_{n-1}, \vec{v}_n\} \quad \text{(A.1)}$$

A set of user-configurable rules dictate partner matching during cross-breeding. These are designed to optimize diversity, and thus reduce the time required to perform a stability assessment. The first rule ensures that two partners are not family relatives. A family policy then limits the permitted number of children per couple. Finally, an option allows partner exclusivity to be enabled or disabled.

The genetic algorithm converges to a solution when a minimum number of generations have been created and if no new fittest solution was found during the course of a second user-defined number of generations.

A.2.3. Slope stability assessment along a transect

The safety factor (F_s) is used to quantify the stability of a slope, assuming a given geometry of slip surface, i.e., the potential solutions generated by the genetic algorithm. The two-dimensional Bishop's method of slices is employed to perform the geotechnical evaluation (Figure A.4a). The following set of equations is solved iteratively:

$$F_s = \sum_{i=1}^{n} \frac{cb_i + \frac{[\sigma_i - U_i b_i]\tan\phi}{m_i}}{\tau_i} \quad \text{(A.2)}$$

$$\sigma_i = W_{s,i}\cos\beta_i + F_{cp,i}\cos\delta_i \quad \text{(A.3)}$$

$$\tau_i = W_{s,i}\sin\beta_i + F_{cp,i}\sin\delta_i \quad \text{(A.4)}$$

$$m_i = \cos\beta_i + \frac{\sin\beta_i \cdot \tan\phi}{F_s} \quad \text{(A.5)}$$

in which $W_{s,i}$ = weight of soil material in slice i; U_i = pore water pressure at the base of slice; b_i = slice width; $F_{cp,i} = W_{w,i}\cos\beta_i$ = confined water pressure exerted by the flow; $W_{w,i}$ = weight of water content; β_i = slice base angle; α_i = slice top angle; δ_i = angle between the result of hydrostatic confining force and normal to failure plane; ϕ = friction angle; m = a term in Bishop formula; and n = number of slices. A slope is expected to fail if the safety factor associated with its critical slip surface is less than 1.0.

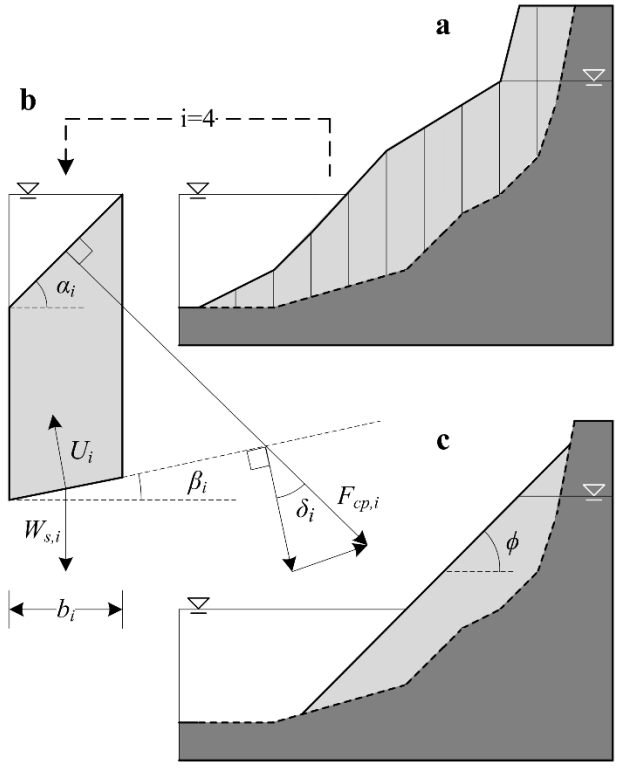

Figure A.4. Slope stability assessment in 2D using Bishop's simplified method of slices.

The light-shaded area represents the unstable portion of the river bank, whereas the dark-shaded portion is stable. The initially unstable river bank profile shown in **a)** is transformed into the profile shown in **c)** after disintegration of the slump block, entrainment of the finer particles by the flow, and deposition at the bank toe of the coarser sediment fraction at the friction angle ϕ. The forces acting on a slice *i* and the variables used in Equations A.2–A.5 are shown in **b)**.

A.2.4. River bank hydrology management

The soil material comprised in a slice may be partially or entirely saturated with water if the elevation of its base is located below the water table, thereby increasing its weight (W_s in Equations A.3–A.4) relative to that of its dry state. Thus, the elevation of the water table needs to be determined prior to calculating the weight of a slice. A river bank's water table responds slower to fluctuations in flow discharge than the river's water elevation. To account for the lag effect between flow and water table elevations, the following exponential function is used to calculate the elevation of the water table (z'_{wt}) at a time t=t_0+Δ_t:

$$z_{wt}' = z_{fs} - \left(z_{fs} - z_{wt}\right)e^{-k\Delta_t} \tag{A.6}$$

where z_{wt} and z'_{wt} = water table elevation at times t_0 and $t=t_0+\Delta_t$; z_{fs} = flow surface elevation at time t_0; and k = rate of convergence of the water table elevation toward z_{fs}. Note that the value of the constant k must be adjusted to take account of the hydraulic conductivity of the simulated floodplain, and thus of the rapidity by which it adapts to a change in the river's free surface elevation. Since a different response time is expected between the rising and falling stages of the water table (faster response during the rising than the falling limb), two k-values must be provided per simulation.

A.2.5. Slump block removal and deposition

Two options are available in the geotechnical module to determine the fate of the soil material comprised in a failing slump block. The first option assumes that the material is immediately disintegrated and entirely entrained by the flow. With the second option, the finer material (clay, silt, and sand) is entrained by the flow while the coarser fraction (gravel) is deposited downslope at the friction angle of the bank material. The latter option is illustrated in Figure A.4, assuming that the bank material consists of equal volumes of fine and coarse particles, a friction angle of 45º, and constant hillslope morphology along the river channel length. According to this scenario, the area of the slump block (zone in pale grey) is halved as a result of a mass wasting event (from Figure A.4a–A.4c).

An iterative procedure is employed to update the computational mesh following a slope failure event along an unstable transect. Note that the transects (used in the 2D geotechnical assessment) and the computational mesh (described in 3D) are comprised in two different layers. Hence, the location of a transect node generally does not coincide with that of a mesh node. In addition, mesh nodes are mobile vertically, but fixed laterally. Therefore, the nodes of the mesh elements overlaying the unstable transect nodes are displaced vertically until the difference in volume between the pre- and post-failure computational meshes matches the desired volume of eroded material (according to the fraction of fines), and in a manner such that the gradient of the updated mesh elements (along the transect) form a slope at the friction angle (e.g., Figure A.4c). A 3D solver is necessary to manage sediment deposition due to the morphological heterogeneity of landscapes (e.g., longitudinal variation in river bank morphology), and due to the option available in the geotechnical module that allows to determine the volume of material to be deposited downslope based on the fraction of coarse material in the slump block.

A.3. Discussion and conclusion

The geotechnical module presented in this paper was developed and integrated into the computational fluid dynamics model (CFD) TELEMAC to provide a physically-based tool to study the dynamics of alluvial rivers. The set of algorithms provide a universal and efficient solution to describe lateral channel erosion in a range of river environments (e.g., single- or multi-threaded), geomorphic features and evolutionary phenomena, without the need to define context-based assumptions and rules. This is mainly attributed to the fact that the geotechnical module performs stability assessments independently of the structure of the computational mesh, and considering the morphology of a landscape rather than solely that of a channel bed, keeping track of paleo-channels and considering secondary channels. Therefore, the module is suitable to the examination of interactions between a river channel and its floodplain.

The inclusion of a slope stability analysis that takes into account the elevation of the water table (which varies with a lag as a function of river flow depth) and the confining pressure of the flow provides a modelling solution that is well suited for the examination of meander morphodynamics in floodplains with cohesive soils, but also for the study of alluvial rivers in general. Since the use of CFD models results in computationally intensive simulations, a genetic algorithm was implemented to converge more quickly to a solution during geotechnical assessments.

Future work will consist in validating the model against datasets from real rivers. Particular attention will be given to the predicted location, magnitude and timing of river bank failures during isolated flow events and over periods of several months.

Appendix B

Implementation of geotechnical and vegetation modules in TELEMAC to simulate the dynamics of vegetated alluvial floodplains

Yannick Rousseau, **Pascale Biron** and **Marco Van de Wiel**

TELEMAC User Conference: 169–177 (2014)

Abstract: Amongst the most widely used computational fluid dynamics models, some include a sediment transport module that enables the examination of river channel dynamics. However, most ignore two families of processes influencing lateral erosion rates, and thus channel evolution mechanisms: lateral transport of sediment through mass wasting along river banks and valley walls, and soil reinforcement created by plant roots. A few modelling packages consider geotechnical processes, albeit with important limitations. Indeed, most solutions are solely compatible with single-threaded channels, impose a given computational mesh structure (e.g., body-fitted coordinate system), derive lateral migration rates from hydraulic properties, adjust bank morphology solely based on the angle of repose of the bank material, rely on non-physical assumptions to describe certain processes (e.g., channel cut offs in meandering rivers), and exclude floodplain processes. This paper describes the development and testing of two modules that were recently added to the mathematical suite of solvers TELEMAC-MASCARET to address the aforementioned limitations. The first module includes an algorithm that scans the computational domain in an attempt to detect potentially unstable slope profiles across the domain or intersecting with water-soil boundaries. The module relies on a fully configurable, universal genetic algorithm with tournament selection to delineate the shape of the surface along which a slump block detaches itself from a river bank or slope by translational or rotational mechanism. Both the hydrostatic pressure caused by the flow and the elevation of the water table are used in the Bishop's method to quantify slope stability. Another algorithm computes the surface of the coarse fraction of the block material which is deposited at the toe of the slope. The second module simulates the evolution of floodplain vegetation, whose properties affect the geotechnical stability of slopes present in the computational domain by imposing a surcharge and increasing soil cohesion near the soil surface. Plants develop in height,

weight and rooting depth at a rate that depends on the species and plant age. The two modules, combined with the flow and sediment transport models included in TELEMAC, provide a holistic solution to study the dynamics of a broad range of alluvial river types. The model is currently being tested, calibrated and validated using datasets from meandering rivers.

B.1. Introduction

Numerical models are frequently employed by researchers and practitioners to predict the morphodynamics of river channels (e.g., Rinaldi et al. 2008; Tal and Paola 2010; Ham and Church 2012). The sediment transport sub-model they include enables the computational mesh to evolve and allows researchers to elaborate hypotheses regarding the evolution of a river in the natural environment. However, existing models often do not have the capacity to simulate additional important river channel and floodplain processes. In particular, the mechanical effects of soil texture and riparian vegetation on geotechnical slope stability are largely ignored (Malkinson and Wittenberg 2007; Lai et al. 2012) despite their recognized key role in the evolution of river channels. Vegetation provides mechanical soil reinforcement (Abernethy and Rutherfurd 1998) whose magnitude varies with the density of the root network (Wu and Watson 1998), but also with soil texture, species, plant age, and location relative to stem or trunk (Van de Wiel and Darby 2007; Thomas and Pollen-Bankhead 2010). The magnitude of the reinforcement is attenuated by a large soil moisture content (Pollen 2007). The evolution of vegetation across the floodplain, and the species assemblage is influenced by stream hydrology, with vegetation density varying as a function of the distance to the river, elevation relative to the water table, and tolerance of plants to disturbance events such as flooding (Mitsch and Gosselink 2010; Perucca et al. 2007). Therefore, floodplain vegetation, river bank hydrology, and soil properties are known to influence lateral channel adjustments, but are often left out of the modelling experiments.

A large number of assumptions are used to simplify numerical calculations and reduce simulation times. For example, the HIPS formulation relies on an erodibility coefficient that combines lateral erosion rates due to fluvial entrainment and river bank failures (see Ikeda et al. 1981; Johannesson and Parker 1989; Zolezzi and Seminara 2001), thus making it impossible to isolate the specific causes for retreat and to "entirely" simulate long-term planimetric and morphological evolution due to the lack of analytical solution of neck/chute cutoff (Chen and Tang 2012). In addition, these models to not guarantee sediment continuity and ignore in-channel topography (Coulthard and Van de Wiel 2006). When riparian vegetation is considered, it only modifies flow conditions by altering bed roughness, although a few notable exceptions exist (e.g., Collins et al.

2004). In addition, the simulation domain in meandering models usually defines a channel deprived from a floodplain, ignoring the presence of a complex topography due to paleochannels and making it impossible for multiple threads to coexist.

This paper describes a new physics-based, deterministic model of channel-floodplain co-evolution that takes into account the biophysical context to examine the interaction between a river channel and its surrounding vegetated floodplain at the spatial scale of an extended river reach. In particular, this model simulates the lateral river channel adjustments that can lead to the development of meandering and wandering river planform geometries. The model integrates geotechnical processes into the TELEMAC computational fluid dynamics model, while taking into account hydraulic, biological and sediment processes for the floodplain as a whole. This paper also presents the results of sensitivity analyses conducted with the altered TELEMAC model. A reach along the semi-alluvial Medway Creek (London, Canada) is employed to examine the effects of soil texture and riparian vegetation cover on river bank stability and resulting topographic changes during a 4.2-year recurrence interval hydrological event.

B.3. Model description

B.3.1. Overview

A geotechnical module and a riparian vegetation module were developed and integrated into the hydraulic solver suite TELEMAC-MASCARET to include the transport of sediment through mass wasting and the effects of floodplain vegetation on river channel evolution. The transport of sediment by flow entrainment is included in the existing module SISYPHE. Since the geotechnical module was presented in detail in Rousseau et al. (2014a), this paper puts greater emphasis on describing the riparian vegetation module and explaining the interaction between the different modules of the coupled morphodynamic model (Figure B.1).

B.3.2. Geotechnical Module

The module is divided into five components (Figure B.1). A landscape analysis algorithm generates a network of transects along which slope stability assessments are performed during a morphodynamic simulation (G_1). This algorithm can be configured to detect potentially unstable slopes anywhere across the simulation domain, and not strictly along the external river bank of meander bends. A genetic algorithm searches for the geometry of the most likely failure profile along each transect (G_2). It is assisted by an algorithm that performs slope stability assessment to obtain

the safety factor associated with potential failure profiles (G_3). The geotechnical module also includes a river bank hydrology manager that computes water table elevation in the floodplain, near the river bank (G_4). Finally, a slump block analyzer removes the unstable slump blocks, deposits the material downslope and updates the computational mesh (G_5).

Landscape analysis (G1)

The geotechnical model evaluates the stability of the terrain along multiple transects placed evenly across the landscape. Each transect is oriented in the direction of the steepest ascent then shortened or stretched to extend from the lowest to the highest point in the current direction. An option is available to filter out transects that are not at least partially submerged.

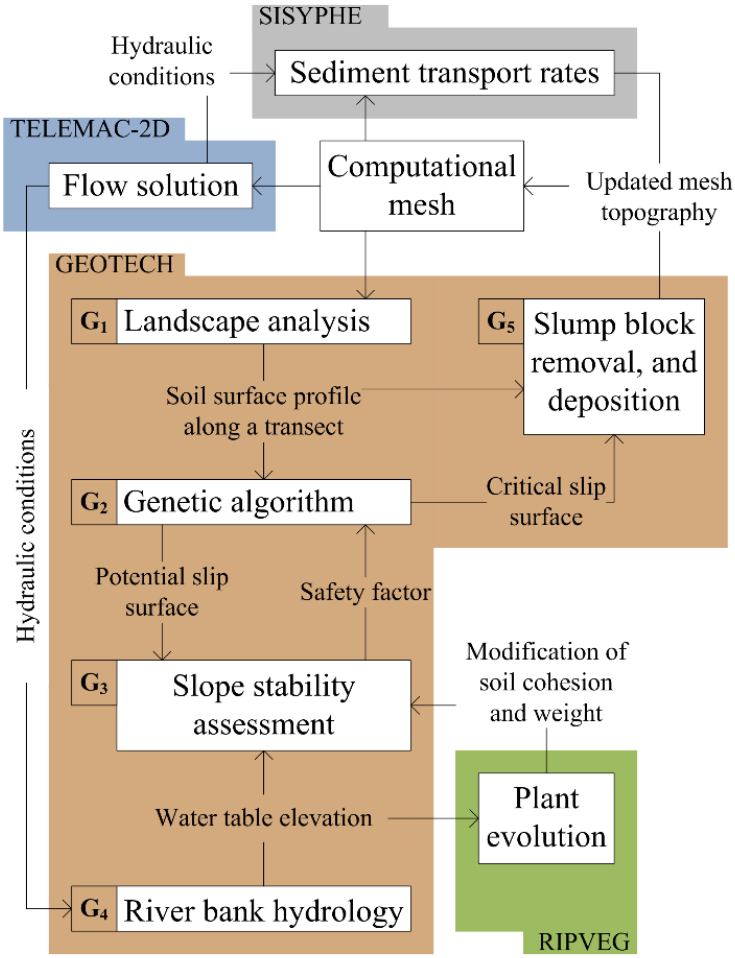

Figure B.1. Interaction between the modules of the morphodynamic module

Genetic algorithm (G2)

Any slope stability analysis includes an algorithm that devises a set of potential slip surfaces to be evaluated for their geotechnical stability. Assuming a two-dimensional analysis, we can define a solution with identifier id as a series of connected nodes delineating the lower limit of an unstable soil block, i.e., the dashed line in Figure 2a. Therefore, a solution can be described by the following vector:

$$\vec{S}_{id} = \{\vec{v}_1, \vec{v}_2, \ldots, \vec{v}_{n-1}, \vec{v}_n\} \tag{B.1}$$

where $\vec{v}_i$ is the node at rank *i* along a slip surface. The solution with the lowest F_s value is the most likely to occur.

Grid-search patterns are usually employed to list potential slip surfaces. For instance, this can be achieved by varying the location of the centre of the arc describing the shape of a circular slip surface, along with its radius. Here, a genetic algorithm with tournament selection, improved over the work of Li et al. (2010), was implemented in the geotechnical modules to converge toward a critical solution more rapidly. A solution *k* is created by combining two existing solutions, *i* and *j*, such that:

$$\vec{S}_k = \eta\vec{S}_i + (\eta - 1)\vec{S}_j \tag{B.2}$$

where $\eta = [0,1]$ is a randomly generated cross-over ratio. During cross-over, mutation has a probability of happening, in which case a randomly selected node comprised in solution *k* is displaced. A set of matching rules, namely partner exclusivity, child count policy, and prevention of breeding between relatives, allows the variability within the pool of solutions to be optimized. Finally, a user-specified migration rate dictates the probability for a solution to be created randomly rather than being the result of a cross-over.

In the current context, we can define a generation as the set of *n* solutions that were created from an initial population. After each generation, the most critical slip surface(s) are kept, the least critical are discarded, and new randomly selected surfaces survive to the next round. The search process terminates when the most critical slip surface remains unaltered for a number of consecutive generations.

Several parameters of this algorithm can be adjusted, including for the efficiency and accuracy of the stability assessments. The algorithm can generate planar, circular, and non-circular slip surfaces, all of which are monotonically increasing from slope toe to peak.

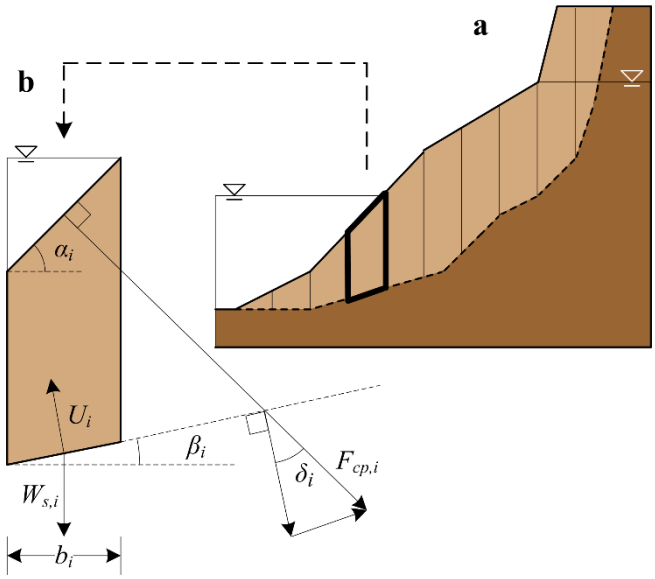

Figure B.2. Slope stability evaluation with Bishop's simplified method of slices

The light-shaded area represents the unstable portion of the river bank, whereas the dark-shaded portion is stable. The forces acting on **a)** slice *i* and the variables used in Equations B.3-B.6 are shown in **b**).

Slope stability assessment (G3)

The Bishop's method of slices (Figure B.2) is used to quantify the geotechnical stability of the soil along a transect. It can produce planar, circular and non-circular slip surfaces. The following set of equations must be solved:

$$F_s = \sum_{i=1}^{n} \frac{cb_i + \frac{[\sigma_i - U_i b_i]\tan\phi}{m_i}}{\tau_i} \tag{B.3}$$

$$\sigma_i = W_{s,i}\cos\beta_i + F_{cp,i}\cos\delta_i \tag{B.4}$$

$$\tau_i = W_{s,i}\sin\beta_i + F_{cp,i}\sin\delta_i \tag{B.5}$$

$$m_i = \cos\beta_i + \frac{\sin\beta_i \cdot \tan\phi}{F_s} \tag{B.6}$$

where $W_{s,i}$ = weight of soil material in slice i out of n; U_i = the pore water pressure at the base of a slice of width b_i, basal angle β_i and top angle α_i; δ_i = angle between the result of hydrostatic confining force and normal to failure plane; ϕ = friction angle of the soil material; and m = a term in Bishop formula. Pore water pressure is given by:

$$U = \frac{\rho g}{z_{wt} - z_b} \tag{B.7}$$

where ρ = water density, g = acceleration due to gravity, z_{wt} = elevation of the water table, and z_b = elevation at the base of a slice. The confined water pressured is given by:

$$F_{cp,i} = W_{w,i} \cos\beta_i \tag{B.8}$$

where $W_{w,i}$ = weight of water. Any solution resulting in a safety factor (F_s) lower than unity is said to be critical and is expected to result in a slope failure.

River bank hydrology (G4)

A saturated river bank, combined with a falling flow stage can trigger mass wasting events (Thorne 1982). To account for the lag effect between free surface and water table elevations, a simple river bank hydrology sub-model is used to calculate water table elevation. According to this sub-model, water table elevation (z'_{wt}) at a time $t=t_0+\Delta_t$ is given by:

$$z_{wt}' = z_{fs} - \left(z_{fs} - z_{wt}\right)e^{-k\Delta_t} \tag{B.9}$$

where t_0 = time at the previous iteration, Δt = time step, $t=t_0+\Delta t$ = time at the current iteration, z_{wt} = water table elevation at time t_0, z'_{wt} = water table elevation at time t; z_{fs} = flow surface elevation at time t_0; and k = rate of convergence of the water table elevation toward z_{fs}. The constant k is adjusted according to the hydraulic conductivity of the bank material, and thus represents the rapidity by which the water table adapts to a change in the river's flow stage. Two k-values are required per simulation: one for the rising limb of a flood hydrograph, and one for its falling limb.

Slump block removal and deposition (G5)

If the genetic algorithm calculates a safety factor below unity for a given transect, the unstable transect nodes relocate downward vertically (e.g., from the soil to the slip surface in Figure B.2a) and the computational mesh nodes (located in a different layer) adjust accordingly. It is assumed that the mesh nodes affected by a slope failure are those comprised in an elliptical zone having the length of the unstable section of the analysis transect and a user-defined relative width (i.e., a width-to-length ratio) (i.e., the red ellipse in Figure B.3a,c). A mesh node located along the edge of the ellipse or beyond will not be displaced vertically. Conversely, the displacement is greatest along the transect. Therefore, a mesh node located in the ellipse has a vertical displacement that is a linear function of

the distance between the edge of the ellipse and the transect, in the direction orthogonal to the transect, and thus that:

$$dz = dz_A \cdot \frac{d_B}{r_B \sqrt{1 - \left(\frac{d_A}{r_A}\right)^2}} \tag{B.10}$$

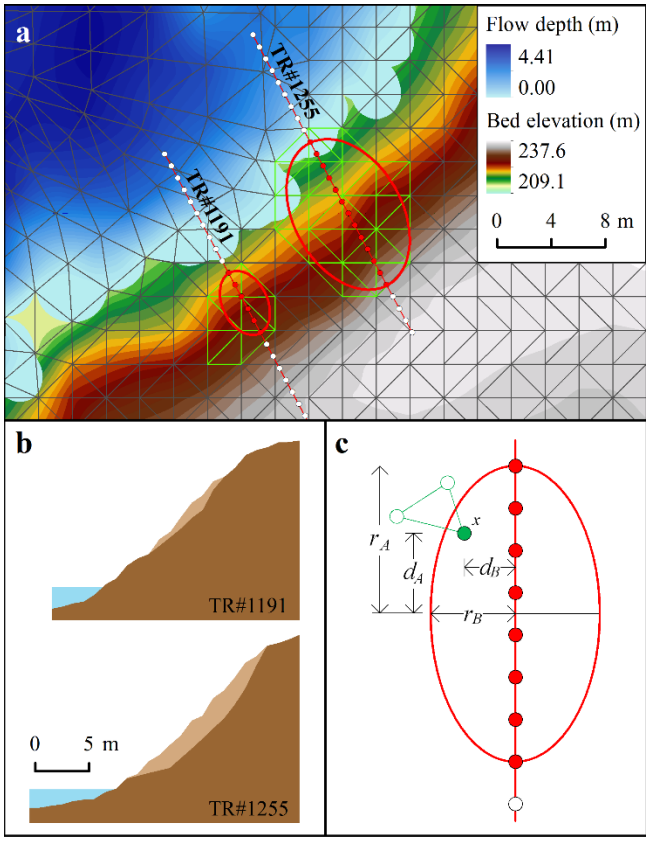

Figure B.3. Discretization of a failure block

a) Map illustrating the effects of two mass failures on the elements of the computational mesh of Medway Creek, London, Canada. The red nodes along the analysis transect represent the unstable nodes, whereas the white nodes are stable. The red ellipses are the zones in which the mesh nodes are affected by mass movement. Each element with a green edge includes at least one node that will need to be displaced downward vertically due to erosion. **b)** River bank profiles along the two analysis transects. The light-shaded area represents the unstable portion of the river bank whereas the soil in the dark-shaded zone is stable; the water level at the toe of each slope appears in blue. The elevation of the water table is assumed to be the same as that of the free surface of the flow. **c)** Measurements required to calculate the elevation change due to mass movement at a mesh node *x* in Equation B.10. The computational element shown in green needs to be updated since one of its three nodes falls within the erosion zone (i.e., the red ellipse).

where r_A and $r_B = r_A \cdot k_f$ = lengths of the semi-axes A and B, k_f= width-to-length ratio of all ellipses defining an erosion or deposition zone, d_A and d_B = distances from the ellipse's centre to the mesh node along each semi-axis, dz_A = elevation change at a distance d_A from the centre of the ellipse in the direction of the mesh node *x* along the axis A. The value of dz_A is obtained by interpolating elevation change at node *x* using the two nearest transect nodes.

The volume of soil eroded during a mass wasting event is calculated by subtracting the pre- and post-failure computational meshes. The geotechnical model allows to define the percentage of the soil material that is too coarse to be instantaneously entrained by the flow. The coarse fraction of the unstable slope material deposits in an elliptical zone at the toe of the slope at the friction angle.

B.3.3. Riparian vegetation module

The plant evolution module optionally generates an initial plant cover, manages plant growth, and transfers information to the geotechnical module regarding the plant properties that can influence the mechanical properties of the river bank at any given location. These properties are root depth, apparent cohesion due to roots, trunk height, and trunk width.

Representation and physiological properties

Although the module allows for multiple species to occupy a simulation domain, a single one is associated with each computational mesh node. Each plant is defined by its current and termination ages, which are defined at initialization of the plant cover.

The physical properties of a plant (i.e., at a mesh node) are species-dependent and are determined at run-time using species growth curves. These properties are plant type (none, herbaceous, shrubby, arboreal), trunk height diameter (at base and top) and length, life expectancy (mean and standard deviation), growth and decay rates, root cohesion and depth. Each value represents the magnitude of a property at maturity. In addition, the plants from each tree species are assumed to have a given wood density and spacing. All plants have user-specified resistances to flooding and to a lack of flooding. The latter properties allow to distinguish between terrestrial and aquatic plants and to represent the effects on plant succession of changes in water table elevation.

Initialization of cover

Plant cover can be initialized in different manners, depending on the option selected by the user. The first implemented method is the random generation of plants according to user-specified percentages for terrestrial and aquatic species. The initial plant age (a) is generated randomly, given the mean (μ_A) and standard deviation (σ_A) values associated with a species' life expectancy, and

assuming a normal distribution of ages within the simulation domain. The probability *P* for a species to be *a* years old is given by the normal cumulative distribution function:

$$P(a) = \frac{1}{2}\left[1 + erf\left(\frac{a - \mu_A}{\sigma_A\sqrt{2}}\right)\right] \tag{B.11}$$

where the error function (*erf*) is approximated using Press et al. (1992):

$$erf(x) = 1 - \tau \qquad \text{for } x \geq 0 \tag{B.12a}$$

$$erf(x) = \tau - 1 \qquad \text{for } x < 0 \tag{B.12b}$$

$$\tau = t \cdot e^{\left(\begin{array}{l}-x - 1.26551223 + 1.00002368t + 0.37409196t^2 \\ +0.09678418t^3 - 0.18628806t^4 + 0.27886807t^5 \\ -1.13520398t^6 + 1.48851587t^7 - 0.82215223t^8 \\ +0.17087277t^9\end{array}\right)} \tag{B.12c}$$

$$t = \frac{1}{1 + 0.5|x|} \tag{B.12d}$$

The second method relies on an input file that defines the likelihood of generating a plant of each species at each mesh node. This option is useful if the land cover is heterogeneous and requires zones with distinct species distributions to be defined. Note that this method relies on Equations B.11–B.12) to randomly generate plant ages. Finally, a third method reads an input file that defines the species code, along with the initial and termination ages of the plant at each node. This option is useful when land cover is known, or when running comparative simulations which require identical plant cover. Also note that this option must be used when continuing a simulation.

Growth, termination and succession

The generalized logistic sigmoid growth equation Birch (1999) is employed to describe the evolution of plant's physiological characteristics. This equation was found to represent well the growth of grazed plant communities, with a potential to relate its parameters to meaningful biological growth characteristics Birch (1999). This equation is given by:

$$y = Y\left[1 + e^{\left(d - R_y b(t/T - 0.5)\right)}\right]^{-1/b} \tag{B.13}$$

where y = magnitude of a plant physiological characteristic, Y = value of this characteristic at plant maturity, d = parameter to vary the time at which $y = Y/2$, t = time elapsed since germination, T = life expectancy, R_y = maximum rate of increase of y, b = parameter to modify symmetry. During our

simulation, parameter values of b = 1, d = 0, R_y = 10, and R_y = -10 were assigned to all plant species. Ideally, however, each species would be assigned a unique set of parameter values.

A plant dies if its roots are submerged (terrestrial plant) or not submerged (aquatic plant) for a prolonged period of time. At this moment, the plant starts decaying and a new plant of the same species starts growing. In nature, the roots of a decaying plant continue to enhance soil cohesion and the trunk continues to exert a downward force on the soil for a period of time after a plant dies Sidle et al. (1985). Growth and decay curves must, therefore, be combined to calculate plant properties (see the example in Figure B.4). This strategy is especially relevant in a case where the plants located in a frequently flooded area die at an age that is considerably smaller than their life expectancy. In that case, the biomass of the different plants decomposing (of the same species) must be combined to correctly account for the effects of roots and trunks.

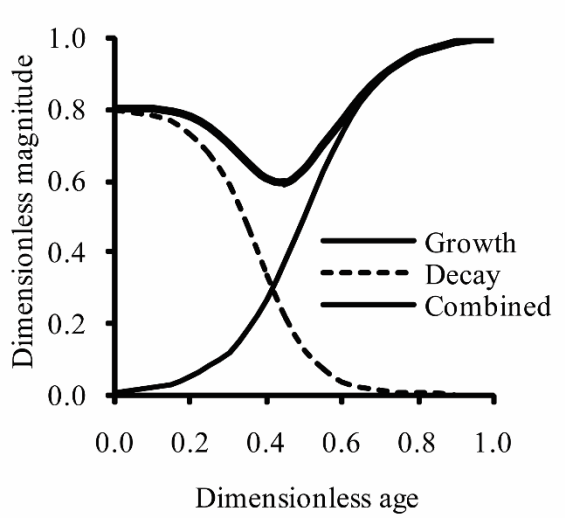

Figure B.4. Dimensionless growth curve

This assumes that the magnitude of a physical trait was at 80% of the maximum value (at maturity) when the plant died.

B.4. Exploration of model behaviour

B.4.1. Study reach and experiment

A 1.5 km reach of the semi-alluvial river Medway Creek, London, Canada, is employed to calibrate the coupled morphodynamics model and explore its sensitivity to variations in geotechnical and vegetation parameters. The channel is on average 20 m wide in this reach. A total of 69,073 mesh nodes (138,280 triangular elements) spread over an area of 440,808 m^2 (3.2 m^2 per element) describe the topography of the channel and floodplain (Figure B.5). A steady flow discharge of 70 m^3/s is used, which corresponds to a recurrence interval of 4.2 years. In the absence of data on

soil texture for this fine fraction for this reach, the soil was assumed to have the same texture as that along Dingman Creek, located near our study site and consisting of 24% clay, 61% silt and 13% sand Kamphuis et al. (1990). The coupled model was run for a single iteration, for multiple soil and vegetation configurations. This allowed the safety factor and eroded profile area (along each transect) for multiple combinations of soil and vegetation characteristics to be computed.

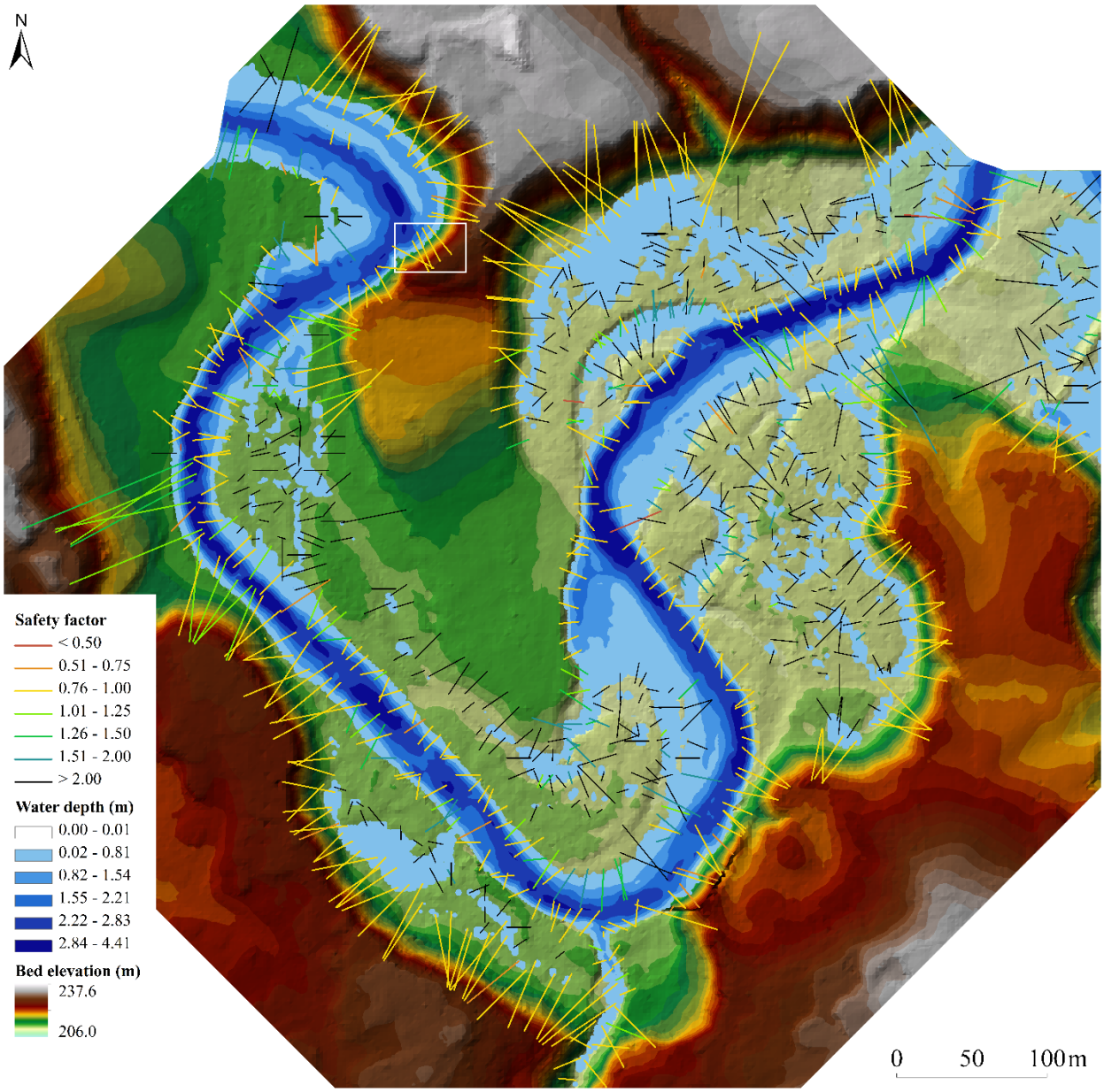

Figure B.5. Topography of the study site at Medway Creek

The white rectangle corresponds to the zone shown in Figure B.3c. The 960 transects generated for the geotechnical analyses are shown in black for stable slopes and in colour for the slopes that are expected to be unstable according to the most accurate simulation performed during the calibration of the genetic algorithm.

Simulations were carried out to test the sensitivity of key parameters in the coupled geotechnical-vegetation modules to variations in soil and plant cover properties. Three series of experiments were performed. First, the parameters of the genetic algorithm were calibrated to maximize the percentage of the slope failures detected and minimize simulation times. In a second experiment, the influence of grain size was evaluated. Mean grain size was varied from fine clay to fine sand, assuming moderate soil compaction for each grain size class and moderate stiffness for the clay fraction. Finally, in a third experiment, vegetation cover, in terms of plant type, species, and assemblage, was varied using the physiological plant properties defined in Simon and Collison (2002) and Adhikari et al. (2013). The selected plants are not found at our field site, and are unlikely to be all present in a single area. However, they are employed here to represent a range of values on root strength. The properties of the two grass species, four shrub species, and four tree species are summarized in Table B.1. The values of apparent cohesion are depth-averaged and exclude the roots below which the cohesion is lower than 0.25 kPa. In our simulations, the spacing between tree trunks of the same species is equal to the drip line, assumed to be 25% of plant height. All tree species have a diameter of 41 cm, a height of 18 m and a wood density of 0.94 g/cm^3.

Table B.1. Physiological properties of plants used in the geotechnical evaluations

Species		*Properties*	
Code	*Common name – Latin name*	*Root depth (m)*	*Apparent cohesion (kPa)*
A[a]	Gamma grass – Tripsacum dactyloides	0.6	6.40
B[a]	Switch grass – Panicum virgatum 'Alamo'	0.9	6.87
C[b]	Quail bush – Artiplex lentiformis	0.8	55.24
D[b]	Wolfberry – Lycium andersonii	0.5	54.60
E[b]	Creosote bush – Larrea tridentata	0.8	23.70
F[b]	Iodine bush – Allenrolfea occidentalis	0.7	21.41
G[a]	Sycamore – Platanus occidentalis	0.9	9.84
H[a]	River birch – Betula nigra	0.9	12.66
I[a]	Sweetgum – Liquidambar styroflora	0.8	6.64
J[a]	Black willow – Salix nigra	0.8	4.29

The superscript indicates data sources: **a)** Simon and Collison (2002) and **b)** Adhikari et al. (2013).

B.4.2. Calibration of genetic algorithm parameters

The sensitivity analysis of the genetic algorithm was achieved assuming moderated silt texture (0.031 mm) and moderate soil compaction. Depending on the combination of parameters used, between 290 and 364 failures were detected. The result of the latter combination is shown in Figure B.5. An accuracy of 95.9% was reached (i.e., detection of 95.9% of the failures) with a population size of 48 slip surfaces evolving over four generations, a 3-child-per-couple policy, no genetic restriction for parent matching, a migration rate of 65%, and a mutation rate of 12.5%. Due to the selected configuration, one individual of the population survives to the next generation, 31 are randomly generated (65% of 48), and 16 (the remainder to maintain population size) are created by cross-over. Since mutation only affects the individuals that were created by cross-over, the location of one node along the profile of two surfaces (12.5% of 16) is expected to be slightly altered. Once calibrated, the 960 cross-sections could be evaluated in 255 seconds using a high-performance notebook. Note that the model overestimates the number of slope failures that occur along the study reach for the selected flow discharge. Future efforts will include the analysis of soil samples from the study reach to accurately measure their geotechnical properties.

B.4.3. Variation in mean grain size

Three observations can be drawn from the grain size sensitivity analysis (Figure B.6). First the selected grain size affects both the number of slope failures and volume of eroded material. In the cases of silt- and sand-textured soils, the number of failures decreases with an increase in grain size. There is no clear trend for clay. The second observation is that the number of failure events is not correlated with the resulting amount of eroded material. It is for fine sand, but not for clay and fine sand. For instance, an increase in mean grain size for silt-textured soils results in a decrease in the number of block failures, but it has no effect on the total eroded area (Figure B.6). Finally, the eroded areas are orders of magnitude lower with clay soils. The sharp increase in the incidence of mass wasting events between clay and silt size classes may be due to the use of moderate stiffness and compaction with clay.

B.4.4. Variation in vegetation cover

Based on a series of paired two-tail *t*-tests, the number of failures is significantly different (α = 0.05) between all pairs of two plant species (Figure B.7), with the exception of three pairs: A–B (i.e., the herbaceous plants), C–D (i.e., two shrub species), and G–I (i.e., two tree species) (Table B.2). Due to the facts that the weight of shrub plants is neglected and the tree trunks were assumed to have

identical weights, a variation in apparent cohesion is expected to result in a significantly different number of mass wasting events. The conclusions are different when performing the same statistical analysis for the eroded areas. The predicted areas of the failure blocks are significantly different between herbaceous and tree plants, but not between herbaceous and shrub plants. Most of the shrub-tree pairs have significantly different eroded areas, whilst the other pairs are associated with a low *P* value ($0.05 \leq P \leq 0.10$). Note that a significant reduction in the eroded areas is noted for three out of four tree species, relative to a bare soil.

Using an aerial photograph including the area of the field site and multiple visits to the river reach and floodplain, zones with consistent land cover were delineated in a geographical information system. This allowed to attribute a percentage of bare soil, grass, shrubs, and trees to each zone of the vegetation layer, and thus to create the probability input file that can be used by the riparian vegetation module to initialize plant properties. A series of 32 simulations were launched to evaluate the sensitivity of the geotechnical stability to the selection of herbaceous, shrub and tree species

Table B.2. Similarity in failure predictions for different plant assemblages

	Species code[a]										
	ϕ[b]	A	B	C	D	E	F	G	H	I	J
ϕ[b]	-	**0.00**	**0.00**	**0.00**	**0.00**	**0.00**	**0.00**	**0.00**	**0.00**	**0.00**	**0.00**
A	0.45	-	0.75	**0.00**	**0.00**	**0.00**	**0.00**	**0.00**	**0.00**	**0.00**	**0.00**
B	0.38	0.98	-	**0.00**	**0.00**	**0.00**	**0.00**	**0.00**	**0.00**	**0.00**	**0.00**
C	0.66	0.73	0.73	-	0.44	**0.00**	**0.00**	**0.00**	**0.00**	**0.00**	**0.00**
D	0.22	0.67	0.65	0.35	-	**0.00**	**0.00**	**0.00**	**0.00**	**0.00**	**0.00**
E	0.59	0.83	0.81	0.91	0.54	-	**0.01**	**0.00**	**0.00**	**0.00**	**0.00**
F	0.97	0.43	0.49	0.71	0.23	0.61	-	**0.00**	**0.00**	**0.00**	**0.00**
G	**0.04**	**0.03**	**0.02**	0.05	**0.01**	0.05	0.06	-	**0.04**	0.96	**0.01**
H	0.09	**0.04**	**0.02**	0.06	**0.00**	0.09	0.10	0.92	-	**0.04**	**0.00**
I	**0.00**	**0.00**	**0.00**	**0.01**	**0.00**	**0.01**	**0.01**	0.30	0.34	-	**0.01**
J	**0.04**	**0.02**	**0.02**	**0.03**	**0.00**	**0.05**	**0.04**	0.76	0.66	0.50	-
	P-value (total eroded areas)										

P-value (number of failures)

P-values were obtained from the statistical analysis of differences between each pair of two species for the number of failures and total eroded areas. **a)** Species codes described in Table B.1. **b)** The symbol ϕ represents a lack of plant cover.

(Figure B.7). A total of 1056 *t*-tests were performed between each pair of two species assemblages, for the number of failures and total eroded areas, in order to verify the extent to which the selected species in an assemblage determines the geotechnical outcome.

Overall, the simulations with mixed vegetation cover resulted in fewer slope failure events and a reduced total eroded area with *P*-values of 0.019 and 0.001, respectively for each variable. This is consistent with previous students that found vegetated strips consisting of woody and grass species to be associated with enhanced soil strength Simon and Collison (2002) and Simon et al. (2006). With the species considered, our results suggest a weak influence of species assemblage on geotechnical stability, with 53/528 assemblages being significantly different for the number of failures and only 19/528 for the eroded areas. Whereas we noted significant differences in the case of single species (Figure B.6), we find here that the species composition of the vegetation assemblage is less critical (Figure B.7). For this experiment, we employed data from plant species that are not found on the field site, and thus, introduced error. However, the comparison of the different plant assemblages suggests that obtaining exact species physiological details may not be critical when this assemblage includes multiple plant types. Note also that the four species used in the simulations are deciduous, and thus that different results could have been obtained with coniferous trees, which tend to have shallower rooting systems.

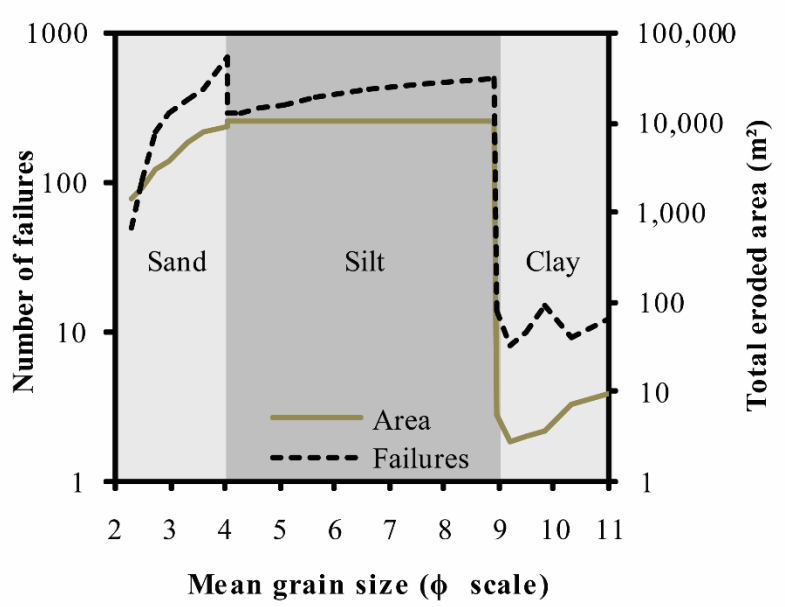

Figure B.6. Number of failures and eroded area as a function of mean grain size

This shows the effect on the number of failures detected and total eroded area of a variation in the mean grain size for clay, silt, and fine sand classes.

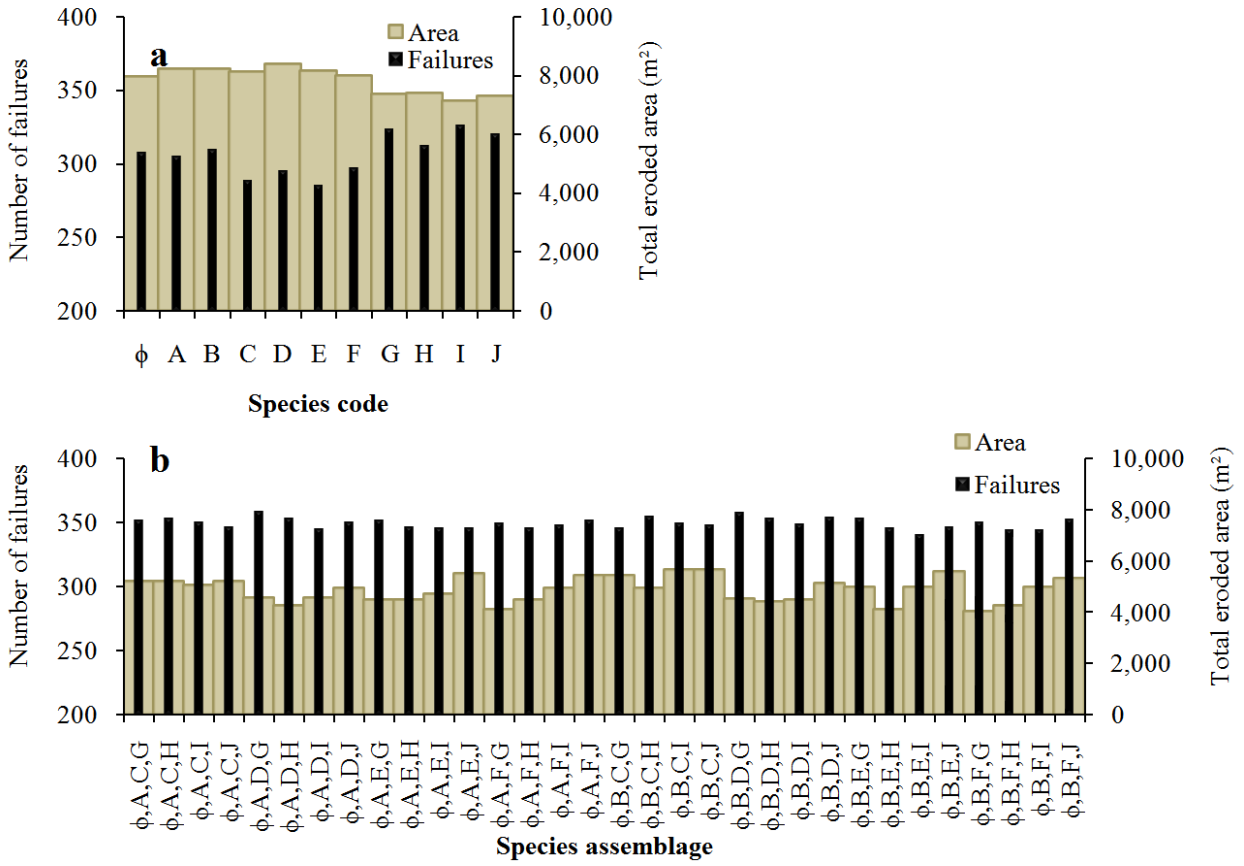

Figure B.7. Number of failures and eroded area as a function of vegetation

This shows the effect on the number of failures detected and total eroded area of a variation in **a)** plant species and **b)** assemblage of species. The code attributed to each species is listed in Table B.1. The symbol ϕ represents no plant cover.

B.5. Discussion and conclusions

B.5.1. Features, benefits and limitations of the new morphodynamic model

A geotechnical module and a riparian vegetation module were developed and coupled to TELEMAC to build a river morphodynamics model that includes a physical description of floodplain processes that are usually left out of the computational fluid dynamics models or embedded within non-tangible coefficients. The new modules allow the examination of a diversity of alluvial and semi-alluvial river channels and floodplains with limited impact on simulations times. This model offers the following features and benefits:

- Capacity to simulate river morphodynamics in single and multi-threaded channels.
- Independence of the slip search algorithm with respect to the structure of the computational mesh.
- History of previous erosion and deposition events that occurred on the floodplain embedded in the computation mesh.
- Fully configurable genetic algorithm to efficiently locate planar, circular and non-circular slip surfaces.
- The geotechnical and riparian vegetation modules can run separately or together.
- Consideration of water table elevation in river bank.
- Strong physical basis of the equations employed to simulate lateral erosion rates due to the inclusion of the two new modules in a CFD model.

B.5.2. Influence of soil texture and plant cover on slope stability

The improved morphodynamic model TELEMAC was used to evaluate the sensitivity of geotechnical stability to variations in mean grain size and species assemblage. The number of slope failures and the total eroded area were used to compare the outcome of the simulations. Our results indicate clear patterns in the case of silt- and sand-textured soils, but a more chaotic response for clayey soils. Statistical methods were used to evaluate the effect of different species and different assemblages of species on slope stability. We found important interspecies differences that influence more the number of slope failures detected than the total eroded areas. However, our experiment reveals fewer significant differences between species assemblages consisting of herbaceous, shrub and tree species.

B.5.3. Future development

The performance of TELEMAC coupled with the two modules described in this paper is currently being evaluated. The study reach along the semi-alluvial Medway Creek, London, Canada, is appropriate for that purpose since it exhibits a complex topography with islands and ephemeral channels forming and disappearing with changes in flow stage. It is also vegetated and is subject to bank retreat. The evaluation of the geotechnical module and the riparian vegetation module mainly consists in testing their robustness and efficiency in a variety of environmental contexts. Once calibrated, the model will need to be validated against time series of topographic datasets.

The structure of the developed riparian vegetation module is in its present form very simple. Two important limitations should be addressed in future versions: 1) bed roughness, which currently

remains uniform across the domain, should be calculated at runtime based on the characteristics of the vegetation cover; and 2) species at one mesh node, which currently remain the same throughout each simulation, should be allowed to vary to allow for newly created habitats to be colonized. Also, research on interactions between geomorphology and riparian ecology may benefit from the access to a model that can simulate competition between species. This competition could be implemented relatively easily by defining species-specific growth curves and tolerance to shade.